Republic of Iraq
Ministry of Higher Education
and Scientific Research
University of Babylon
College of Materials Engineering
Department of Metallurgical Engineering

Investigation Effects of MWCNTs Addition on Corrosion and Mechanical Behavior of High Entropy Alloys Thin Films for Low Alloy Steel 4140

A Thesis
Submitted to the Council of the Faculty of Materials Engineering / University of Babylon in a Partial Fulfillment of the Requirements for the Degree of Doctor of Philosophy in Materials Engineering / Metallurgical

By

Ahmed Saleh Abdul-Hussein Musarhad

(B.Sc. in Metallurgical Engineering , 2016)

(M.Sc. in Metallurgical Engineering , 2019)

Supervised by

Prof. Abdul Raheem K.Abid Ali (Ph.D)

2022 A.D. **1444 A.H**

جمهورية العراق
وزارة التعليم العالي والبحث العلمي
جامعة بابل
كلية هندسة المواد
قسم هندسة المعادن

تقصي تأثيرات اضافة الكاربون النانوي المتعدد الجدران على السلوك الميكانيكي والتأكل لسبائك الاغشية الرقيقة عالية العشوائية على الصلب السبائكي الواطئ ٤١٤٠

اطروحة
مقدمة إلى قسم هندسة المعادن في كلية هندسة المواد/ جامعة بابل
وهي جزء من متطلبات نيل درجه الدكتوراه فلسفة في
هندسة المواد/ معادن

من قبل

احمد صالح عبد الحسين مسرهد

بإشـــــراف

الأستاذ الدكتور
عبد ألرحيـــــم كاظم عبد علي

٢٠٢٢م **١٤٤٤هـ**

Supervisors Certificate

I certify that this thesis entitled "***Investigation Effects of MWCNTs Addition on Corrosion and Mechanical Behavior of High Entropy Alloys Thin Films for Low Alloy Steel 4140"*** was prepared by (***Ahmed Saleh Abdul-Hussein***) had been carried out under my supervision at the University of Babylon/ College of Material's Engineering / Department of Metallurgical Engineering in partial fulfillment of the requirements for the degree of doctor of Philosophy in Materials Engineering / Metallurgical Engineering

Signature :

Prof. Dr. Abdul Raheem K.AbidAli

(supervisor)

Date : / / 2022

بسم الله الرحمن الرحيم

وَمَنْ يَتَّقِ اللَّهَ يَجْعَلْ لَهُ مَخْرَجًا(٢) وَيَرْزُقْهُ مِنْ حَيْثُ لَا يَحْتَسِبُ ۚ وَمَنْ يَتَوَكَّلْ عَلَى اللَّهِ فَهُوَ حَسْبُهُ ۚ إِنَّ اللَّهَ بَالِغُ أَمْرِهِ ۚ قَدْ جَعَلَ اللَّهُ لِكُلِّ شَيْءٍ قَدْرًا (٣)

صدق الله العلي العظيم

(سورة الطلاق / آية ٢-٣)

Dedication

To

My parents

A strong and gentle soul who taught me to trust in Allah, believe in hard work and that so much could be done with little

To my lovely Wife

To my Brothers

To my Sisters

To My friends

With respect and love

Ahmed

2022

″Acknowledgement ″

First of all, profusely all thanks be for ALLAH who enable me to achieve this work.

I would like to express my sincere gratitude to my supervisor **Prof. Dr. Abdul-Raheem Kadhem Abid Ali**, for his continuous support in my PhD. study, and also for his scientific interest and valuable guidance for the completion of this work.

I wish to express my deepest thanks to the staff of laboratories of my department, Metallurgical Engineering and my College, Materials Engineering, for their help and good facilities.

I am grateful to my family , especially to my mother and father, my wife, and also to my brothers and my sisters for their assistance, encouragement and support during the period of preparing this work.

Ahmed Saleh Abdul-Hussein

2022

ABSTRACT

In this study, microstructure and properties of low alloy steel AISI (4140) by electrodeposition of medium and high entropy alloys thin films were studied. Specimens with dimensions (20 * 10 mm) have been prepared for coating. Medium entropy alloys (MEAs) of FeNiCoCu with and without the addition of 0.2% CNTs were deposition at current 0.16A, 30^{o}C temperature, for 15 minutes under magnetic stirring. At the same condition of MEAs, high entropy alloys (HEAs) of (AlFeCoNiCu) with and without CNTs addition were prepared. (MnCrFeCoNi) HEAs with/without CNTs were prepared at conditions like the MEAs except for the current which is equal to 0.4 A. Also, HEAs of six elements (AlCrFeCoNiCu) without and with 0.2 % CNTs at 0.63A current under 830rpm of stirring were deposited on 4140 steel.

Several tests such as microhardness, corrosion, adhesion, wear, surface roughness, contact angle, coating thickness, X-Ray diffraction, and the microstructure examination were studied for all coating specimens. Metallography was carried out by Field Emission Scanning Electron Microscope (FESEM) and Scanning Electron Microscope (SEM) with energy dispersive spectroscopy (EDS).

The best results of the microhardness were obtained for HEAs of (AlCrFeCoNiCu)-CNTs composite coating that reached 783 HV with improve percent of (75.8%) where the hardness increased as 2.5 times higher than the substrate. also, this specimen display the best value of corrosion rate which equals 1.15 mpy and the protective efficiency was enhanced for this composite coating by 92.8%.

HEAs of (AlCrFeCoNiCu)-CNTs composite coating also show the best result of adhesion and wear tests as compared with the other specimens that strength of adhesion reached 21.5 MPa and specific wear rate of (1.2, 1.4) *10^{-4} (mm^3/N.m) at (5, 10N) respectively.

The surface of MEAs of (FeNiCoCu) coating was the rough surface which reached 0.35µ that leading to a lower contact angle as compared to the other specimens. The AlCrFeCoNiCu HEAs show a large thickness of the coating layer which equal to18.36 µm .

The microstructure examination of the coating specimens shows that the morphology was dense, uniform, and homogeneous with granular grains that became finer when adding the CNTs. Also, the EDS test of coatings surface emphasizes containing all the constituent components of the alloys coating. Analysis of the XRD patterns revealed that all the coatings contained a mixture of BCC and FCC phases.

List of Contents

List of Abbreviations and Symbols

Abbreviations

Abbreviations	*Description*
AFM	Atomic Force Microscopy
AISI	American Iron And Steel Institute
ASTM	American Society For Testing and Materials
BCC	Body Centered Cubic
CALPHAD	Computer Coupling of Phase Diagrams and Thermochemistry
CFC	Corrosion-Fatigue Cracking
CNTs	Carbon Nano Tubes
EDS	Energy Dispersive Spectroscopy
EIC	Environmentally Induced Cracking
EIS	Electrochemical Impedance Spectroscopy
FCC	Face Centered Cubic
FESEM	Field Emission Scanning Electron Microscopy
GO	Graphene Oxide
HCP	Hexagonal Closed Pack
HEAs	High Entropy Alloys
HIC	Hydrogen-Induced Cracking
HVOF	High Velocity Oxy- Fuel
LPE	Lattice Potential Energy
MA	Mechanical Alloying
MPEAs	Multi-Principal-Element Alloys
MWCNT	Multi Walled Carbon Nano Tubes
N	No of Elements
SCC	Stress Corrosion Cracking

SDS	Sodium Dodecyl Sulfate
SWCNT	Single Walled Carbon Nano Tubes
XRD	X-Ray Diffraction

Symbols

Symbol	Description	Unit
A	Exposed Specimen Area	cm^2
AC	Alternating Current	Ampere
at.%	Atomic-Percentage	%
CR	Corrosion Rate	mpy
DC	Direct Current	Ampere
Eq	Equivalent Weight of Deposited Element	
F	Faraday Constant	Coulombs
I	Current Flow	Amperes
P_{eff}	Protection Effeceincy	
R	Ideal Gas Constant	J/K.mol
T	Temperature	C^o, K
t	Time	Sec.
W	Weight of Deposit	Gram
wt.%	Weight Percentage	
Xi	The Atomic Fraction	
ΔG_{mix}	Gibbs Free Energy of Mixing	KJ/mole
ΔS_{conf}	Configurational Entropy	J/K
ρ	Density	g/cm^3
Ω	Dimensionless Parameter	
ΔH_{mix}	Enthalpy Of Mixing	J/K. mole

Chapter One

Introduction

Chapter One: Introduction

1-1 General View

One of the fundamental and practically oriented tasks of solid-state physics and physical materials science is the development of physical bases of creating new metallurgical materials with a complex of necessary physico-mechanical and operational properties and technologies of their production. As it is known, mechanical properties of materials depend essentially on their chemical composition and characteristic features of the structural state, such as type, grain size, form of their boundaries, grade, quantity and distribution in size and volume of excessive phases, density and type of dislocation substructure, etc [1].

Metallic systems are continuously being developed for improved properties such as high yield strengths, enhanced ductility, good thermal properties, for various technological applications such as in aerospace, energy and nuclear engineering [2], [3], [4]

Ashby map shown in Figure (1.1) gives a panoramic view of the development in the use of materials over 10 millennia. A graphic depiction of the different classes of materials from ceramics to metals, polymers, and more recently to composites is vividly displayed. The passage from discovery through development to design of materials can be noted [5]. Traditional or conventional alloying involves one or two elements with similar chemistries with either interstitial or substitutional alloying following the Hume-Rothery rule of solvent-solute mixing [6].

Multi-component alloys of the composition Fe20Cr20Ni20Mn20Co20 which gave a single FCC structure explored by Cantor while Yeh explored different combinations of several elements such as Cu, Ti, V, F, Ni, Zr, Al,

Mo, Co, which showed improved properties in hardness and strength when more elements were added. The multi-component alloys had strengths about three times greater than Hastelloy C, Stellite 6 and Ti-6Al-4V. Simple crystal structures, FCC, BCC or a combination of both, were also observed depending on the combining elements [7][8].

High-entropy alloys (HEAs) are described as a relatively novel class of material which have multiple principal elements in equi-molar or near equi-molar ratios (5 to 35 molar % of each components) that form stable solid solutions because of the large mixing entropies [8].

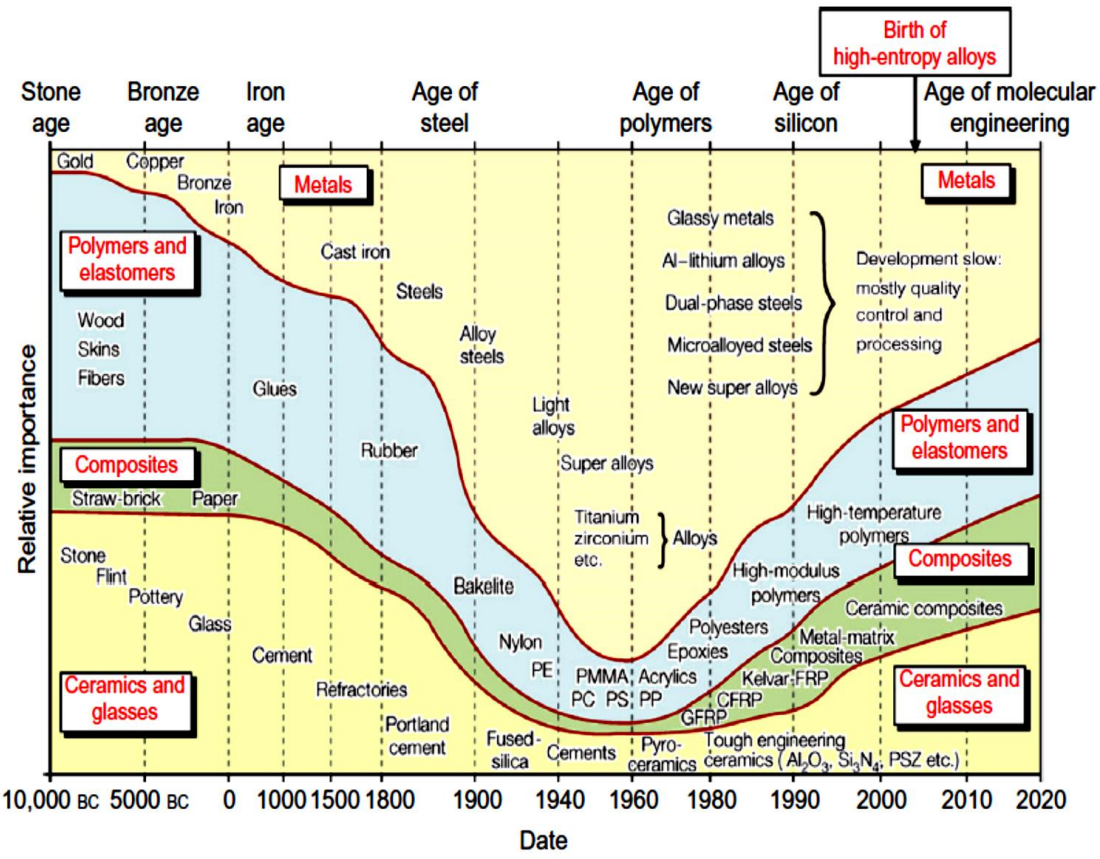

Figure (1.1): Historical evolution of engineering materials—marked with the birth of HEAs published in Advanced Engineering Materials [5]

HEAs have four core effects that set them apart from the conventional alloys. The core effects are high entropy effect, severe lattice distortion effect, sluggish diffusion effect, and cocktail effect [8],[9]. High entropy effect can be understood from multi-component alloys having medium $\Delta Hmix$ and highest $\Delta Sconf$ [5], [9]. Enthalpy plays a role in the phase stability of HEAs, multi-component metallic system with systems having medium $\Delta Hmix$ causes unlike pairs in the solid solution, while systems with large positive $\Delta Hmix$ can lead to elemental phase separations, for example, in Cu- containing HEAs. This further indicates that the high entropy effect is essentially related to the interplay of enthalpy of mixing and configurational entropy[10][11].

1-2 High Entropy Alloy Types

HEAs are mostly classified based on their composition and functional properties. HEAs represent a class of metallic materials containing typically five or more principal alloying elements in equiatomic or near equiatomic proportions which known as equiatomic HEAs. The non-equiatomic HEAs represent a class of materials having alloying elements in non-equiatomic proportions. A five-component, equiatomic alloy will have a mixing entropy of 1.61R which larger than non-equiatomic HEAs.

For example, the Al-containing HEAs are known to have single and/or dual phase microstructure. Refractory HEAs containing refractory metals such as Mo, Ta, Nb, W, etc. are also classified based on their functionalities. The illustration in Figure (1.2) below gives a layout of HEA classification based on their crystal structure [12].

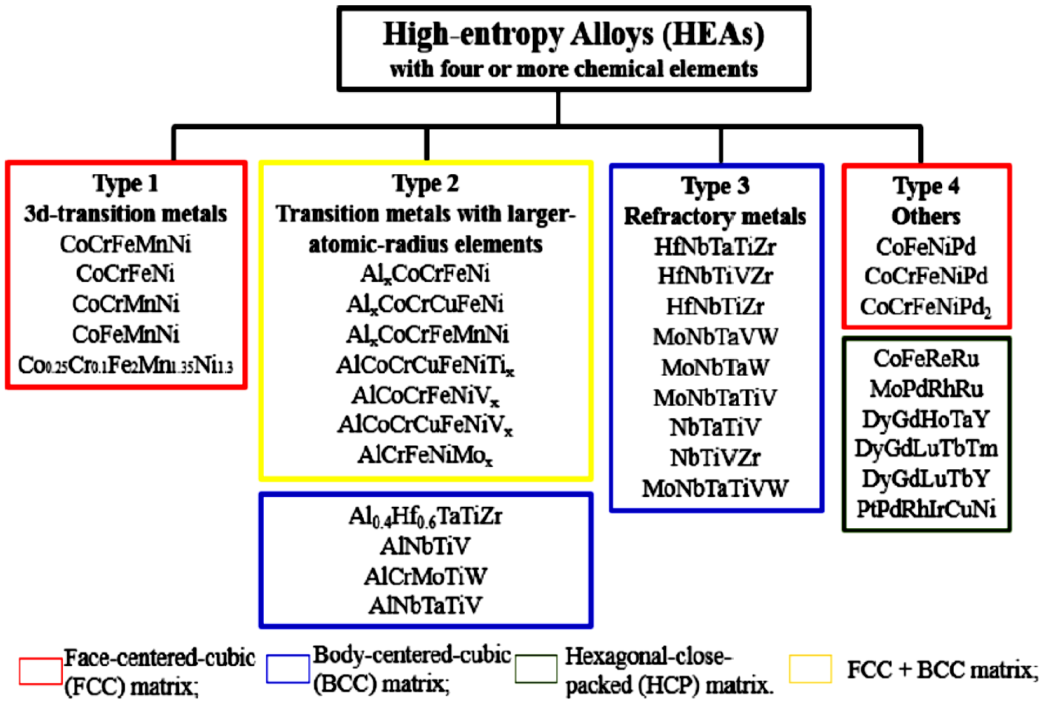

Figure (1.2): HEAs Classification Based on Their Crystal Structure and Composition [12]

Al-containing HEAs are flexible in adjusting their crystal structure; it is possible to vary the Al ratio in an alloy with other principal elements. Increasing the relative ratio of Al induces a larger lattice strain, and the ensuing distortion leads to relaxation via phase change in the crystal structure [9],[13].

1-3 Application of HEA

HEAs can be used in a wide range of fields through proper composition design and processing. Its high-temperature phase stability, radiation resistance, high hardness, high strength, and high wear resistance make HEAs widely used in structural materials, including high-temperature structural materials, high-temperature heat-resistant coatings. In addition, HEAs can also be used as functional materials, such as thermoelectric materials, superconducting materials, and magnetic materials.

Thin-film HEAs could be used as heat-or wear-resistant coatings, diffusion barriers, and hard coatings for cutting tools , and the HEA powders are used in many aspects such as fuel cells for their unique properties[14].

1-4 Problem Statement

Improving the performance of the gearbox is important in improving the overall performance of an automobile. Gears transmit power through the rotational motion they create at different speeds, direction, and torques. This power, however, can be lost through the heat dissipation caused by unnecessary friction between these parts. When left unsolved, this problem can cause a great impact on transmissions. One of the ways to prevent unnecessary friction on the transmission is to coat the gears by HEAs which is reduced the friction and resisted the heat.

1-5 Objective

In this study, electro-deposition of AISI 4140 substrate are done with electrochemical bath of MEAs and three types of HEAs as well as with and without carbon Nanotubes to enhanced mechanical, microstructure, and electrochemical properties of gears box.

Chapter Two:

Theoretical Considerations and Literature Review

Chapter Two: Theoretical Considerations and Literature Review

2-1 General View

In this chapter, the definition of high entropy alloys, their properties, manufacturing methods, classification, their use in industry, and then special alloys (AISI 4140 grade) used in the manufacture of parts of the gears and the problems they are exposed to it have been presented. Also, study the electrodeposition techniques and their parameters that are influenced on the coating and then touches on previous research and studies on the electrodeposition of HEAs to reach the best results, taking into account previous experience in this field have been presented.

2-2 Materials of Coating

2-2-1 High Entropy Alloy

Metallic materials play an important role in the world. They are the basic materials for human survival and development, and can promote the development of human society [15][16]. In 1981, Cantor initiated research on equi-atomic multicomponent alloys with his undergraduate student Alain Vincent [17]. One of the experimental alloys had 20 components. They found that only one composition of Co20Cr20Fe20Mn20Ni20, in atomic percentage, is of a single FCC phase, which means that all these five elements are mixed into a solid solution.

Also, in 1995, Yeh began exploring the world of multi-principal elemental alloys (MPEAs). He believed that high mixing entropy could enhance mixing among components and reduce the number of phases. Figure (2.1) shows a solid solution forming a crystal structure with ten types of dissolved atoms and a solid solution forming an amorphous structure simulated by eight types of coins with large size differences [10].

From the original pure copper, cast iron to aluminum-magnesium alloys, amorphous alloys, until the high-entropy alloys in the 2004, just as shown in the Figure (2.2) [18], the configurational entropy of materials seems to be increasing with time. Throughout the history of materials, the increasing of entropy is the most important law that guides the development of materials [14].

HEAs were first proposed by Professor Ye Junwei in 2004. Originally, Yeh et al. defined a high-entropy alloy comprising of five and more than five elements, and each element has an atomic percentage greater than 5% and less than 35% [8]. The second definition is based on the concept of entropy. It defines HEAs as an alloy that has a configurational entropy larger than 1.61R in their random solution state which were claimed to form stable single-phase solid solutions , where R is the gas constant. This stability was attributed to the high entropy of mixing associated with a disordered solution of several elements, which was presumed to overwhelm the enthalpy of phase formation[19].

Simple crystal structures, FCC, BCC or a combination of both, were also observed depending on the combining elements. These studies were conducted independently and published in 2004 and were referred to as High-Entropy Alloys (HEAs). Concurrent with Cantor, Ramachandran [20] proposed the concept of “cocktail alloys” in which metals can be mixed as a multi-element mixture to form bulk metallic glasses or single-phase crystalline alloys. For metallic materials, the “cocktail effect” is not particularly scientific but simply implies that unexpected properties could be obtained after mixing many elements together, something which cannot be achieved in a material comprised of a single independent element[19] .

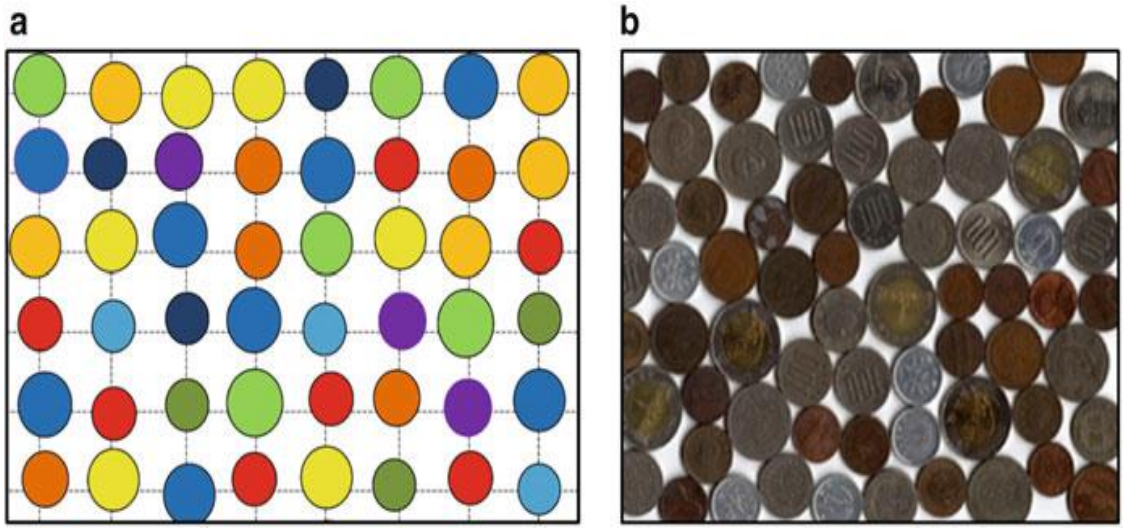

Figure (2.1): (a) A schematic crystal structure with ten kinds of atoms and (b) a simulated amorphous structure with eight kinds of coins [10].

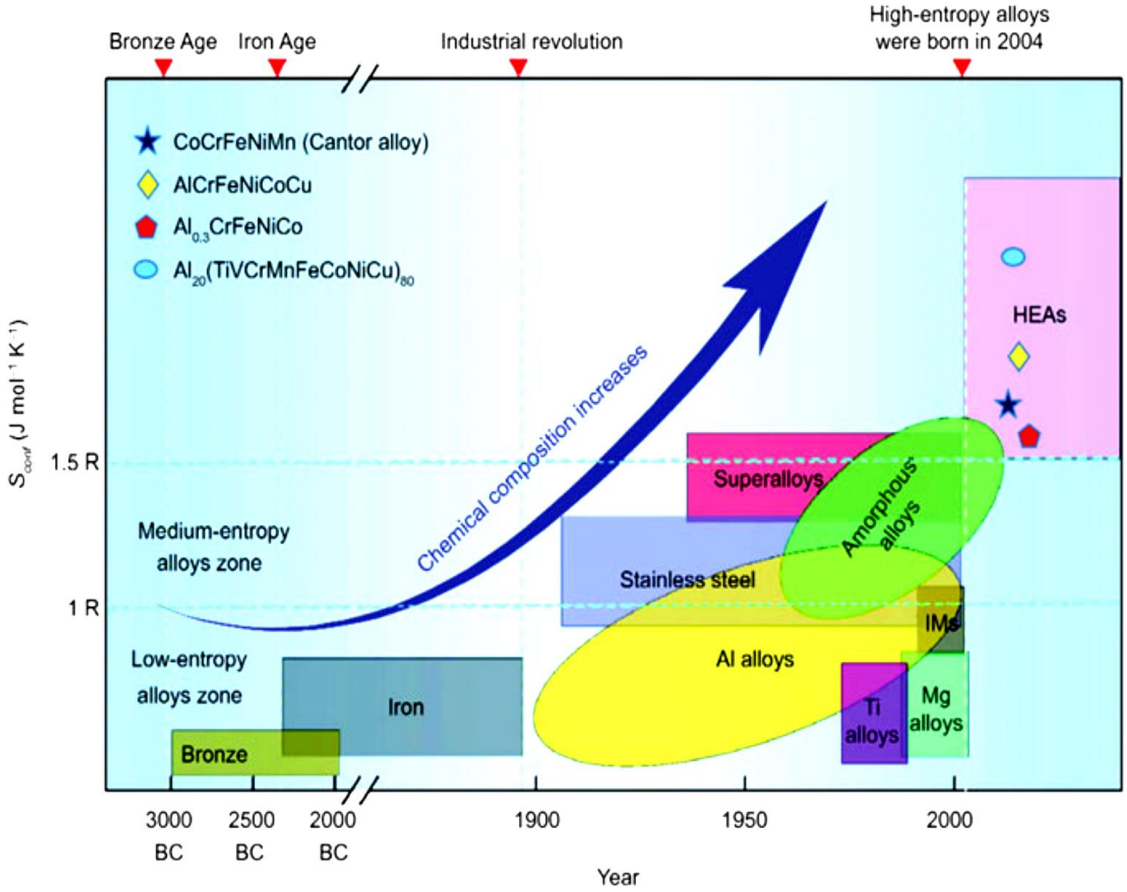

Figure (2.2): Entropy increasing in the developments of materials [18].

Figure (2.3) shows the materials hypertetrahedron for the HEAs, which shows in a nutshell the broad spectrum of research and development that is taking place in this field [5].

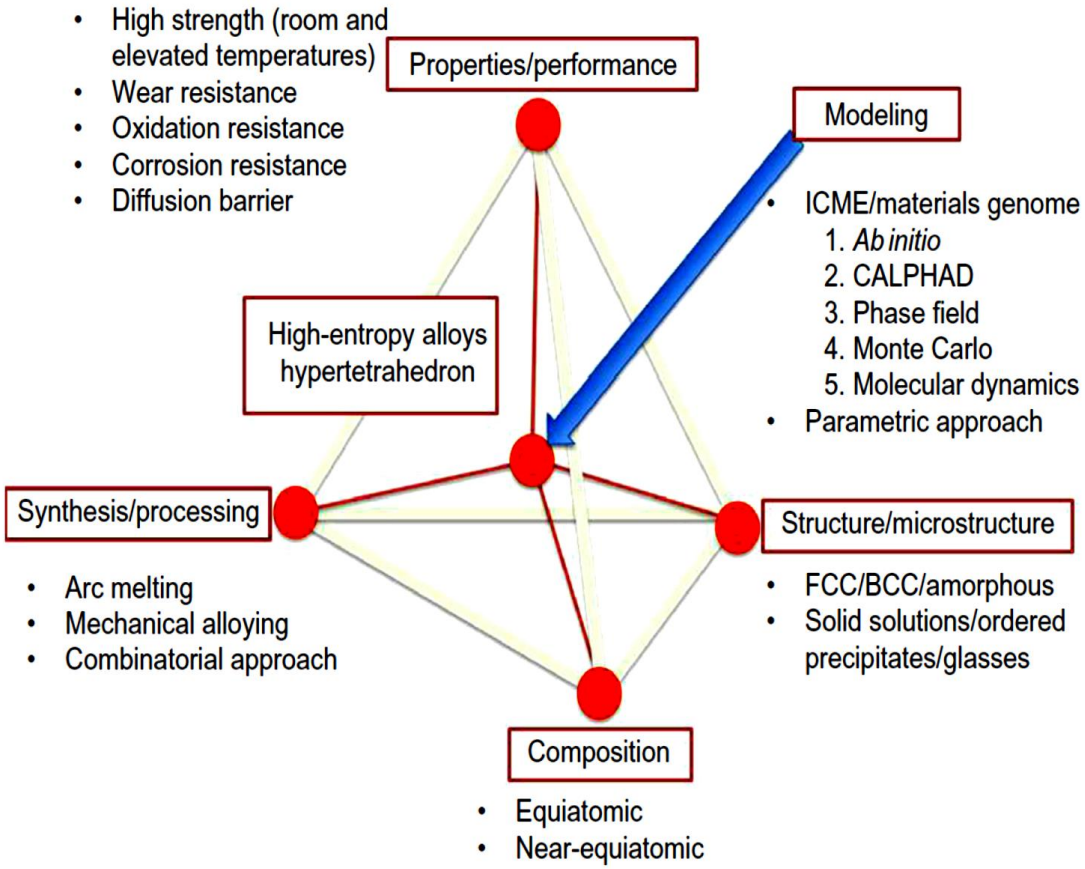

Figure (2.3): The materials hypertetrahedron for HEAs [5].

The configurational entropy has the highest contribution to the entropy of mixing of high entropy alloys as compare to other sources, such as vibrational, electronic and magnetic entropy. For an equiatomic HEA, the entropy would reach a maximum with the configurational entropy ($\Delta S_{conf.}$) expressed by:

$$\Delta S_{conf.} = R \ln n \qquad (2.1)$$

where n is the no of elements. As a result, the $\Delta S_{conf.}$ for an equimolar alloy with 3, 5, 6, and 9 elements will result in to 1.10R, 1.61R, 1.79R and 2.20R, respectively. Thus, in order for a multicomponent alloy to be classified as HEA, the lower limit of $\Delta S_{conf.}$ has been suggested to be 1.5R [18] .

2-2-2 Medium Entropy Alloy

Among the HEAs, the Cantor alloy is known as one of the few to crystallize as a single-phase fcc solid solution and one that displays a remarkable synergy in strength and ductility which is progressively enhanced at cryogenic temperatures. Several medium-entropy alloys (MEAs) have been produced based on the combination of elements of the Cantor alloy: cobalt, chromium, iron, manganese, and nickel. If only equiatomic MEAs are considered with three or four main elements, then as noted the possible combinations of elements are restricted to 15 new alloys. However, if non-equiatomic configurations are considered, then the number of different alloys becomes unlimited. Considering four principal elements, five different alloys can be identified, while for three main elements ten possible combinations can be obtained [21].

MEAs are composed of three or more principal elements with near-equal atomic percentages, and their configurational entropies are in the range of 1–1.5R (R = 8.314 mol−1·K−1). HEAs are comprised of five or more principal elements with near-equal atomic percentages, and their configurational entropies are larger than 1.5R. Due to the high mixing entropy associated with a disordered solution of several elements, both MEAs and HEAs can form stable single-phase solid solutions, in which atoms with different sizes are homogeneously distributed in the ideal situation [22].

2-3 Synthesis and Processing of HEAs

During the manufacturing of HEAs many techniques are used, such as arc melting, Bridgman solidification, mechanical alloying, sputtering, laser cladding and electrodeposition. The processing routes for the synthesis of HEAs can be classified according to their initial states for alloy

preparation. Specifically, these states are distinguished into the liquid state, the solid state, the gas state and last the electrochemical process [23].

2.3.1 Preparation from the liquid state

The majority of HEAs have been produced using liquid processing methods, such as arc melting, induction melting and Bridgman solidification. During arc melting, the torch temperature in the furnace is very high, approximately 3000 oC, and it is controlled by the adjustment of the electrical power. This method is not suitable for the low melting elements such as Mg, Zn or Mn because they can evaporate. In these cases the induction heating is a more adequate method as shown in Figure (2.4) [23].

For coating fabrication in HEAs, a thermal spray technology was applied. In this process the material is gradually heated up until melting and a thermal spraying gun strikes its surface to flatten and to form thin compatible platelets. Next, the sprayed particles are accumulated on the substrate during cooling, creating in this way a cohesive structure (coating) [24][25].

2.3.2 Preparation from the solid state

The solid state processing route is performed by mechanical alloying (MA) technique. This method involves repeated cold welding, fracturing and re-welding of powder particles in a high energy ball mill. The mechanical alloying is capable of synthesizing a variety of equilibrium and non-equilibrium alloys starting from blended elemental or pre-alloyed powders. The MA process occurs in three steps. At the beginning, the alloy materials are combined in ball mill and stranded in fine powders. Then the powders are compressed and sintered during a hot isostatic pressing process. In the final step, the powders are relieved by internal stresses

during heat treatment. Many high heat turbine blades, aerospace components and a variety of advanced materials have been made with the MA process as shown in figure (2.5 a) [24].

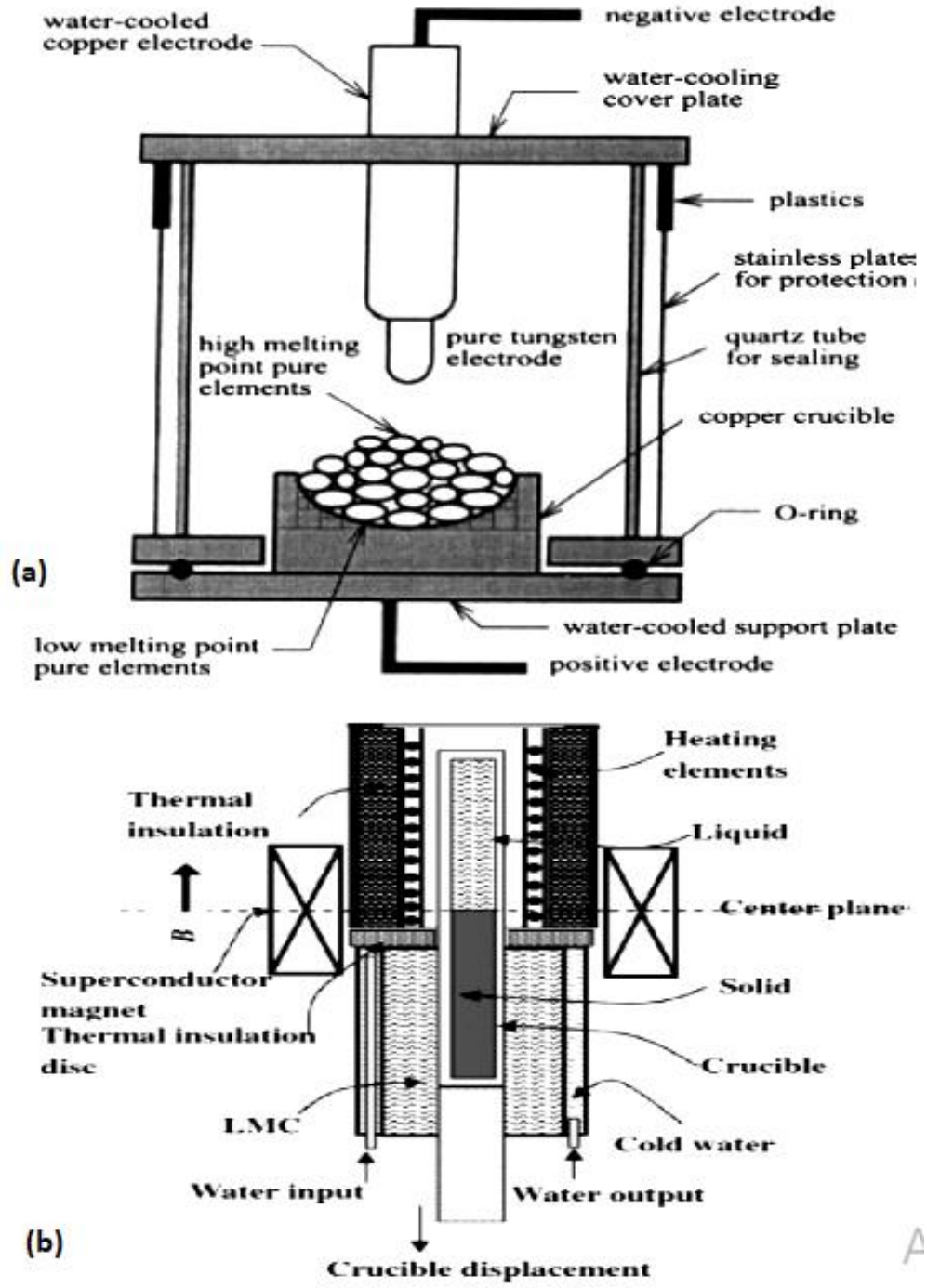

Figure (2.4): A schematic diagram of (a) the arc melting method and (b) the Bridgman solidification from the liquid state preparation [23].

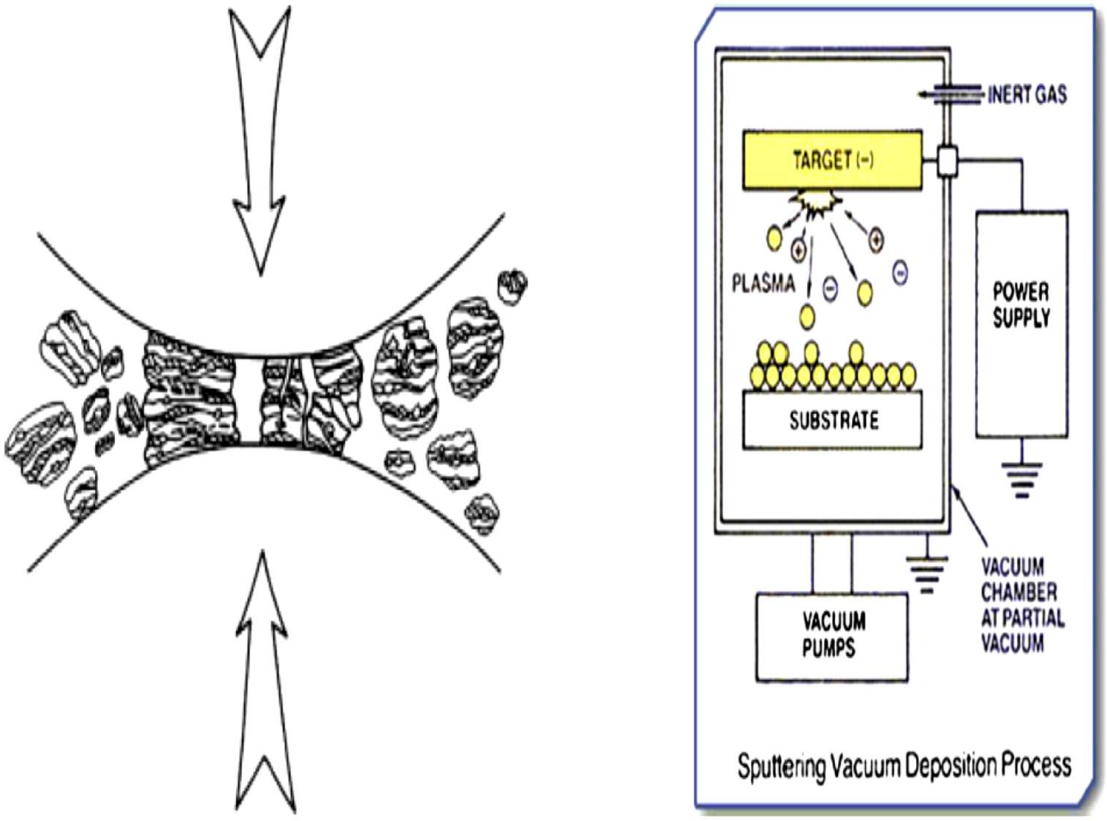

figure (2.5): A shematic diagram of (a) the MA process from the solid state prepration, (b) the sputter method from the gas state prepration[24].

2.3.3 Preparation from the gas state

Magneton sputtering and plasma nitriding techniques are quite popular among the methods for preparation from the gas state. These techniques are used to produce thin films or layers of HEAs on the surface of the substrates. The magneton sputtering is a technique for depositing a thin film into a substrate by sputtering away atoms from a target under the bombardment of charged gas ions as shown in figure (2.5 b). The magneton sputtering can be distinguished between DC sputtering and radio frequency sputtering (RF)[23][25].

2-4 Thermodynamic Analysis of HEAs

Before the discovery of HEAs, it was believed that combining multiple elements in near equimolar compositions would result in a mixture

of brittle compounds with no significant technological application. In contrast to those beliefs HEAs commonly consist of a single solid solution or a mixture of solid solution phases. These phases resemble the common FCC, BCC and HCP structures, although they might be severely distorted due to the different atomic volumes among the constituent atoms [23].

It is important to note that the number of phases observed in these HEAs is significantly less than the maximum number of phases expected from the phase rule, suggesting that large configurational entropy in these alloys enhances the mutual solubility for forming solid solution phases (disordered or partially ordered) and thus restricts the formation of a large number of phases. Furthermore, HEAs being MPEAs, the diffusivities of atoms are expected to be low and hence the formation of a number of phases is kinetically constrained in such alloys. Thus, the observation of less number of phases in HEAs is not only due to high configurational entropy of these alloys but also due to low diffusivities in these multicomponent alloys [5].

The thermodynamic consideration of phase selection among different phases is determined based on the competition between ΔH_{mix} and $T\Delta S_{mix}$ [26].

The increase in entropy of mixing in multicomponent alloy results in decreasing the Gibbs free energy of mixing (ΔG_{mix}) leading to formation of stable solid solution of face-centered cubic (FCC), body-centered cubic (BCC) or hexagonal close pack (HCP) crystal structures. The relation between ΔS_{mix} and ΔG_{mix} can be given by the equation [25][27] :

$$\Delta G_{mix} = \Delta H_{mix} - T\Delta S_{mix} \qquad (2.2)$$

Where ΔH_{mix} is enthalpy of mixing and T is the absolute temperature. The phase formation is determined by the competition between ΔH_{mix} and $T\Delta S_{mix}$. With increasing temperature, a higher $T\Delta S_{mix}$ term becomes more dominant and will lead to formation of solid solution [28]. Mixing entropy is correlated with the possible atomic arrangements that the system can take and for multicomponent systems can be calculated using Eq.2.3 [28].

$$\Delta S_{mix} = -nR \sum_i^j X_i \ln X_i \qquad (2.3)$$

Where n is the number of Moles, R is the Ideal Gas Constant and X_i is the Atomic Fraction in a j element system. Using Eq.(2.3) it can be proven that ΔS_{mix} is maximized when the system is equimolar. Mixing entropy can also increase by the addition of more alloying elements. Subsequently, solid solutions in HEAs have extraordinarily high configurational entropy. In near equimolar compositions and when temperatures are sufficiently high the term $T\Delta S_{mix}$ overpowers mixing enthalpy ΔH_{mix} as a result of the term ΔG_{mix} can become negative even though ΔH_{mix} is positive [23][10].

Yang and Zhang[29] proposed the dimensionless parameter Ω, by considering the contribution both from ΔH_{mix} and ΔS_{mix} for the design of HEAs, as:

$$\Omega = (T_m \Delta S_{mix}) / |\Delta H_{mix}| \qquad (2.4)$$

where T_m is the weighted average melting point of the alloy system. Based on Equation (2.4), it can be stated that the probability of solid solution-forming ability of HEAs will be more for the larger value of the dimensionless parameter Ω.[29]. Figure (2.6) shows the variation of estimated mixing configurational entropy of alloys having an ideal random

solid solution as a function of atomic percentage aluminum with an increase in the number of constituent elements.[30]

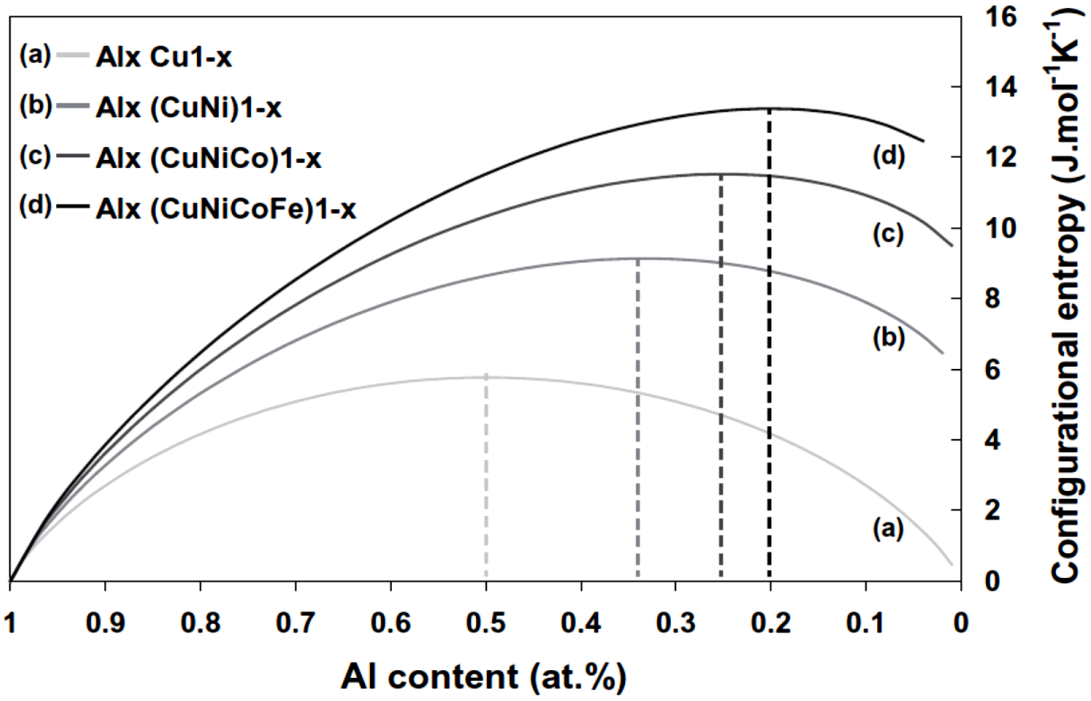

Figure (2.6): Variation of estimated configurational entropy of mixing of alloys, having an ideal random solid solution, as a function of atomic percent aluminum[30].

2-5 Alloy Steel

It has been generally believed that steel is a kind of advanced materials, presenting characteristics to meet a variety of requirements. They could be applied to the circumstances subject to the elevated temperature up to 650C and cryogenic temperature down to -196C, to the applied stresses from 100 up to 5,000 MPa, to the corrosion of atmosphere, acid, alkali, salt, etc. Steels has been widely used for construction, automobile, rails, shipbuilding, petrochemistry, machinery, weaponry, daily life, etc. [31]. Since their invention in 1865, alloy steels have found broad application in multiple industries; the automotive, aerospace, heavy equipment, and pipeline industries to name a few[32].

Alloy steel is a type of steel alloyed with several elements such as molybdenum, manganese, nickel, chromium, vanadium, silicon, and boron. These alloying elements are added to increase strength, hardness, wear resistance, and toughness. The amounts of alloying elements may vary between 1 and 50%. Alloy steels may be classified into two groups: low and high alloy steels. The boundary between low alloy and high alloy steel is commonly accepted as 5% alloying element. For all practical purposes in the oil and gas industry, alloy steel means low alloy steel [33].

2-5-1 Low alloy steel grade 4140

The topic of alloy steels contains both the common 4140 and 316 alloys to more exotic alloys such as the Hadfield steels. These steels can form a wide variety of microstructures such as pearlite, bainite, or martensite, which result in an equally broad range of properties. It is this range that has made them useful to so many industries. In some cases, these are the only steel alloys that can provide the required combination of properties. Their use in the automotive industry has been key to the development of safer vehicles and improved fuel efficiency. Therefore, continued development is necessary to expand markets, improve products, and enhance the human condition[32]. Where the chemical composition requirements of standard 4140 low-alloy steel are listed in Table (2.1) [34].

AISI 4140 steel is a low alloy steel containing chromium, molybdenum, and manganese. It is widely used across numerous industries and is an excellent material choice due to its toughness, high fatigue strength, and abrasion and impact resistance. Not many grades can match the versatility and usefulness of 4140. It is important to understand what the grade number means where the number (4) designates that 4140 steel is molybdenum steel, indicating that it possesses higher amounts of molybdenum than other steels, such as the 1xxx series , the number (1)

designates that 4140 steel has additions of chromium as well; more so than 46xx steel for example, and number (40) used to differentiate 4140 Steel from other steels in the 41xx series [35].

Table (2.1): Composition ranges and limits for AISI-SAE standard 4140 low-alloy steel applicable for structural applications [34]**.**

Element	C	Mn	Si	Cr	Mo
Wt%	0.36-0.44	0.70-1.00	0.15-0.30	0.80-1.15	**0.15-0.25**

2-6 Four Core Effects of HEAs

There are many factors affecting microstructure and properties of HEAs. Among these, four core effects are most basic. Because HEAs contain at least five major elements, and conventional alloys are based on one or two metal elements, different basic effects exist between these two categories. The four core effects are high entropy, severe lattice distortion, sluggish diffusion, and cocktail effects [36][37].

2-6-1Thermodynamics: High-Entropy Effect

High-entropy effect is the most important effect because it can enhance the formation of solid solutions and makes the microstructure much simpler than expected[5]. There are three possible competing phases in a solidified alloy among which random solid-solution phases tend to have the lowest Gibbs free energy of mixing ($\Delta G= \Delta H_{mix}-T\Delta S_{mix}$), especially at high temperatures, and hence they get stabilized. Moreover, it has been found that the number of phases formed in HEAs are much lower than those predicted by Gibbs phase rule ($P = C + 1 - F$), specifying that the high entropy effect increases the mutual solubility between the elements [30]. Besides high entropy can reduce the electronegativity difference and avoid phase separation, formation of some terminal solid solution or intermetallic compound in the alloys may occur[14].

2-6-2 Kinetics: sluggish diffusion effect

Phase transformation requires co-operative movement of atoms. But in HEAs, every atom has a different neighborhood, and hence lattice potential energy (LPE) will vary from site to site. Due to large fluctuation in the LPE from one site to another, it is expected that activation energy will be higher and diffusion will be sluggish. Because of the sluggish diffusion effect, one can easily get a supersaturated state, nano-precipitates, decreased grain growth, increased recrystallization temperature, and improved creep properties[30].

It is expected that sluggish diffusion might affect phase nucleation, growth and distribution, and morphology of new phase through diffusion controlled phase transformation. It also provides various advantages in controlling microstructure and properties: easiness to get supersaturated state and fine precipitates, increased recrystallization temperature, slower grain growth, reduced particle coarsening rate, and increased creep resistance [5] [38]. As a result, diffusional phase transformation would be slower in HEAs. In brief, the sluggish diffusion effect implies slower diffusion and phase transformation[10][39].

2-6-3 Structures: severe lattice distortion effect

Because the multicomponent matrix of each solid solution phase in HEAs is a whole-solute matrix, every atom is surrounded by different kinds of atom and thus suffers lattice strain and stress mainly due to the atomic size difference. Besides atomic size difference, different bonding energy and crystal structure among constituent elements are also expected to cause even higher lattice distortion in consideration of the nonsymmetrical neighboring atoms, that is, nonsymmetrical bindings and electronic structure, around an atom, and the variation of such nonsymmetry from site

to site. Figure (2.7) shows the severe lattice distortion of a five-component BCC lattice [5] [14] [30].

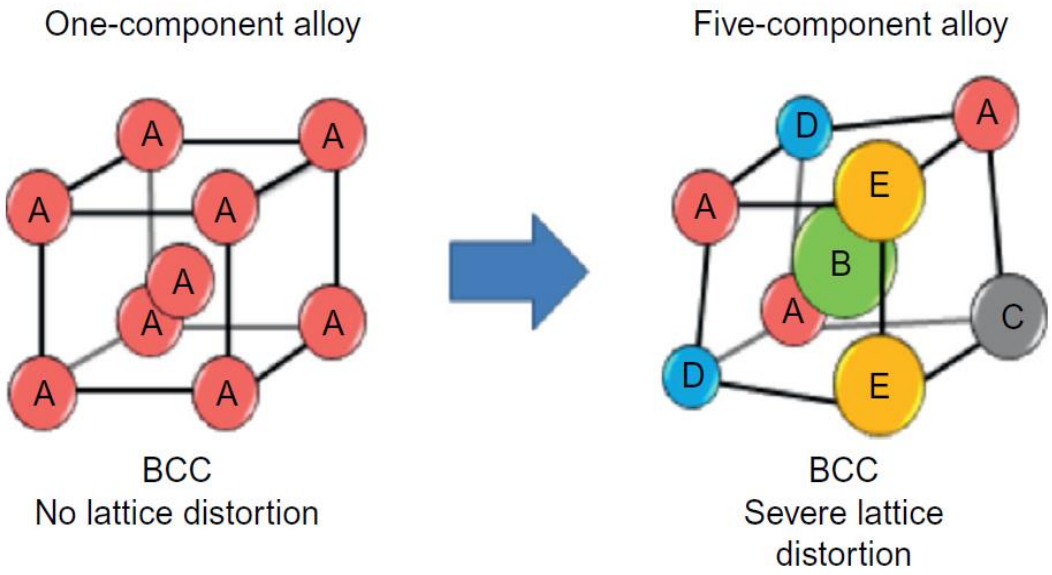

Figure (2.7): Schematic diagram showing large lattice distortion exists in the five-component BCC lattice[30].

Lattice distortion not only affects various properties but also reduces the thermal effect on properties. Hardness and strength effectively increase because of large solution hardening in the heavily distorted lattice. For the x-ray diffraction peak intensity, the distorted atomic planes increase x-ray diffuse scattering effect and give smaller peak intensity. Lattice distortion also causes electron scattering and significant decrease in electrical conductivity[14] [5] [30].

2-6-4 Properties: cocktail effect

The various elements of HEAs have different characteristics, and the interaction between different elements makes the HEAs exhibit a composite effect, that is the “cocktail” effect, first proposed by Indian scholar Ranganatha [20]. In HEAs, cocktail effect is used to emphasize the enhancement of the properties by at least five major elements.

Because HEAs might have single phase, two phases, three phases, or more depending on the composition and processing, the whole properties are from the overall contribution of the constituent phases[5] [10]. However, each phase is a multi-principal-element solid solution and can be regarded as atomic-scale composites. The interaction and influence of the alloy components on the atomic scale will ultimately be reflected in the macroscopic comprehensive properties of the alloy, and even produce additional effects[14].

2-7 Coating techniques

The surface is the most important component of a material that is associated with the performance of material for industrial applications. The application of various surface modification techniques allows an economic substitution of a low-grade base alloy with a coating for better surface characteristics and performance in various demanding conditions, e.g., thermal insulation, erosion, corrosion, and stress[40].

Surface coatings can enhance the mechanical and functional properties of substrates and keep good balance between specific mechanical properties and sufficient surface performance of the components. Coatings composed of HEAs and HEA-based materials, including metallic, ceramics, and composites have attracted the global attention and developed rapidly over the last decade, owing to their outstanding properties. HEA-based coatings materials, deposited on the substrate surfaces in the form of thick layers or thin films, can enhance the surface performances under the preconditions of proper compositions and deposition parameters. [41].

The use of the electrochemical method in HEAs is limited, because the combination of many electrochemical parameters affect the predicted structure. Despite this fact, with this processing route, unique properties

can be accomplished. With the potentiostatic electrodeposition method, a film can be produced at low temperatures. It was observed that in the as-deposit films, soft magnetic behavior and magnetic anisotropy take place. By adjusting the electrochemical parameters, the thickness and the morphology of the structure can be controlled and high deposition rates can be obtained. Generally, the electrochemical deposition is one of the most simple and efficient methods which allow easy control of the nucleation and growth of metal nanoparticles[23].

2-8 Electro-deposition Coating

Electroplating is the coating of an electrically conducting surface by application of an electrical potential in a suitable solution that contains the ions of the metals to be deposited. The electrode to be coated is the cathode. The counter electrode, the anode, can be of the soluble type, so that it supplies metal ions to the solution. Alternatively, the anode can be insoluble, in which case the ions of the metals to be deposited must be continuously or periodically added to the plating solution to compensate for the depletion[42][43].

It is the electrodeposition of an adherent metallic coating upon an electrode for the purpose of securing a surface with properties or dimensions different from those of the basis metal. Electrodeposits are applied to metal substrates for decoration, protection, corrosion resistance, chemical inertness, wear resistance, buildup of substrate dimensions, electrical properties, magnetic properties, solderability, reflectance, and reduction of friction [44][45].

The deposition rate depends primarily on the current density. If all supplied electrons reduce the metal ions, then the deposition rate can be readily calculated from Faraday's law which is expressed as [45] :

$$W = (I.t.Eq) / F \quad (2.5)$$

where: W = weight of deposit in grams, I = current flow in amperes, t = time in seconds, Eq = Equivalent weight of deposited element, F = Faraday constant, = 96,500 coulombs (approx.) [45].

The microstructures of electrodeposits, which to a large extent determine their properties, depend on a number of factors. These factors include the microstructure of the surface to be coated, the plating conditions (that is, the current density), the temperature and composition of the plating solution, as well as the degree and type of agitation. The composition and the pH of the plating solution in the vicinity of the cathode (which generally differs from that of the bulk) can have a large effect on the structure and properties of the deposit[42][46].

Figure (2.8) represents a simplified plating cell. A DC source, usually a rectifier or motor generator, supplies current flowing in one direction through the external portion of the circuit when a potential difference is imposed across the system. The current flow is that of electrons in the external conductors. The mechanism of electrical transfer in the solution is by means of electrically charged “particles” called ions. Positive ions (cations) travel toward the negative electrode (cathode) and negative ions (anions) travel toward the positive electrode (anode) when the potential is applied, thus completing the electrical circuit. The electrolyte usually contains other components which influence the process [45].

The cathode or deposition reactions are characterized as reduction reactions since electrons are “consumed,” and the valence states of the ions involved are reduced. The anodic reactions are oxidation reactions wherein electrons are liberated, and the valence states are increased. Each set of reactions represents half-cell reactions and proceeds independently of the

other, limited by a condition of material balance, i.e., electrons liberated in the anode reactions must equal the number of electrons "consumed" in the cathode reactions[45][47][48].

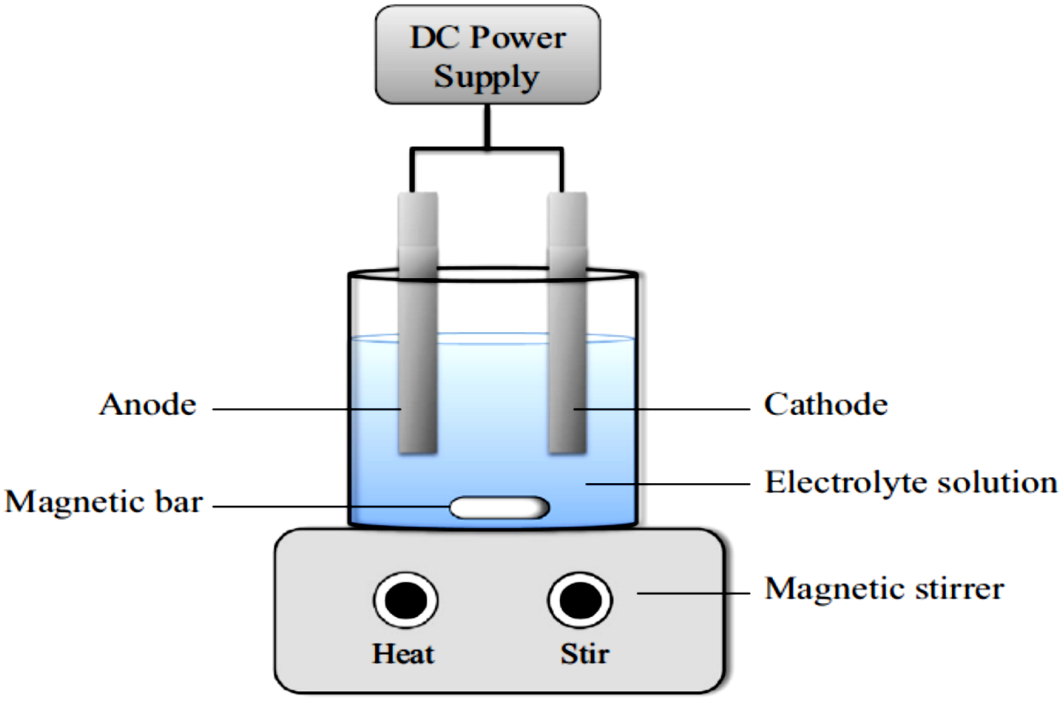

Figure (2.8): The typical electrochemical cell[49].

2-8-1 Mechanisms of Electroplating

The electrodeposition of an alloy requires, by definition, the codeposition of two or more metals. In other words, their ions must be present in an electrolyte that provides a cathode film, where the individual deposition potentials can be made to be close or even the same.

One recognizes three main steps in the cathodic deposition of alloys or single metals:

1. Ionic migration, meaning that the hydrated ion(s) in the electrolyte migrate(s) toward the cathode under the influence of the applied potential as well as through diffusion and/or convection.

2. Electron transfer, meaning that at the cathode surface the hydrated metal ion(s) enter(s) the diffusion double layer where the water molecules of the hydrated ion are aligned by the weak field present in this layer. Subsequently, the metal ion(s) enter(s) the fixed double layer, where, due to the higher field present, the hydrated shell is lost. Then on the cathode surface, the individual ion is neutralized and is adsorbed.

3. Incorporation, meaning that the adsorbed atom wanders to a growth point on the cathode and is incorporated in the growing lattice.

In general, when a metal is immersed in a solution of (i.e., containing) its own ions, some surface atoms in the metal lattice do become hydrated and dissolve into the solution. At the same time, ions from the solution are deposited on the electrode. The rate of these two opposing processes is controlled by the potential differences at the metal–solution interface. The specific potentials at which these two reaction rates are equal, called standard potentials, are usually given in the literature for solutions at 25°C (room temperature) and at an activity value of unity.

The individual polarization curves for the metals are often modified as a result of interactions resulting from codeposition. If the alloy deposition occurs at low polarization, the nobler metal will be deposited preferentially. All factors, however, that increase polarization during electrodeposition, such as high current density, low temperature, and quiescent solution—factors that increase concentration polarization—will favor the deposition of the less noble metal [45][50].

Viewed electrochemically when metal deposition is accompanied by hydrogen evolution, it may be said that one deals with alloy plating in which hydrogen is the codepositing element. This is so even when

hydrogen is discharged as gas since the conditions for codeposition are met. Alloy plating of metals makes it into a process of production of hydrogen and two or more metals.

The evolution of hydrogen during electrodeposition of an alloy has a significant effect on the polarization and composition of the alloy deposited. If a significant amount of hydrogen is evolved, the potential of the cathode during alloy deposition may be determined almost totally by the hydrogen evolution reaction. If, as is usually the case, the overpotential for hydrogen evolution is high in the preceding case, the currents corresponding to the individual metals will be close to limiting values. Under these conditions, an increase in current will increase the amount of hydrogen evolved, resulting in a poor efficiency for alloy deposition with a minor change in the composition of the alloy deposited [48][50].

2-8-2 Quality and Cost Effectiveness

In order to meet the requirements imposed by designers and production engineers, the following are the main requirements made of electroplated coatings : as thin as possible with uniform thickness, smooth surface, dense and the fine-grained structure, good adhesion to the substrate, high corrosion resistance, free from internal stress, sufficient ductility, high hardness and strength, high wear resistance, uniform and low coefficient of friction.

These properties should be able to be specified as appropriate, and coatings should be reproducible to such specifications [51].

2-8-3 Parameters of Electrodeposition

The parameters generally controlling the composition, structure and properties of the deposit are shown in Figure (2-9).

- ***Current*** A high current density is also anticipated to promote grain refinement. An increase in the current density is expected to result in a higher overpotential, which should increase the nucleation rate. However, surprisingly, Cziraki et al. have reported that increasing the current density from 100 to 500 (mA/cm^2) using a sulfate-based solution results in an increase in the grain size of d.c.-electroplated nickel [52].

  Some of the advantages claimed for pulse plating are: Faster plating rates due to increased permissible current densities, Denser deposits (less porosity), Higher purity of deposits, less tendency for impurities to deposit, Smoother, finer-grained deposits, Reduced need or elimination of addition agents, Less hydrogen evolution, providing sharper, finer lines at masking interfaces and possibly less hydrogen embiittlement, and decreased stress in deposits[45].

- ***Temperature*** T is one of the most important parameter. The operation temperature is ordinarily in the range from 15 to 70°C. In some cases (e.g. the autocatalytic deposition of Ni–P alloy) T may be as high as 99°C. Elevated temperatures provide some advantages: solubility and electric conductivity improve, and the tendency for anodic passivation decreases. High T on the other hand tends to accelerate solution evaporation and corrosion processes, limiting the practical temperatures achievable. Additionally, an increase in T stifles additive adsorption, decreasing their efficacy; as a consequence, deposits become more coarse-grained [45][48].

  A low solution temperature requires a drop in current density (and in growth rate) in order for deposition not to occur under diffusion limiting conditions. Lower temperatures slow down diffusion kinetics, often resulting in stressed deposits, prone to embrittlement. In different instances the role of temperature may vary, since each process has its own optimum operating temperature. With regard to temperature

control, in most cases a deviation of ±3°C from the optimum one is acceptable; however, some processes, in particularly at the laboratory scale, require rigourous temperature control[53].

- ***Solution PH*** also plays an important role because of its influence on hydrogen evolution and hydroxides precipitation. pH dictates bulk electrochemical equilibria and the relative concentration of the various compounds formed by the electroactive species[54].
- ***Bath Concentration*:** This includes the compounds supplying the metal ions (to be deposited) and the supporting ions. The basic functions of the supporting ions or compounds are to stabilize the electrolyte, to improve solution conductivity, to prevent excessive polarization and passivation (especially anodic), and to provide compatibility with the desired plating conditions. Supporting ions or conducting salts reduce the current shared by the metallic ions or complexes, making convection (agitation) a more significant factor[45].
- ***Stirring*** of the solution is desirable since it enhances ion transport to the substrate and decreases the thickness of the diffusion layer. Stirring is performed by mechanical (magnetic) stirrers or by compressed air[54].

  The effect of agitation on the composition of the deposit is due to the concentration changes which it produces at the cathode-solution interface. During alloy deposition the cathode diffusion layer is depleted in metal ions and, furthermore, the ratio of the concentrations of the metals in the layer differs from that in the body of the bath. Agitation of the bath or rotation of the cathode, by decreasing the thickness of the cathode diffusion layer not only results in an increase in the concentration of metal ion in the cathode diffusion layer, but also causes the metal ratio of the diffusion layer to approach more closely to that of the solution in the body of the bath[48].

- ***Distance between the electrodes***, the surface morphology and the thickness of deposition on substrate are influenced by the gap maintained between electrodes. The distance influences the current density which in turn affects the deposition thickness. The higher density of potential lines around the edges rise to non-uniformity in the deposition. The resistance increase due to the higher electrode gap leads to higher energy consumption. Hence varying electrode distance is not a factor that can be neglected in the process of electrodeposition. In fact, it is a vital factor that can influence the deposition properties by regulating the average current density and electrolyte resistance[55].

- ***Additives***, In addition to metal salts, electrodeposition electrolytes usually contain various other species. Thus both inorganic and organic salts, acids or alkalis will be added to increase electrolyte conductivity. Other species, both organic or inorganic, may be added for specific purposes, for example, to increase bath stability, or improve leveling or metal distribution, or to optimise the chemical, physical or technological properties of the deposited metal (corrosion resistance, brightness or reflectivity, hardness, mechanical strength, ductility, internal stress, wear-resistance or solderability).

In working with such additives, it should be recognised that they are often effective over only a defined concentration range, and should their concentrations fall outside this range, all kinds of problem can arise either in the deposition process or the deposit properties. In the following sections, such addition agents are considered in greater detail[51].

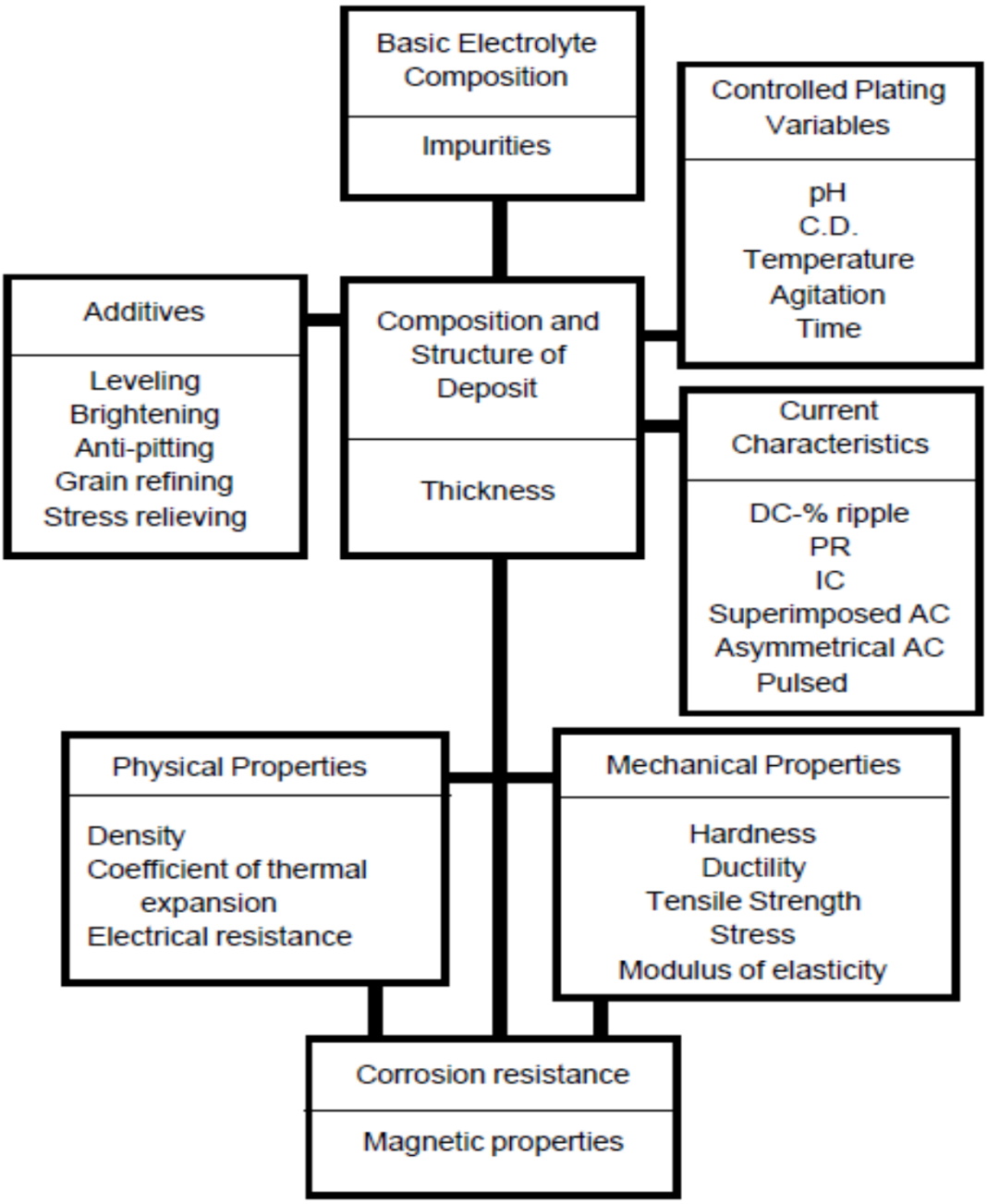

Figure (2-9): Factors influencing the properties of deposition [45].

2-8-4 Advantage of Electroplating

- Variety of Coatings.
- Versatility of Application: Plated coatings can be applied to racked parts.
- Availability of Applicators.

- The electrical conductivity of electrodeposited and other metallic coatings gives them an advantage over most organic and ceramic-base coatings in applications that require this characteristic.
- Galvanic Protection of Substrates. Zinc and cadmium deposits protect steel substrates by sacrificial action in many wet environments.
- Weldability and Solderability. Metal deposits are amenable to welding and soldering.
- Control of Thickness. Unlike hot-dip coating, electrodeposition affords a means of predicting and controlling the amount of metal deposited[44].

2-8-5 Disadvantage of Electroplating

- Inhospitable Substrates. Some substrates, such as cast iron, and certain substrate conditions, such as porosity, require special plating procedures.
- Limitations of Design. Parts are designed to function in the most economical manner. This is not always compatible with plating.
- Size Limitations. Large metal structures are often beyond the capabilities of electrodeposition. The limitation lies in the capacity of tanks to contain the electrolyte[44].

2-9 Classification of HEA

The classification of HEA coating systems can be summarized pictorially as shown in Figure (2.10). The three HEA groups can be possible based on the recent developments in this area; (1) Metallic HEAs, (2) ceramic HEAs (or high entropy ceramics), and (3) high entropy composites. The metallic HEA coatings include initially developed Cantor-

based HEAs and their derivatives with other lightweight HEA based on Al, Mg, Si, etc structural elements. Refractory alloys are also included in metallic HEAs. The high entropy ceramics include oxides, carbides, nitrides, and other hard refractories coatings Figure (2.10). Based on the metallic and ceramic coating, high entropy composite coatings are also in development in the last few years[41][56][57][58].

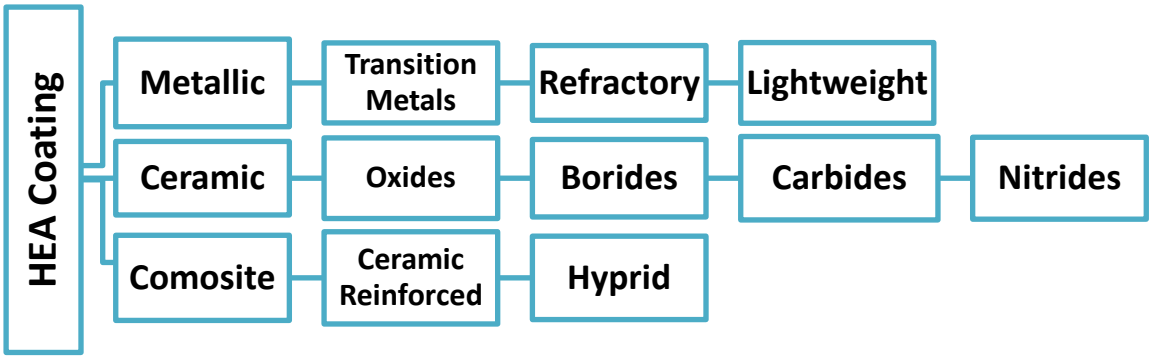

Figure (2.10) : Various Classification of HEA Coating[57].

2-9-1 Metallic Coatings

Metallic HEA-related coatings consist of basically FeCoNiMnCr series elements which are generally known as Cantor-based alloys, developed initially by cantor et al. in 2004 [59]. The constituents in this class of HEAs are mostly transition elements such as Al, Cr, Co, Mn, Fe, Ti, Ni, V. The refractory HEAs are mainly composed of harder refractory elements such as Ta, Mo, Hf, Nb, Zr, W, Ti, V, Cr, etc [60]. Various refractory HEAs developed so far are TaNbCrMo, TaMoNbW, TaNbZrHf, CrNbVZr series [61]. Metallic lightweight alloys have based on light elements to reduce their density for various lightweight structural

applications, such as AlCuSiZnFe, AlLiMgScTi, AlCuFeMnMgTi, Al20Be20Fe10Si15Ti35, etc[62].

2-9-2 Ceramic Coatings

Several HEA oxides, nitrides, and carbides materials have been deposited by various routes such as magnetron sputtering in various atmospheres [63]. In such hard ceramic HEA coatings, the constituent impurities such as O, C, N, H are present in the solid solution and show a high-entropy effect. Various ceramic forming elements are used for hard ceramic HEA coatings such as Cr, Si, Zr, Ti, Al, etc. Such HEA coatings possess extraordinary surface protection ability, in terms of high strength, thermal stability, anti-corrosion performance, and sluggish diffusion rate [64]. Therefore, these coatings have been applied to thermal diffusion barrier, oxidation, and hard radiation resistant coatings applications in nuclear plants [65].

2-9-3 Composite Coatings

Similar to conventional composite materials, the HEA composites can be synthesized by reinforcing the HEA matrix with suitable ceramic reinforcements. Metallic reinforcements have been also used in HEA coatings. Tian et al. fabricated AlCoCrFeNiTi reinforced Ni powder by plasma spray deposition and demonstrated a significant enhancement in the high-temperature hardness and wear resistance of the final coatings[41] [66].

2-10 Application of HEAs

High-entropy alloys constitute a new class of materials, quite different from the traditional alloys, with high research prices value and development application significance. Although the research of high-entropy alloys started late, the excellent performance of high-entropy alloys

makes it a broad application prospect in industrial production, as shown in Figure (2.11).

1. Engine materials: higher elevated-temperature strength, oxidation resistance, hot corrosion resistance, and creep resistance.
2. Nuclear materials: improved elevated-temperature strength and toughness with low irradiation damage.
3. Tool materials and hard-facing materials: improved room and elevated-temperature strength and toughness, wear resistance, impact strength, low friction, corrosion resistance, and oxidation resistance.
4. Waste incinerators: improved elevated-temperature strength, wear resistance, corrosion resistance, and oxidation resistance.
5. Chemical plants: improved corrosion resistance, wear resistance and cavitation resistance for chemical piping systems, pumps, and mixers
6. Marine structures: improved corrosion resistance and erosion in seawater .
7. Heat-resistant frames for multifloor buildings: higher elevated temperature strength which could sustain during incidences of fire
8. Light transportation materials: improved specific strength and toughness, fatigue strength, creep resistance, and formability
9. High-frequency communication materials: high electrical resistance and magnetic permeability above 3 GHz
10. Functional coatings for 3C (Computers/Communications/ Consumer, meaning electronic) products: better wear and corrosion resistances, antisticky, antifingerprint, antibacterial, and esthetics.

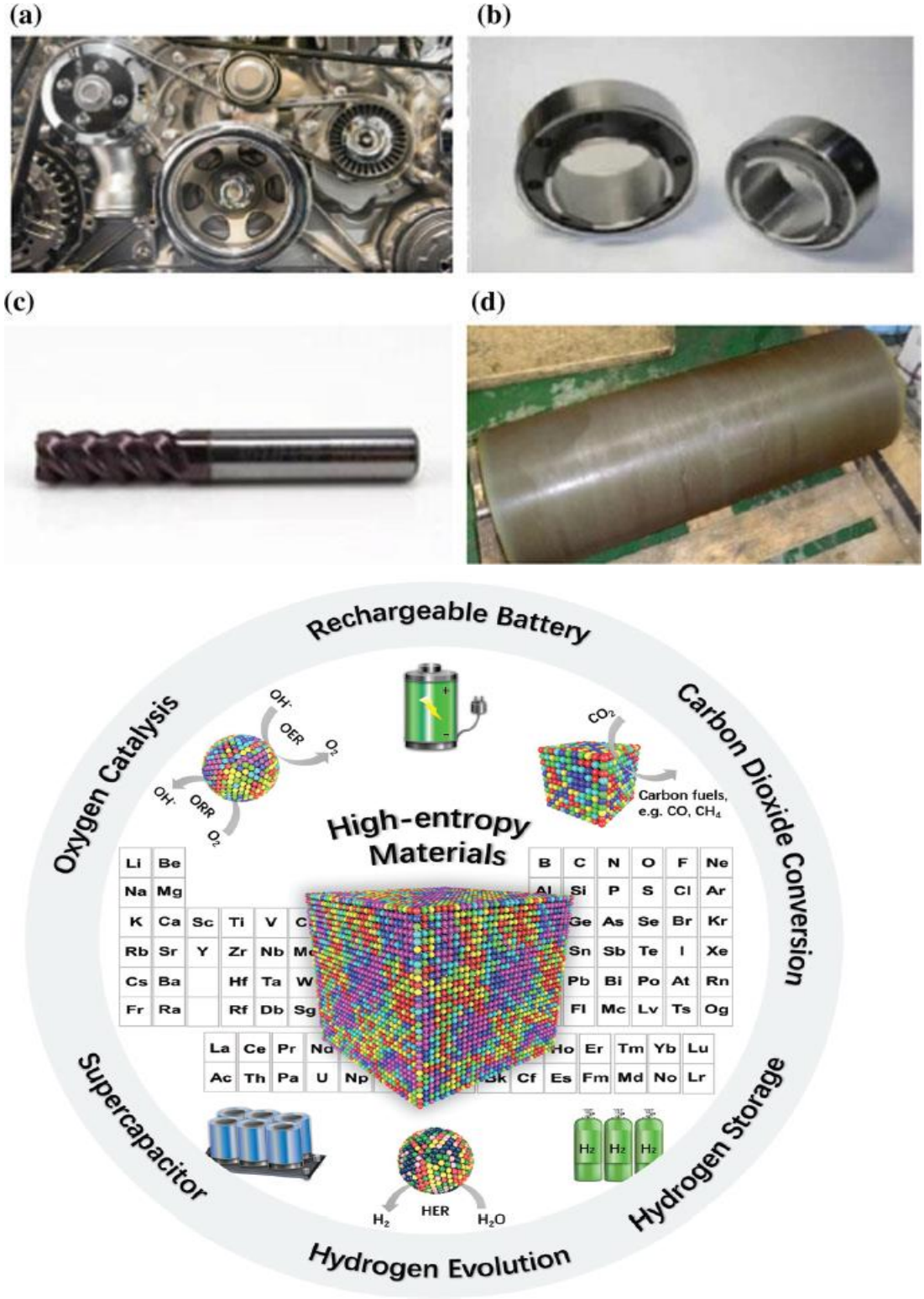

Figure (2.11): Applications of high-entropy alloys. **a)** High entropy alloy mechanical components; **b** high entropy alloy specimens; **c** high entropy alloy high speed cutting tool; **d** high entropy alloy nitride film[14] **e** applications in energy storage and conversion[67].

11. Functional coatings for molds and tools: improved hot hardness, toughness, wear and corrosion resistances, and low friction coefficient

12. Hydrogen-storage materials for automobiles: low cost, high reversible volumetric and gravimetric density of hydrogen, and near ambient cycling condition

13. Interconnect alloys for solid oxide fuel cell: high oxidation and creep resistances, low coefficient of thermal expansion, low area specific resistance, and good weldability.

14. Superconductors: higher critical temperature and critical current

15. Thermoelectric materials: higher thermoelectric figure of merit at medium and high temperatures for converting waste heat into electricity

16. Electric and magnetic materials: constant thermal coefficient of resistivity and thermally stable magnetization in larger temperature range for precision electric and electronic devices

17. Golf-club-head materials: lower density, higher strength, and greater resilience[14] [5][37]

2-11 Corrosion Resistance of HEAs

Metals in service often give a superficial impression of permanence, but all except gold are chemically unstable in air and air-saturated water at ambient temperatures and most are also unstable in air-free water. Hence almost all of the environments in which metals serve are potentially hostile and their successful use in engineering and commercial applications depends on protective mechanisms[68].

Corrosion is the destructive attack of a metal by chemical or electrochemical reaction with its environment. Deterioration by physical causes is not called corrosion, but is described as erosion, galling, or wear. In some instances, chemical attack accompanies physical deterioration, as described by the following terms: corrosion – erosion, corrosive wear, or fretting corrosion[69].

Surface coating is an effective method to enhance the performance and durability of substrate. It is more adoptable to utilize HEAs as corrosion resistance coatings than the bulk HEAs so as to take advantage of the anti-corrosion properties. In the multi-principal element composition of HEAs, the Cr, Ni, Co, and Ti element are noted to be positive to enhance the corrosion resistance in acid solutions. Meanwhile, the Mo element might prevent the pitting corrosion in Cl^- containing solutions. On the contrary, the Al, Cu, and Mn element are reported to have negative effect on anti-corrosion. Meanwhile, the microstructure and phase constitution that could be altered by the given fabrication procedure and the interactions among the constituent elements might present different effects. Therefore, it is vitally important to conduct actual experimental study about electrochemical behaviors of different HEA-based coatings with different processing conditions[41].

2-11-1 Localized Corrosion of HEAs

Passive films, their breakdown, and subsequent contribution to pit formation have been studied in detail [70]. Similarly, pitting corrosion of alloys, caused by a break in the passive film, has also been studied extensively for stainless steels and other corrosion-resistant alloys. One of the major disadvantages of passive materials is their susceptibility to localized corrosion. In pitting corrosion, the passive film breaks resulting in a surface that is susceptible to pitting.

The nature of HEA pitting is still relatively unexplored. The general methods used to study the phenomena are largely electrochemical tests consisting of potentiodynamic polarization as well as critical pitting temperature testing. Potentiodynamic polarization allows for the determination of an alloy's pitting potential. The pitting potential can be described as the potential at which a stable pit begins to grow. The nobility of this potential, along with repassivation potentials that can be obtained from cyclic polarization experiments, have been used to describe the susceptibility of alloys to pitting corrosion. The nobility of this pitting potential represents the alloy's resistance to pitting. The nobler the pitting potential, the less likely the alloy is to undergo pitting under a specific electrolyte. Pitting is known to be associated with metallographic features such as second phases particles, inclusions, and defects. The resulting segregation caused by these features, decreases an alloy's resistance to pitting corrosion, due to their greater susceptibility to pit initiation [71].

Temperature has been studied as a critical factor in pitting corrosion of alloys. There is often a critical temperature below which an alloy will not pit, and above which pitting is observed. At temperatures below the critical pitting temperature (CPT) an alloy will undergo transpassive dissolution at high potentials, while above the CPT the alloy will be susceptible to pitting at potentials below the transpassive potential. The CPT is commonly used to describe an alloy's resistance to pitting corrosion—the higher the CPT, the greater the resistance to pitting corrosion [70].

2-12 Wear

Wear can be defined as the removal of material from solid surfaces by mechanical action. An acceptable amount of material removed is often quite small for rolling and sliding contact surfaces in high-performance

machines. Wear can appear in many ways, depending on the materials of which the interacting contact surfaces are made, the operating environment, and the running conditions[72].

On the other hand, the wear process can be extremely gross and thus result in the bulk removal of material from one surface or both in sliding, rubbing, or rolling contact with the result that the removed material is visible to the naked eye. Wear can take place gradually over a prolonged period of time with small amounts of material removed, or wear can take place rather drastically with the instantaneous loss of material from a surface[73]. Wear is not a material property; however, it is a systems response. The wear rate of a material can vary from 10^{-3} to 10^{-10} mm^3/Nm depending on contact conditions, such as the counterpart material, contact pressure, sliding velocity, contact shape, suspension stiffness, environment and the lubricant[74].

2-12-1 Types of Wear

Wear has been associated with friction, and the wear mechanisms have been classified as adhesion, abrasion, erosion, fatigue and chemical wear as shown below and in figure (2.12).

2-12-1-1 Adhesive Wear

The various steps in adhesive wear are:

- Formation of microwelds between asperities which are deformed under load.

Shear of the two surfaces leading to fracture in or near the microweld region causing the generation of wear debris which can then cause abrasive wear.

2-12-1-2 Abrasive Wear

Abrasive wear may be described as damage to a surface by a harder material. Other terms used to describe abrasive wear are scratching, scoring, gouging. There are two types of abrasion wear:

Two body abrasion, where the harder surface cuts into the softer surface such as in grinding, cutting, and machining operations.

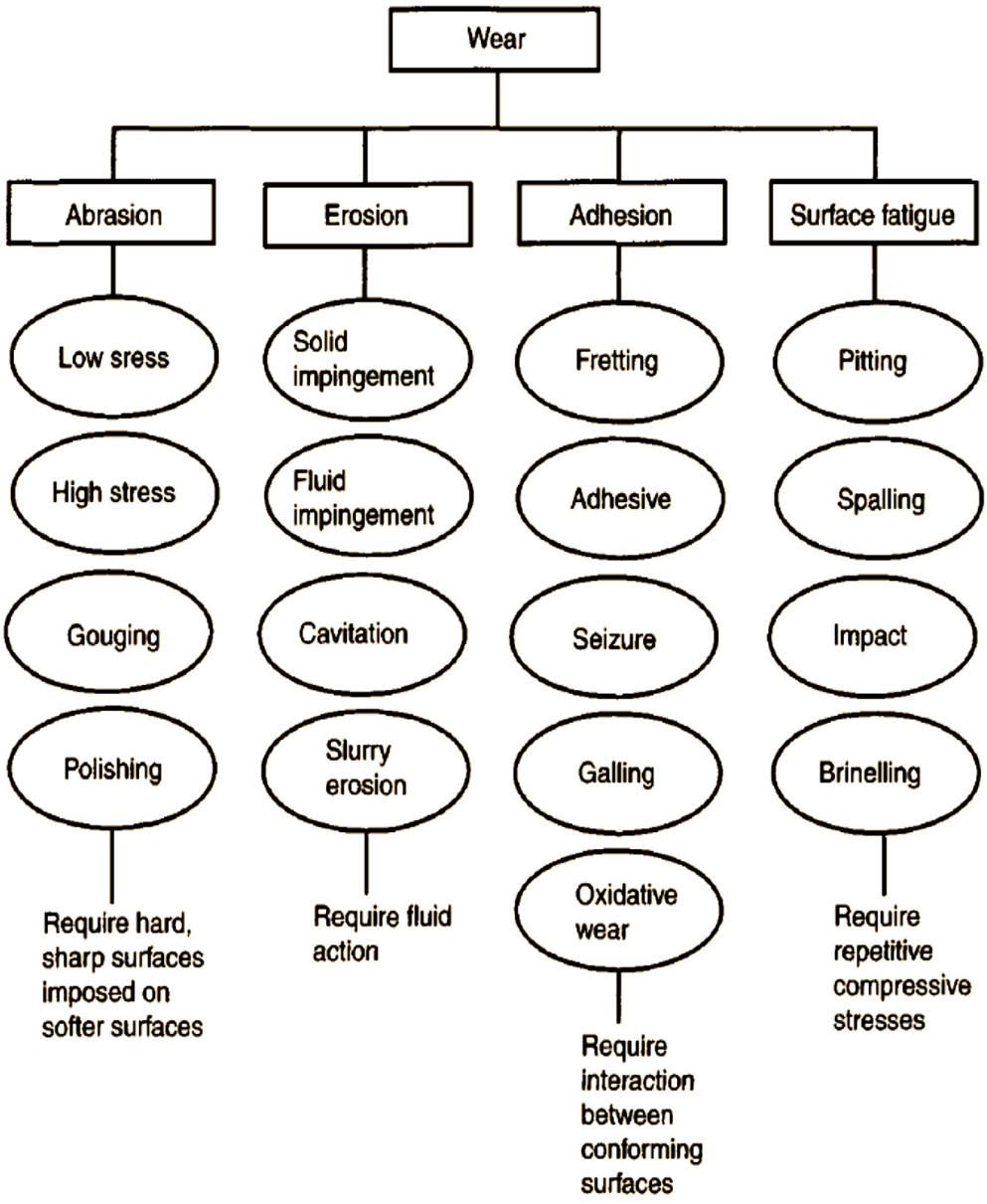

figure (2.12): Major categories of wear based on abrasion, erosion, adhesion, and surface fatigue[75].

2-12-1-3 Fatigue Wear

Repeated stresses or stress cycles with two surfaces in contact cause initiation of failure at subsurface levels, finally leading to delamination of the surface.

2-12-1-4 Fretting Wear

Two loaded surfaces in contact undergo relative oscillating tangential movement known as “slip” as a result of vibration or cyclic stressing. The amplitude of slip is 2 - 20 μm.

The mechanism is somewhat similar to adhesive wear and consists of:

- Adhesion by microwelding causing material to be raised above the level of the original surface.
- Shearing of the raised regions.
- Removal of material by delamination causing the formation of wear debris [45].

2-13 Carbon Nanotubes

Carbon nanotubes are high aspect ratio hollow cylinders with diameters ranging from one to tens of nanometers, and with lengths up to centimeters. As the name implies, carbon nanotubes are composed entirely of carbon, and represent one of many structures that carbon adopts in the solid state[76].

The basic structure of CNTs is shown in Figure (2.13) . A single - walled CNT (SWCNT) can be thought of as a rolled - up graphene sheet in which the edges of the sheet are joined together to form a seamless tube. By changing the direction in the roll -up, different chiralities can be created. Further, several tubes of different diameter can be fitted into each other to make a multi - walled carbon nanotube (MWCNT), as shown in Figure (2.15).

The band structure of graphene is the basis for understanding the electronic behavior of carbon nanotubes. Graphene has a honeycomb lattice structure of carbon atoms in the sp^2 hybridization state[77].

The mechanical properties of carbon nanotubes have attracted just as much interest as their electronic properties, and with good reason as listed in table (2.2). It is now well established that nanotubes are the stiffest and strongest fibres ever produced. Thus, the Young's modulus of the best nanotubes can be as high as 1000GPa, approximately five times higher than steel, while their tensile strength can be up to 63GPa, around 50 times higher than steel. These properties, coupled with their low density, give nanotubes huge potential in a whole range of structural applications[78].
Crystalline carbons display the highest measured thermal conductivities of all known materials. For pure diamond the thermal conductivity, k, is 2000–2500Wm−1K−1, while for graphite, the in-plane conductivity at room temperature can reach 2000Wm−1K−1. For carbon nanotubes, a value of 6600Wm−1K−1 for an isolated (10, 10) nanotube at room temperature[78].

The amazing electrical, mechanical, chemical, and optical properties of CNTs enable a wide range of various applications such as electronic devices, field emission displays, energy storage devices, and drug-delivery devices . CNTs are successfully used in fuel cells for energy storage. In addition, CNTs are very good shields of electromagnetic energy due to their high electrical conductive properties. CNT composite polymer can be utilized in shielding different components from electromagnetic radiation. Due to their remarkable mechanical properties, CNTs are excellent candidates as reinforcing fibers for different composite materials [79].

Table (2.2): Physical properties of CNTs[80].

Physical properties	Parameter	Range
Structure during equilibrium	Mean diameter	1.3–1.5 nm
Density	Zig zag (16,0)	1.33 g/cm^3
	Armchair (10,9)	1.32 g/cm^3
	Chiral (12,5)	1.41 g/cm^3
Lattice parameter	Zig zag (16,0)	16.53 nm
	Chiral (12,5)	16.53 nm
	Arm chair (10,9)	16.55 nm
Interlayer distance	Zig zag	3.40 Å
	Chiral	3.38 Å
	Arm chair	3.37 Å
Elastic nature	Young's modulus	1.0–1.27 TPa
	Tensile strength	About 100 GPa
Thermal property	Mean free path	Around 100 nm
	Thermal conductivity	Around 2000 W/m-K
Electrical behavior	Current density	1015 A/m^2
	Conductance	13.0 (K.Ohms)$^{-1}$

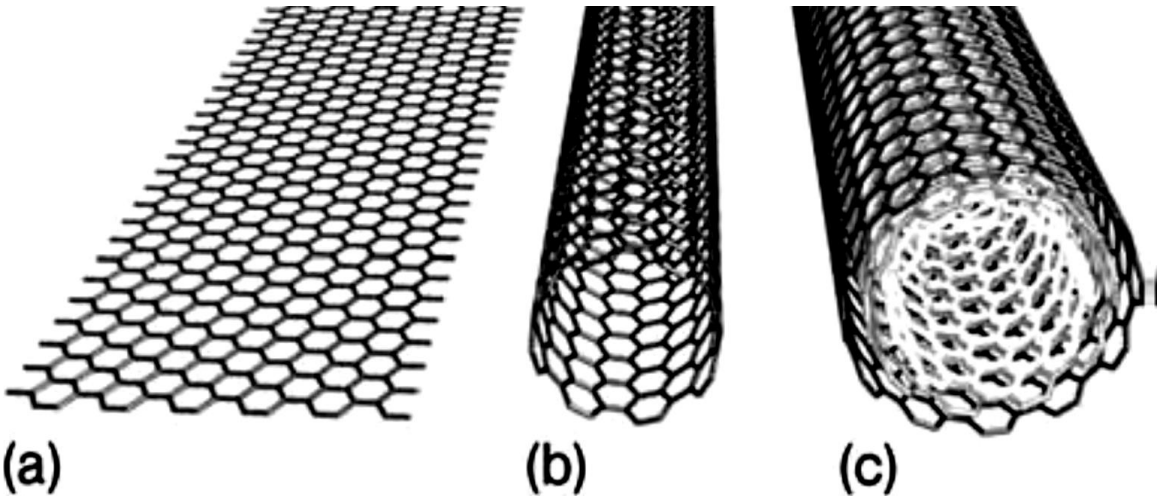

Figure (2.13): Structure of a single layer of graphite (graphene) (a), single – walled carbon nanotube (b) and a multi – walled carbon nanotube with three shells (c)[77].

2.14 Electrochemical Baths for Electroplating

The baths for electroplating containing the additives to enhance the coating morphology, cohesion, etc. The bath additives were explained as follows :

2-14-1 Gelatin

Gelatin or gelatin ($C_{16}H_{12}O_6$) is a translucent, colorless, flavorless food ingredient, commonly derived from collagen taken from animal body parts. It is brittle when dry and rubbery when moist. It may also be referred to as hydrolyzed collagen, collagen hydrolysate, gelatine hydrolysate, hydrolyzed gelatine, and collagen peptides after it has undergone hydrolysis. Gelatine was used as a bonding agent in this electrodeposition path[81].

2.14.2 Sodium Dodecyl Sulfate (SDS)

Dispersed uniformly carbon nano-tubes in coatings electrodeposition HEAs and no agglomeration are to provide stable and homogenous dispersion in the metallic matrix phase. Surfactants SDS (sodium dodecyl sulfate) should be used with CNTs and together mixed with water by ultrasonic device for 45 min. sodium dodecyl sulphate ($C_{12}H_{25}NaOSO_3$) was used for cohesion between the elements.

2.14.3 Sulphanilic Acid

Sulfanilic acid (4-aminobenzenesulfonic acid) is an organic compound with the formula $H_3NC_6H_4SO^3$. It is an off-white solid. It is a zwitterion, which explains its high melting point. It is a common building block in organic chemistry. As the compound readily forms diazo compounds, it is used to make dyes and sulfa drugs.[3] This property is also used for the quantitative analysis of nitrate and nitrite ions by diazonium coupling reaction with N-(1-Naphthyl)ethylenediamine, resulting in an azo dye, and

the concentration of nitrate or nitrite ions were deduced from the color intensity of the resulting red solution by colorimetry. sulphanilic acid (C6H7NO3S) was used to improve the brightness and uniformity of coatings[82].

2.14.4 Ascorbic Acid

Ascorbic acid is an organic compound with formula $C_6H_8O_6$, originally called hexuronic acid. It is a white solid, but impure specimens can appear yellowish. It dissolves well in water to give mildly acidic solutions. It is a mild reducing agent. $C_6H_8O_6$ were used to improve process efficiency and appearance[83].

2.14.5 Boric Acid

Boric acid, also called hydrogen borate, boracic acid, and orthoboric acid is a weak, monobasic Lewis acid of boron. However, some of its behaviour towards some chemical reactions suggest it to be tribasic acid in the Brønsted sense as well. Boric acid is often used as an antiseptic, insecticide, flame retardant, neutron absorber, or precursor to other chemical compounds. It has the chemical formula H_3BO_3 (sometimes written $B(OH)_3$, and exists in the form of colorless crystals or a white powder that dissolves in water. When occurring as a mineral, it is called sassolite. Boric acid (H_3BO_3) was used in the path of deposition to reduce hydrogen evolution [84].

2.14.6 Formic Acid

Formic acid, systematically named methanoic acid, is the simplest carboxylic acid, and has the chemical formula H_2CO_2. It is an important intermediate in chemical synthesis and occurs naturally, most notably in some ants. The word "formic" comes from the Latin word for ant, formica, referring to its early isolation by the distillation of ant bodies. Esters, salts,

and the anion derived from formic acid are called formates. Industrially, formic acid is produced from methanol.

Formic acid is a colorless liquid having a pungent, penetrating odor[5] at room temperature, comparable to the related acetic acid. It is miscible with water and most polar organic solvents, and is somewhat soluble in hydrocarbons. In hydrocarbons and in the vapor phase, it consists of hydrogen-bonded dimers rather than individual molecules. In the deposition path, formic acid (CH_2O_2) was used for surface morphology improvement[85][86].

2.14.7 Ammonium Chloride

Ammonium chloride that used in electrodeposition process to improve process efficiency and appearance, is an inorganic compound with the formula NH_4Cl and a white crystalline salt that is highly soluble in water. Solutions of ammonium chloride are mildly acidic. Sal ammoniac is a name of the natural, mineralogical form of ammonium chloride. The mineral is commonly formed on burning coal dumps from condensation of coal-derived gases. It is also found around some types of volcanic vents. It is mainly used as fertilizer and a flavouring agent in some types of liquorice. It is the product from the reaction of hydrochloric acid and ammonia [87].

2.14.8 Potassium Chloride

Potassium chloride (KCl, or potassium salt) is a metal halide salt composed of potassium and chlorine. It is odorless and has a white or colorless vitreous crystal appearance. The solid dissolves readily in water, and its solutions have a salt-like taste. Potassium chloride can be obtained from ancient dried lake deposits. KCl is used as a fertilizer,[8] in medicine, in scientific applications, and in food processing. KCl was used to improve the conductivity of the electrolyte in the deposition path[88].

2.15 Wettability

Wettability is the relative adhesion of two fluids to a solid surface. With respect to two immiscible fluids in a porous media, wettability is the measure of the preferential tendency of one of the fluids to wet (spread or adhere to) the interstitial surfaces of the porous medium in the presence of the other fluid[89].

Many industrial processes depend on controlling the hydrophobicity of the solids involved. These include flotation, wetting, filtration, adhesion, etc. The most commonly used measure of hydrophobicity is water contact angle (θ). It can be readily measured by placing a drop of water on the surface of a solid of interest, and measuring the angle through the aqueous phase at the three-phase contact. In using this method, known as the sessile drop technique, it is necessary that the solid surface be flat and smooth [90].

Wetting usually occurs within an environment that may consist of a gas or another immiscible liquid, each of which may be referred to as a fluid. A wetting system is characterized by a contact angle (CA), which is defined as the angle between the tangent to the liquid–fluid interface and the tangent to the solid surface at the contact line between the three phases Figure (2.14). The CA is usually measured on the liquid side (when the system involves two liquids, it is usually measured on the denser liquid side). A low contact angle means that the solid is well wetted by the liquid (hydrophilic solid surface), while a high contact angle indicates a preference for solid–fluid contact (hydrophobic solid surface) [91]..

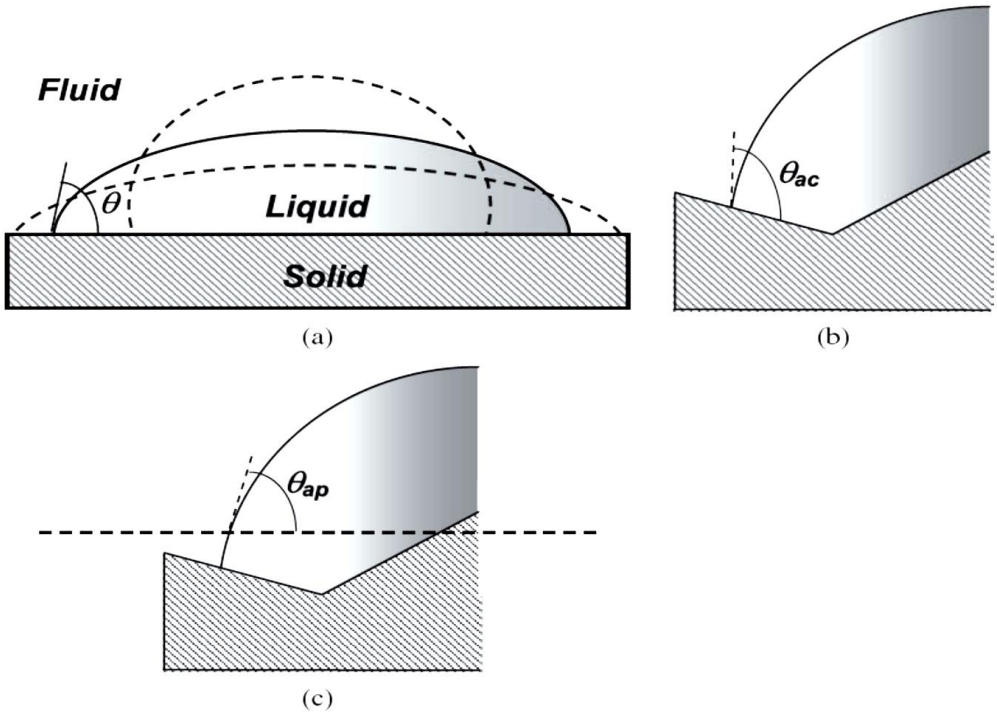

Figure (2.14): Contact angles: (a) various geometric contact angles for the same volume of the drop; (b) the actual contact angle; (c) the apparent contact angle [91].

2.16 Literature Review

Details of literature review will be presented covering the papers, researches, technical reports, data, and other documents that are concerned with the problem of the present work.

Hsu et al., (2005), reported the corrosion behavior of FeCoNiCrCux high-entropy alloys in 3.5% NaCl solution. The corrosion resistance has been evaluated using immersion tests and potentiodynamic polarization measurements. The results show that the increase of copper content in FeCoNiCrCux alloys also increases the tendency to localized corrosion of these alloys. This is due to Cu-rich interdendrite and Cu-depleted (Cr-rich) dendrite in these alloys set up an active/noble cell of appreciable potential difference, and the galvanic action results in preferentially attack along the interdentrites of copper containing high-entropy alloys[92].

Tsai et al., (2006), studied the effect of the substitution of Co by Mn in Al-Cr-Cu-Fe-Co-Ni High-Entropy alloys. The addition of Mn was found to enhance the formation of a BCC structure and inhibit Cu segregation to the interdendrite region. These changes, particularly the formation of a stronger BCC phase, led to a hardness increase of about 100 to 200 Hv for the Mn-containing alloys. Moreover, the ordering of the B2 phase that occurs for Co-containing alloys was suppressed when using Mn, which in turn improved the toughness. The Mn-containing alloys were also found to exhibit excellent age hardening phenomenon at 800^{o}C. This was particularly true of the AlCrCuFeMnNi, Al0.8CrCuFeMnNi, and Al0.8CrCuFe1.5MnNi alloys [93].

Manzoni et al., (2013), investigated the microstructure of the as-cast AlCoCrFeNi high entropy alloy by transmission electron microscopy and atom probe tomography. The alloy shows a very pronounced microstructure with clearly distinguishable dendrites and interdendrites. In both regions a separation into an Al–Ni rich matrix and Cr–Fe-rich precipitates can be observed. Moreover, fluctuations of single elements within the Cr–Fe rich phase have been singled out by three dimensional atom probe measurements. The results of investigations show Cr–Fe-rich precipitates a small scale decomposition within the phase. Anti-correlated fluctuations of Fe- and Cr-rich domains have been attributed to the spinodal decomposition[94].

Zheng et al., (2014), reported the preparation of FeNiCoBiMn high entropy alloy film by electroplating deposition method, and the test results of microscopic observation, energy dispersive spectrometer and X-ray diffraction analysis. Research results indicates that the film is amorphous, the molar content of each element in the high entropy alloy film is greater than 5%, the surface of the film is granular structure with grain size of

about 1μm. It provides a new way for exploring preparation of high entropy alloy[95].

Soare et al., (2015), prepared Al-Cr-Fe-Mn-Ni and Al-Cr-Cu-Fe-Mn-Ni high entropy alloy thin films by potentiostatic electrodeposition and the microstructure of the deposits was investigated. The thin films were co-deposited in an electrolyte based on a DMF (N,N-dimethylformamide)-CH_3CN (acetonitrile) organic compound. The energy dispersive spectrometry investigation (EDS) indicated that all the five respectively six elements were successfully co-deposited. The scanning electron microscopy (FESEM) analysis revealed that the film consists of compact and uniform particles with particle sizes of 500 nm - 4 μm. The X-Ray diffractometry (XRD) patterns indicated that the as-deposited thin films were amorphous. Body-centered-cubic (BCC) structures were identified by XRD after the films were annealed at various temperatures under inert Ar atmosphere. The alloys adhesion on the substrate was determined by the scratch-testing method, with higher values obtained for the Al-Cr-Cu-Fe-Mn-Ni alloy[96].

Licavoli et al., (2015), investigated the mechanical behavior, fracture characteristics, and microstructure of two single-phase FCC HEAs CoCrFeNi and CoCrFeNiMn with some detailed attention given to melting, homogenization, and thermo-mechanical processing. The alloys were fabricated in the usual way (forging, followed by hot rolling) with typical thermo-mechanical processing parameters employed. Transmission electron microscopy was subsequently used to assess the single-phase nature of the alloys prior to mechanical testing. Tensile specimens (ASTM E8) were prepared with tensile mechanical properties obtained from room temperature through 800C. Material from the gage section of selected tensile specimens was extracted to document room and elevated

temperature deformation within the HEAs. Fracture surfaces were also examined to note fracture failure modes. The tensile behavior and selected tensile properties were compared with results in the literature for similar alloys[97].

Löbel et al., (2017), investigated Microstructure and Wear Resistance of AlCoCrFeNiTi High-Entropy Alloy Coatings Produced by HVOF. In this study, The microstructure and phase composition of the atomised powder and the HVOF coating were investigated, as well as the wear behaviour under various conditions. A multiphase microstructure was revealed for the powder and coating, whereas a chemically ordered bcc phase occurred as the main phase. In comparison with a hard chrome-plated specimen, an increase in wear resistance was achieved. Furthermore, no brittle behaviour occurred under abrasive load in the scratch test. The investigation of wear tracks showed only minor cracking and spallation under maximum load[98].

Luo et al., (2018), investigated the corrosion resistance and passive film properties of an equiatomic CoCrFeMnNi high-entropy alloy (HEA) compared with 304L stainless steel in 0.1M H_2SO_4 solution. The in-situ element-resolved corrosion analysis shows that selective dissolution of elements in the HEA is not evident compared to a 304 L stainless steel during passivation. The passive film formed on the HEA is enriched in Fe and Mn but depleted in Cr. The low content of Cr and the extensive formation of metal hydroxide in the passive film are responsible for the lower anti-corrosion performance of the HEA[99].

Aliyu and Srivastava, (2019), electrodeposited AlCrFeCoNiCu HEAs (HEA) composite coating with and without graphene oxide (GO) over mild steel substrate. Potentiodynamic polarization and electrochemical

impedance spectroscopy tests performed in 3.5 wt% NaCl aqueous solution showed that the corrosion resistance of the HEA-GO composite coatings was higher than the HEA coating without GO. The corrosion resistance gradually increased with increase in the GO amount in the coating. Detailed microstructural characterization performed using transmission electron microscopy technique revealed that addition of GO facilitated microstructural and compositional homogeneity which eliminated localized corrosive attack due to elemental segregation induced galvanic coupling thereby increasing the corrosion resistance for the HEA-GO composite coatings[100].

Aliyu and Srivastava, (2019), conducted microstructure and corrosion properties evaluation of MnCrFeCoNi HEAs (HEA) composite coatings containing five different graphene oxide (GO) amounts. The HEA coatings were electrodeposited over mild steel substrate. The corrosion resistance properties of the HEA and HEA-GO composite coatings determined using potentiodynamic polarization and electrochemical impedance spectroscopy tests conducted in 3.5% NaCl solution revealed that with the addition of GO the corrosion resistance of the coating increased. Detailed microstructural characterization using the electron microscopy technique showed that GO enhanced the amount of Mn and Cr in the coatings leading to higher corrosion resistance[101].

Aliyu and Srivastava, (2019), studied AlFeCoNiCu HEA coating containing different amounts of graphene oxide (GO) was electrodeposited on mild steel substrate. As-deposited HEA-GO composite coatings exhibited a granular morphology which became finer and relatively more compact with increase in the GO amount. Structural characterization revealed the presence of mixture of BCC and FCC phase with fraction of the FCC phase increasing with the amount of GO. Potentiodynamic

polarization and electrochemical impedance spectroscopy (EIS) showed that the corrosion rate of HEA-GO coatings progressively decreased with increase in the GO content. Transmission electron microscopy revealed the presence of highly Al-rich matrix phase and Co, Ni, Cu and Fe containing dendritic phase in the coating microstructure. Microstructural homogenization which reduced the extent of mutual galvanic coupling between phases and uniform distribution of Al which can form stable and protective alumina phase along with the impermeability properties of GO enhanced corrosion resistance performance of the HEA-GO coatings when compared to pristine HEA coating[102].

Yoosefan et al., (2020), prepared CoCrFeMnNi high entropy alloy (HEAs) thin films using the pulse electrodeposition method. The films were co-deposited in an electrolyte based on an N,N-dimethylformamide—acetonitrile (CH3CN) organic system containing Co, Cr, Fe, Mn, and Ni chloride cations using the pulse electrodeposition method at frequencies of 2500 and 5000 Hz as well as duty cycles of 50% and 60%. The composition and morphology of the resulting thin films were studied. The energy-dispersive X-ray spectroscopy analysis revealed that all five elements were successfully co-deposited. The calculated entropy of mixing in different conditions ranged between 11.86 and 12.46 J K−1 mol−1 for a duty cycle of 60% in frequencies of 2500 and 5000 Hz, respectively, this indicates that the resulting materials are HEAs. The scanning electron microscopy investigations revealed that the prepared films at a duty cycle of 50% in frequencies of 2500 and 5000 Hz exhibit an inhomogeneous morphology with crystal clusters measuring between 330 and 399 nm. The grazing incidence X-ray diffraction patterns indicated that the as-deposited CoCrFeMnNi thin films consisted of a single face-centered-cubic structure[103].

Premlata et al., (2020), narrates about the production and characterization of HEA (CuNiFeCrMo)- Graphene oxide (GO) nano composite coating deposited by electroless deposition method, in order to improve the mechanical and surface properties of mild steel substrate. Their microstructure, surface morphology, phase and structure analysis, roughness analysis and micro hardness is observed using scanning electron microscopy - Energy dispersive spectroscopy (FESEM-EDS), X-ray diffraction (XRD), Atomic force microscopy (AFM) and micro hardness testing respectively. The incorporation of Graphene oxide nanoparticles into CuFeNiCrMo matrix exceedingly improves their mechanical and surface properties. Uniform dispersion of graphene oxide into HEA matrix is confirmed by FESEM images. No chloride formation is seen. Microhardness test reveals that HEA-GO nanocomposite coating improves the hardness of mild steel[104].

Singh et al., (2020), studied the Microstructural homogenization and substantial improvement in corrosion resistance of mechanically alloyed FeCoCrNiCu HEAs by incorporation of carbon nanotubes. FeCoCrNiCu high entropy alloy (HEA) powder was produced by mechanical alloying. Carbon Nanotubes (CNTs) were mixed in the HEA powder (0.1, 0.2, 0.5, 0.7 wt.% of CNT) and then the mixture was consolidated by spark plasma sintering at 800°C. Phase constitution of the pellets was sensitive to the CNT amount. With smaller quantities of CNTs (upto 0.2 wt.%), the pellets contained a mixture of two different face centred cubic (fcc) phases along with σ phase. With increase in the CNT amount (till 0.2 wt.%), a gradual decrease in the volume fraction of one of the fcc phase occurred leading to microstructural homogenization. Higher CNT additions (0.3, 0.5 and 0.7 wt.%) led to re-evolution of inhomogeneous microstructure containing chromium carbide phase and the two different fcc phases. Corrosion

behaviour measurements showed that with continued addition of CNTs, reduction in the corrosion rate happened till 0.2wt.% CNT. Beyond this, a significant enhancement in the corrosion rate was noticed for pellets with 0.3, 0.5 and 0.7 wt.% CNT additions. Between the pristine HEA pellet and the pellet with optimum CNT amount (0.2 wt.%), 88.6 % reduction in the corrosion rate was measured. The enhancement in the corrosion resistance was attributed to an increase in the chemical homogeneity, which reduced the possibility of galvanic coupling. The decrease in the corrosion resistance beyond the optimum CNT (0.2 wt.%) was attributed to the re-appearance of chemical heterogeneity and evolution of chromium carbide ($Cr_{23}C_6$) phase, which causes intergranular corrosion in these systems[105].

2-17 Summary

From the review of literatures, it is clear that many researchers have dealt with HEAs and their synthesis. Some researchers studied the microstructure and properties of these alloys.

From the literature survey summery, it was found that little studied about the electrodeposition of HEAs. As a result of this work deals with improvement of microstructure and mechanical properties, corrosion, and wear of low alloy steel surface by High-Entropy Alloys thin films which has shown superior and unusual properties.

Chapter Three: Experimental part

Chapter Three: Experimental Part

3.1 Introduction

This chapter deals with materials, used equipments, and preparation method of specimens for coating processes. It also contains several tests such as: microhardness, corrosion, wear, and the microstructure. Metallography was carried out by Field Emission Scanning Electron Microscope (FESEM) and Scanning Electron Microscope (SEM).Figure (3.1) shows the block diagram of procedures for experimental part.

3.2 Materials Used.

3.2.1 Metal Substrate

The substrate metal used in this work was AISI 4140 steel grade as shown in figure (3.2). The launch tube of the Kalashnikov (MK47) was used from low alloy steel and part of it was cut in the shape of a disk (20mm diameter×10mm height) by the (EDM) device in the laboratories of the Ministry of Science and Technology – Baghdad. The chemical analysis of this alloy was conducted in general company for examination and rehabilitation engineering /Baghdad. Details composition are shown in a Table (3.1).

Table (3.1): Chemical Compositions for AISI 4140 steel.

Element	Cr	Mn	C	Si	Mo	S	P	Fe
Standard AISI	0.8-1.1	0.75-1	0.38-0.43	0.15-0.3	0.15-0.25	0.04	0.035	Bal.
Wt%	1.094	0.997	0.41	0.21	0.245	0.0368	0.0281	Bal.

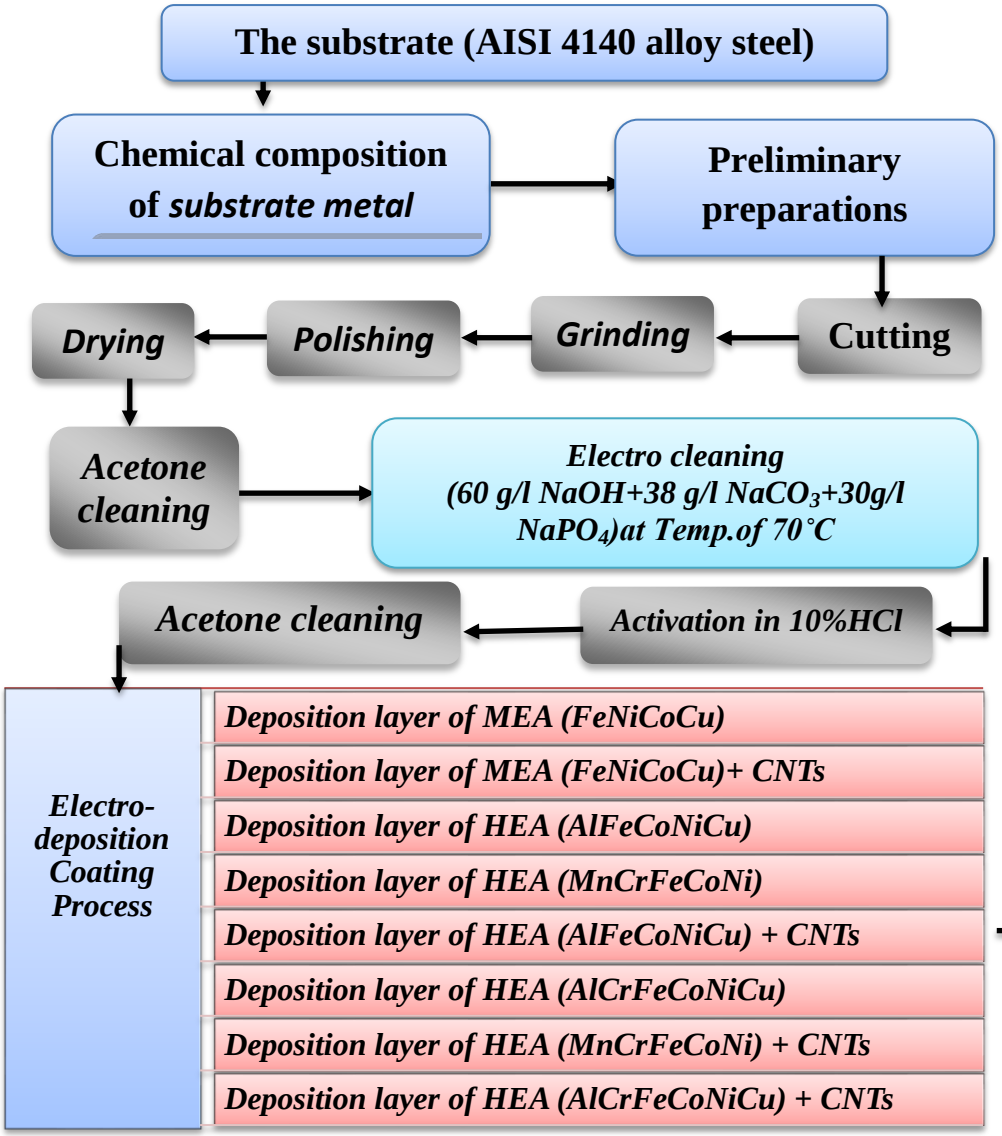

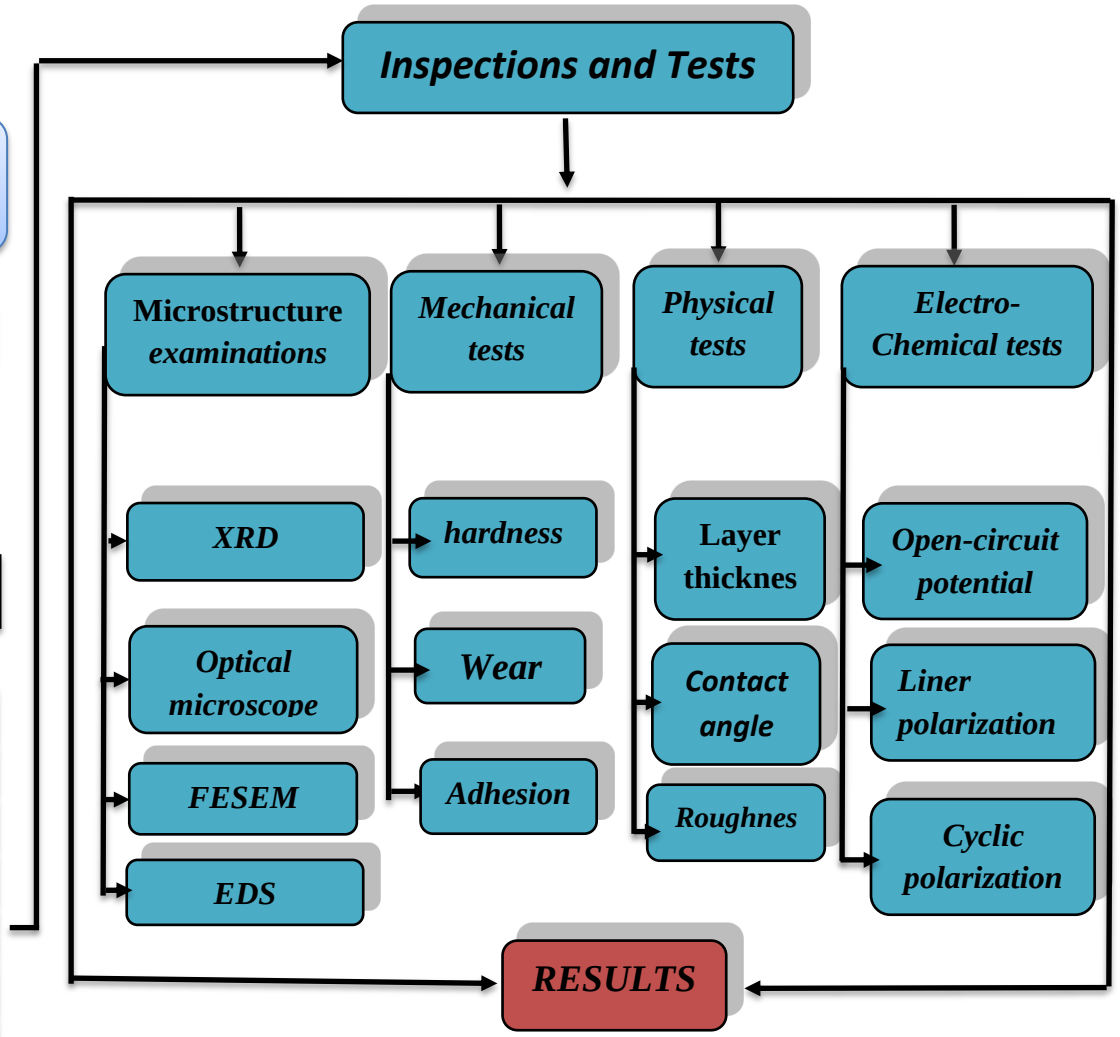

Figure (3.1): The block diagram of the experimental procedure

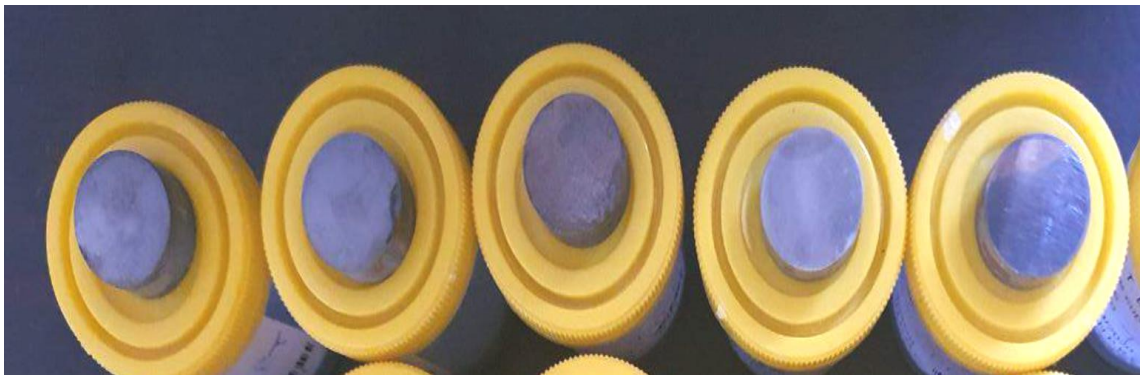

Figure (3.2): Shows low alloy steel (AISI 4140) specimens were used in this work

3.2.2 Carbon Nanotube (CNT).

MWCNT with purity more than 95%, 10-30 µm of length, 5-10nm in inner diameter and 20-30 nm of outer diameter, were be supplied from (US Research Nanomaterials). To enhance dispersion for CNT in electrodeposition coating bath, as-received CNTs were put at (1 -1.5 hours) using by machine of ultrasonic homogenizer. Figure (3.3) shows Field Emission Scanning Electron Microscopy in MIRA3 TESCAN Company in Iran, images as-received CNTs.

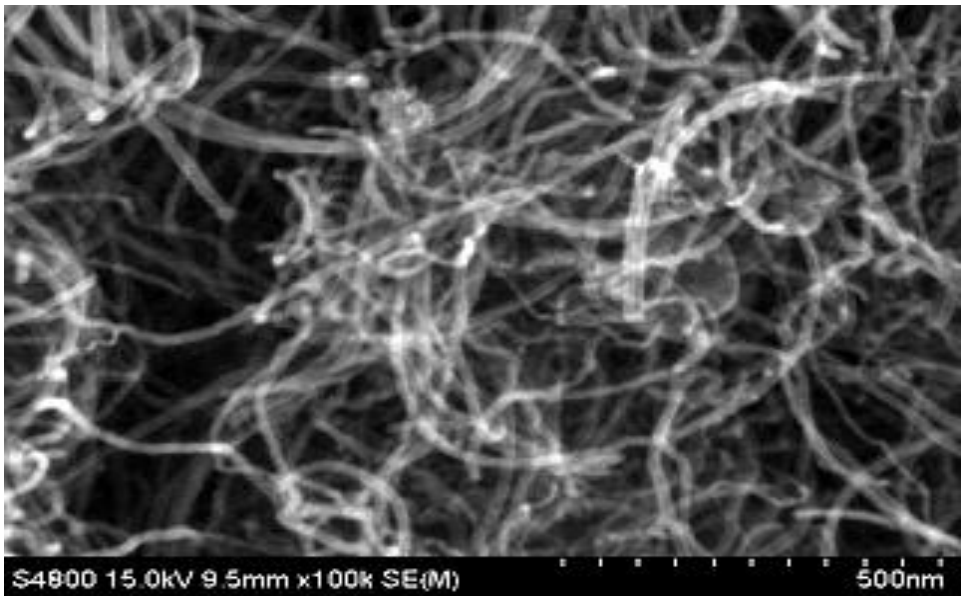

Figure (3.3): Images FESEM for as-received CNT.

3.3 Specimen Preparation for Coating Process.

The specimen was prepared before coating by:

- All specimens were grinded and polished using emery paper (SiC paper) No. (220, 400, 800, 1000, 1500 and 2000) respectively. Then specimens were washed with distilled water and, then dried by using an electrical dryer. A polishing was conducted by diamond paste.
- Specimens were immersed in acetone for 30 min[51].
- Before coating ,specimens are immersed in solution electro cleaning include materials (60g/l NaOH ,38g/l $NaCO_3$ and 30g/l $NaPbO_4$) for one minute period at 70^oC temperature with moving the electrolyte using magnetic stirring with (5 volt) in order to eliminate the dust and the oil from the metal surface, follow that specimens are washed by distilled water and then dried and after that, the specimens were washed with distilled water and put for (10 sec) in hydrochloric acid (HCl) solution (10 percent) to activate the surface of the substrate after which it guided immersion in coating solution[101].
- Then the specimens are washed with distilled water, dried, and then put directly in the coating solution for immersion.

3.4 Electrodeposition Bath Preparation.

The materials used in the electrodeposition bath are listed in the Table (3.2). After completion of preparing surfaces for coating, electrodeposition bath was prepared for the process according to the concentrations and operation condition as shown in Tables (3.3) and (3.4) respectively. The coating of MEAs and HEAs was deposited on the 4140 steel via electrodeposition coating procedure. The pH, time to immersion, and temperature values of coating bath was kept constant equal to (1.5, 15min, and 30^oC respectively). Through of coating, solution of bath agitate by a magnetic stirring to avoid localized overheating and reduce the fluctuation of ionic concentration. As the coating procedure of MEAs-CNTs and

HEAs-CNT deposition by concentrations of the CNT (0.2 g/100ml CNTs), firstly CNTs were dispersed in an ultrasonic bath, then the addition of CNT to the MEAs and HEAs prepared bath.

Specimens Codes ,

A = (FeNiCoCu) MEAs , B = (FeNiCoCu) MEAs + 0.2%CNTs

C= (AlFeCoNiCu) HEAs, D = (AlFeCoNiCu) HEAs + 0.2% CNTs

E = (MnCrFeCoNi) HEAs F = (MnCrFeCoNi) HEAs + 0.2% CNTs

G = (AlCrFeCoNiCu) HEAs, H =(AlCrFeCoNiCu) HEAs + 0.2% CNTs

Table (3.2): The Materials that Used in the Electrodeposition Bath

Materials	Chemical symbol	Additive	Chemical symbol
Aluminum Chloride Hexahydrate	($AlCl_3 \cdot 6H_2O$)	Gelatin	$C_{16}H_{12}O_6$
Iron Chloride Tetrahydrate	($FeCl_2 \cdot 4H_2O$)	Sodium dodecyl sulfate (SDS)	$C_{12}H_{25}NaOSO_3$
Cobalt Chloride Hexahydrate	($CoCl_2 \cdot 6H_2O$)	Ascobic acid	($C_6H_8O_6$)
Nickel Chloride Hexahydrate	($NiCl_2 \cdot 6H_2O$)	Ammonium chloride	(NH_4Cl)
Cupric Chloride Dehydrate	($CuCl_2 \cdot 2H_2O$)	Potassium chloride	(KCl)
Manganese Chloride Tetrahydrate	($MnCl_2$•4H2O)	Boric acid	(H_3BO_3)
Chrome Chloride Tetrahydrate	($CrCl_3 \cdot 4H_2O$)	Sulphanilic acid	($C_6H_7NO_3S$)
Carbon Nano-tubes	(CNTs)	Formic acid	(CH_2O_2)

Table (3.3): Electrodeposition Bath Concentration of Specimens in (g/100ml)[101] [102][106]

N	*Material*	*Specimen-A-*	*Specimen-B-*	*Specimen-C-*	*Specimen-D-*	*Specimen-E-*	*Specimen-F-*	*Specimen-G-*	*Specimen-H-*
1	($AlCl_3 \cdot 6H_2O$)	------	------	2.4	2.4	------	------	2.414	2.414
2	($FeCl_2 \cdot 4H_2O$)	0.795	0.795	0.7	0.7	0.795	0.795	0.795	0.795
3	($CoCl_2 \cdot 6H_2O$)	0.9517	0.9517	0.95	0.95	0.9517	0.9517	0.952	0.952
4	($NiCl_2 \cdot 6H_2O$)	1.664	1.664	1.9	1.9	1.902	1.902	1.664	1.664
5	($CuCl_2 \cdot 2H_2O$)	0.5114	0.5114	0.51	0.51	------	------	0.682	0.682
6	($MnCl_2$•4H2O)	------	------	------	------	2.97	2.97	------	------
7	($CrCl_3 \cdot 4H_2O$)	------	------	------	------	3.33	3.33	3.73	3.73
8	(CNTs)	------	0.2	------	0.2	------	0.2	------	0.2
9	Gelatin	------	------	0.7	0.7	0.7	0.7	------	------
10	(SDS)	0.25	0.25	0.25	0.25	0.25	0.25	0.25	0.25
11	Ascobic acid	------	------	0.5	0.5	0.5	0.5	------	------
12	NH_4Cl	------	------	11.98	11.98	11.98	11.98	------	------
13	KCl	------	------	12	12	12	12	------	------
14	Boric acid	4.94	4.94	4.94	4.94	4.94	4.94	------	------
15	Sulphanilic acid	------	------	0.52	0.52	0.52	0.52	------	------
16	Formic acid	------	------	0.5	0.5	0.5	0.5	------	------

Table (3.4): Operating Conditions for Electrodeposition Bath[101] [102][106]

Operating conditions	Current	Stirring
Specimen -A-	***0.16 A***	*900rpm*
Specimen -B-	***0.16 A***	*900rpm*
Specimen -C-	***0.16 A***	*600rpm*
Specimen -D-	***0.16 A***	*600rpm*
Specimen -E-	***0.4 A***	*600rpm*
Specimen -F-	***0.4 A***	*600rpm*
Specimen -G-	***0.63 A***	*850rpm*
Specimen -H-	***0.63 A***	*850rpm*

3.5 Tests

Carried out the present research for procedure of the upcoming tests for evaluating performance of coating layers.

3.5.1 Microstructure Characterization

3.5.1.1 X-ray Diffraction.

XRD was used for phase identification of coating by using (EQuinox X-3000, by Cu Ka (X=1.54187A) radiation. Scanning domain of 20,(40kV and 30mA)) is used, for identification the specimen crystal structure after coating MEAs and HEAs and after the addition of CNTs to the electrodeposition paths operating at a scanning speed of 6° (2ϴ) per minute.

3.5.1.2 Light Optical Microscope (LOM)

Involved identification and measurement of the phases, shape and grain size are some characteristics of grain boundaries could be evaluated

by optical microscope, it was professional metallurgical microscope with polarizing dark field reflected light, as shown in Figure (3.4).

Figure (3.4): Shows Optical microscopy.

3.5.1.3 SEM and FESEM

Field Emission Scanning Electron Microscope (FESEM) and SEM (Scanning Electron Microscope) are used to study topography of the coating in the MIRA3 TESCAN Company in Iran. SEM and FESEM, are carried out at different magnifications for electrodeposition layer, as shown in Figure (3.5).

Figure (3.5): The Field Emission Scanning Electron Microscope and Scanning Electron Microscopy are used.

3.5.1.4 Energy Dispersive Spectrometry (EDS)

Energy Dispersive Spectrometry was used by MIRA3 TESCAN company in Iran. An analytical method is used to determine the chemical compositions for coating layers of specimens (A, B, C, D, E, F, G, and H) .

3-5-2 **Mechanical Test**

3.5.2.1 Microhardness Test.

Microhardness test was carried out according to ASTM E92-17 using digital Vickers hardness tester (HVS-1000) which is presented in the metallurgy dep. lab./ materials engineering college-Babylon University. This process was carried out on the coated layer for the specimens (O, A, B, C, D, E, F, G, and H). A load of 50 g was applied for 15 Sec.[107] The three readings are recorded for each specimen coated and for the substrate, and then, the average value was taken.

3.5.2.2 Wear Test.

This test was conducted by Pin-on-disc technique. The test was performed at room temperature (25ºC) and relative humidity of (40%). The used load was 5N and 10N. Velocity of sliding is (0.1 m/s) and distance of sliding was (500m). The disc was carbide steel. Figure (3.6) shows the wear machine. Wear specimens tests were carried out which are low alloy Steel (4140) specimen without plating, MEAs, MEAs-CNTs, HEAs, and HEAs-CNTs. The specimens are weighed by a sensitive balance before and after the wear test to calculate the weight loss of coatings.

The wear rate of the specimen is calculated (ASTM G99) and is defined as :

$$W_{rate} = \Delta w / \pi D N t \qquad (3.1)$$

W_{rate} is wear rate (g/cm)

ΔW (g) Weight loss after (5,10,15 and 20)min.

D=Diameter of the sliding circle (4mm)

N=speed of rotation disk (96 rpm)

t= wear test time (20)min

The drawings of the friction coefficient with distance are plans automatically by a device as shown in Figure (3.6).

Figure (3.6): Expresses operating instructions of wear test.

3.5.2.3 Adhesion Test.

Adhesion Testing plays a significant role in coatings inspection, whether the user is trying to adhere to industry standards, maintain quality control, or follow customer specifications. This test done using the PosiTest AT Adhesion Tester using 14- millimeter loading fixture and equal amounts of the included epoxy were applied as an adhesive. The test was carried out in university of Babylon/ materials engineering college-metallurgy department labs according to ASTM D4541.

3.5.3 Physical Tests

3.5.3.1 Coating Thickness Measurements

A digital coating thickness gage Type (TT260), is used to determine the coating thickness in this work as shown in Figure (3.7). The device accuracy of ± 0.1 µm. In this method, measurement is taken in the three places to give averaged thickness for coated specimen. The test was carried out in university of Babylon/ materials engineering college- ceramic department labs.

Figure (3.7): Coating thickness instrument.

3.5.3.2 Contact Angle Measurement

Contact angle test was accomplished to evaluate the effect of coating on the wettability with and without the addition of CNTs. The instrument used was with contact angle range of (0º to 180º) type SL 200KS - Optical Dynamic I Static Interfacial Tensiometer and Contact Angle Meter that has been manufactured in KINO Industry U.S. This device used for calculation the contact angle and determine its average value to create a real-time data graph that tracks changes in contact angle. The test was carried out in university of Babylon/ materials engineering college- Ceramic department labs according to ASTM D7334.

3.5.3.3 Surface Roughness Test.

The value of surface roughness measurement was carried out to the coated specimens with and without the addition of CNTs using a common parameter Ra in μm. In this test, the surface roughness calculated a mean of (10) measurements was recorded.

3.5.4 Electro-chemical test

3.5.4.1 Open Circuit Potential (OCP)- Time Measurements

The goal of the OCP-time measurement is to better understand the corrosion behavior of coated and uncoated specimens in 3.5 %NaCl solution under equilibrated conditions. The OCP-time measurement is a crucial metric for determining the stability of the specimens' passive film. The working electrode's potential is monitored in relation to a Saturated Calomel electrode (SCE). Between the working electrode and the reference electrode is a voltmeter that is saturated. For each specimen 30 min open circuit potential measurement was performed. The first record was taken immediately after immersion then the voltage was monitored for the interred period of test at an interval of (5min).

3.5.4.2 Potentiodynamic Liner Polarization

The simple immersion method is adopted to evaluate the corrosion behavior of the coatings. The technique of Tafel extrapolation was also used in a solution of (3.5% NaCl). This test was done in the Corrosion Laboratory in the Laboratories of the Department of Metallurgical Engineering / University of Babylon. A 500 ml capacity glass electrolytic cell is used. The potentiodynamic curves of polarization are planned, and both corrosion current density ($i_{corr.}$) and corrosion potential ($E_{corr.}$) are valued by plots of Tafel with using anodic and cathodic curves. A cell of the corrosion test used is shown in Figure (3.8).

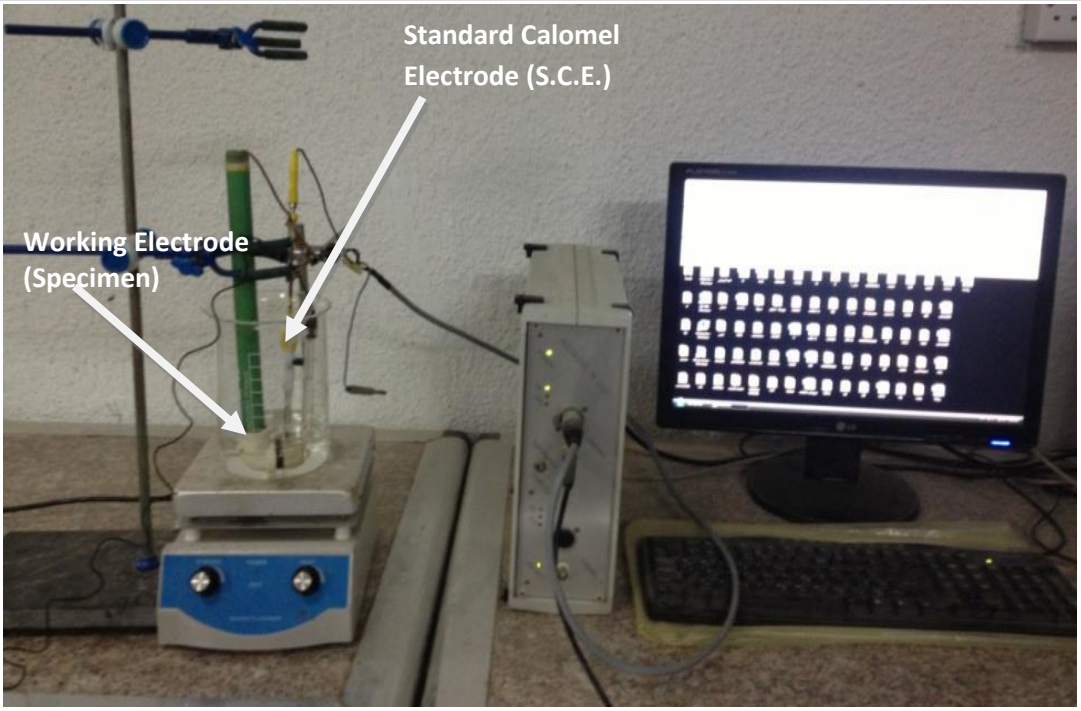

Figure (3.8): Instrument of corrosion test

The corrosion rate calculation follows Faraday's law in ASTM standard G 102 and is defined as [108]:

$$\textbf{Corrosion rate (mpy)} = \frac{K_I i_{corr}\, EW}{\rho} \qquad (3.2)$$

(**CR**) is corrosion rate, (mpy),

$\mathbf{i_{corr}}$ is density of corrosion current, $i_{corr} = \mathbf{I_{corr}} / \mathbf{A}$ ($\mu A / cm^2$)

$\mathbf{I_{corr}}$ is total anodic current, (μA)

A is exposed specimen area, (cm^2)

ρ is a density of steel specimen and coating that is used in the corrosion test(g/cm^3) that are listed in Table (3.5).

$\mathbf{K_1}$ is a constant value in Faraday's law, which is (0.13, mpy g/μA cm)

EW is equivalent weight of specimen steel and coating in dimensionless.

Table (3.5): Density of Steel Specimen and Coating Specimens

Specimen	O	A	B	C	D	E	F	G	H
Density, g/cm^3	7.85	8.67	8.36	8.06	8.15	8.05	8.14	7.9	7.99

3.5.4.3 Cycle Polarization Test

Cyclic polarization test was introduced for the first time in the 1960s. It is widely used to determine resistance to localized corrosion or degradation rate in a short time. Thus this technique is applicable as a method for prediction of localized corrosion also beneficial for alloys that are passivized spontaneously and underwent localized corrosion [109].

As an electrolyte cyclic polarization test, electrochemical tests were conducted in three electrode cells containing NaCl solution. The counter electrode was Pt, the reference electrode was SCE, and the working electrode was a specimen.

The corrosion cell consists of three electrodes:

1. The working electrode (4140 low alloy steel).

2. The counter electrode (platinum rod).

3. The saturated calomel electrode (SCE).

Chapter Four :

Results & Discussions

Chapter Four: Results and Discussion

4.1 Introduction

This chapter presents and discusses results that were obtained from several tests that were conducted throughout this work. These tests included mechanical and electrochemical tests of the examined specimens, such as metallography, microhardness, wear test, Tafel extrapolation, inspection of surface roughness using scanning electron microscope (SEM), optical microscope, field emission scanning electron microscope (FESEM), x-ray diffraction (XRD), energy dispersive spectrometry (EDS), adhesion test, contact angle measurement, and coating thickness measurement.

4.2 Microstructure Characterizations

4.2.1 X-Ray Diffraction (XRD)

The high-entropy effect and sluggish diffusion of HEAs make the solid-solution phases stable, as compared to intermetallic compounds, thus allowing them to form single phases [36]. There are three major families of HEAs, namely the fcc-, bcc-, and hcp-structured HEA families. Most of the widely-studied HEAs are fcc/bcc-structured, and their compositions are mainly transition metals [110]. Conventional XRD was used to identify the FCC and BCC crystal structures in this system.

The XRD patterns show the structure of phases in specimens (A & B) are provided in Figure (4.1). The pristine MEA coating showed peaks of face centred cubic (FCC) structure ((111), (222)) and peaks of body centred cubic (bcc) structure ((310), (110)). The prominent FCC phase in the pristine MEA coating is the Cu-rich phase, while the disordered bcc phase contained Fe, Ni and Co, since these elements (Fe, Ni and Co) can form solid solution due to their lower enthalpy of mixing as compared to the

enthalpy of mixing between Cu and other elements that's agreed with Aliyu [111].

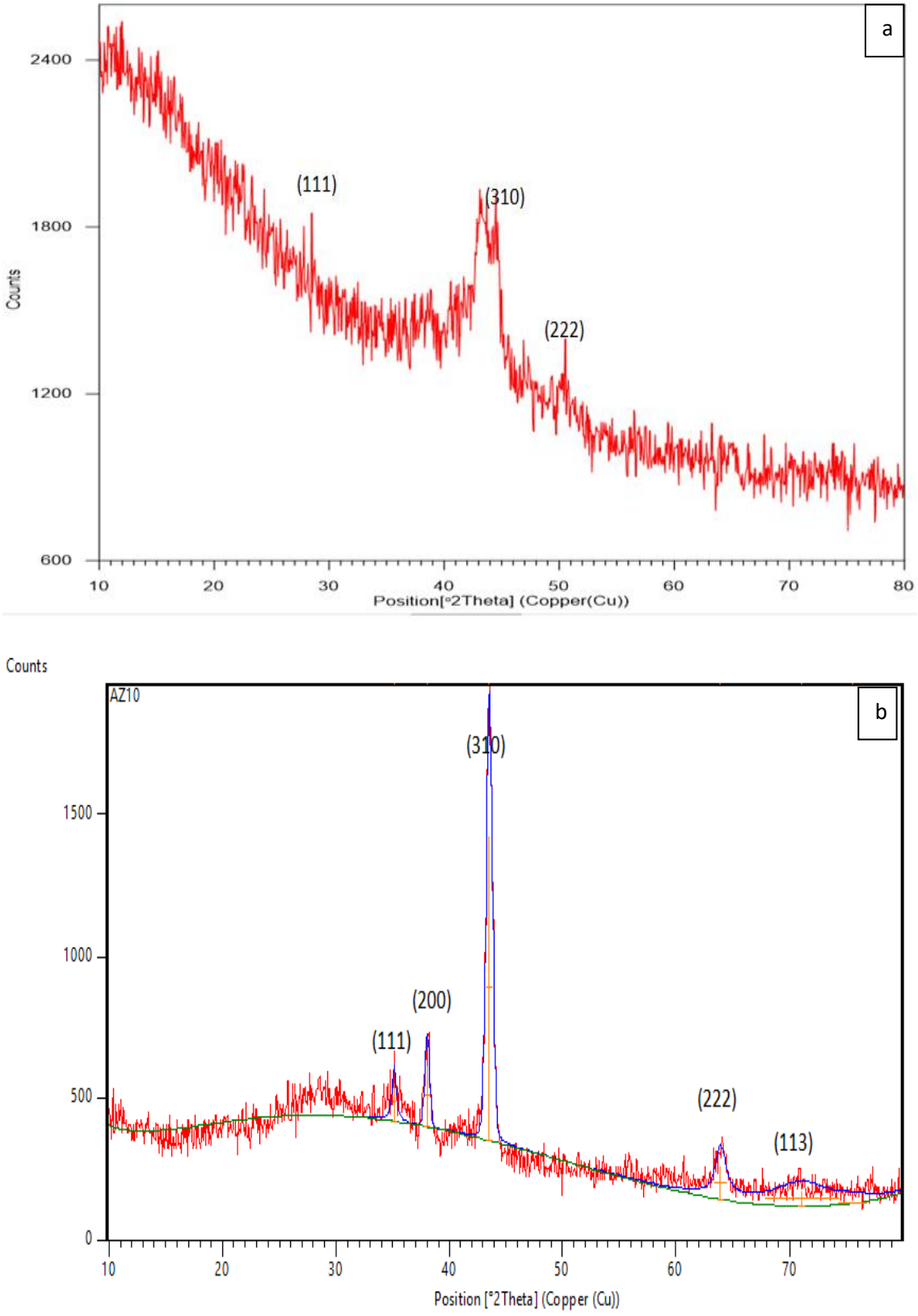

Figure (4.1): XRD Patterns of a) Specimen A and b) Specimen B.

With addition of the CNTs from MEA-CNTs, a continuous decrease in the fcc (111) peak intensity and increase in the bcc (310) peak intensity were observed, suggesting that the CNTs incorporation into FeNiCoCu matrix changes the coatings phase constitution by enhancing the volume fraction of the bcc phase and decreases the fcc volume fraction within the coating matrix.

The average crystallite size of the fcc and bcc phase of specimens (A & B) calculated using the Scherrer formula that listed in equation (4.1) was 13.6, 6.5, 16.8, 13.8, 8.3 and 5.4 nm for the fcc phase and 13.8, 2.5, 8.3, and 1.5 nm for the bcc phase of MEA-CNTs and MEA coatings respectively as listed in Table (4.1).

$$D = K\lambda/(\beta \cos\theta) \qquad 4\text{-}1$$

Where D the average size of the crystal, K = 0.94 for cubic structure, λ is wavelength of X-ray, and β is the full width at half maximum intensity of the peak.

The changes in the SEM microstructures may be correlated with the XRD studies, such that the alloy phases for the low aluminum content are FCC (a Cu-rich FCC phase in the interdendrites and a multi-principal element FCC phase in the dendrites) and mixed-phase FCC/BCC at higher aluminum contents[10] .

XRD patterns of as-deposited AlFeCoNiCu HEA and HEA-CNTs composite coatings are shown in Figure (4.2). Analysis of the XRD patterns revealed that all the coatings contained a mixture of BCC and FCC phases. It was also noticed that the volume fraction of the FCC phase increased with increase the amount of CNTs in the composite coatings.

Table (4.1) : The Crystalline Size and Crystal Structure of the Specimens.

Specimen code / peak		(110)	(111)	(200)	(211)	(220)	(222)	(310)	(113)
CRYSTALINE SIZE, nm	A	--	13.57	--	--	--	6.5	2.5	--
	B	--	16.8	13.8	--	--	8.38	1.5	5.04
	C	--	3	11.5	--	37.7	--	--	--
	D	21.4	21.4	29	--	9.56	--	--	--
	E	--	17.1	5.45	7.6	--	--	--	68.1
	F	--	28.5	21.8	--	5.96	--	8.27	--
	G	--	26.3	9.9	--	10.35	--	--	--
	H	--	9.35	6.12	--	31	--	--	--
Crystal Structure		BCC	FCC	FCC+ BCC	BCC	FCC+ BCC	FCC	BCC	FCC

It has been discussed by researchers that incorporation of Al in HEAs causes the evolution of BCC phase. Lattice distortion introduced into the FCC phase due to the incorporation of large sized Al atoms can be relaxed by adoption of BCC lattice which has lower packing fraction and more open structure. Presence of BCC phase in the present case can also be attributed to the fact that the electronic structure of Al favor bonds between the Al and transition metals with an incompletely filled d-shell. Microstructure of all the coatings indeed contained Al rich phase and the relative increase in the FCC phase volume fraction with the addition of CNTs was due to increase in the compositional uniformity of the microstructure. The crystallite size of the coatings determined by Scherrers formula was 3 nm, 11.47 nm, 37.7 nm, 21.4 nm, 29.3 nm and 9.5 nm for HEA and HEA-CNTs coatings respectively. The observed gradual reduction in the crystallite size can be attributed to the increased addition of

CNTs which provided heterogenous sites for nucleation and growth of grains.

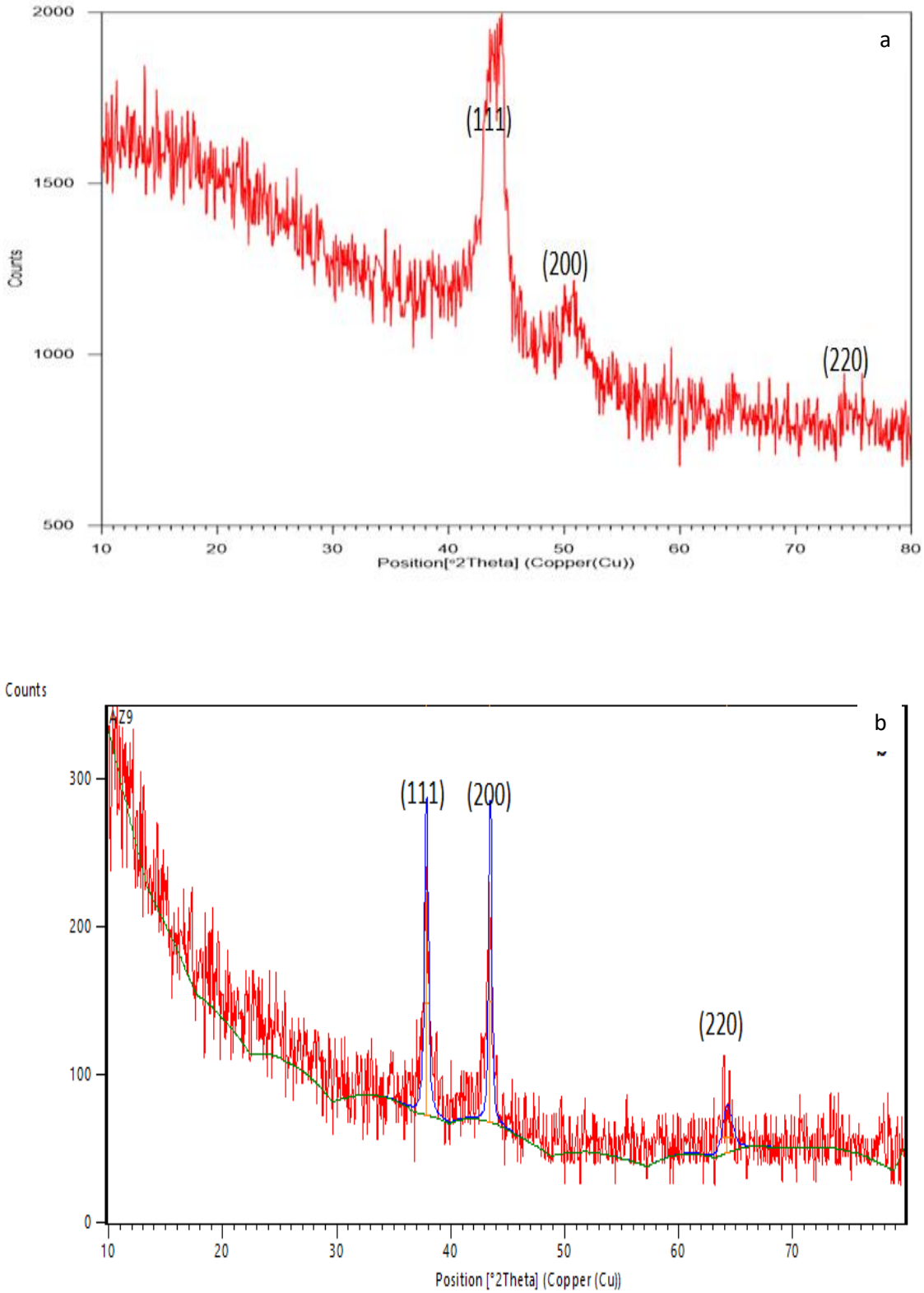

Figure (4.2): XRD Patterns of a) Specimen C and b) Specimen D.

As the XRD profiles in Figure (4.2 a & b) that compared with standard chart of constituent element as shown in Appendix C, do not reveal any peak at these two theta value so it can be concluded that the coatings procedure used in the present study did not produce any detectable amount of Al_2O_3 phase in the coatings.

Figure (4.3) shows the X-ray diffraction patterns of the HEA coatings with and without CNTs. All the coatings exhibit a (BCC and FCC) structure. The average crystallite size calculated using the Scherrer formula [45] was 68.18, 65.1, 17.13, 7.6, 5.96, 28.5, 21.8, 8.27, and 5.4 nm for HEA and HEA-CNTs coatings respectively. The observed decrease in the average crystallite size can be attributed to the increase in the heterogenous sites for nucleation and growth of grains as a results of CNTs addition. The microstructure of HEA that Mn element substitutes for Co element in alloy is FCC + BCC structure.

According to the XRD patterns, the coatings exhibit a mixture of FCC and BCC phases. It is shown later that the CNTs in the AlCrFeCoNiCu HEA-CNTs composite coatings increases the coating compositional homogeneity with respect to the distribution of component atoms leading to the formation of relatively more open BCC solid solution structure. Furthermore, the average crystallite size obtained using the Scherrer formula was 31.1, 26.3, 10.35, 9.89, 9.35, and 6.12 nm for HEA and HEA-CNTs coatings respectively as listed in Appendix

The observed decrease in the average crystallite size with the addition in the CNTs contents can be attributed to the increase in the heterogeneous sites for nucleation of grains during the electrodeposition. The BCC phase in the electrodeposited is expected to form due to the presence of chromium which is a BCC stabilizer.

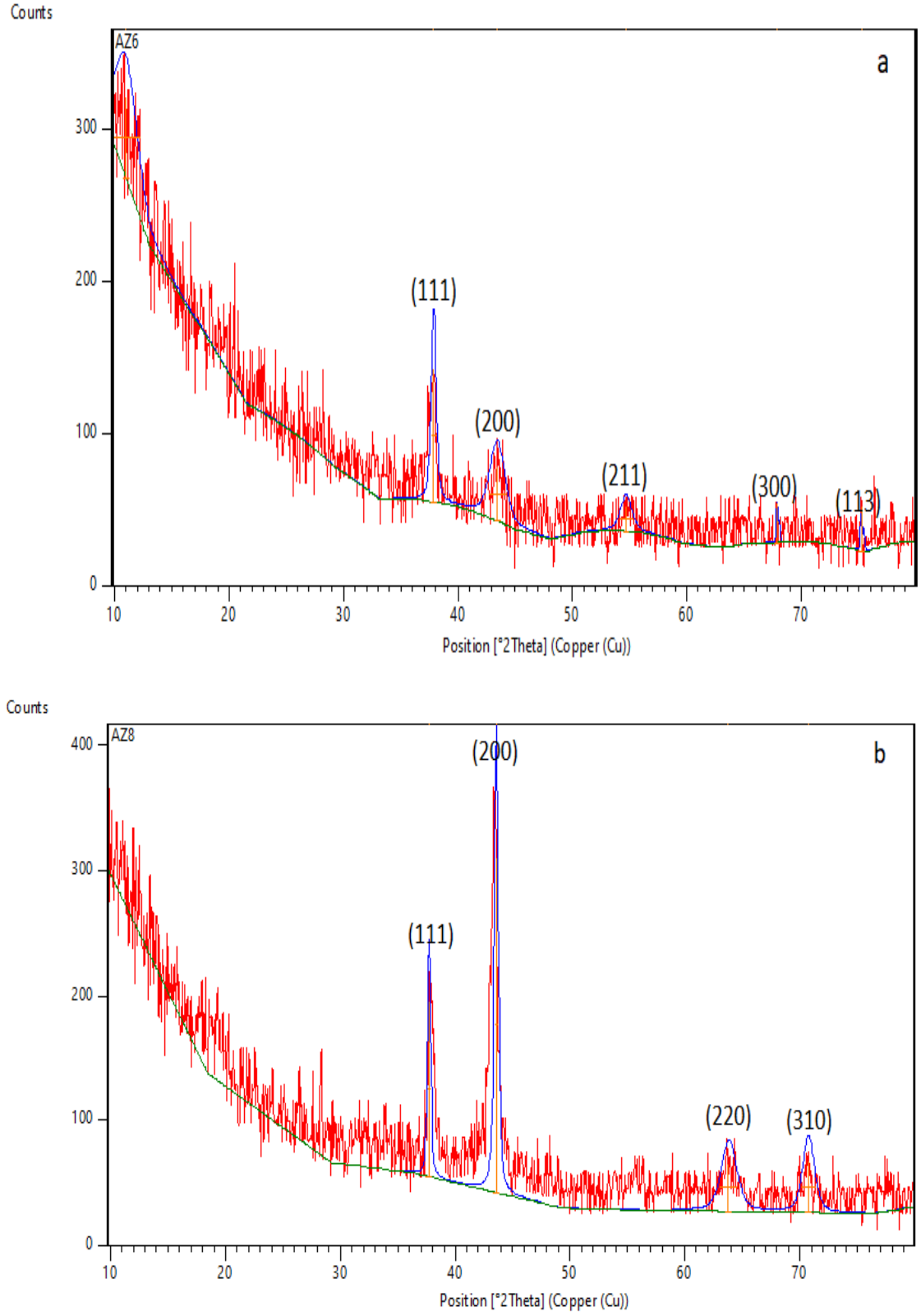

Figure (4.3): XRD Patterns of a) Specimen E and b) Specimen F

XRD profiles of the electrodeposited specimens (G&H) are shown in Figure (4.4).

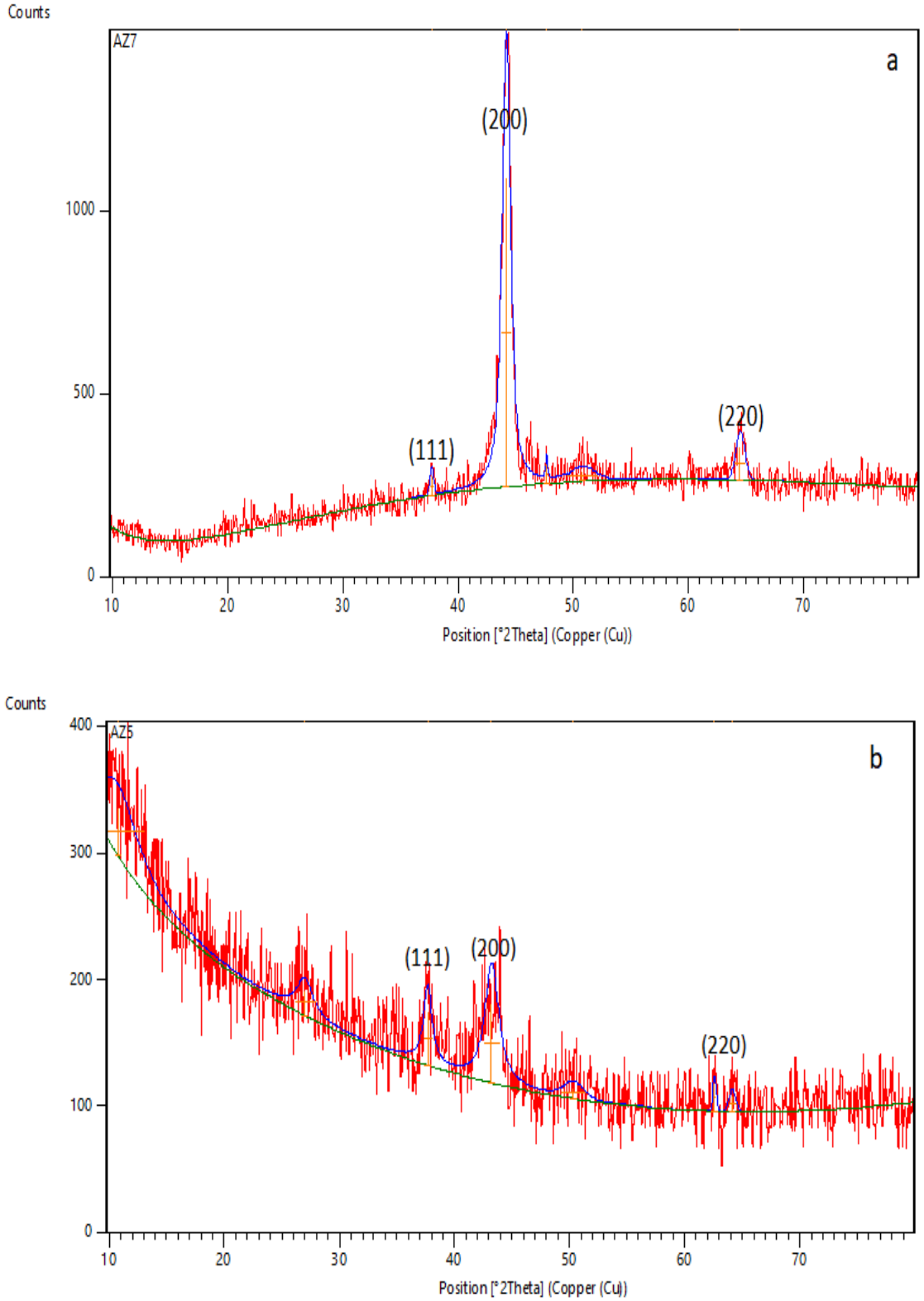

Figure (4.4): XRD Patterns of a) Specimen G and b) Specimen H

It is confirmed that these HEAs are composed principally of simple FCC and BCC crystal structures, although the specimen G also contain some ordered BCC phase. In other words, no complicated intermetallic

compounds can be found in any of the as-deposited alloys. This is similar to the observations in other HEAs systems. This phenomenon is attributed to the high-entropy effect which enhances the stability of multielemental solid-solution phases.

The increased amount of the stronger BCC phase at higher Al contents is considered to be the main reason for the associated increase in the hardness. It can be seen that there is a general increase in the lattice constants for greater additions of Al. This is reasonable since the Al atom has a larger atomic size, and thus has a tendency to expand the crystal lattice. From the XRD analyses shown in Figure (4.4), it can be seen that the crystal structures of the HEAs system were characterized, and only simple solid-solution structures, essentially FCC and BCC, were identified. Normally, the heights of FCC (111) peaks were higher than those of FCC (200), but their relative height might be affected by the preferred orientations of the dendritic phases in the alloy specimens as compatible with [112].

The XRD patterns for the Specimen C and Specimen G alloys are given in Figures (4.2) and (4.4). For the as-deposited thin films only diffraction peaks of Cu are identified, which are present due to the deposition substrate.

No other complex structures were detected by X-ray diffraction analysis. The absence of such phases can be attributed to the lower free energy resulting from the high entropy effect, which can significantly reduce the free energy and make random solid solutions more stable than the ordered phases.

4-2.2 Crystal structure determination

It is very important as the properties of substance are never fully understood until its structure is known. Its necessary prerequisite to any

understanding of phenomena such as, plastic deformation, alloy formation, or phase transformation. So actually, to know the physical properties or the chemical properties of any kind of materials, should to know the crystal structure of that particular materials. The relation between the Bravais lattice and its diffraction is shown in the Table (4.2).

Table (4.2): The Bravais lattice and its diffraction relation.

Bravais lattice	Allowed Reflection
Simple	All
BCC	(h+k+l) even
FCC	h, k, and l unmixed (hkl are either all even or all odd)
Diamond crystal	h, k, l are all odd or all even & (h+k+l) divisible by 4

Each of the four common cubic lattice types has a characteristic sequence of diffraction lines, described by their sequential s values:

- Simple cubic: 1, 2, 3, 4, 5, 6, 8, 9, …
- BCC : 2, 4, 6, 8, 10, …
- FCC: 3, 4, 8, 11, 12, 16, …
- Diamond cubic: 3, 8, 11, 16,…

If the set of integers cannot be found, then the substance involved does not belong to the cubic system, and other possibilities (tetragonal, hexagonal, etc) must be explored.

Suppose when we are talking about the seven because the 7 is not present because any how the h square plus k square plus l square value is

the summation h square plus k square plus l square is not equal to seven. So that is why 7 its totally silent.

Table (4.3): the lattice structure relation with the hkl [113]

$(h^2+k^2+l^2)$	hkl			
	Simple	FCC	BCC	Diamond
1	100	---	…	---
2	110	---	110	---
3	111	111	---	111
4	200	200	200	---
5	210	---	---	---
6	211	---	211	---
7	---	---	---	---
8	220	220	220	220
9	300, 221	---	---	---
10	310	---	310	---

4-2-2-1 Indexing pattern of cubic crystals:

For cubic crystals,

$$\frac{1}{d^2} = \frac{(h^2 + k^2 + l^2)}{a^2} \qquad (4.2)$$

From Braggs law : $\lambda = 2d\sin\theta$ (4.3)

Combining above 2 equations

$$sin^2\theta = \frac{\lambda^2}{4a^2}(h^2 + k^2 + l^2) \qquad (4.4)$$

Where $s=(h^2+k^2+l^2)$ is always integral, $\frac{\lambda^2}{4a^2}$ is constant for any one pattern, λ is wavelength of incident radiation, a is lattice parameter [113].

Steps for indexing the pattern of a cubic substance:

- Finding a set of integers which will yield quotient when divided one by one into the observed $sin^2\theta$ values.
- Once the proper integers s are found, the indices hkl, of each line can be written down by inspection or form the tabulation given on next slide.

Steps for indexing the pattern of a cubic substance by analytical method:

Establishing the conditions for a cubic crystal structure:

- For cubic crystal, we have:

$$sin^2\theta = K(h^2 + k^2 + l^2) \qquad (4.5)$$

Where K=$\frac{\lambda^2}{4a^2}$ is constant for all the diffraction lines in the pattern.

That means:

$$\frac{sin^2\theta_1}{(h_1^2 + k_1^2 + l_1^2)} = \frac{sin^2\theta_2}{(h_2^2 + k_2^2 + l_2^2)} = \frac{sin^2\theta_3}{(h_3^2 + k_3^2 + l_3^2)} = \cdots = K \qquad (4.6)$$

Where 1, 2, 3 etc. refer to the lines in the pattern.

- The value of (h^2+k^2+l^2) for any line is integer since h, k, l are individually integers.
- The results of the lattice structure are listed in tables (4-4 to 4-11).

Steps of analytical method:

1. Identify the peaks.
2. Determine the $sin^2\theta$.
3. Divide the $sin^2\theta$ values for different lines by different integers.
4. Identify the lowest common quotient from (3) & identify the integers to which it corresponds.

5. Divide the $sin^2\theta$ by K for each peak. This will give you a list of integers corresponding to ($h^2+k^2+l^2$).
6. Select the appropriate pattern of ($h^2+k^2+l^2$) values and identify the Bravais lattice.
7. Calculate lattice parameters.
8. The results of the lattice parameter are listed in tables (4-12 and 4-13) [113].

4-2-2-2 Determination of Lattice Parameter (α):

Lattice constant/parameter is one of the most principle crystal parameters because it critically governs physical (e.g., electronic, magnetic, optical, thermal, etc.,), chemical (e.g., catalytic, cohesive, etc.), mechanical (e.g., modulus of elasticity, etc.) and thermodynamic (e.g., phase instability, stacking fault energy, etc.), etc. properties [114].

Using Cu K_α radiation wavelength, λ=1.54 Å; lattice parameter is calculated for each line

- The systematic error in $\boldsymbol{sin^2\theta}$ shows **up as a gradual decrease in the value of** $\lambda^2/4a^2$ and a gradual increase in the value of α as θ increases.
- The systematic error in α decreases as θ increases.
- α is calculated From the equation

$$\alpha = \sqrt[2]{\lambda^2(h^2+k^2+l^2)/\mathbf{4}\,\boldsymbol{sin^2\theta}} \qquad (4.7)$$

Table (4.4): The lattice structure determination for specimen A.

Line	1-1	2-2	3-3	4-4	5-5	6-6	Hkl	Lattice structure
Θ	17.55	19.005	21.769	31.945	35.55	37.75		
$\boldsymbol{sin\theta}$	0.301538	0.325651	0.370865	0.529105	0.581413	0.612217		
$\boldsymbol{sin^2\theta}$	0.090925	0.106048	0.137541	0.279952	0.338041	0.37481		
$\boldsymbol{(sin^2\theta)/2}$	0.045463	0.053024	0.068771	0.139976	0.169021	0.187405		
$\boldsymbol{(sin^2\theta)/3}$	0.030308	0.035349	0.045847	0.093317	0.11268	0.124937	**111**	**FCC**
$\boldsymbol{(sin^2\theta)/4}$	0.022731	0.026512	0.034385	0.069988	0.08451	0.093702	**200**	**FCC+BCC**
$\boldsymbol{(sin^2\theta)/5}$	0.018185	0.02121	0.027508	0.05599	0.067608	0.074962		
$\boldsymbol{(sin^2\theta)/6}$	0.015154	0.017675	0.022924	0.046659	0.05634	0.062468		
$\boldsymbol{(sin^2\theta)/8}$	0.011366	0.013256	0.017193	0.034994	0.042255	0.046851	**220**	**FCC+BCC**
$\boldsymbol{(sin^2\theta)/9}$	0.010103	0.011783	0.015282	0.031106	0.03756	0.041646		
$\boldsymbol{(sin^2\theta)/10}$	0.009093	0.010605	0.013754	0.027995	0.033804	0.037481	**310**	**BCC**
$\boldsymbol{(sin^2\theta)/11}$	0.008266	0.009641	0.012504	0.02545	0.030731	0.034074	**311**	**FCC**

Table (4.5): The lattice structure determination for specimen B.

Line	1-1	2-2	3-3	4-4	5-5	6-6	hkl	Lattice structure
Θ	11.82	14.245	21.57	22.27	25.27	32.92		
$\boldsymbol{sin\theta}$	0.204838	0.246069	0.367638	0.378972	0.426884	0.543467		
$\boldsymbol{sin^2\theta}$	0.041958	0.06055	0.135157	0.14362	0.18223	0.295357		
$\boldsymbol{(sin^2\theta)/2}$	0.020979	0.030275	0.067579	0.07181	0.091115	0.147678		
$\boldsymbol{(sin^2\theta)/3}$	0.013986	0.020183	0.045052	0.047873	0.060743	0.098452	**111**	FCC
$\boldsymbol{(sin^2\theta)/4}$	0.01049	0.015137	0.033789	0.035905	0.045558	0.073839	**200**	FCC+BCC
$\boldsymbol{(sin^2\theta)/5}$	0.008392	0.01211	0.027031	0.028724	0.036446	0.059071		
$\boldsymbol{(sin^2\theta)/6}$	0.006993	0.010092	0.022526	0.023937	0.030372	0.049226		
$\boldsymbol{(sin^2\theta)/8}$	0.005245	0.007569	0.016895	0.017952	0.022779	0.03692		
$\boldsymbol{(sin^2\theta)/9}$	0.004662	0.006728	0.015017	0.015958	0.020248	0.032817	**300**	
$\boldsymbol{(sin^2\theta)/10}$	0.004196	0.006055	0.013516	0.014362	0.018223	0.029536	**310**	BCC
$\boldsymbol{(sin^2\theta)/11}$	0.003814	0.005505	0.012287	0.013056	0.016566	0.026851		
$\boldsymbol{(sin^2\theta)/12}$	0.003497	0.005046	0.011263	0.011968	0.015186	0.024613	222	FCC

Table (4.6): The lattice structure determination for specimen C.

Line	1-1	2-2	3-3	4-4	5-5	hkl	Lattice structure
Θ	6.87	21.895	22.22	25.42	37.12		
$\boldsymbol{sin\theta}$	0.119617	0.372907	0.378164	0.42925	0.603486		
$\boldsymbol{sin^2\theta}$	0.014308	0.139059	0.143008	0.184256	0.364196		
$\boldsymbol{(sin^2\theta)/2}$	0.007154	0.06953	0.071504	0.092128	0.182098		
$\boldsymbol{(sin^2\theta)/3}$	0.004769	0.046353	0.047669	0.061419	0.121399	**111**	**FCC**
$\boldsymbol{(sin^2\theta)/4}$	0.003577	0.034765	0.035752	0.046064	0.091049	**200**	**FCC+BCC**
$\boldsymbol{(sin^2\theta)/5}$	0.002862	0.027812	0.028602	0.036851	0.072839		
$\boldsymbol{(sin^2\theta)/6}$	0.002385	0.023177	0.023835	0.030709	0.060699		
$\boldsymbol{(sin^2\theta)/8}$	0.001789	0.017382	0.017876	0.023032	0.045524	**220**	**FCC+BCC**
$\boldsymbol{(sin^2\theta)/9}$	0.00159	0.015451	0.01589	0.020473	0.040466		
$\boldsymbol{(sin^2\theta)/10}$	0.001431	0.013906	0.014301	0.018426	0.03642		

Table (4.7): The lattice structure determination for specimen D.

Line	1-1	2-2	3-3	4-4	5-5	hkl	Lattice structure
Θ	18.9	20.46	21.69	26	32		
$\boldsymbol{sin\theta}$	0.323917	0.349553	0.369585	0.438371	0.529919		
$\boldsymbol{sin^2\theta}$	0.104922	0.122188	0.136593	0.192169	0.280814		
$(\boldsymbol{sin^2\theta})/\boldsymbol{2}$	0.034974	0.061094	0.068296	0.096085	0.140407	110	FCC
$(\boldsymbol{sin^2\theta})/\boldsymbol{3}$	0.034974	0.040729	0.045531	0.064056	0.093605	**111**	**BCC**
$(\boldsymbol{sin^2\theta})/\boldsymbol{4}$	0.026231	0.030547	0.034148	0.048042	0.070204	**200**	**FCC+BCC**
$(\boldsymbol{sin^2\theta})/\boldsymbol{5}$	0.020984	0.024438	0.027319	0.038434	0.056163		
$(\boldsymbol{sin^2\theta})/\boldsymbol{6}$	0.017487	0.020365	0.022765	0.032028	0.046802		
$(\boldsymbol{sin^2\theta})/\boldsymbol{8}$	0.013115	0.015273	0.017074	0.024021	0.035102	**220**	**FCC+BCC**
$(\boldsymbol{sin^2\theta})/\boldsymbol{9}$	0.011658	0.013576	0.015177	0.021352	0.031202		

Table (4.8): The lattice structure determination for specimen E.

Line	1-1	2-2	3-3	4-4	5-5	6-6	hkl	Lattice structure
Θ	5.5096	18.9116	21.72615	27.3312	33.9415	37.61475		
$\boldsymbol{sin\theta}$	0.096013	0.324109	0.370171	0.459133	0.558346	0.610349		
$\boldsymbol{sin^2\theta}$	0.009218	0.105047	0.137026	0.210803	0.31175	0.372526		
$\boldsymbol{(sin^2\theta)/2}$	0.004609	0.052523	0.068513	0.105402	0.155875	0.186263		
$\boldsymbol{(sin^2\theta)/3}$	0.003073	0.035016	0.045675	0.070268	0.103917	0.124175	**111**	FCC
$\boldsymbol{(sin^2\theta)/4}$	0.002305	0.026262	0.034257	0.052701	0.077938	0.093132	**200**	FCC+ BCC
$\boldsymbol{(sin^2\theta)/5}$	0.001844	0.021009	0.027405	0.042161	0.06235	0.074505		
$\boldsymbol{(sin^2\theta)/6}$	0.001536	0.017508	0.022838	0.035134	0.051958	0.062088	**211**	**BCC**
$\boldsymbol{(sin^2\theta)/8}$	0.001152	0.013131	0.017128	0.02635	0.038969	0.046566		
$\boldsymbol{(sin^2\theta)/9}$	0.001024	0.011672	0.015225	0.023423	0.034639	0.041392	**300**	
$\boldsymbol{(sin^2\theta)/10}$	0.000922	0.010505	0.013703	0.02108	0.031175	0.037253	**310**	FCC
$\boldsymbol{(sin^2\theta)/11}$	0.000838	0.00955	0.012457	0.019164	0.028341	0.033866		

Table (4.9): The lattice structure determination for specimen F.

Line	1-1	2-2	3-3	4-4	Hkl	Lattice structure
Θ	18.83675	21.7869	31.8948	35.3432		
$\boldsymbol{sin\theta}$	0.322873	0.371156	0.528361	0.578473		
$\boldsymbol{sin^2\theta}$	0.104247	0.137756	0.279166	0.334631		
$\boldsymbol{(sin^2\theta)/2}$	0.052123	0.068878	0.139583	0.167315		
$\boldsymbol{(sin^2\theta)/3}$	0.034749	0.045919	0.093055	0.111544	**111**	FCC
$\boldsymbol{(sin^2\theta)/4}$	0.026062	0.034439	0.069791	0.083658	**200**	FCC+ BCC
$\boldsymbol{(sin^2\theta)/5}$	0.020849	0.027551	0.055833	0.066926		
$\boldsymbol{(sin^2\theta)/6}$	0.017374	0.022959	0.046528	0.055772		
$\boldsymbol{(sin^2\theta)/8}$	0.013031	0.01722	0.034896	0.041829	**220**	**FCC+BCC**
$\boldsymbol{(sin^2\theta)/9}$	0.011583	0.015306	0.031018	0.037181		
$\boldsymbol{(sin^2\theta)/10}$	0.010425	0.013776	0.027917	0.033463	310	BCC

Table (4.10): The lattice structure determination for specimen G.

Line	1-1	2-2	3-3	4-4	5-5	hkl	Lattice structure
Θ	18.825	22.093	23.84	25.4	32.225		
$\boldsymbol{sin\theta}$	0.322679	0.376111	0.404184	0.428935	0.533245		
$\boldsymbol{sin^2\theta}$	0.104122	0.14146	0.163365	0.183985	0.284351		
$\boldsymbol{(sin^2\theta)/2}$	0.052061	0.07073	0.081682	0.091993	0.142175		
$\boldsymbol{(sin^2\theta)/3}$	0.034707	0.047153	0.054455	0.061328	0.094784	**111**	FCC
$\boldsymbol{(sin^2\theta)/4}$	0.02603	0.035365	0.040841	0.045996	0.071088	**200**	FCC+ BCC
$\boldsymbol{(sin^2\theta)/5}$	0.020824	0.028292	0.032673	0.036797	0.05687		
$\boldsymbol{(sin^2\theta)/6}$	0.017354	0.023577	0.027227	0.030664	0.047392		
$\boldsymbol{(sin^2\theta)/8}$	0.013015	0.017682	0.020421	0.022998	0.035544	**220**	**FCC+BCC**
$\boldsymbol{(sin^2\theta)/9}$	0.011569	0.015718	0.018152	0.020443	0.031595		

Table (4.11): The lattice structure determination for specimen H.

Line	1-1	2-2	3-3	4-4	5-5	hkl	Lattice structure
Θ	18.825	21.63	25.15	31.28	32.05		
$\boldsymbol{sin\theta}$	0.322679	0.368611	0.42499	0.519221	0.530659		
$\boldsymbol{sin^2\theta}$	0.104122	0.135874	0.180616	0.26959	0.281599		
$\boldsymbol{(sin^2\theta)/2}$	0.052061	0.067937	0.090308	0.134795	0.1408		
$\boldsymbol{(sin^2\theta)/3}$	0.034707	0.045291	0.060205	0.089863	0.093866	111	FCC
$\boldsymbol{(sin^2\theta)/4}$	0.02603	0.033969	0.045154	0.067398	0.0704	200	FCC+ BCC
$\boldsymbol{(sin^2\theta)/5}$	0.020824	0.027175	0.036123	0.053918	0.05632		
$\boldsymbol{(sin^2\theta)/6}$	0.017354	0.022646	0.030103	0.044932	0.046933		
$\boldsymbol{(sin^2\theta)/8}$	0.013015	0.016984	0.022577	0.033699	0.0352	**220**	**FCC+BCC**
$\boldsymbol{(sin^2\theta)/9}$	0.011569	0.015097	0.020068	0.029954	0.031289		

After deposition, analysis of XRD pattern based on DE-convolution of peaks indicates the presence of FCC phase with a lattice parameter and major BCC phase with a lattice parameter listed in table (4.12, 4.13).

Table (4.12): The lattice parameter determination for specimens (A, B, C, and D).

Specimen	Θ	$sin^2\theta$	$h^2+k^2+l^2$	Hkl	α (Å)	Average, a
A	19.005	0.106048	3	111	4.095429	4.144689
	21.769	0.137541	4	200	4.15245	
	31.945	0.279952	8	220	4.116176	
	35.55	0.338041	10	310	4.187992	
	37.75	0.37481	11	311	4.171397	
B	11.82	0.041958	3	111	6.510906	6.360728
	14.245	0.06055	4	200	6.258415	
	25.27	0.18223	10	310	6.425161	
	32.92	0.295357	12	222	6.248432	
C	21.895	0.139059	3	111	3.576441	3.590978
	25.42	0.184256	4	200	3.587649	
	37.12	0.364196	8	220	3.608845	
D	18.9	0.104922	2	110	3.361796	3.938958
	18.9	0.104922	3	111	4.117343	
	21.69	0.136593	4	200	4.16684	
	32	0.280814	8	220	4.10985	

Table (4.13): The lattice parameter determination for specimens (E, F, G, and H).

Specimen	θ	$sin^2\theta$	$h^2+k^2+l^2$	hkl	α (Å)	Average, a
E	18.9116	0.105047	3	111	4.11491	4.141822
	21.72615	0.137026	4	200	4.160242	
	27.3312	0.210803	6	211	4.107972	
	37.61475	0.372526	11	311	4.184165	
F	18.83675	0.104247	3	111	4.130664	4.152779
	21.7869	0.137756	4	200	4.149204	
	31.8948	0.279166	8	220	4.121969	
	35.3432	0.334631	10	310	4.20928	
G	18.825	0.104122	3	111	4.133149	4.103966
	22.093	0.14146	4	200	4.094535	
	32.225	0.284351	8	220	4.084215	
H	18.825	0.104122	3	111	4.133149	4.168508
	21.63	0.135874	4	200	4.177842	
	31.28	0.26959	8	220	4.194533	

Formation of Al type FCC phase may also be attributed to the high content of Al which tends some elements to diffuse in the FCC crystal structure. Thus, the alloy is mainly composed of FCC + BCC structure with BCC as major phase. Throughout the deposition process, the decrease in intensity, broadening of the peak and its subsequent disappearance may result from the three following factors: refined crystal size, high lattice strain and decreased crystallinity.

In ZHANG et al., work [115], three parameters were used to characterize the collective behavior of the constituent elements in the multi-component alloys: the atomic size difference (δ), the mixing enthalpy (ΔH_{mix}) and the mixing entropy (ΔS_{mix}).

The atomic size difference (δ) is an important parameter related to the solid-solution phase. A larger δ corresponds to severe lattice distortion and sluggish diffusion effects, resulting in a decrease in the stability and transformation rate of the solid-solution phase and precipitate formation in the HEAs. The hardness changes monotonously with δ, which means that the lattice distortion hinders the dislocation motion of plastic deformation, resulting in solid-solution strengthening [116][117][118].

$$\delta = 100\sqrt{\sum_{i=1}^{n} c_i\left(1 - {}^{r_i}/_{\bar{r}}\right)^2} \qquad (4.8)$$

Where $\bar{r} = \sum_{i=1}^{n} c_i r_i$, *ci* and *ri* are the atomic percentage and atomic radius of the *i*th element. The numerical factor 100 was used to amplify the data for clarity.

The other parameter is the valence electron concentration, VEC, which has been proven useful in determining the phase stability of alloys. VEC is defined by:

$$VEC = \sum_{i=1}^{n} c_i (VEC)_i \qquad (4.9)$$

where (VEC)*i* is the VEC for the *i*th element and mixing entropy (ΔS_{mix}) can be represented by eq.4.10

$$\Delta S_{mix} = -R \sum_{i}^{n} X_i Ln\ X_i \qquad (4.10)$$

Where ΔS_{mix} is the change in mixing entropy, J/k.mole , R is the general constant of gas which equal to 8.3145 J $mole^{-1}$ K^{-1} , and X_i is the elements concentration. The mixing entropy of all constituents elements of the coating alloys is listed in table (4.15) that resulted from EDS test.

Table (4-14): Atomic radii and VEC for elements [119]

Elements	Al	Fe	Co	Cu	Cr	Mn	Ni	CNTs
VEC	3	8	9	11	6	7	10	4
r_i	1.432	1.241	1.251	1.278	1.249	1.350	1.246	0.773

VEC also has a weak effect on the phase stability between the amorphous phases and solid solution phases. It is important to note that, we have shown that VEC plays a decisive role in determining the fcc- or bcc-type solid solution in HEAs, and specially larger VEC(≥8) favors the formation of fcc-type solid solutions, while smaller VEC((<6.87) favors the formation of bcc-type solid solutions. It clearly shows that solid solution phases form and only form when the three parameters, ΔHmix, δ, and ΔSmix are in the suitable range: $0\leq\delta\leq8.5$, $-22\leq\Delta Hmix\leq7$ kJ/mol and $11\leq\Delta Smix\leq19.5$ J/(K·mol [119].

The molar entropies of mixing reach the maximum values of 12.9 J $K^{-1}mol^{-1}$ and the minimum values of 6 J $K^{-1}mol^{-1}$, for the HEA and MEA respectively. From Table (4.15), the specimen E is the stable high entropy alloy because of having a higher molar entropies of mixing which compatible with Refs. [96] [103].

Calculated value of ΔSmix, ΔHmix, ΔG , VEC and δ for proposed non-equiatomic HEA, which is consistent with the criteria of solid solution formation and the phase stability of high-entropy alloy given in previous studies of Zhang and Guo [119]. High value of entropy of mixing (ΔSmix) is mainly responsible for the formation of solid solution and the value of VEC confirmed that it to be a mixture of BCC and FCC phases.

Table (4-15): The Results of ΔS_{mix} , VEC and δ for alloys

Specimen code	VEC	Δ	ΔS_{mix}
A	10.102	0.111447	6
B	8.476	1.686166	7.7
C	8.0214	0.561382	12.3
D	6.7571	2.434187	11.3
E	8.363	0.241663	12.9
F	7.59	1.396605	12.8
G	9.052	0.174923	12.2
H	6.988	1.812152	12.4

4.2.3 Optical Microscope

The initial microstructure of the low alloy steel 4140, the base metal composition, has been listed in Table (3.1). The microstructures of the low alloy steel surface was observed after being etched for (30sec.) in a (2-ml HNO_3) solution and (98-ml ethanol) solution according to (E ASTM [407-99]); the microstructure of the low alloy steel which is agreed with Ref. [120] as shown in Figure (4.5).

From the figure, we notice that the ratio of ferrite to pearlite is approximately equal because these sites have an average carbon ratio. In

addition, the pearlite is in the form of a layer, and this is due to the alloying elements that make up the alloy.

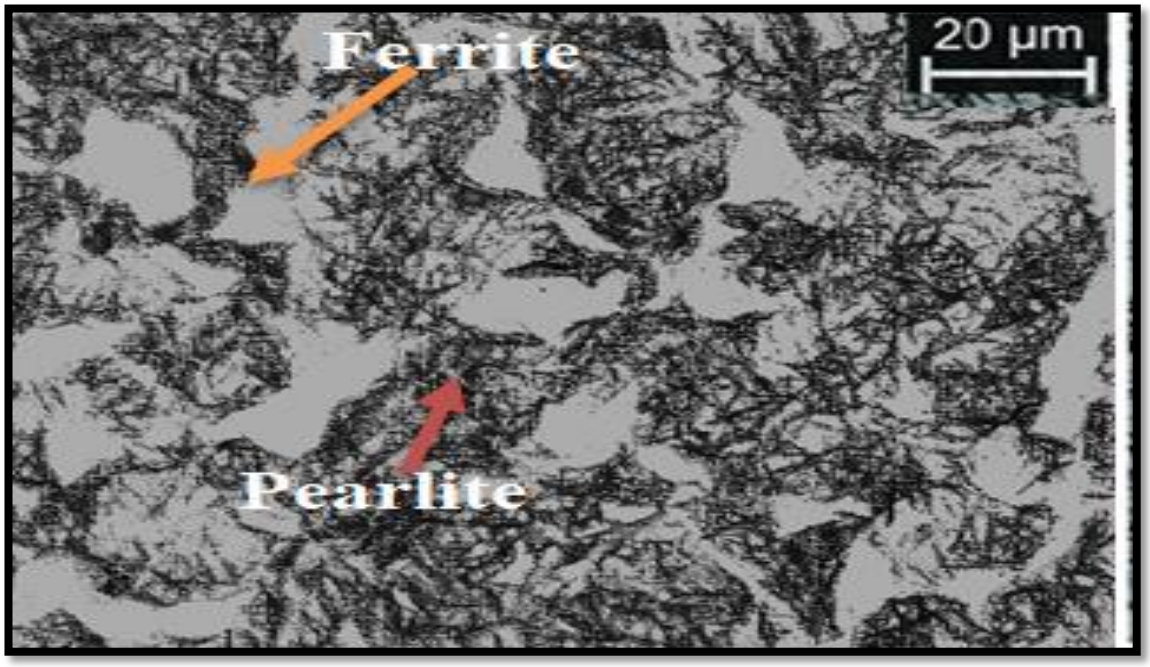

Figure (4.5): images showing the microstructure taken from the center of low alloy steel (4140) before coating.

4.2.4 Surface Morphology

The specimens of 4140 low alloy steel were coated by Medium entropy alloys (MEAs), high entropy alloys (HEAs), MEAs-Carbon nanotube(CNTs), and HEAs-CNTs composite coating at temperature of 30^{o}C for period 15 min. After the coating, it was seen that the surface morphology for the coated specimens is dense, uniform and homogeneous with granular grains that became finer when adding the CNTs. Porosity and micro-cracks are harmful to coating characteristics when present. Some types of coating layers specimens exhibited micro-cracks because several types of cracks are inherently present in the coatings.

The FESEM micrographs of MEA and MEA-CNTs composite coatings presented in Figure (4.6) shows granular morphology for all the

coatings. Coating composition measured by the FESEM-EDS technique is provided in Table (4.16) which shows that all the coatings are nearly equiatomic with respect to the four components. Recently, medium entropy alloys (MEAs) have attracted much attention because they exhibit the outstanding mechanical properties in comparison with (HEAs). For example, the ternary MEAs have better mechanical properties than HEAs at both cryogenic and room temperatures because of the higher yield strength, work hardening rate, and the twinning stress of MEAs is reach earlier at lower strains and nanotwinning occurs over a more extended strain range [121].

Table (4.16): Coating composition measured by the FESEM-EDS technique.

Code / Elements	**Al at%**	**Fe at%**	**Co at%**	**Ni at%**	**Cu at%**	**Mn at%**	**Cr at%**	**C at%**
A	-----	29.3	0.2	1.5	69	----	-----	-----
B	-----	21.5	3.2	7.9	42.6	-----	-----	24.8
C	19.9	35.6	11.26	7.8	25.3	-----	-----	----
D	9.83	9.72	6.17	7.42	24.47	-----	-----	42.39
E	-----	27	23.4	25.7	-----	9.3	14.6	-----
F	-----	38.6	10.9	15.4	-----	13.3	8.9	12.9
G	1	38.2	15.2	28.3	14.6	-----	2.7	-----
H	8.6	10.3	9.1	16.8	10.5	-----	23.2	21.5

A careful observation of Figure (4.6) also reveals that for the addition of CNTs the surface roughness decreased and the particles became more fine and compact. This attributed to CNTs incorporation leads to its uniform distribution within the coating matrix producing compact and uniform morphology for the composite coating.

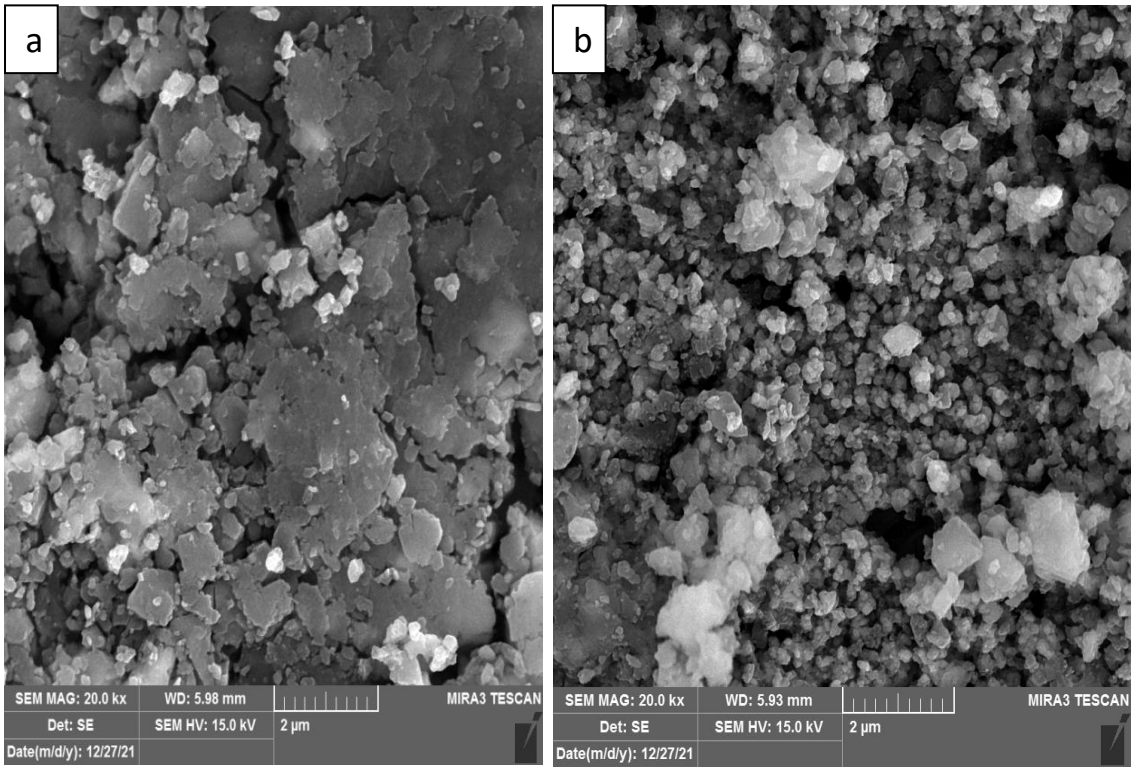

Figure (4.6): The FESEM micrographs of specimens a) A and b) B.

It is apparent from Figure (4.6) that the microstructure of FeNiCoCu MEA coating has two distinct phases, one containing Ni, Co and Fe while other with high concentration of Cu. Therefore, the CNTs addition has an influence on the grain size, and a uniform grain size assures a homogenous plastic deformation for the alloy without introducing the local stress concentration, the fine grain provides a high-volume fraction of grain boundaries, which can impede the dislocation movement. Hence, grain size refinement is of great benefit to improve strength that agreed with [122].

This is depicted by Figure (4.7) which provides the EDS map for the MEAs coatings.

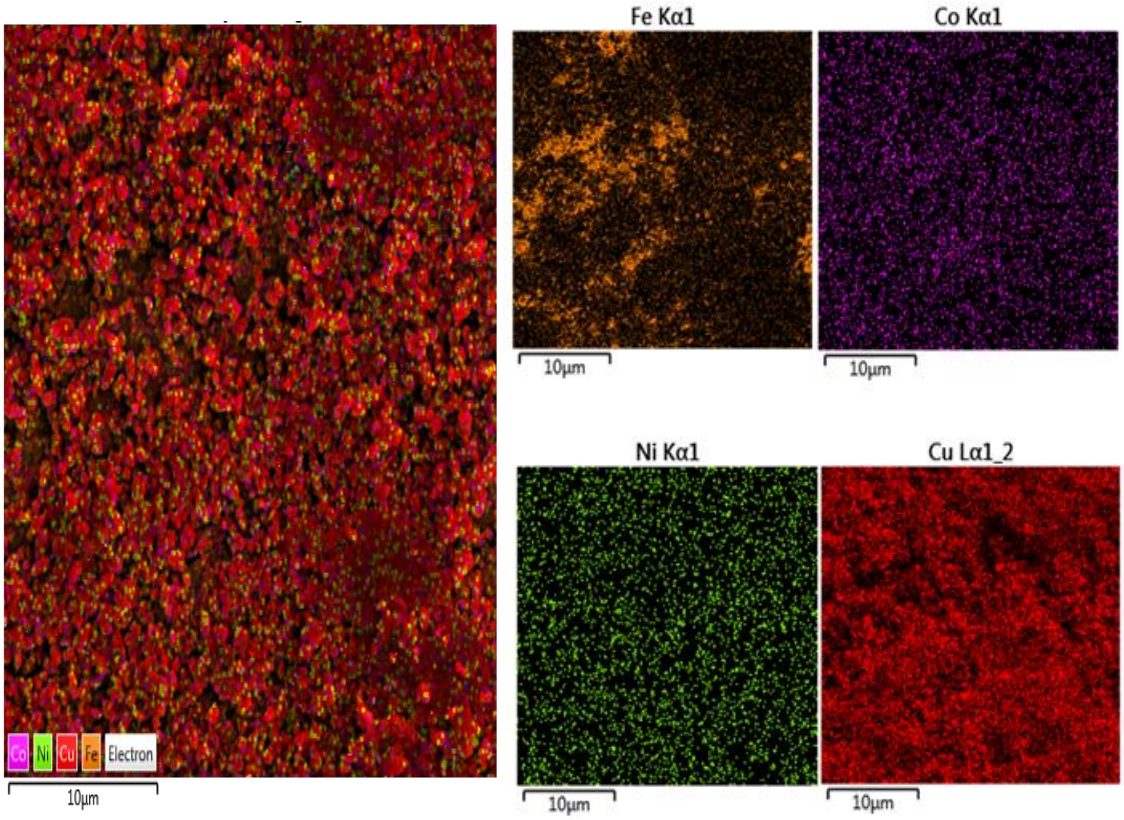

Figure (4.7) : The EDS map for the specimen A.

According to the metallurgy, the microstructure of these materials should consist of a number of intermetallic compounds. Instead, due to their high mixing entropy, HEAs tend to form simple solid-solution structures and single phase crystal structures are quite common. The deposits on the 4140 steel substrate consist of granular particles and particle conglomerates. The films obtained at an electrodeposition current density of specimen C are homogenous and present very thin cracks.

Carbon nanotubes have unique properties and thus adding them to the coating leads to an improvement in the properties of the coating, as shown in Figure (4.8) which represents the FESEM microstructure images of

specimens C & D. Where the figure shows that the addition of CNTs leads to a decrease in the surface roughness by decreasing the particle size, similar to an increase in the compressibility of the coating which essential for obtaining superior resistance of corrosion. The coating composition was examined by the FESEM and EDS procedure. Generally, for HEAs, the main components are estimated to be amid (5-35 at.%) [9][37]. So, coatings surface containing all the five constituent components in proximate equal weight-percentage (wt.%) that listed in Table (4.16).

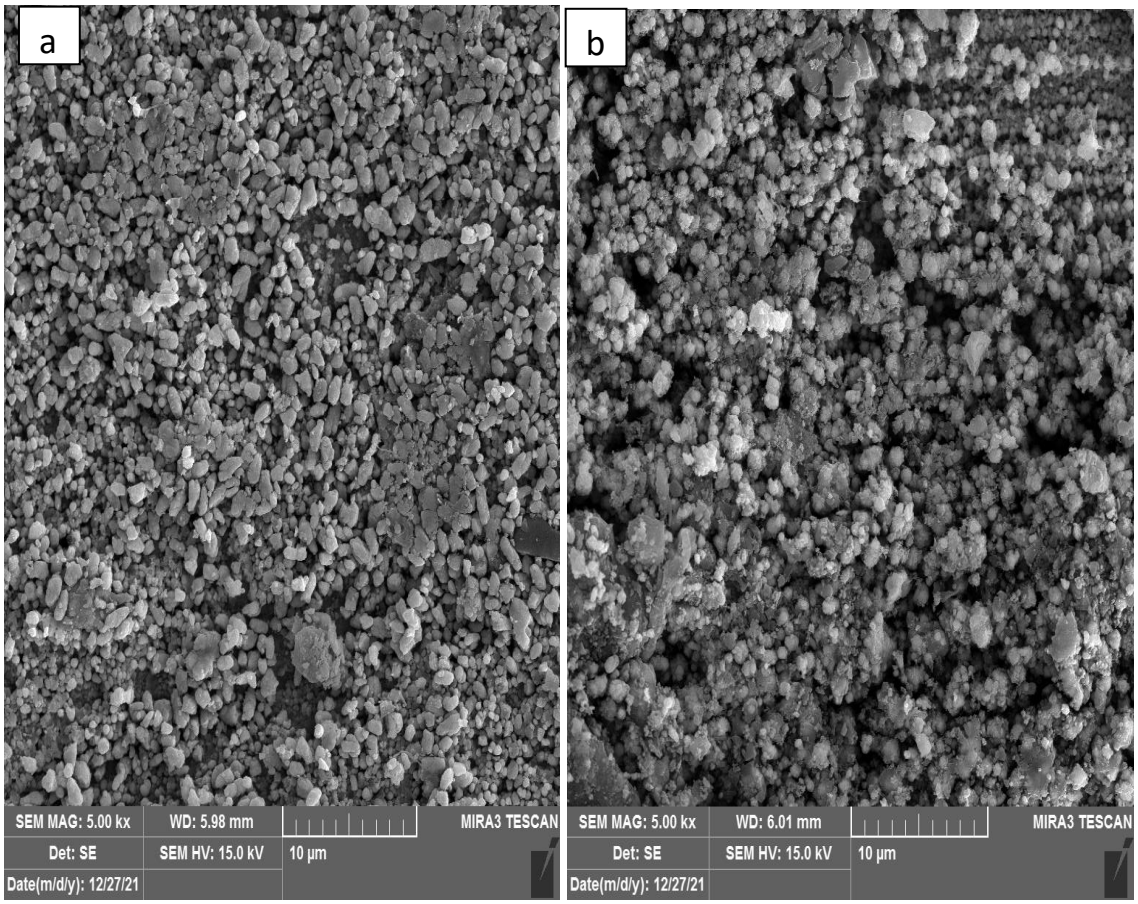

Figure (4.8): FESEM microstructure of specimens (a) C and (b) D .

Compositional analysis was done to calculate the configuration of the consequent components in the HEA-CNTs coating microstructure as shown in Figure (4.9). It can be observed that the dendritic region is mainly composed of Cu, Ni, Fe and Co elements while the matrix region is highly Al rich.

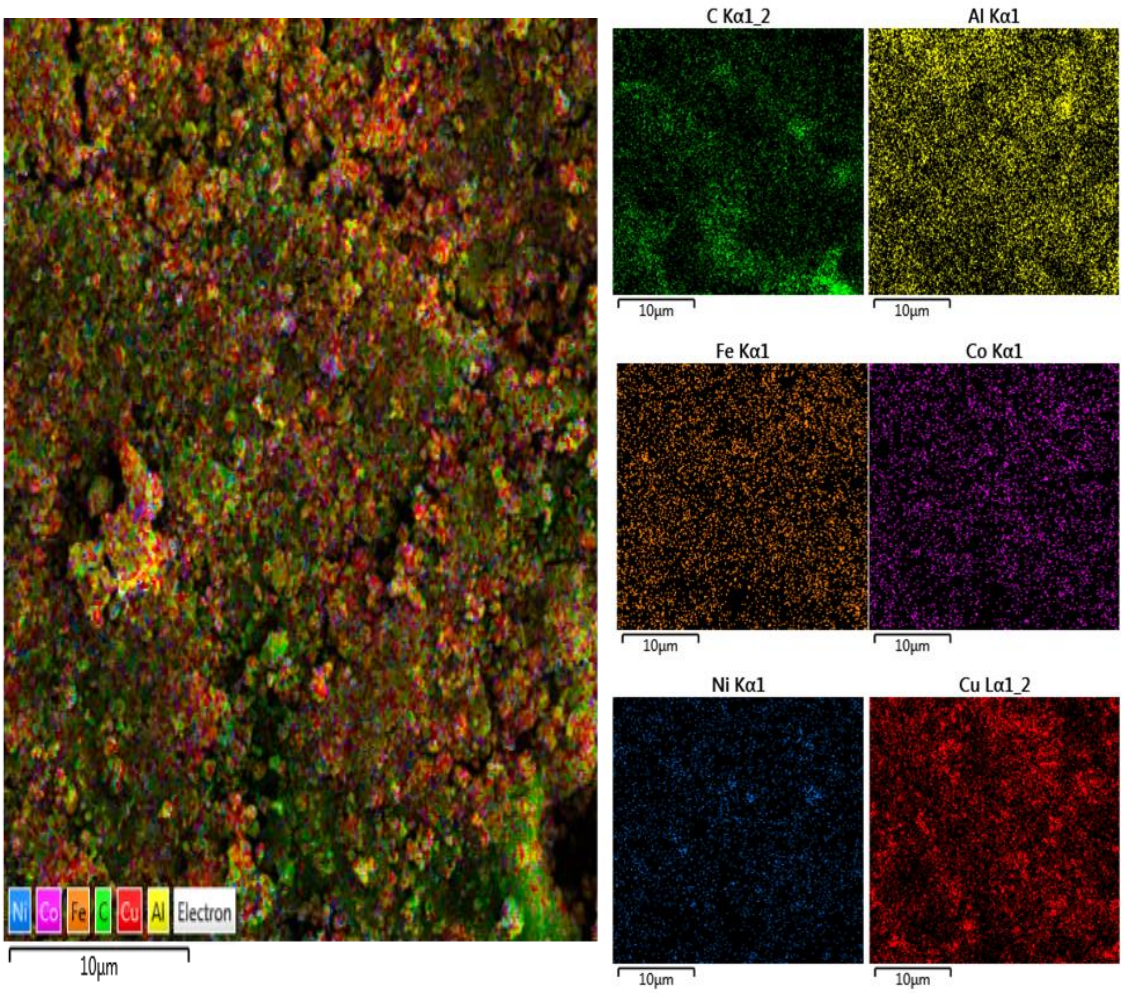

Figure (4.9): The demonstrative compositional plotting of the specimen D.

The specimen C surface morphology of the film deposited at current above 0.16A was heterogeneous, not sticker, crust with non-uniform distribution of particles, and the deposit presents highly visible cracks as shown in Figure (4.10 a). The increase in the deposition current density

leads to the formation of higher internal stresses in the thin films so, the current density keep constant at 0.16 A for this alloy coating that led to a homogenous, sticker, and uniform coating as seen in Figure (4.10 b).

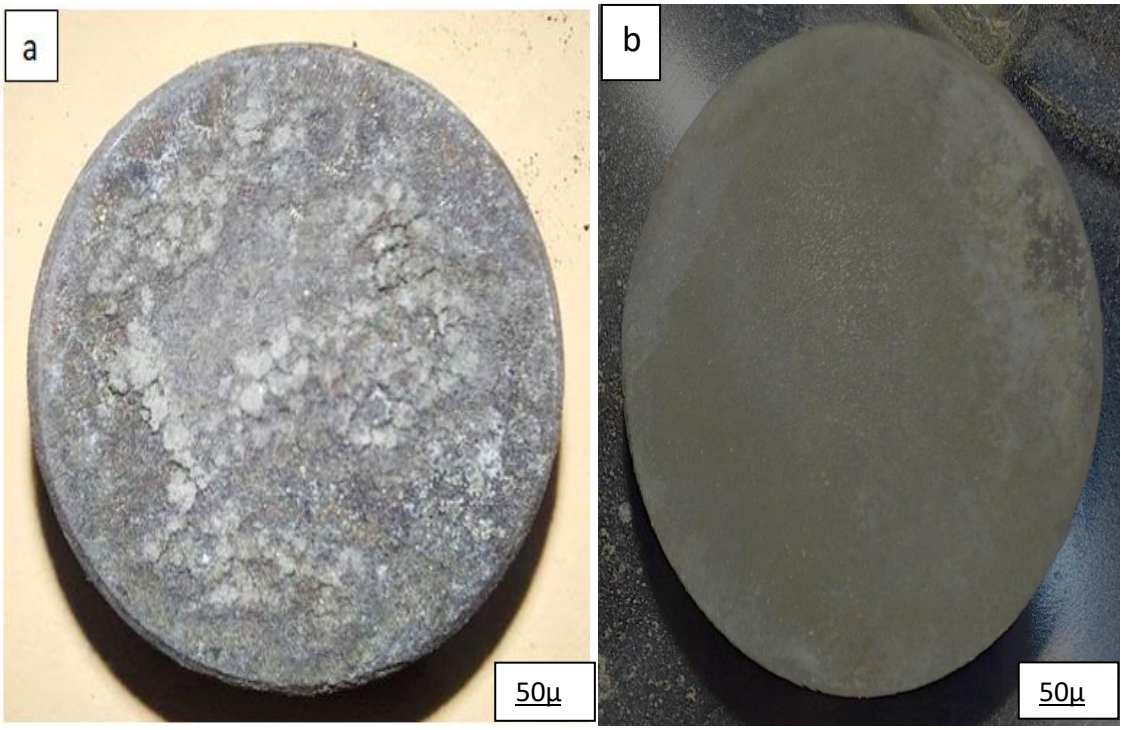

Figure (4.10): the specimen C surface at current density a) above 0.16 A, and b) 0.16 A

The micrographs in Figure (4.11) clearly indicate that CNTs sheets dispersed in the electrolyte with size equal to 58 nm get incorporated within the coating from very early stages of the deposition process and get fairly well distributed within the coating.

Figure (4.12) display the FESEM micrograph for the coating of specimens E & F where the size of the CNTs was 46nm. The morphology of specimens E & F coating is similar to the specimens C & D morphologies.

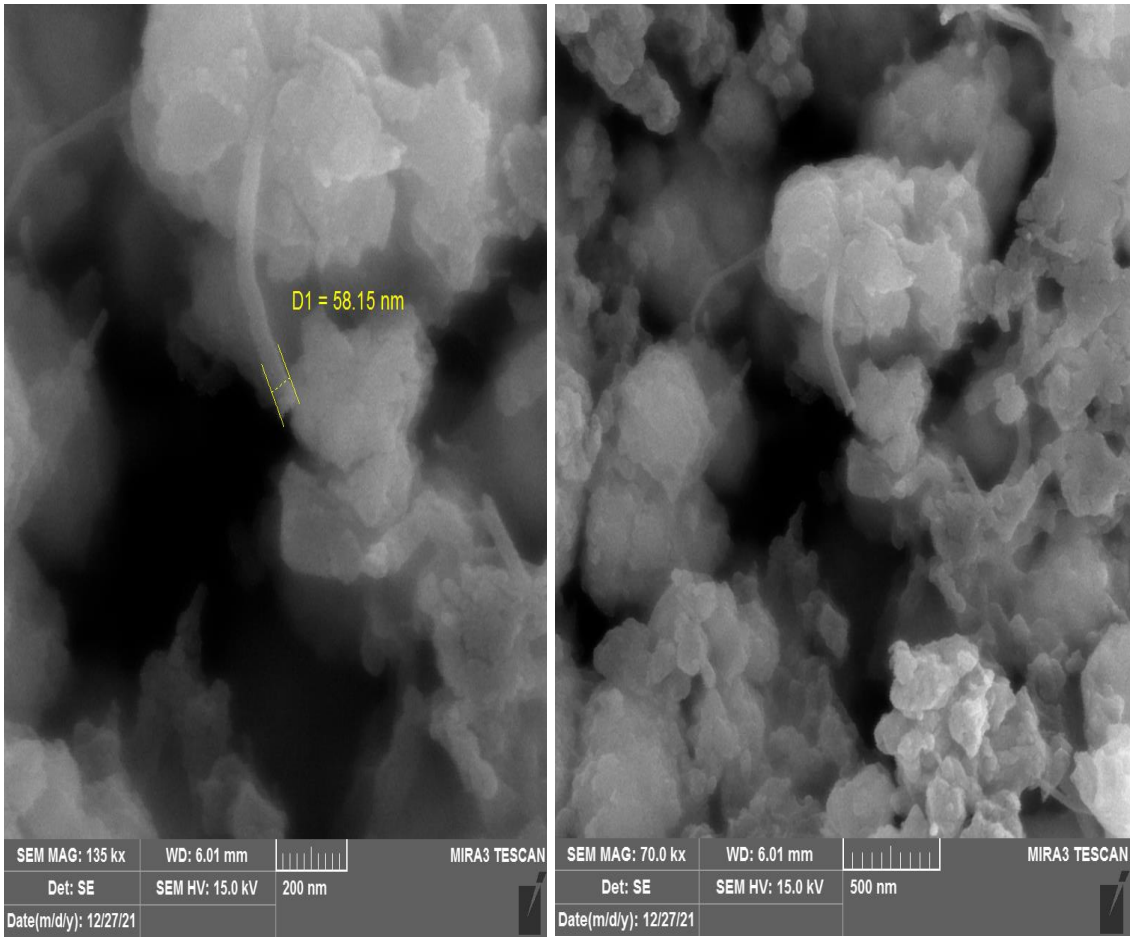

Figure (4.11): Specimen D FESEM image that indicate CNTs sheets dispersed in the electrolyte.

Compositional analysis was done to calculate the configuration of the consequent components in the specimens (E & F) coating microstructure as shown in Figure (4.13).

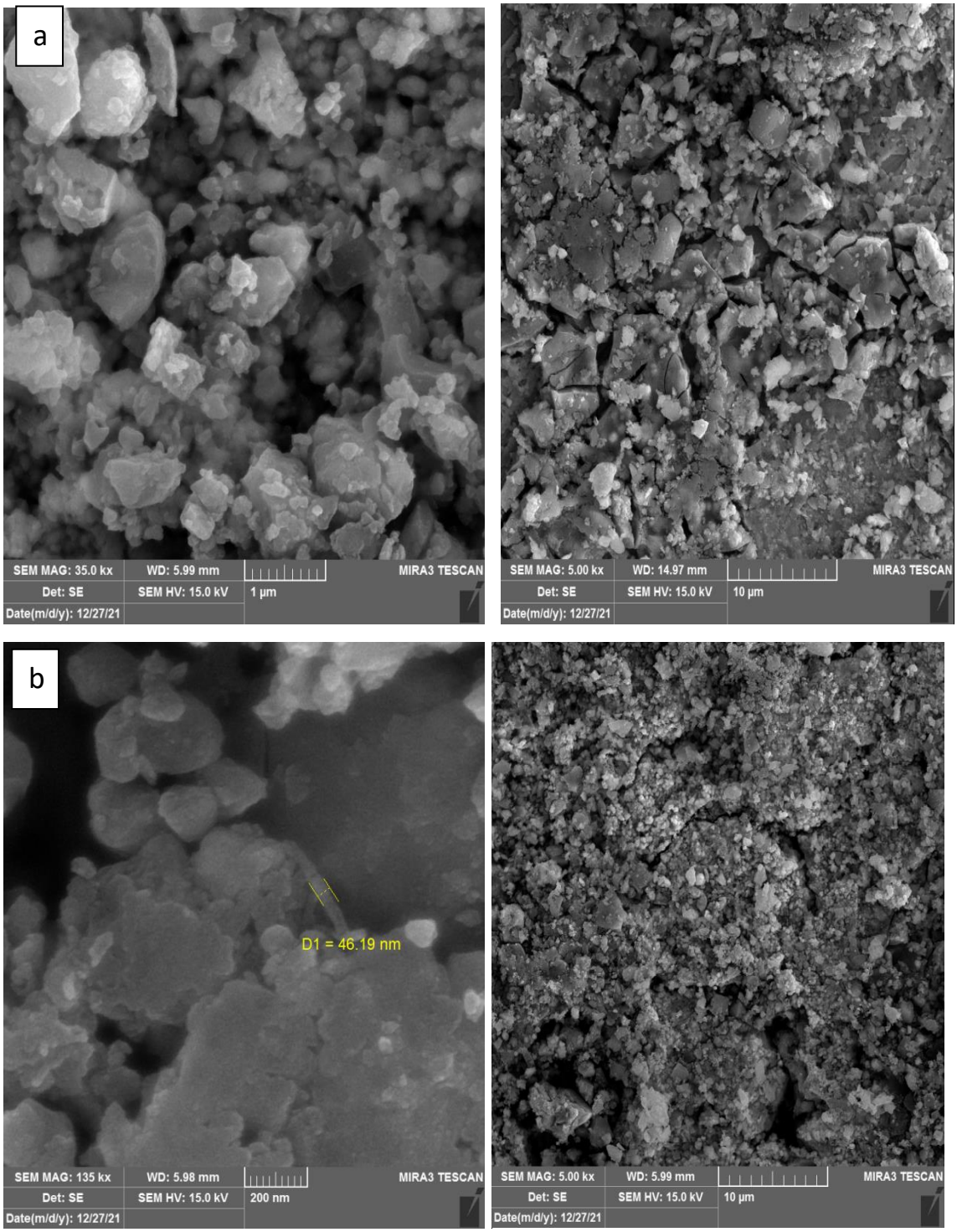

Figure (4.12) : the FESEM micrograph for the coating of a)specimen E and b) Specimen F

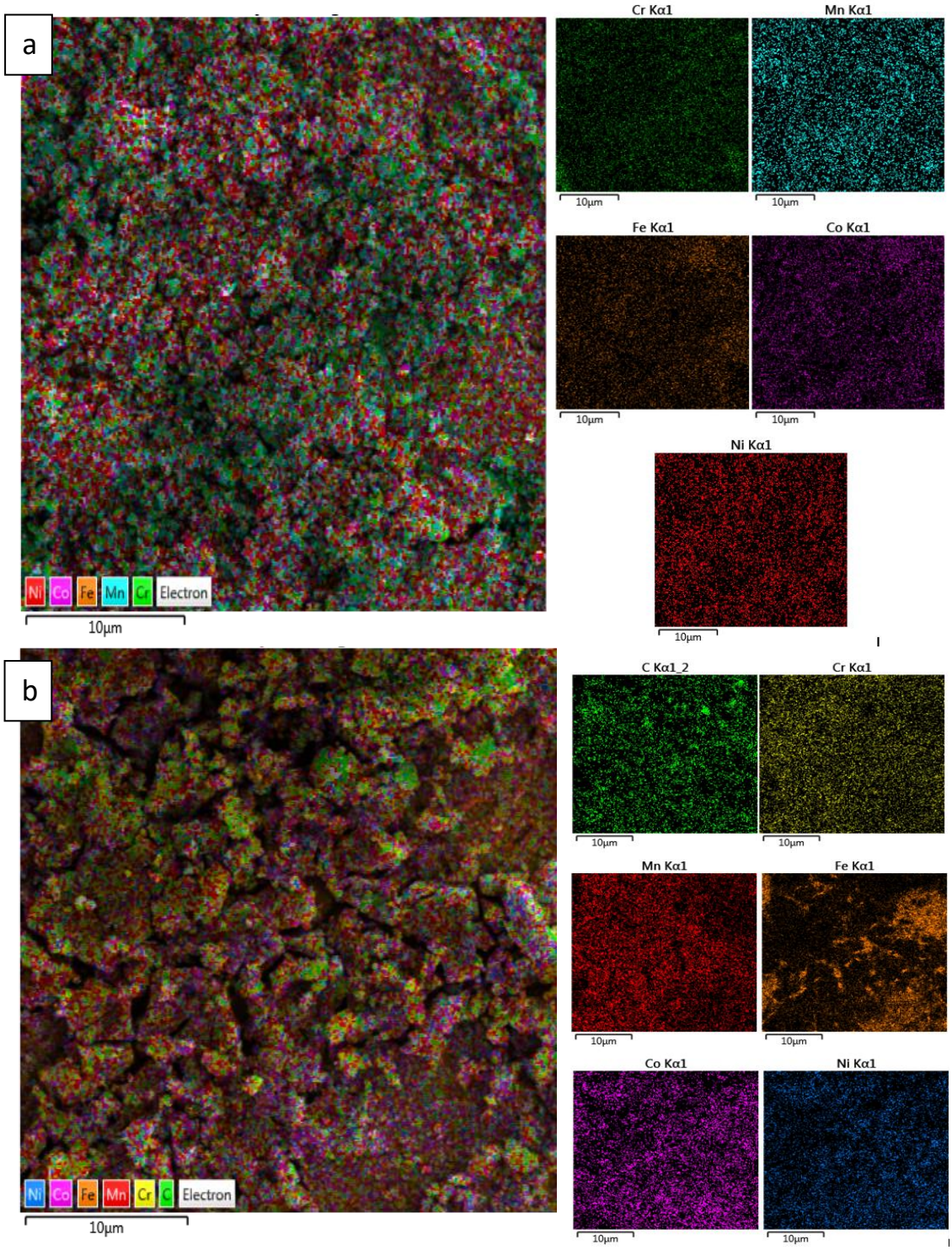

Figure (4.13) : The EDS map for the a) specimen E, and b) specimen F

Figure (4.14), observed the FESEM images of the specimens (G & H). It can be observed that the number of the rounded formations increases with the increasing of the deposition potential. The results indicate that the variation of the electrodeposition potential has a visible effect on the size and structure of the particles which form the high entropy alloy film.

The microstructure and morphology of the thin films are influenced by the composition of the electrolyte. The specimen G thin films exhibit better particle growth and distribution compared to specimen C. The nucleation and growth of the particles which form the thin film is significantly influenced by the presence of Cu in the deposition bath.[96]. In this alloys, the effect of CNTs is the same to the other HEAs. The EDS mapping for specimens (G & H) are shown in Figure (4.15).

As a result of the mentioned above, the increase in the coating compactness due to the addition of CNTs, the achievement of microstructural homogeneity which reduces the chances of galvanic coupling between different phases leading to the uniform distribution of Al that is capable of forming stable protective alumina phase and the impermeability of CNTs to the corrosive media were collectively responsible for the observed enhancement in the corrosion resistance of the HEA coatings with the addition of CNTs.

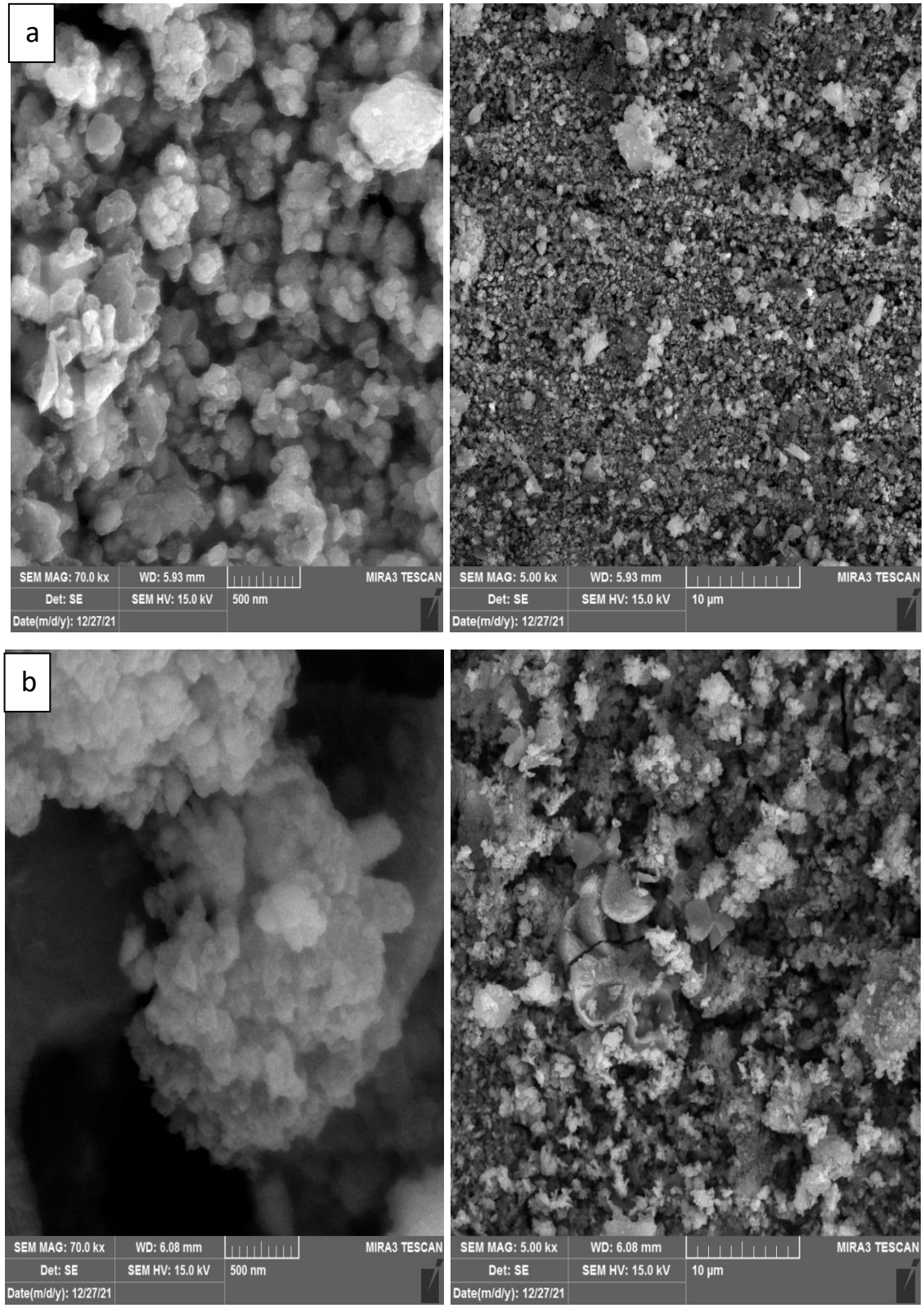

Figure (4.14): the FESEM micrograph for the coating of a)specimen G and b) Specimen H

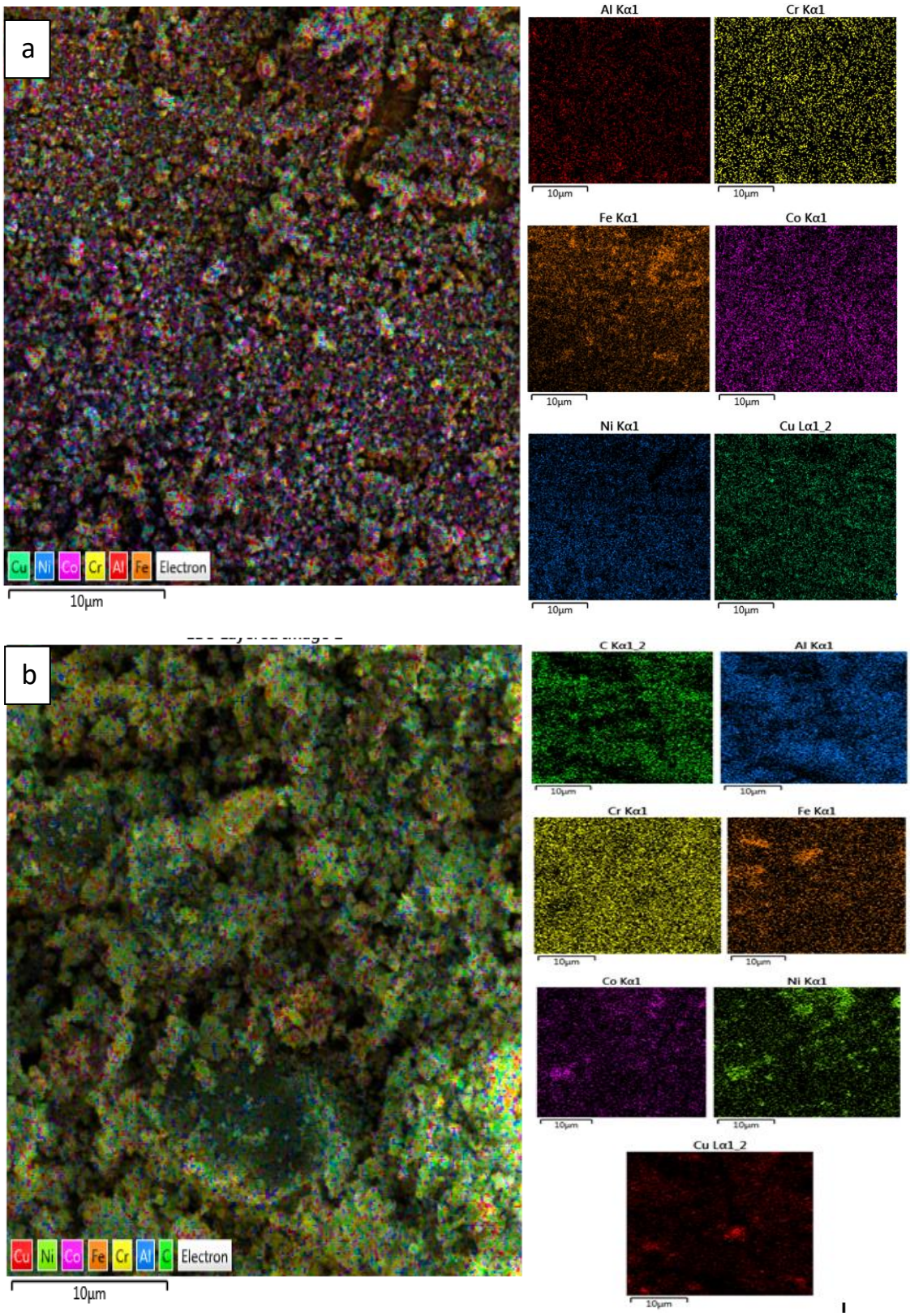

Figure (4.15) : The EDS map for the a) specimen G, and b) specimen H

4.3 Mechanical Tests

4-3-1 Microhardness

Figure (4.16) shows the surface microhardness of the specimens. As noted, CNTs possess the ability to enhance the microhardness of a surface, particularly in the (H) specimen. These results can be associated with the reinforcement and uniform distribution of carbon nanotubes in these specimens.

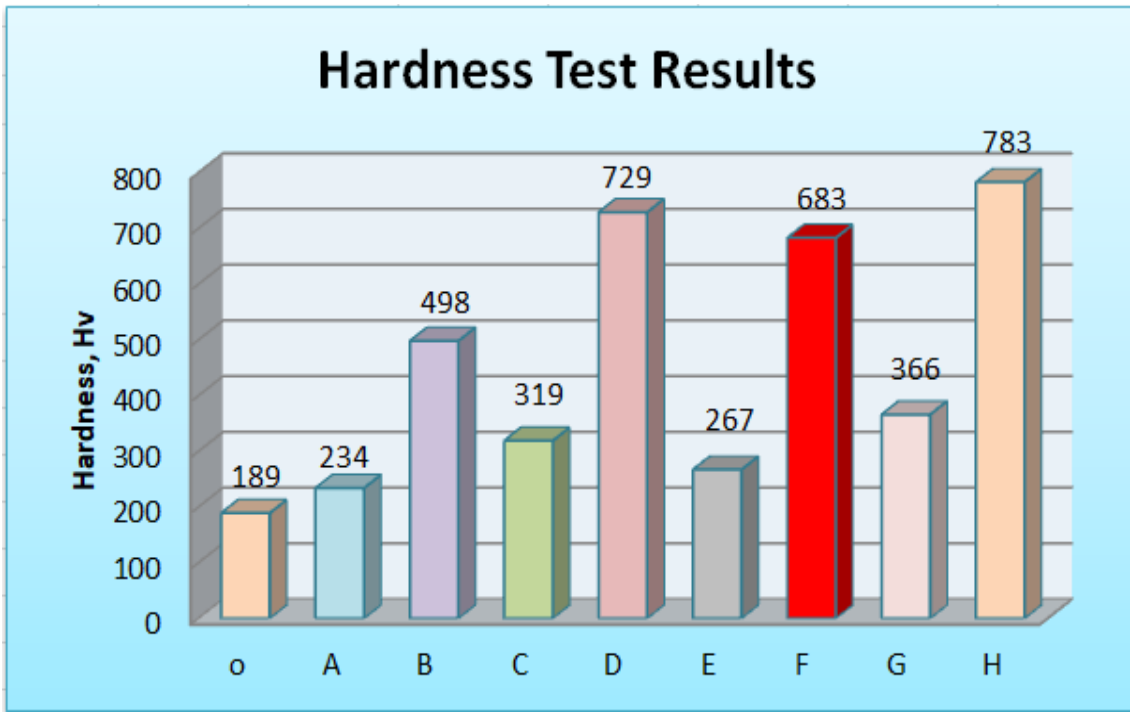

Figure (4.16): The Surface Microhardness Results.

The hardness of HEAs specimens with CNTs is large about 2.5 times when compared with the specimens of HEAs without CNTs as a result of the CNTs refines the grain size which leads to increase the hardness. Also, the HEAs specimens as compared with the substrate specimen is higher due to the HEAs properties which has high hardness due to a large lattice

distortion and stronger bonding were proposed to explain the strong solid solution hardening. The high hardness of the HEAs may result from the stronger interaction between the dislocation and solute atoms, and due to the solid solution strengthening. The HEAs specimen D & H is higher in hardness than specimen F as a result to this might be related to the fact that the distortion in FCC HEA is smaller than that in BCC HEA with improvement 314% as listed in Table 4-17 and that compatible with Ref [10].

Table (4-17): The Results of Specimens Microhardness and Improvement.

Specimen	**0**	**A**	**B**	**C**	**D**	**E**	**F**	**G**	**H**
Microhardness	189	234	498	319	729	267	683	366	783
Improvement%	0	23	163	69	285	41	261	93	314

4-3-2 Wear Test

Wear resistant is the one of the most important coating mechanical properties that wear failure contributes from all failure reasons. The wear rates produced by pin-on disc sliding wear test were determined by means of wear mass loss of test specimens under (5, 10N) load and several times (5, 10, 15, and 20) min. Generally, it can be observed that the weight loss increased with increasing of loading time. The results of the friction and wear tests for substrate, MEAs, MEAs-CNTs, HEAs, and HEAs-CNTs electrodeposition coatings are summarized in Table (4-18) and shown in the appendix A & B.

Table (4.18): Results of average coefficient of friction, and wear rate of coated specimens.

Specimen Code	F= 5N		F=10N	
	Coefficient of Friction	**Wear Rate (g/cm)*10^{-4}**	**Coefficient of Friction**	**Wear Rate (g/cm)*10^{-4}**
O	0.77	1.3	0.77	3.6
A	0.75	1	0.45	2.5
B	0.53	0.95	0.41	2
C	0.39	0.87	0.34	1.6
D	0.37	0.75	0.21	1.9
E	0.24	0.49	0.16	1.2
F	0.21	0.4	0.15	1.2
G	0.18	0.8	0.11	1
H	0.11	0.3	0.14	0.4

Table (4-18) shows that CNTs have a more favorable effect on the tribological properties of electrodeposition coatings than do other specimens. This specimen composite coating possesses not only a higher wear resistance but also a lower friction coefficient. The friction coefficient of the specimens G coating hardly changed before and after addition the CNTs, while those of the other electrodeposition HEAs coatings decrease to some extent. Therefore, it can be concluded that CNTs can significantly improve the tribological performance of electrodeposition composite

coatings. The favorable influences of CNTs on tribological properties may be attributed to their improved mechanical characteristics and the unique topological structure of the central hollow nanotubes as compatible to the Ref [123].

The specimen (H) exhibits higher wear resistance and lower friction coefficient in comparison with the other specimens electrodeposition coatings, both before and after coating. Figures (4.17 – 4.26) indicate the relationship between the weight loss and time for the plated specimens at 5N and 10N.

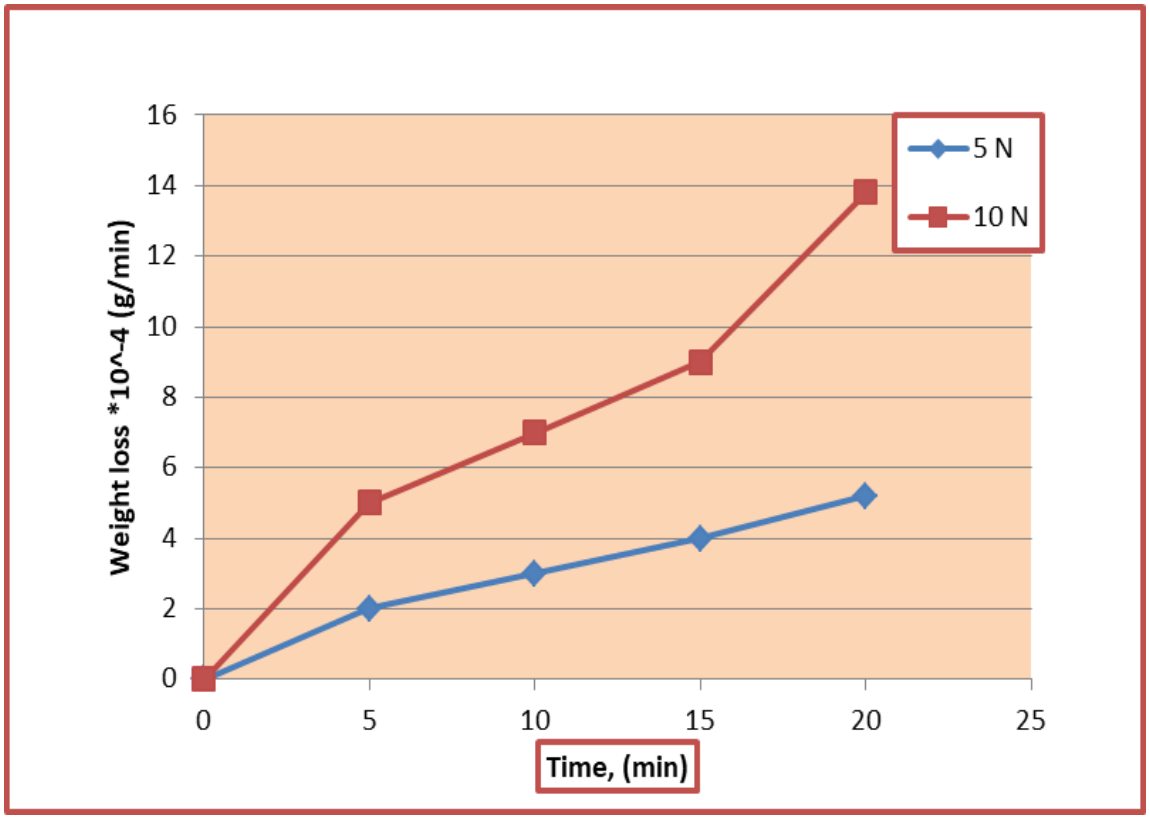

Figure (4.17): Relationship between weight loss and test time for 4140 low allot steel substrate at 5, 10 N.

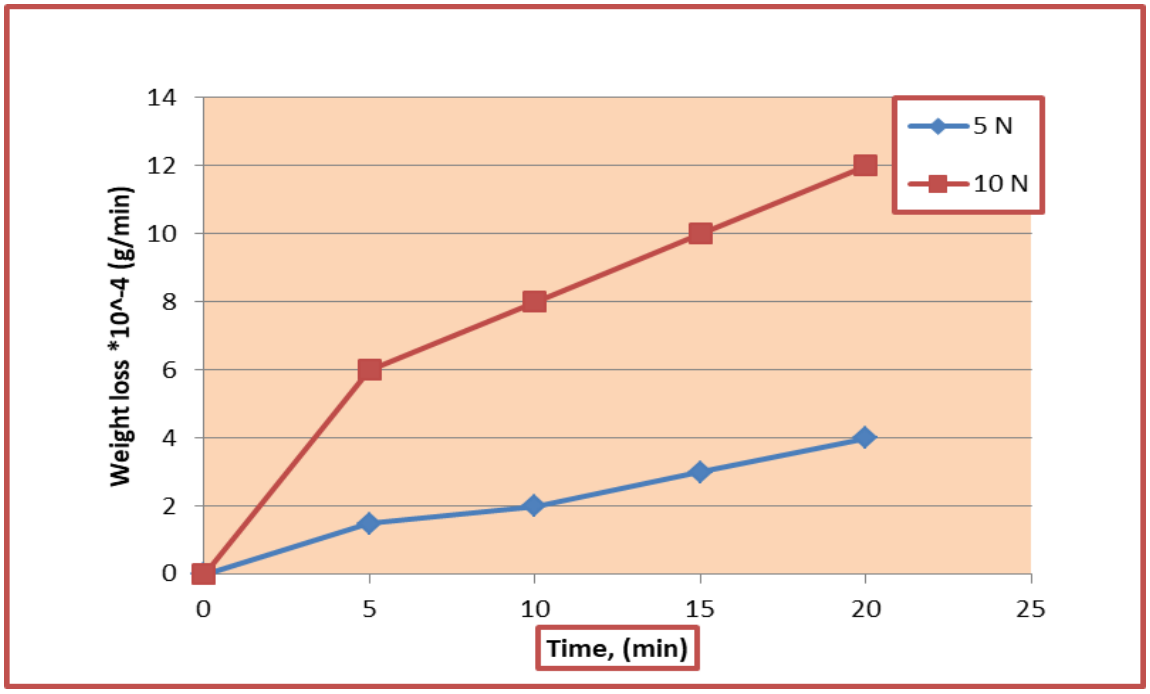

Figure (4.18): Relationship between weight loss and test time for specimen A at 5, 10 N.

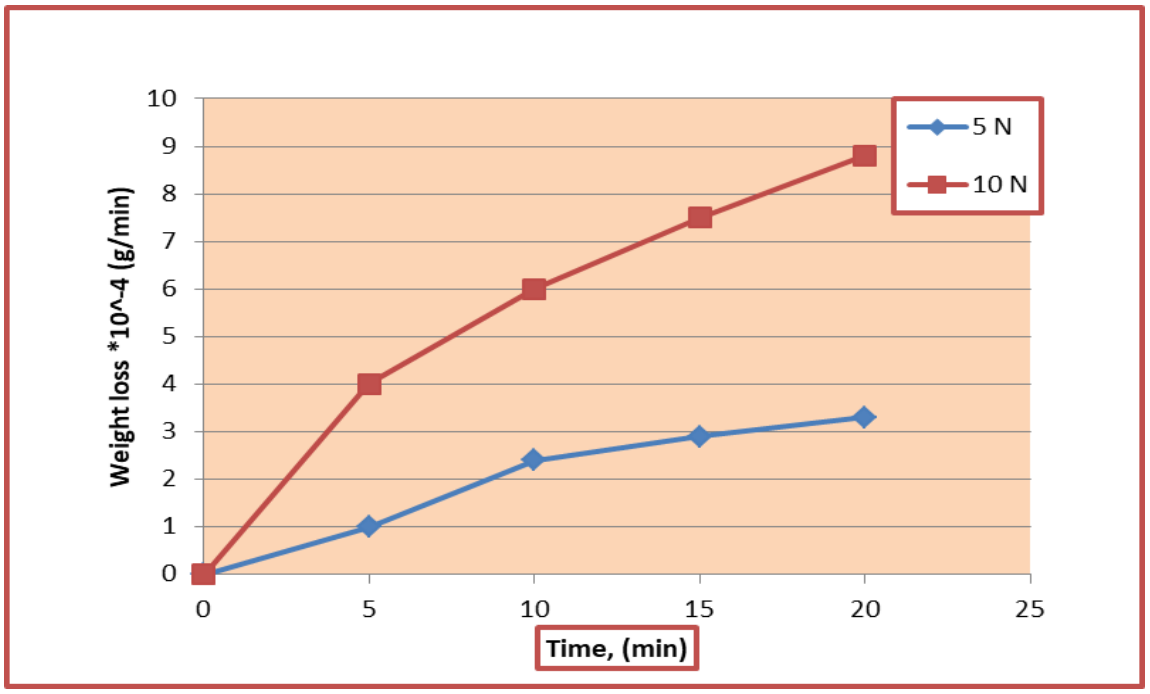

Figure (4.19): Relationship between weight loss and test time for specimen B at 5, 10 N.

There are only some slight scars on the worn surface for the specimen H, while obvious nick lines are found on the worn surface for G and other specimens coatings. Moreover, there are brittle detachments of the wear fragment on the MEA-CNTs electrodeposition coating. It is well known that a MEAs electrodeposition composite coating is highly wear.

Therefore, it is concluded that the main favorable benefits of the CNTs may arise from the following effects. The CNTs in the composite coating will slowly release onto the metal surface during the wear and friction test. The CNTs on the surface serve as spacers, preventing rough contact between the two mating metal surfaces, thereby slowing the wear rate considerably. In addition, the short CNTs would more easily slide or roll between the two mating metal surfaces, resulting in a decrease in the friction coefficient [123].

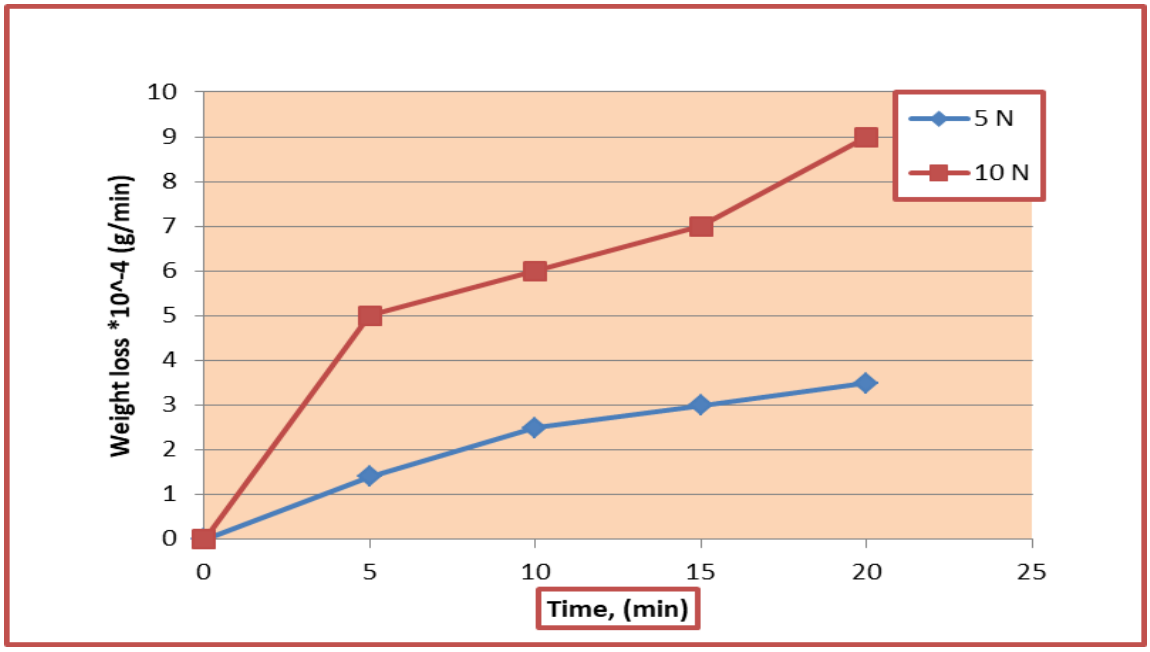

Figure (4.20): Relationship between weight loss and test time for specimen C at 5, 10 N.

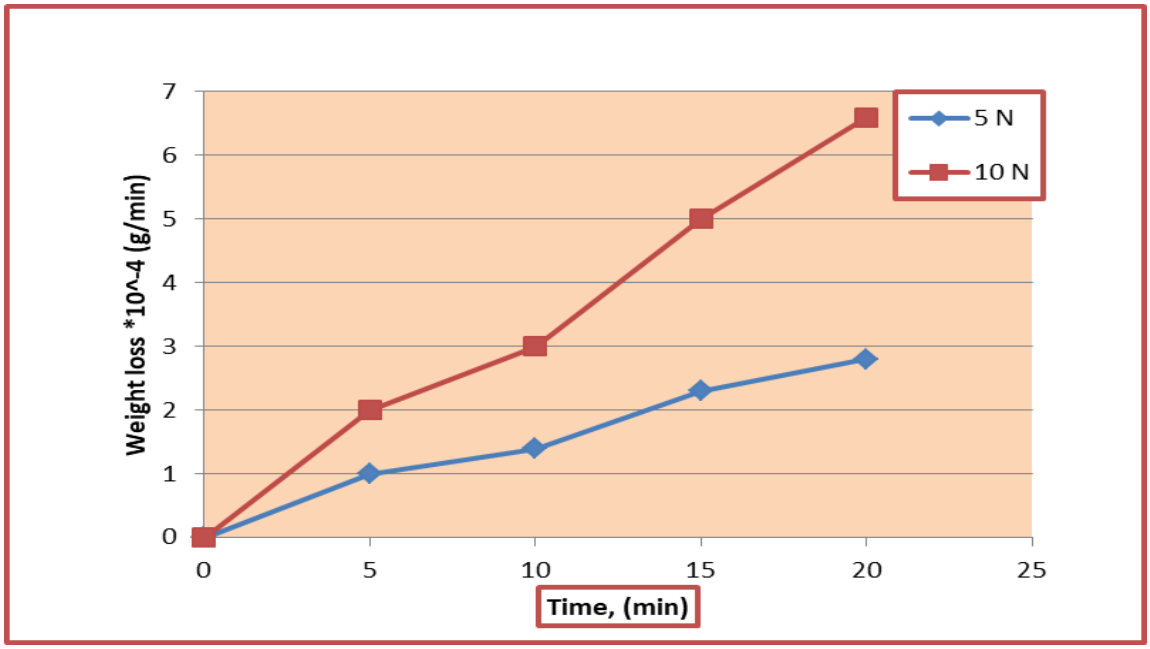

Figure (4.21): Relationship between weight loss and test time for specimen D at 5, 10 N.

After the HEAs coating and addition of CNTs to HEAs for the substrate specimen, the friction coefficient clearly decreases. The reasons for this result are the high microhardness value, which requires more friction for plastic deformation. HEAs coating contains CNTs specimens with a similar decreasing trend for the coefficient of friction.

The basic causes for this behavior include the following: Firstly, The hardness of the composites increases with addition of CNTs. Due to the high hardness value of the composite coating, pin surface was rubbed during the wear test and thereby pin/coating contact surface was increased and grain refinement. Consequently, the friction coefficient of composite coating was enhanced up to the sliding distance. Secondly, the CNTs fill the micro-holes of the surface during the electrodeposition process, which activates the sites for the stress of tensile. Therefore, CNTs can prevent

rapid plastic deformation. Thirdly, the CNTs act as very intense obstacles to the movement of dislocations through hindering the occurrence of the plastic deformation. Fourthly, the slow wear rate of the composite coating can be ascribed to the presence of the CNTs, which may serve as separators, preventing the close touch between the mating metal surfaces as agreed with [124]. Another factor that might affect the wearing of specimens is surface roughness. A larger surface roughness can lead to interactions of asperities between the roughness on surface specimens A& B and the prevailing counterpart. In fact, a higher wear rate and friction coefficient is a product in smaller contact areas that cause higher local pressure among the pin and the surface of the specimen.

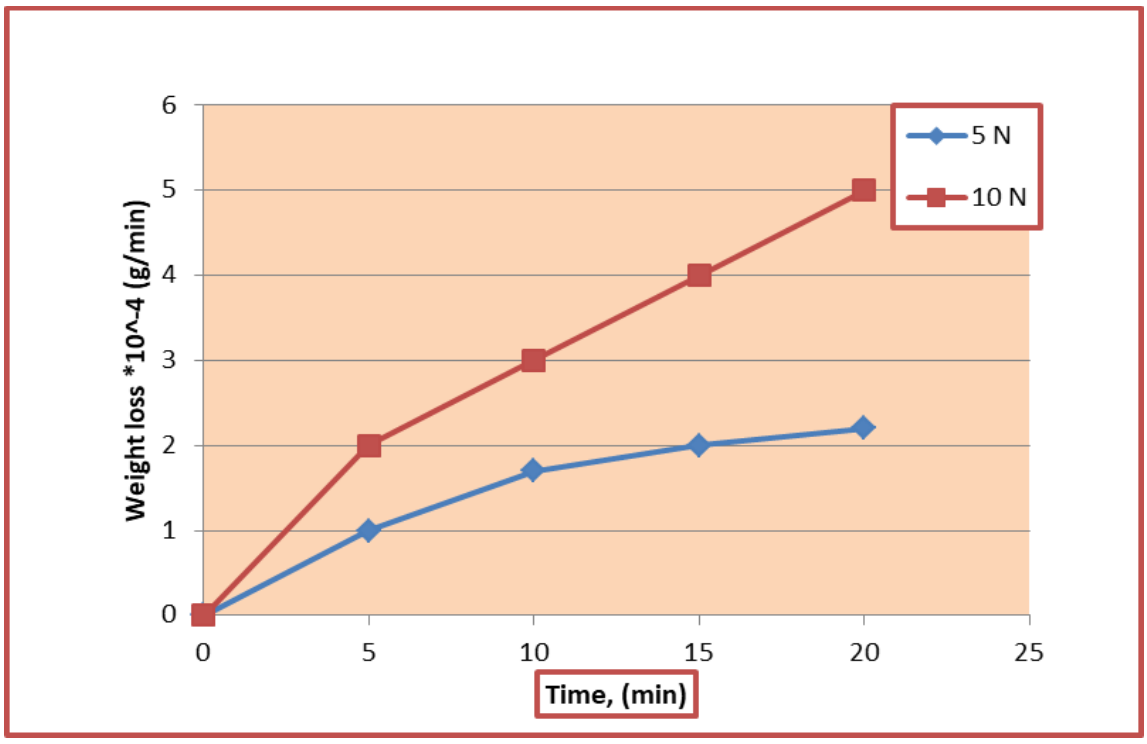

Figure (4.22): Relationship between weight loss and test time for specimen E at 5, 10 N.

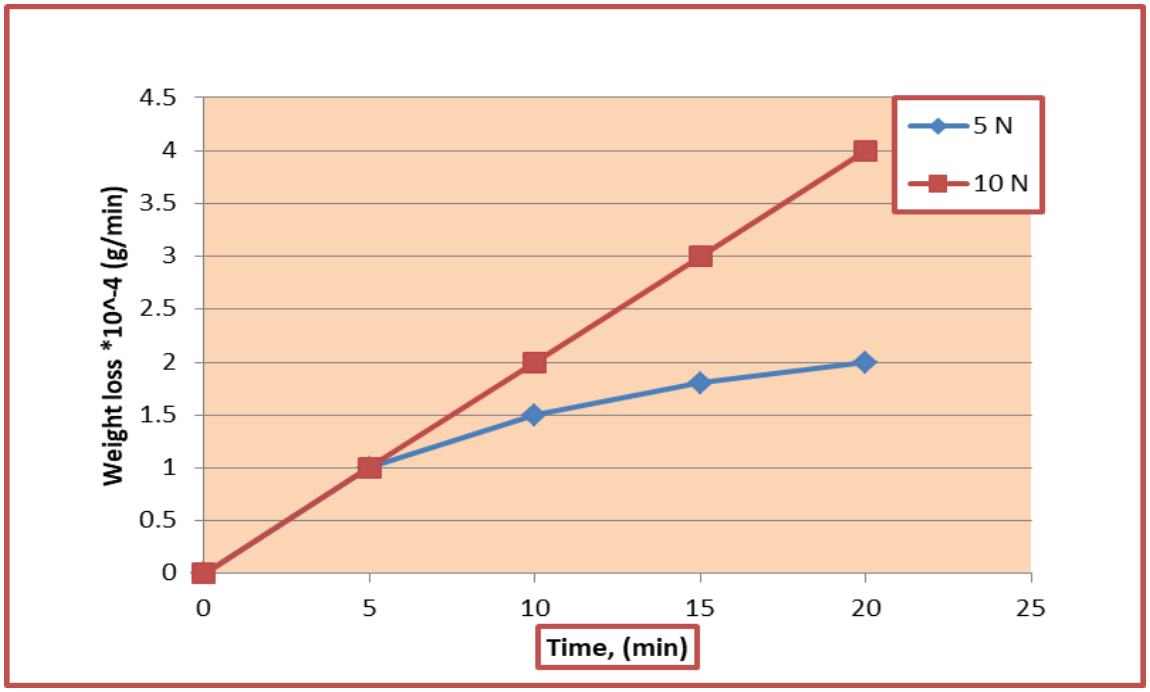

Figure (4.23): Relationship between weight loss and test time for specimen F at 5, 10 N.

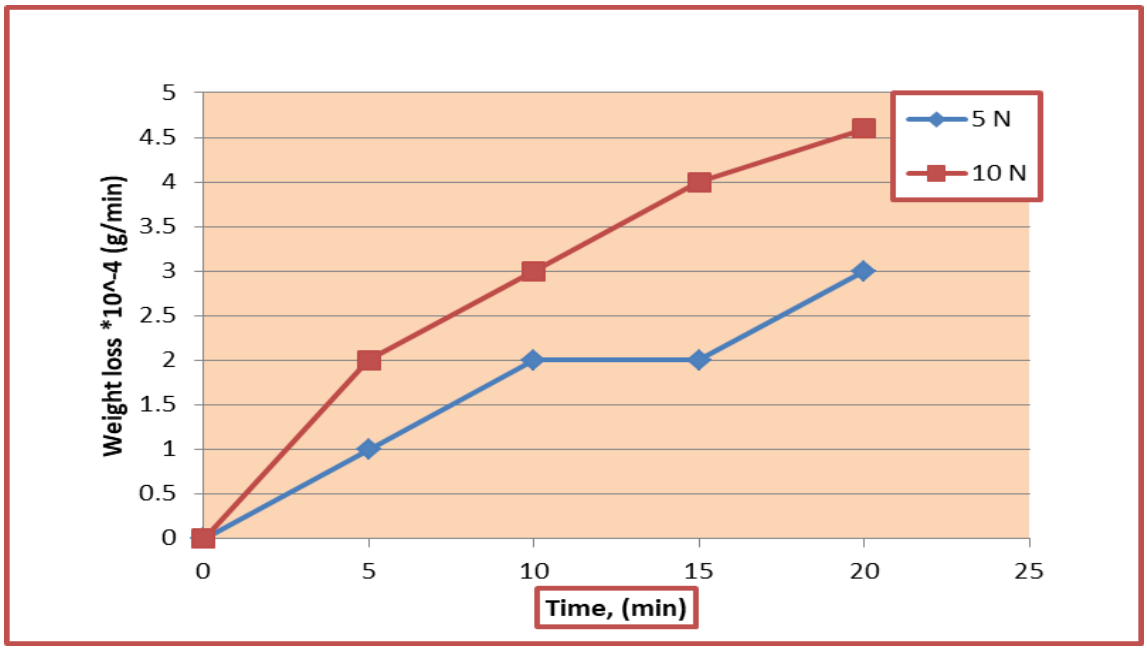

Figure (4.24): Relationship between weight loss and test time for specimen G at 5, 10 N.

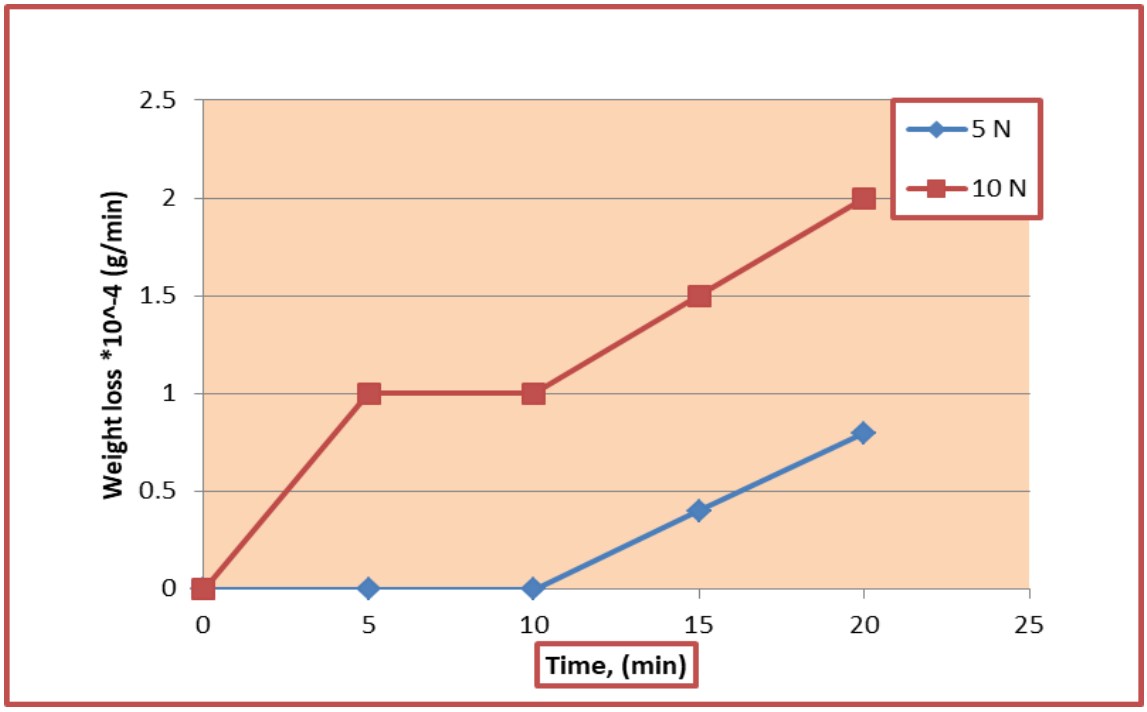

Figure (4.25): Relationship between weight loss and test time for specimen H at 5, 10 N.

Grain size, surface roughness and micro-hardness are important factors affecting the wear property. Figures (4.26-4.27) indicate the wear behavior of specimens coating layer with different coating bath (MEA, MEA-CNTs, HEA, HEA-CNTs), show that lower wear rate (0.4×10^{-4}) at specimen H. Dependence between wear characteristics and hardness was reported earlier and it was observed that wear rate value decreased with hardness increased. According to the Archard's law, the volumetric loss of the material is inversely proportional to the hardness value of the material [125].

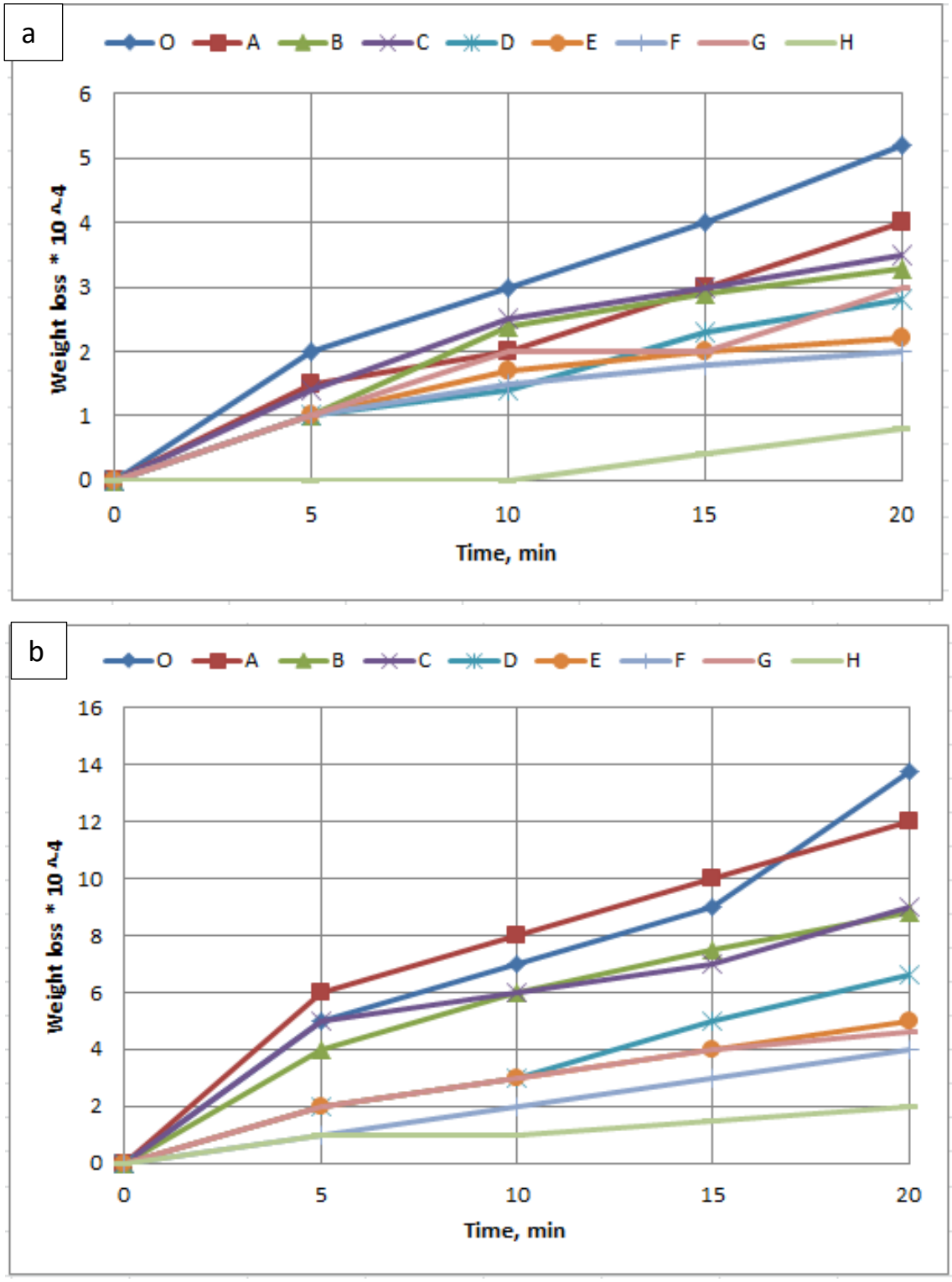

Figures (4.26) the relationship between the weight loss and time for the plated specimens at (a) 5N, and (b)10N

Table (4.18) and figure (4.27) illustrates the mean of friction coefficient and the rate of specific wear of as-substrate, MEAs, MEAs-CNTs, HEAs, and HEA-CNTs specimens. Therefore, it can be noted that the coefficient of the friction is directly related to a specific wear rate. Furthermore, it was noted that the specimen (H) has a lower wear specific rate in comparison to other specimens because of some reasons like larger microhardness, smaller grain size, lower coefficient of friction, and most importantly, homogenous distribution of CNTs.

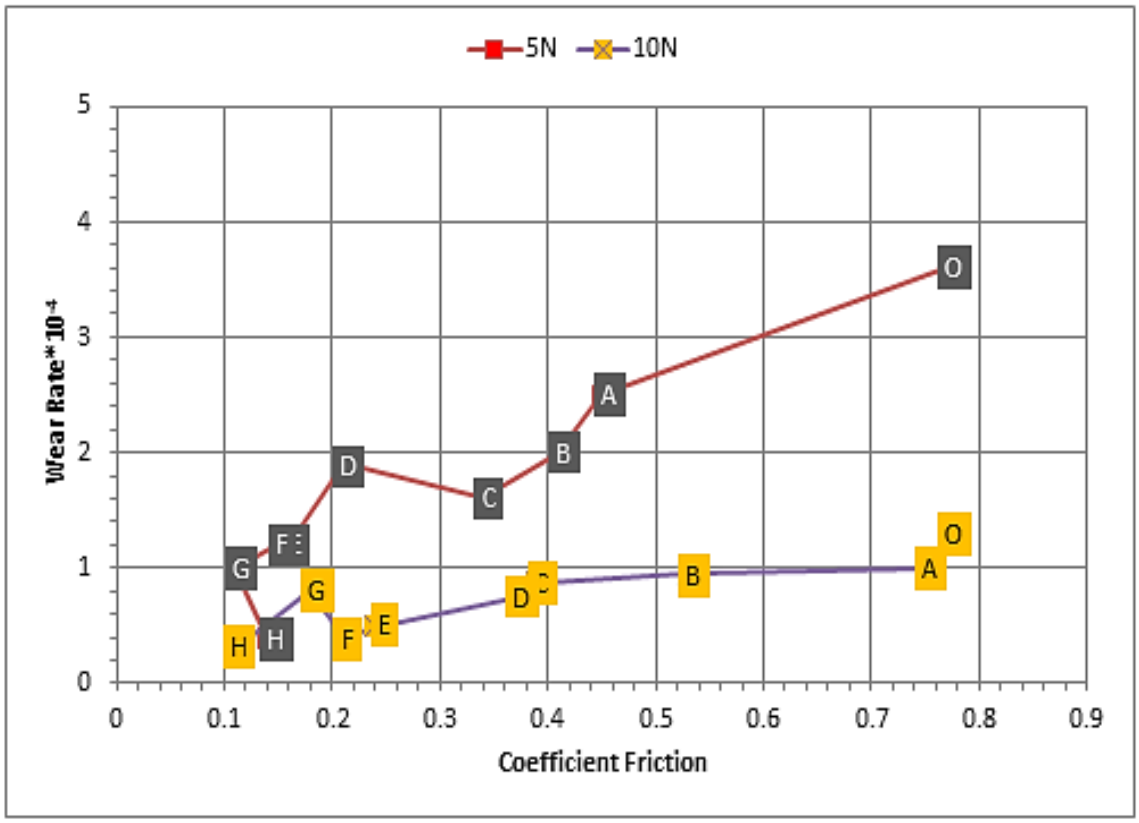

Figure (4.27): comparison between the coefficient of friction and specific wear rate.

Figure (4.28) explains the analysis of the optical microscope of the worn surfaces of the specimens after the wear test. The enhancement of wear resistance is clear.

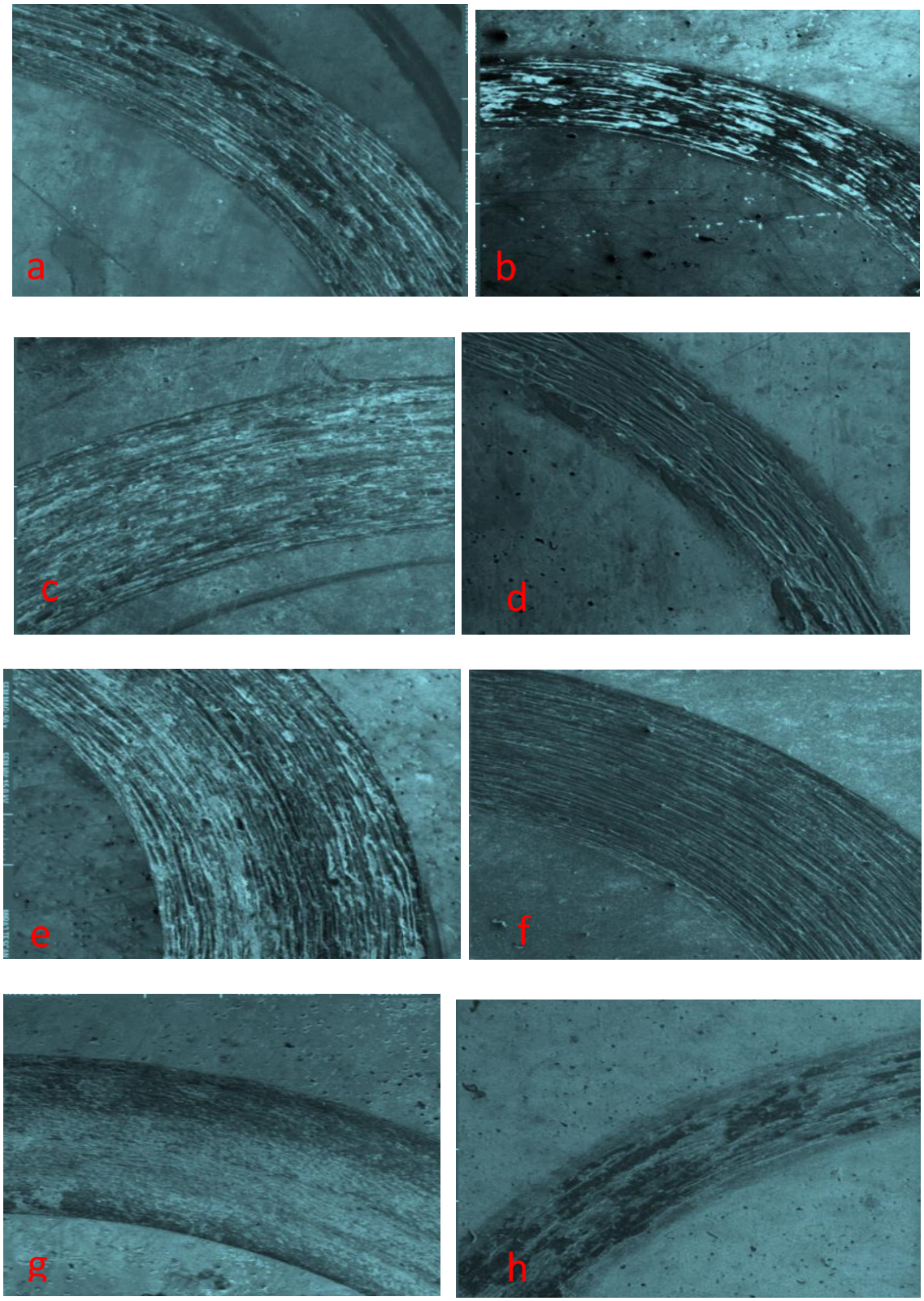

Figure (4.28):optical image of wear track the of (a) specimen A (b) specimen B (c) specimen C (d) specimen D.(e) specimen E (f) specimen F, (g) specimen G (h) specimen H.

Figures (4.28 d, f, and h) show a deep and wide wear track; the lamellar debris of specimen A indicates that delamination happens through wear tests, as shown in Figures (4.28 a). When the CNTs added to HEAs, a fine groove is noted along the sliding direction, as shown in figures (4.28 b). These results can be attributed to the reality that CNTs could prevent the generation of excessive heat through the wear test; thus, plastic deformation decreases and a smooth surface along with fine grooves can be observed in the optical image figure (4.28 h).

4-3-3 Adhesion Test

Adhesion has a strong influence on the wear and friction behavior of engineering materials. The adhesion test results listed in Table (4-19). The epoxy strength value that used in this test equal to 34.6 MPa which obtained from testing the epoxy on the substrate specimen (O). The specimens of HEAs coating were higher than specimen of MEAs coating (specimen A) as a consequence of high hardness of HEAs as compared with MEAs. Also, the CNTs addition to the coating enhance the strength of adhesion where the specimen B is higher in adhesive strength than specimen A, specimen D higher than C, specimen F higher than E, and specimen H higher than specimen G too as listed in Table (4-19). The improvements in the adhesion strength can be attributed to uniform dispersion of CNTs within HEAs coating that agreed with Ref [126] and the mechanical load transfer to the MWCNTs and the high specific surface area of this material which increased the degree of cross-linking with other HEAs coating.

Table (4-19): The Adhesion Test Results of Electrodeposited Specimens.

Specimen Code	O	A	B	C	D	E	F	G	H
Strength (MPa)	34.6	10.8	11.4	11.7	12.2	15.2	16.4	19.8	21.5

The thickness of coating layer was effect on the adhesion strength where the strength increased as the thickness of coating layer decreased as a result of reducing the hardness towards the increment of thickness. In this study, the thickness of the specimens increased as shown in figure (4. 29) and listed in Table (4-20) and the strength of adhesion was increased to the same specimens. The reason for this was due to addition of CNTs to the electro-deposition path that raised the hardness of the coating which in turn led to enhance the adhesion strength.

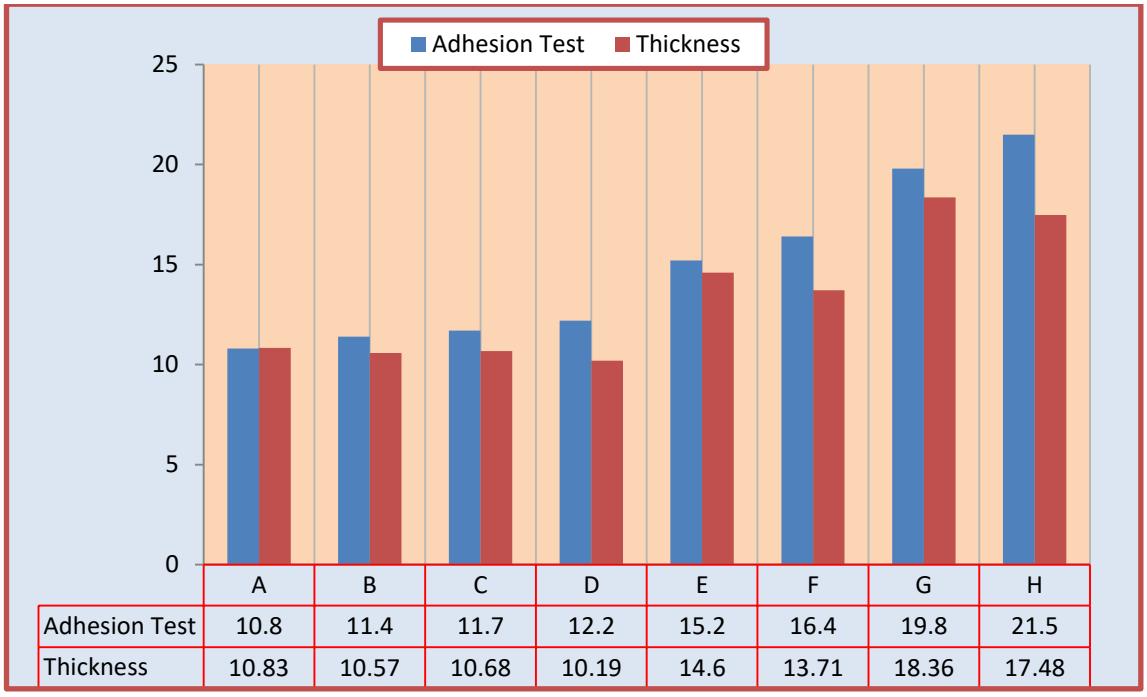

Figure (4.29): the relation between the thickness of coating layer and strength of adhesion.

From the table, it is clear that the specimens (G & H) are higher in adhesion strength than the other specimens because of that specimens G & H were HEAs coating consisting of 6 elements, unlike other specimens that consist of 5 elements or MEAs specimens that consist of 4 elements and this corresponds to the Ref [96]. Also, the lattice distortion that happens in HEAs coating led to increase the adhesion strength as a result to hardness increment.

4-4 Physical Tests

4-4-1 Coating Thickness

The coating thickness (t) measured by coating thickness gage type (TT260 country) and SEM cross section as shown in the figures (4.30) (4.31) (4.32). The coating layer thickness results are shown in the Table (4-20).

The thickness of the coating layer for the specimen C was measured by TT260 device equal to (14.79) μm as compared to the same specimen but was measured by FESEM cross section equal to (10.68) μm, so the device TT260 accuracy of (+4 μm). When the layer thickness of specimen was smaller than to the other specimens, the parts with this thickness were stronger than those with a thickness is higher, so the specimen D is the stronger as compared with the other specimens which thickness equal to (10.19) μm.

Table (4-20): The coating layer thickness results of the specimens

Specimen	A	B	C	D	E	F	G	H
t (μ)	10.83	10.57	10.68	10.19	14.6	13.71	18.36	17.48

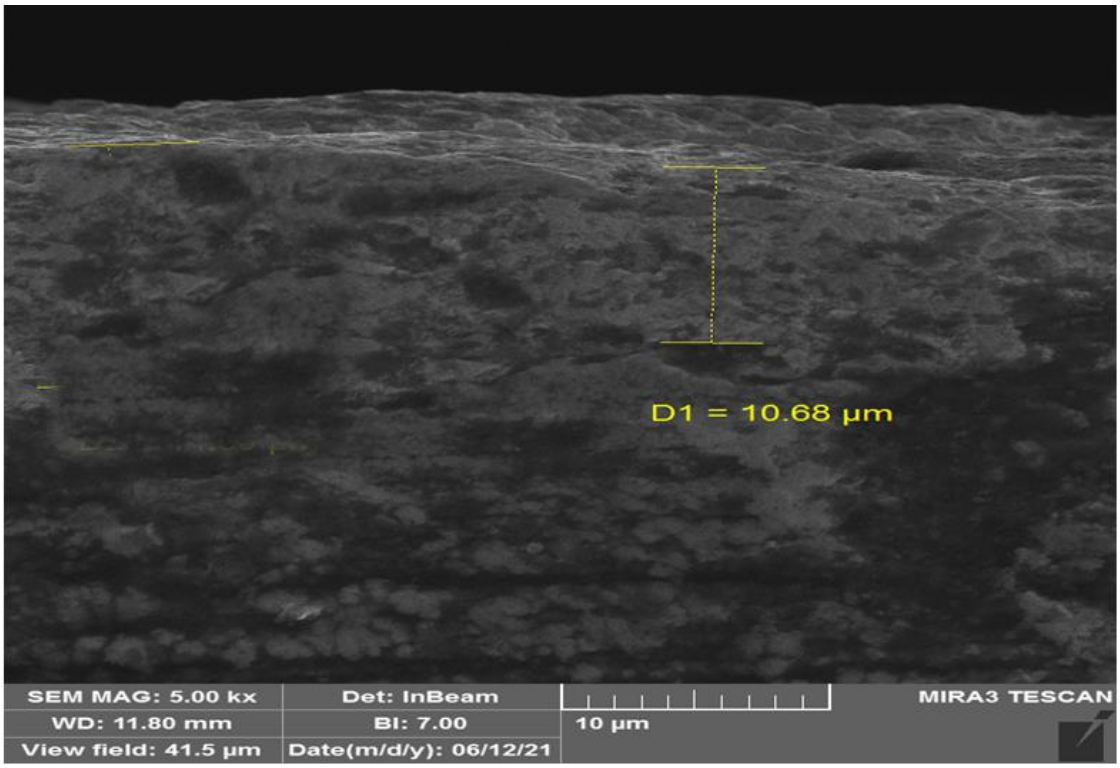

Figure (4-30): FESEM image of Specimen C that show the thickness of coating layer.

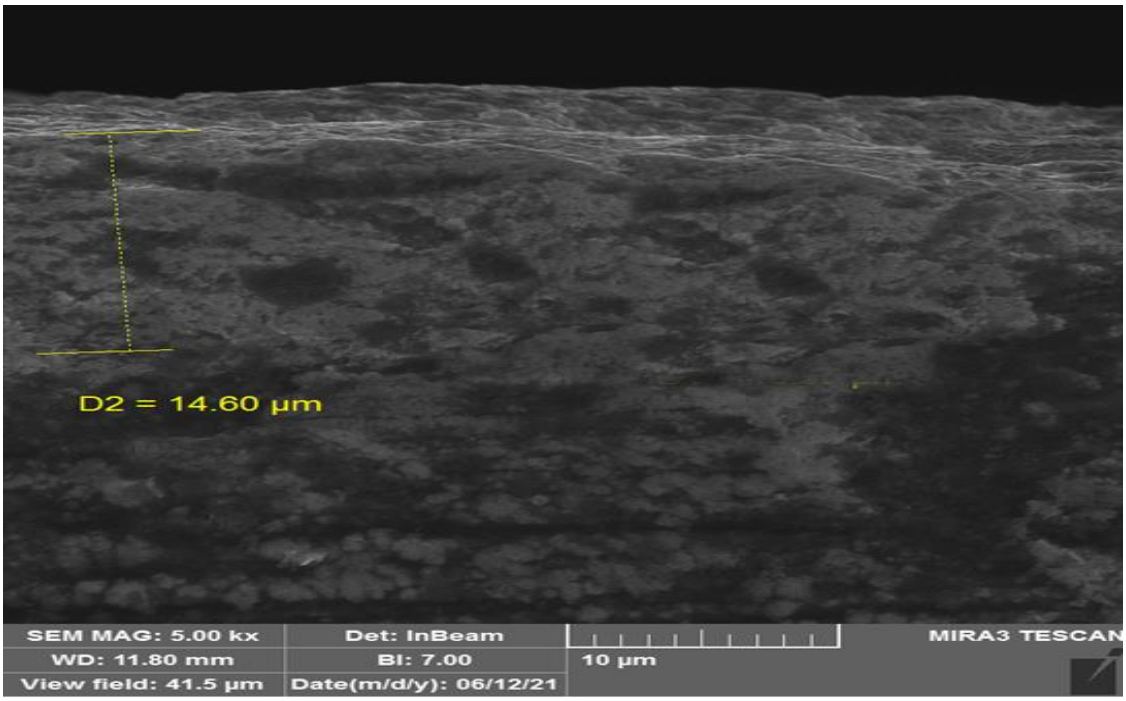

Figure (4-31): FESEM image of Specimen E that show the thickness of coating layer.

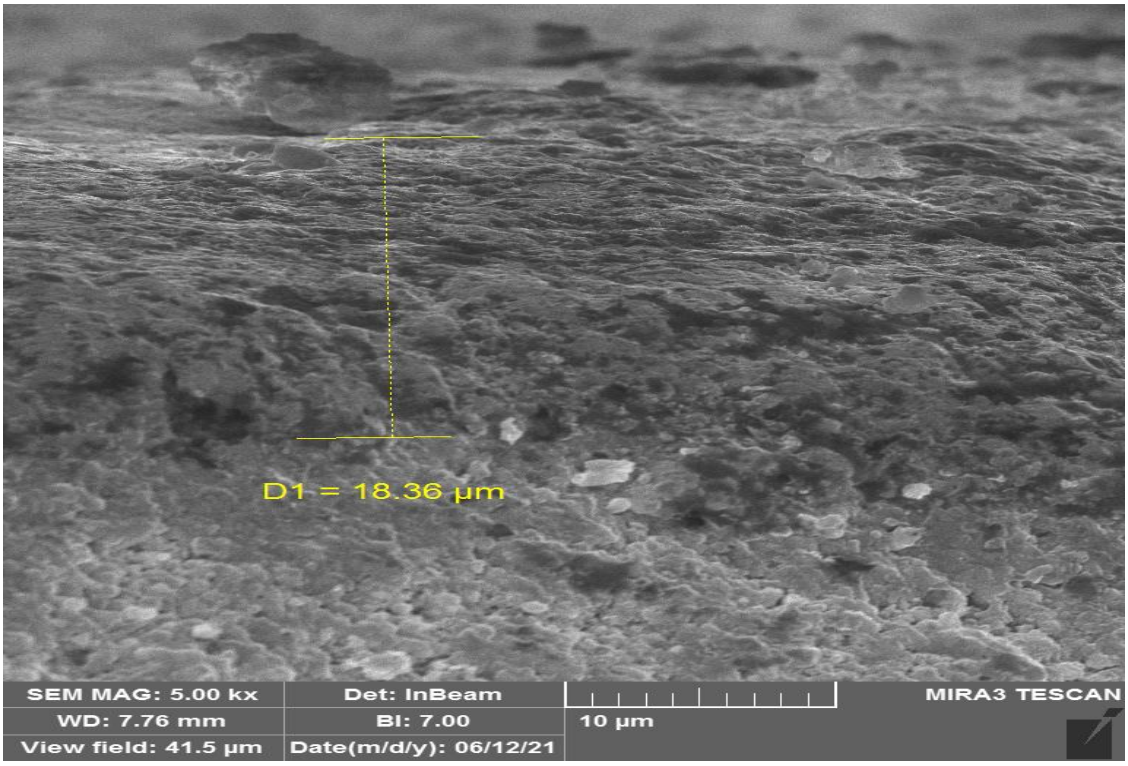

Figure (4-32): FESEM image of Specimen G that show the thickness of coating layer.

Figure (4-33) shows the optical image of coating layer thickness of specimens. Agitation of an alloy plating bath or rotation of the cathode can directly affect the composition of the alloy by reducing the thickness of the cathode diffusion layer that led to reduce the thickness of specimen D as a result of high stirring as compared with other specimens [48]. The reduction in the thickness enhance the mechanical properties of the coating specimens. The thickness of coating don't influenced by the CNTs but the deposited specimens with CNT have uniform thickness that depends on both the applied electric field and deposition time as agreed with Cho et al [127].

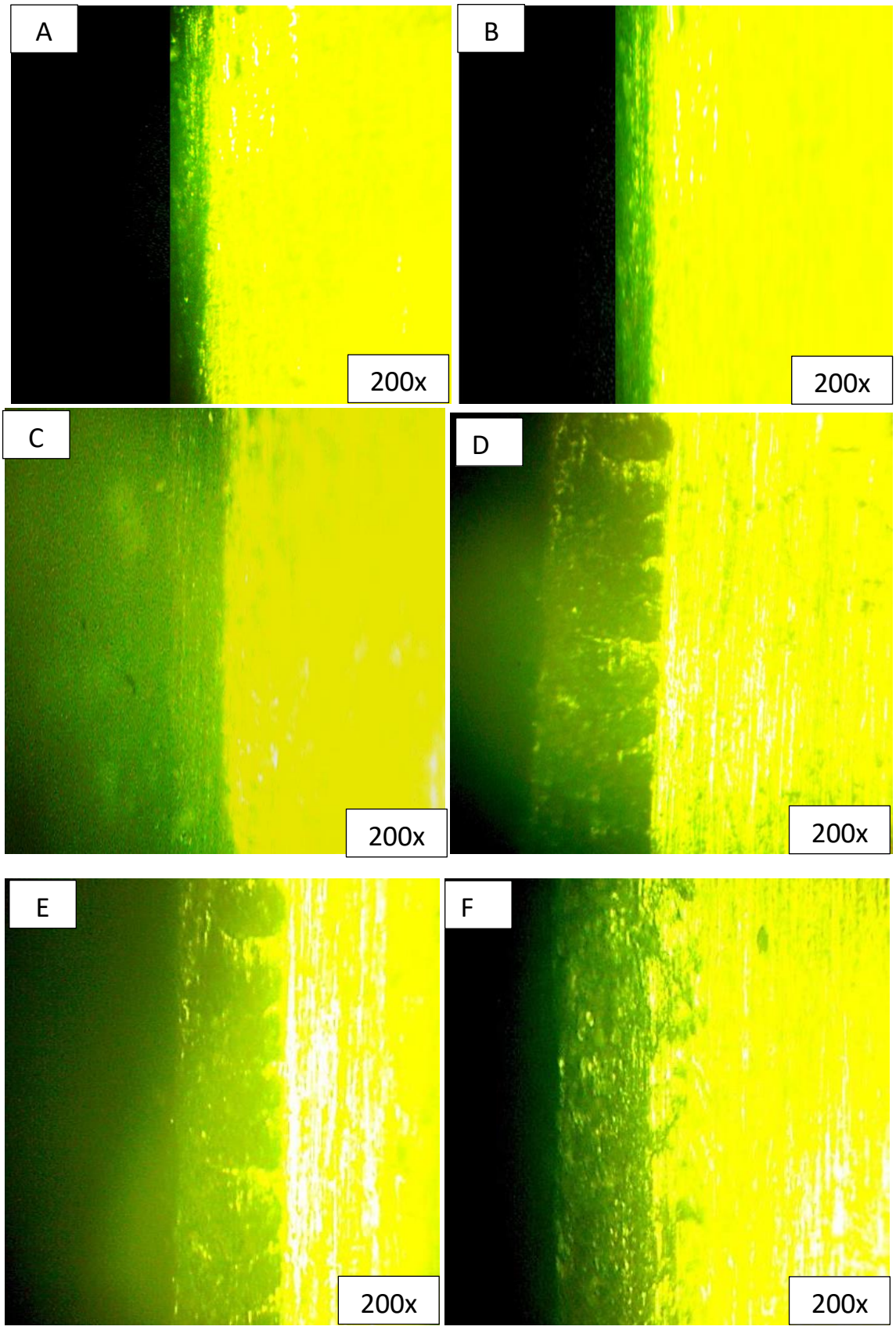
A
200x
B
200x
C
200x
D
200x
E
200x
F
200x

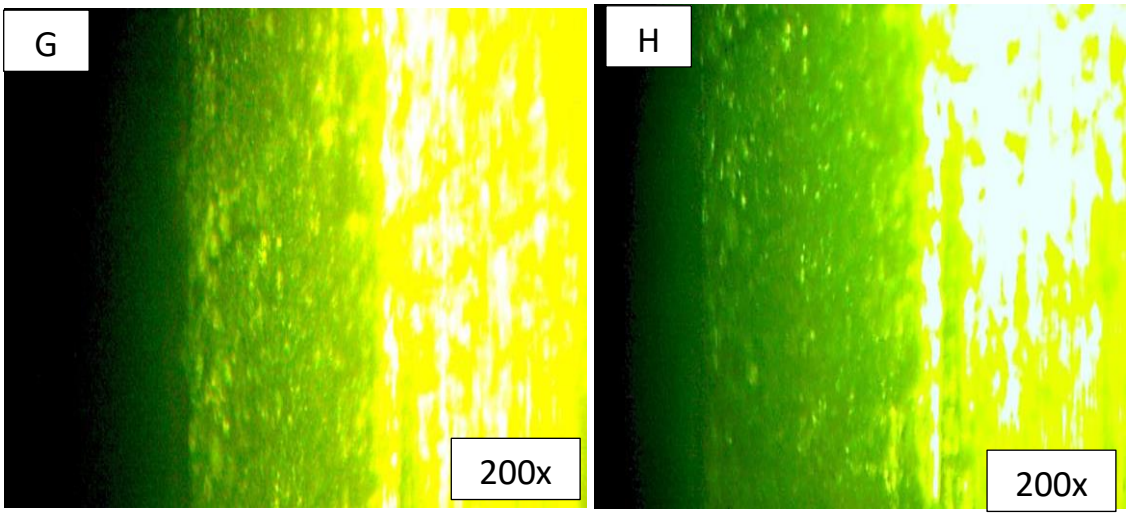

Figure (4-33): Optical image that show the thickness of coating layer of Specimens.

4-4-2 Contact Angle Measurement

From the FESEM observation with different magnifications, the surfaces of the as-prepared coating were covered by some spherical clusters in micrometer scale which was piled up by some nano-soft flaky structures. The coating was quite compact and uniform, without the defects of traditional inorganic coatings such as cracks or pores.

Wettability depends on the contact angle of the liquid with the surface of solid and is derived from intermolecular forces; it is determined via the balance between cohesive and adhesive forces[128]. According to the wetting test results of the specimens, it was observed that the coating created in some the investigated conditions was poor wetting. Table (4-21) presents the results of the wetting test and the diagrams of the angular change of wetting concerning the shifts of coating conditions, and coating parameters are presented in Figure (4.34).

Table (4-21) : The Results of the Wetting Test.

Specimen Code	O	A	B	C	D	E	F	G	H
θ	81.5	26	28	35	40	43	46	69.7	77

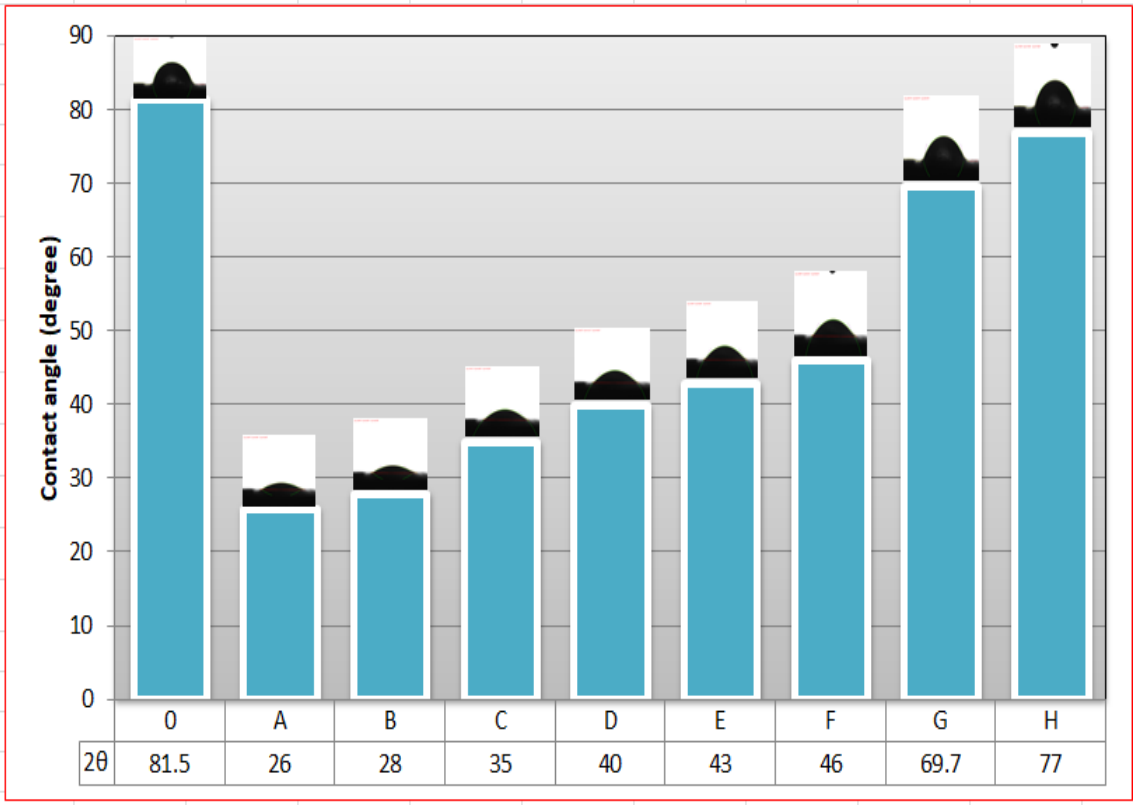

Figure (4-34): The Contact Angle Results of the Specimens.

In specimen H was the maximum contact angle measured. The surface of this specimen is hydrophobic in comparison to the other specimens but is less than 90^{o} that indicate to its considered a hydrophilic. A rough surface of specimen -A- with large blisters has the smallest contact angle among other specimens, and due to surface roughness, it has the highest

angle tolerance at various points. Specimens C, D, E and F have a flat surface and are hydrogen blisters and salient particles. In specimens G and H, due to the uneven distribution of blisters, contact angles and tolerance are higher than the other specimens due to uniform blisters on the surface as agreed with the Ref [129].

The contact angle measurement on the surfaces indicates that the CNTs coating leads to a significant decrease in wetting property of coating surfaces with HEAs as shown in figure (4.34). When the CNTs added to the HEAs coating, the contact angle increase which led to reduce the wettability. The angle value of specimen C increase about 5^{o} when added the CNTs HEAs to became specimen D which were similar to specimens E and F. The MEAs were the lower contact angle specially without the CNTs as compared to the other specimens because of the flat surface and the higher smoothness.

Also, the increment of surface roughness effect on the contact angle by increasing the wettability (decrease the contact angle) as shown in specimens G and H that have the lower roughness. Figure (4.35) shows the relation between the surface roughness and the contact angle where the roughness decrease, the angle increase. Ma and et al, [130] explained that the values of the contact angle indicate the degree of wettability as: ($0° < \theta < 30°$) very good wetting, ($30° < \theta < 40°$) good wetting, ($40° < \theta < 55°$) acceptable wetting, ($55° < \theta < 70°$) poor wetting, and ($\theta > 70°$) very poor wetting and from these values it seems that specimens (A and B) very good wetting, specimen (D) good wetting, specimens (C, E, and F) acceptable wetting, and specimens (O, G, and H) poor wetting.

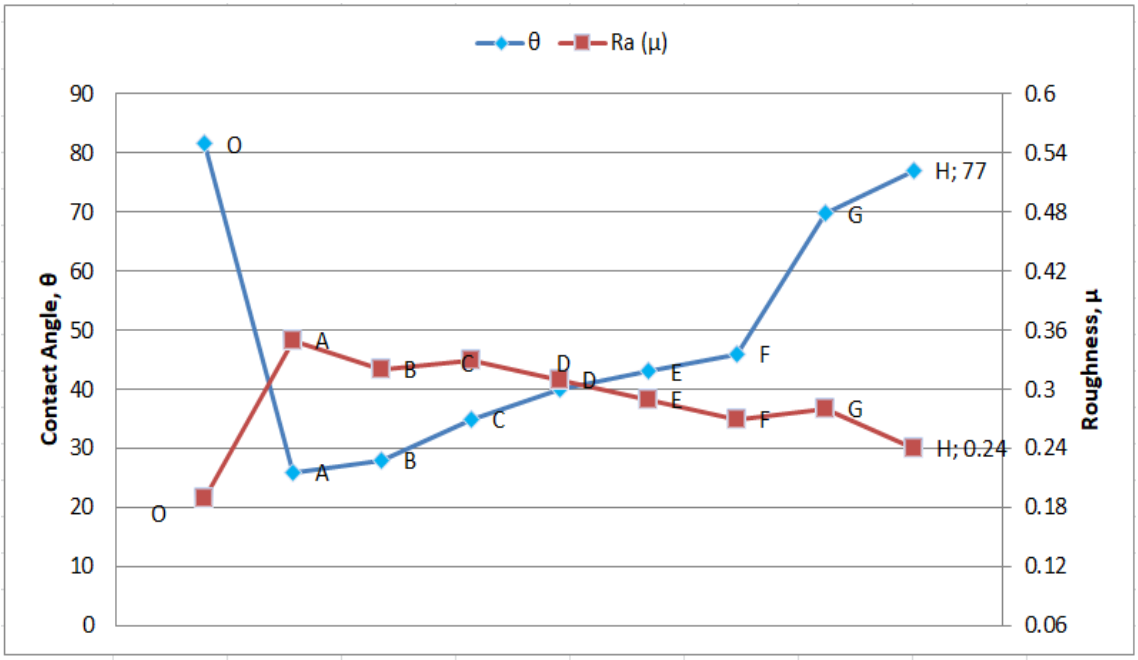

Figure (4.35): The Relation between the Contact Angle and Surface Roughness

4.4.3 Surface Roughness

Data regarding the roughness of the substrate, coating specimens has been illustrated in Table (4.22). As mentioned above, an added the CNTs' concentration to coating solution as 0.2g/l causes a significant decrease in roughness. A high CNTs amount prevents the uniform coating morphology and creates roughness. The roughness of specimen H is lower when compared with other specimens, as a concentration of CNTs may result in compactness of morphology.

It was observed that the coating morphology became progressively finer for the substrate. The Ra increased from specimen as the number of element in HEAs increased which led to non-uniform morphology. The CNTs additions with finest morphology observed for (H) specimen. Further addition of CNT progressively enhanced the surface roughness resulting in

a non-uniform coating morphology. This was speculated to be due to non-uniform distribution of CNTs in coating arising from the CNT agglomeration in the electrolyte bath[131].

The specimens (D & F) with CNTs addition to the HEAs show decrease in the roughness which is possibly due to the incorporation of the CNTs that is a nano sized and leads to a uniform morphology on the opposite of what is in the specimen G which is agreed with Ref [124].

Table (4.22): Results of roughness test of specimens surface.

Specimen	0	A	B	C	D	E	F	G	H
Ra (μ)	0.19	0.35	0.32	0.33	0.31	0.29	0.27	0.28	0.24

4.5 Electrochemical Tests

4-5-1 Corrosion Behavior

Investigation of corrosion behavior of coating is obtained by potentiodynamic and cyclic polarization tests. At first, the specimen is immersed in (3.5% NaCl) solution and the open circuit potential (OCP) has been recorded after this period, where a steady state potential is attained. The corrosion behavior has been studied for substrate and all specimens coating.

4.5.1.1 Open Circuit Potential (OCP)- Time Measurements

Open circuit potential (OCP) variations with time are related to the nature of reactions at the surface of the electrode when in contact with a

specific medium (passivation, dissolution, or immunity) and therefore can be used as a criterion for corrosion behavior.

Table (4-23) and Figure (4.36) shows the specimen variations with respect to voltage and time for the coating specimens and the corresponding comparison with uncoated alloy in (3.5%NaCl) solution at room temperatures. They indicate that this change is related to the formation of an oxide film that passivates the metallic surface. On the other hand, OCP profiles for specimens exhibited very stable potentials during the test.

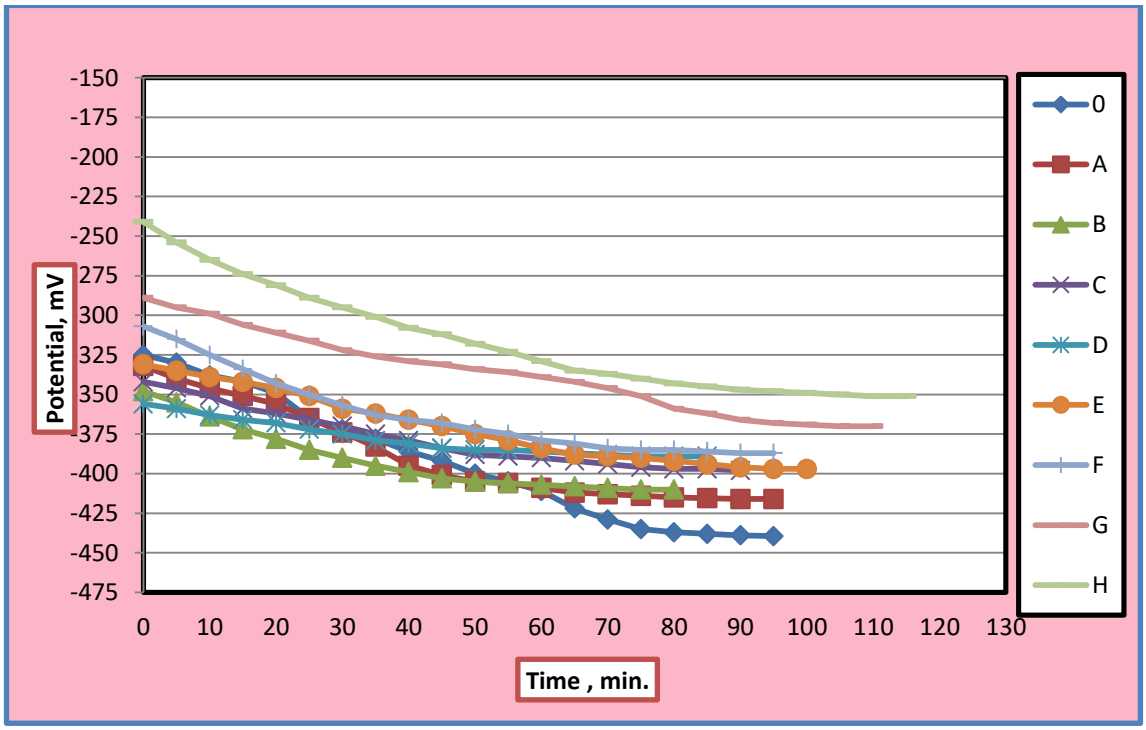

Figure (4.36): OCP-time of substrate and coated specimens in NaCl solution

They showed a stable scan with nobler potential values than non-coated specimen while for the coated specimen, the OCP decreased with the voltage and time until it stabilized at a stationary value more positive for specimen A. A variety of parameters of the surface films (composition,

phases, and structural defects as porosity and cracking) could explain the different susceptibility to degradation of the modified surface..

Table (4-23): E_{OCP} results of specimens in NaCl solution.

Time/code	0	A	B	C	D	E	F	G	H
0	-325	-332	-348	-342	-356	-331	-307	-289	-241
5	-330	-340	-355	-346	-359	-335	-315	-295	-254
10	-338	-346	-364	-351	-363	-339	-325	-299	-265
15	-342	-351	-372	-359	-366	-342	-334	-306	-274
20	-349	-356	-378	-362	-368	-346	-343	-311	-281
25	-365	-365	-385	-366	-372	-351	-350	-316	-289
30	-372	-374	-390	-370	-375	-359	-357	-322	-295
35	-378	-383	-395	-375	-379	-362	-363	-326	-301
40	-386	-395	-399	-379	-381	-366	-366	-329	-308
45	-392	-401	-403	-384	-384	-370	-368	-331	-312
50	-400	-405	-405	-388	-385	-375	-372	-334	-318
55	-405	-406	-406	-389	-385	-379	-375	-336	-323
60	-411	-409	-407	-390	-386	-384	-379	-339	-329
65	-422	-412	-408	-392	-387	-388	-381	-342	-335
70	-429	-413	-409	-394	-388	-389	-384	-346	-337
75	-435	-414	-410	-396	-389	-390	-385	-351	-340
80	-437	-415	-410	-397	-389	-392	-385	-359	-343
85	-438	-415		-397	-389	-394	-386	-362	-345
90	-439	-416		-398		-396	-387	-366	-347
95	-439	-416				-397	-387	-368	-348
100						-397		-369	-349
105								-370	-350
110								-370	-351
115									-351

4.5.1. 2 Potentiodynamic Liner Polarization

Table (4.24) includes the results of the corrosion test ($E_{corr.}$, $i_{corr.}$) and the protective efficiency of coatings, as evaluated by the Tafel extrapolation technique in a solution of 3.5% NaCl.

Table (4.24): The results of corrosion test in 3.5% NaCl solution.

Specimen Code	E_{corr} (mV)	I_{corr} (µA)	Protective Efficiency	Corrosion Rate (mpy)
O	-203	130.7	--	14.5
A	-96	84.7	35.2	12
B	-301	81.9	37.3	11.2
C	-348	105.4	19.4	13
D	-928	82.3	37	9.6
E	-1340	63.4	51.5	9.1
F	-167	46.27	65	6.2
G	-625	14.47	88.9	1.8
H	-579	9.42	92.8	1.15

The corrosion parameters: corrosion potential (E_{corr}) and corrosion current (I_{corr}), extracted from the potentiodynamic polarization curves by Tafel extrapolation, are plotted in figure (4.37). A decrease in I_{corr} was observed in the specimen (H) coating. This decline in I_{corr} indicate a reduction in the corrosion rate, which implies an enhancement in the corrosion resistance of the specimen H. By comparison of the results in figure (4.37), it is deduced that the CNTs incorporation into HEAs has a significant effect on the protection effeceincy (P_{eff}) of MEAs, HEAs coating and the polished low alloy steel substrate figure (4.38).

The P_{eff} with respect to the I_{corr} of the polished AISI 4140 steel substrate are calculated using the relation below:

$$\textbf{Protective Efficiency}\ (P_{eff}) = \frac{I_{corr(substrate)} - I_{corr(HEA/HEA-CNTs)}}{I_{corr(substrate)}} \times 100\% \qquad (4.12)$$

Where I_{corr} (substrate) and I_{corr} (HEA/HEA-CNTs) represent the corrosion current of the polished AISI4140 steel and HEAs with/ without CNTs, respectively. It is evident that P_{eff} of the substrate can be improved to 35.2% by the HEAs of specimen A. However, this P_{eff} can further be enhanced up to 92.8% with CNTs addition as specimen H which were agreed with the Ref [132].

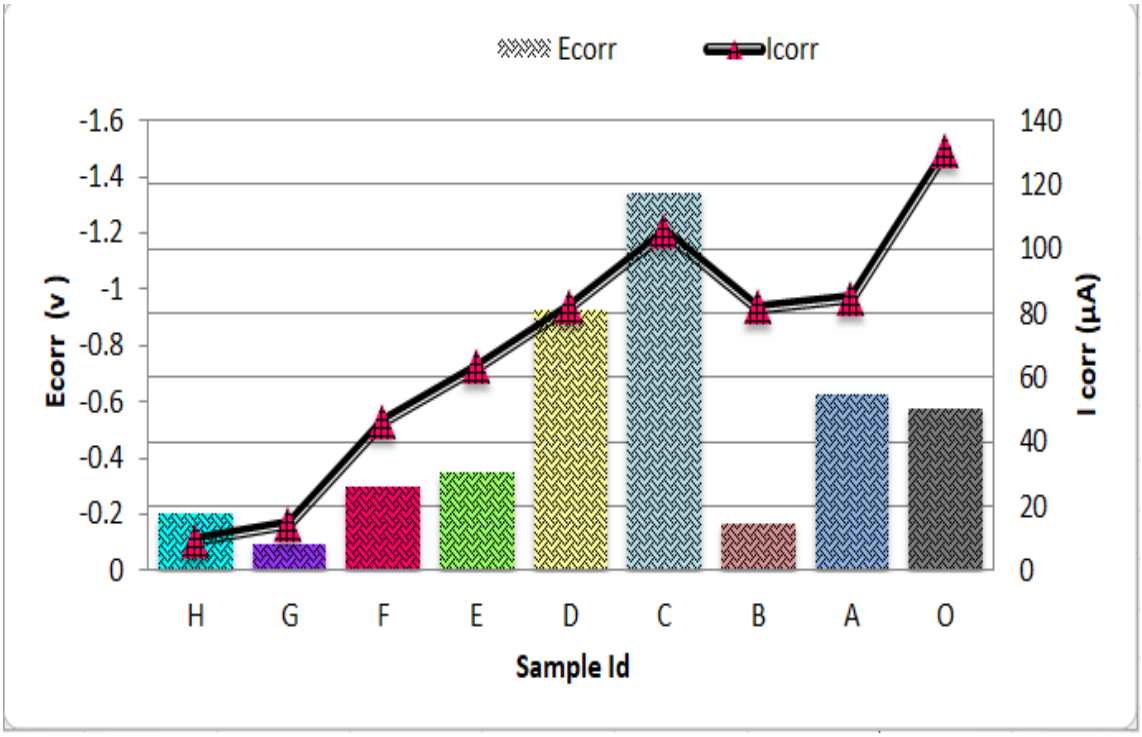

Figure (4.37): Comparison of Corrosion Potential and Current of Corrosion.

Potentiodynamic polarization curves were measured on uncoated and HEAs coated 4140 steel, as shown in Figure (4.39). It is clear that HEA

coating is used in the enhancement of properties of the corrosion of AISI 4140 steel is due to the ability of HEA coating to act as an effective barrier between metal and corrosion media; it should be noted that the high corrosion rate and I_{corr} is lower on the plated specimen than on the uncoated specimen that agreed with the Ref. [133]. However, the addition of CNT is really innovative.

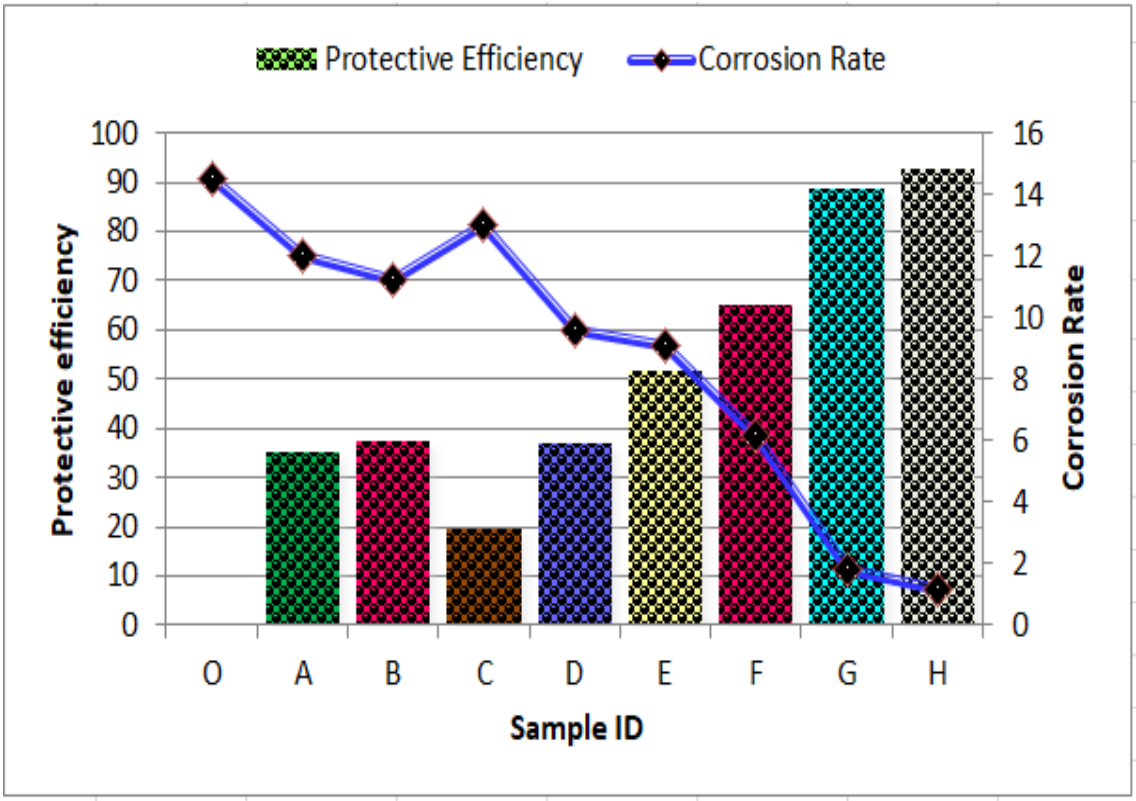

Figure (4.38) : Protective Efficiency and Corrosion Rate of Specimens.

The potentiodynamic polarization curve of both MEA and MEA-CNTs coatings are shown in Figure (4.39 b). Table (4.24) shows the results of liner polarization test.

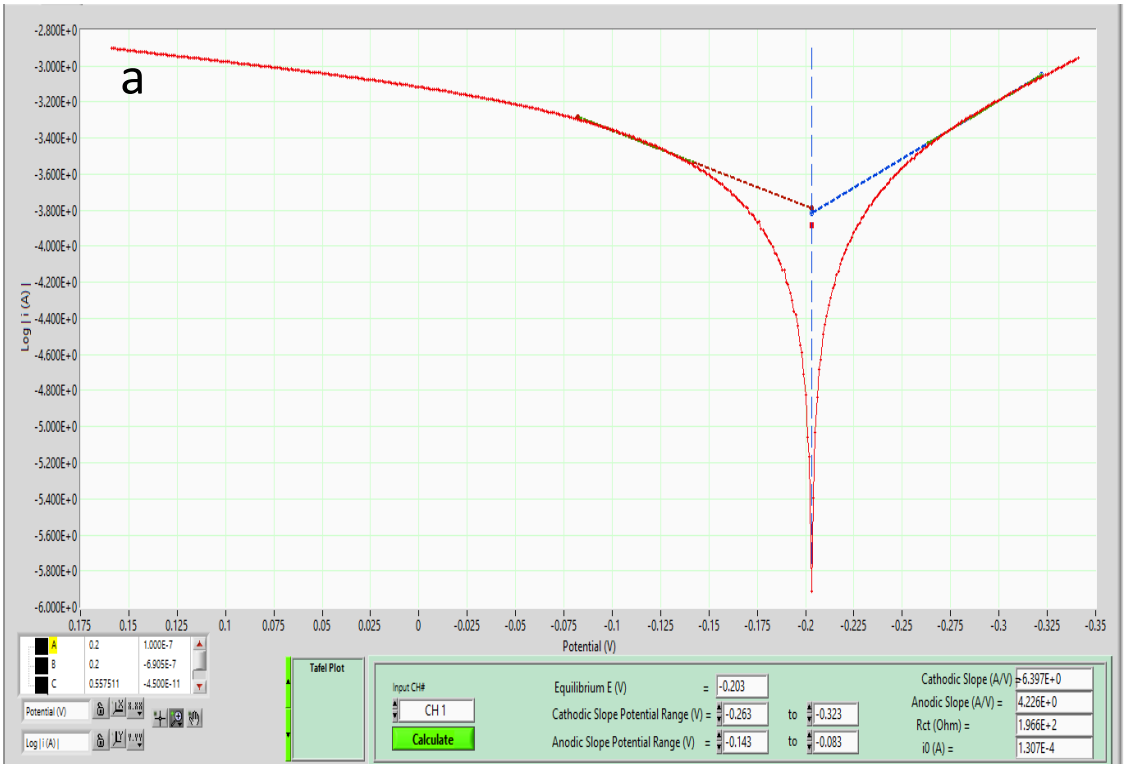
a
Log | i (A) |
Potential (V)
Tafel Plot
Input CH#
CH 1
Calculate
Equilibrium E (V) = -0.203
Cathodic Slope Potential Range (V) = -0.263 to -0.323
Anodic Slope Potential Range (V) = -0.143 to -0.083
Cathodic Slope (A/V) = 6.397E+0
Anodic Slope (A/V) = 4.226E+0
Rct (Ohm) = 1.966E+2
i0 (A) = 1.307E-4

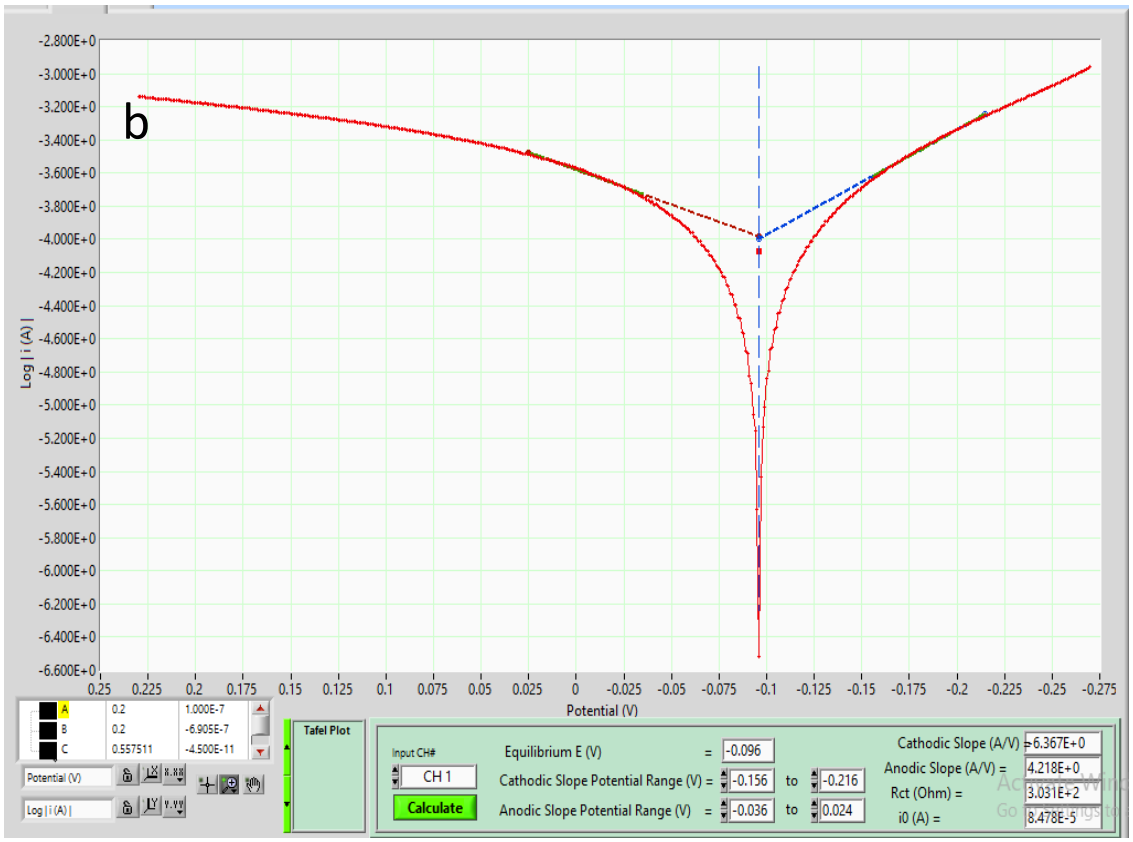
b
Log | i (A) |
Potential (V)
Tafel Plot
Input CH#
CH 1
Calculate
Equilibrium E (V) = -0.096
Cathodic Slope Potential Range (V) = -0.156 to -0.216
Anodic Slope Potential Range (V) = -0.036 to 0.024
Cathodic Slope (A/V) = 6.367E+0
Anodic Slope (A/V) = 4.218E+0
Rct (Ohm) = 3.031E+2
i0 (A) = 8.478E-5

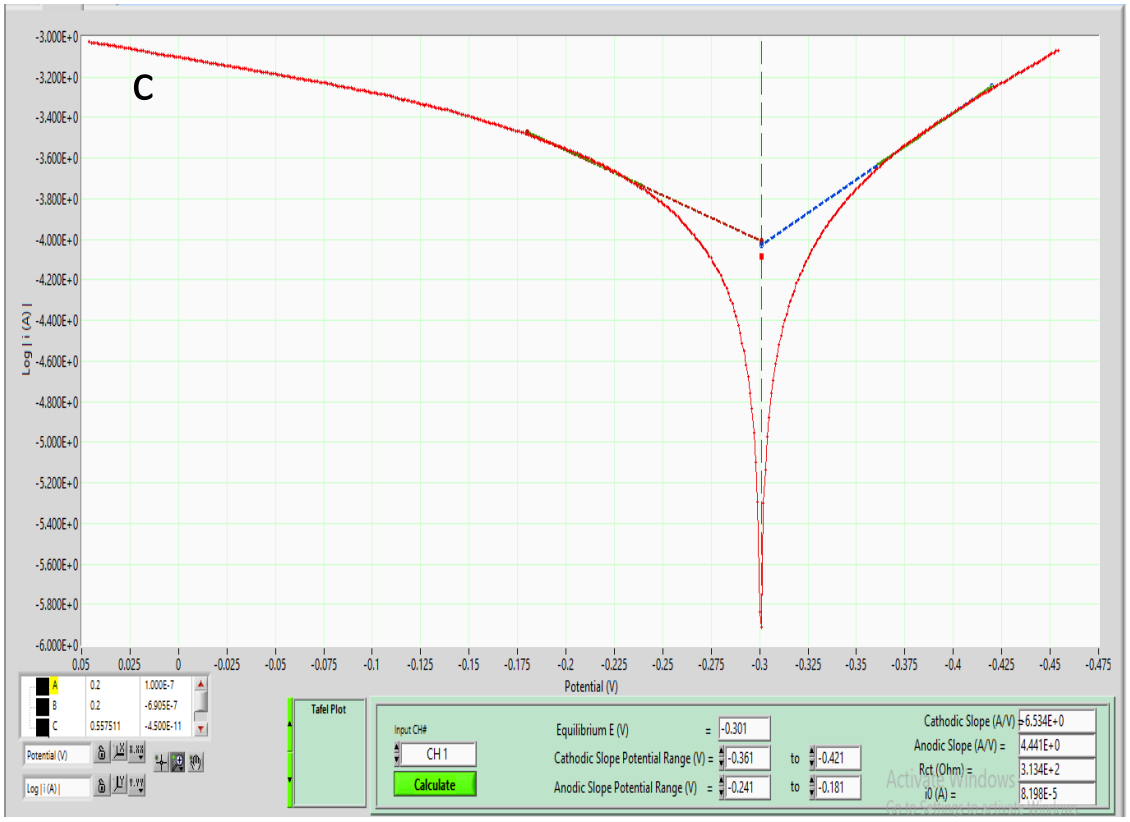
c
Log | i (A) |
Potential (V)
Tafel Plot
Input CH#
CH 1
Calculate
Equilibrium E (V) = -0.301
Cathodic Slope Potential Range (V) = -0.361 to -0.421
Anodic Slope Potential Range (V) = -0.241 to -0.181
Cathodic Slope (A/V) = 6.534E+0
Anodic Slope (A/V) = 4.441E+0
Rct (Ohm) = 3.134E+2
i0 (A) = 8.198E-5

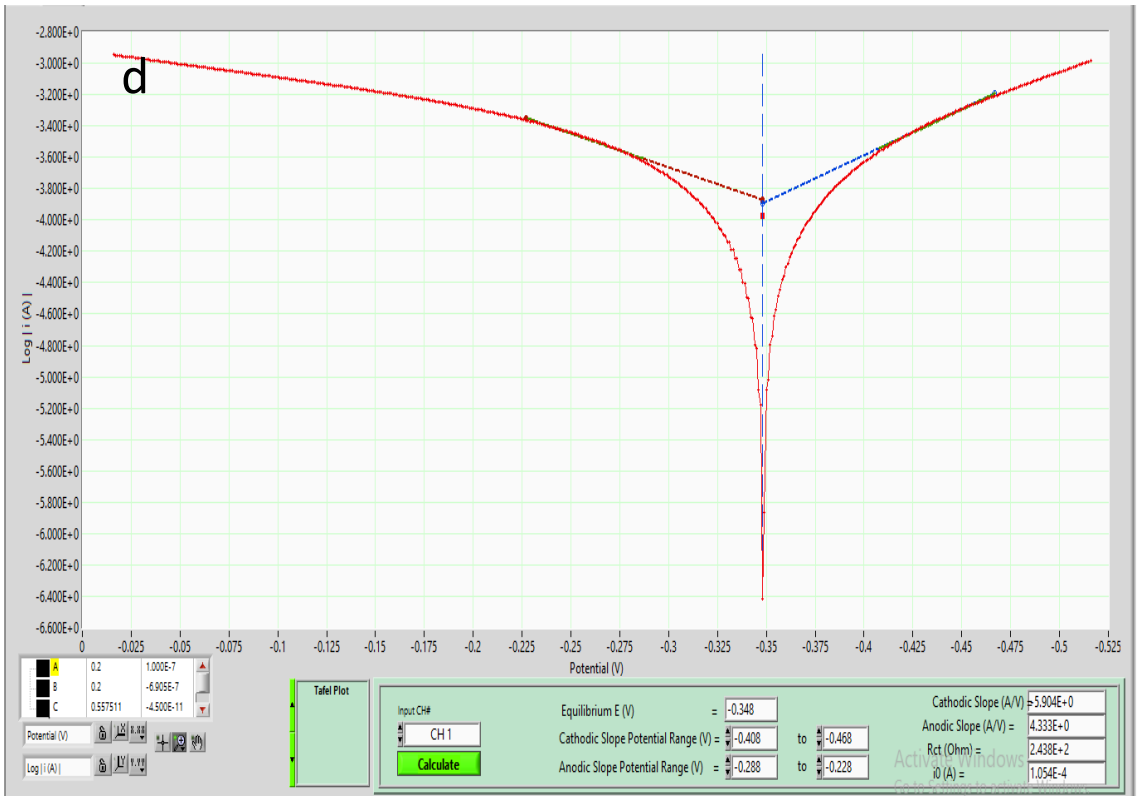
d
Log | i (A) |
Potential (V)
Tafel Plot
Input CH#
CH 1
Calculate
Equilibrium E (V) = -0.348
Cathodic Slope Potential Range (V) = -0.408 to -0.468
Anodic Slope Potential Range (V) = -0.288 to -0.228
Cathodic Slope (A/V) = 5.904E+0
Anodic Slope (A/V) = 4.333E+0
Rct (Ohm) = 2.438E+2
i0 (A) = 1.054E-4

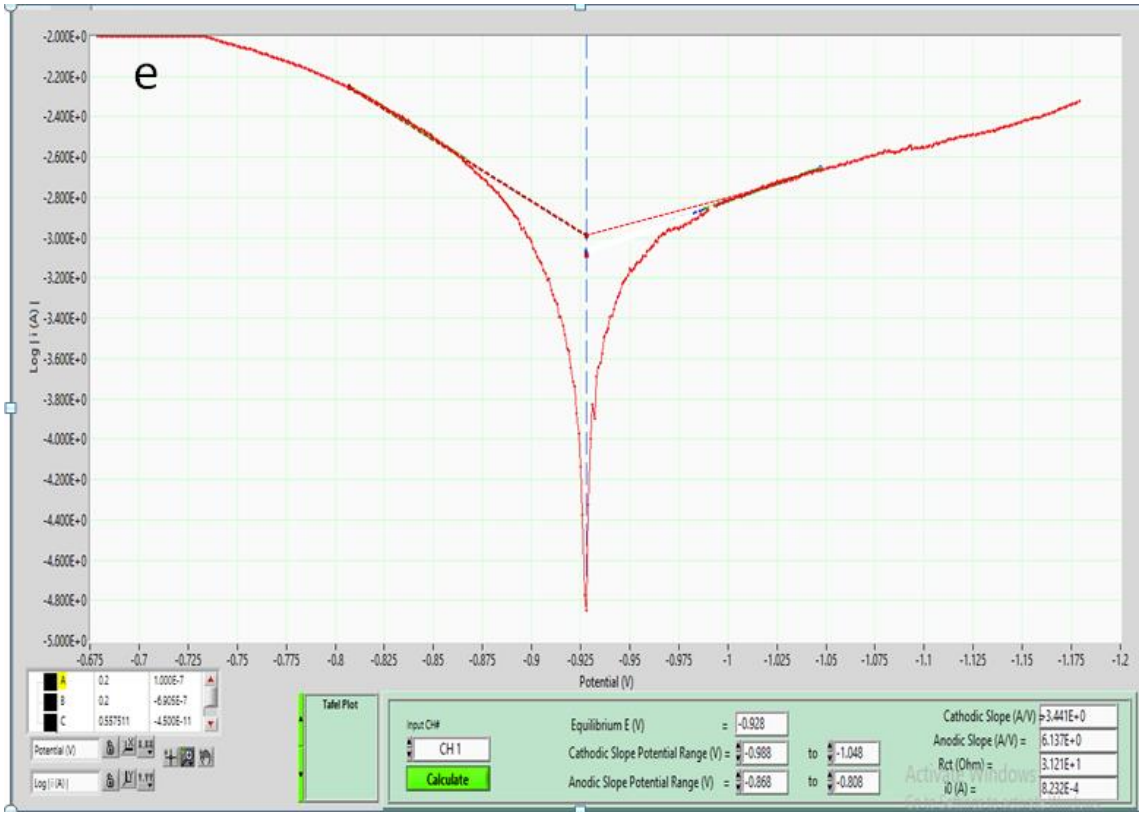
e
Log | i (A) |
Potential (V)
Tafel Plot
Input CH#
CH 1
Calculate
Equilibrium E (V) = -0.928
Cathodic Slope Potential Range (V) = -0.988 to -1.048
Anodic Slope Potential Range (V) = -0.868 to -0.808
Cathodic Slope (A/V) = 3.441E+0
Anodic Slope (A/V) = 6.137E+0
Rct (Ohm) = 3.121E+1
i0 (A) = 8.232E-4

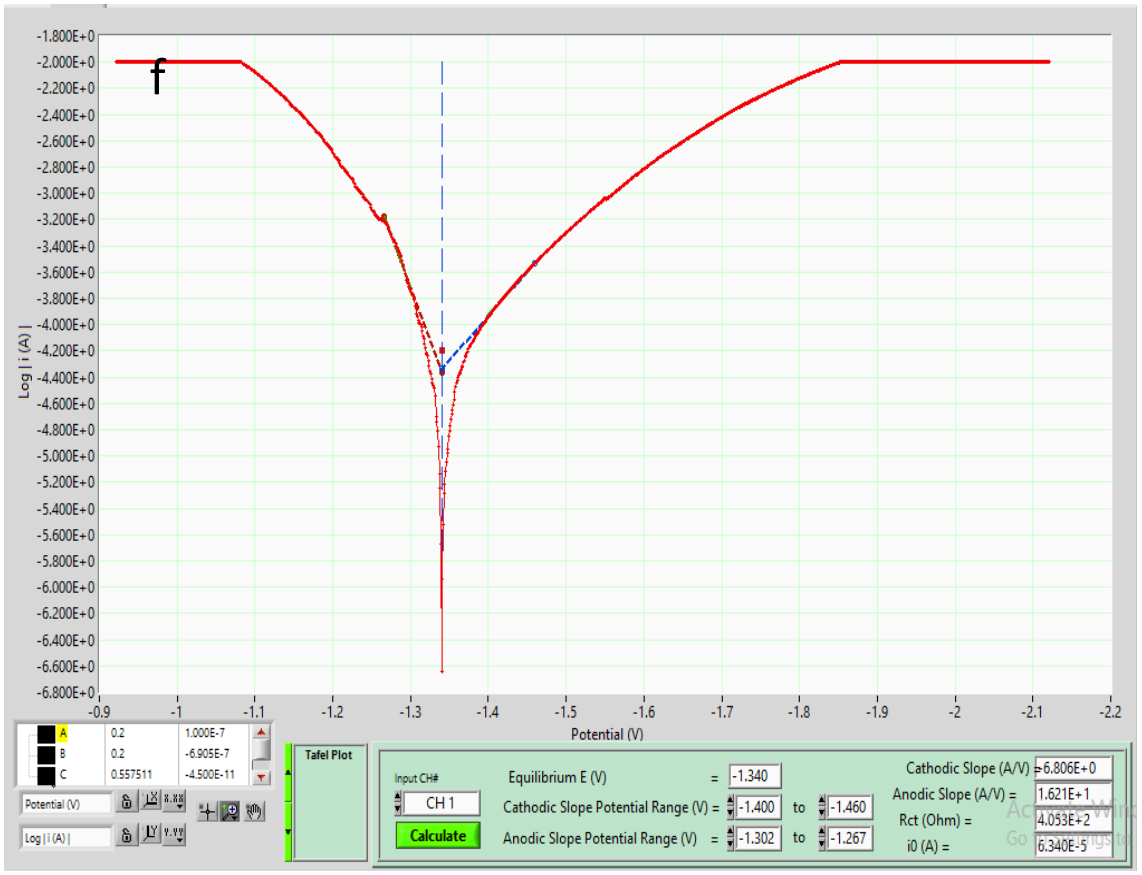
f
Log | i (A) |
Potential (V)
Tafel Plot
Input CH#
CH 1
Calculate
Equilibrium E (V) = -1.340
Cathodic Slope Potential Range (V) = -1.400 to -1.460
Anodic Slope Potential Range (V) = -1.302 to -1.267
Cathodic Slope (A/V) = 6.806E+0
Anodic Slope (A/V) = 1.621E+1
Rct (Ohm) = 4.053E+2
i0 (A) = 6.340E-5

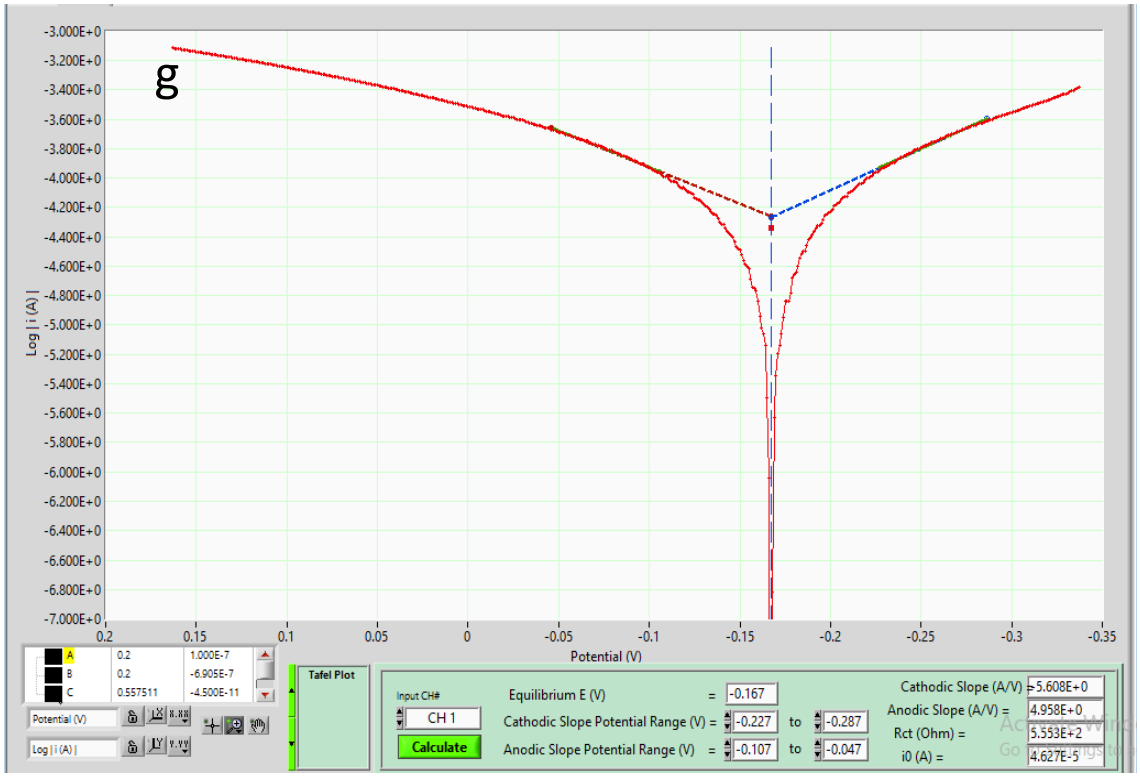
g
Log | i (A) |
Potential (V)
Tafel Plot
Input CH#
CH 1
Calculate
Equilibrium E (V) = -0.167
Cathodic Slope Potential Range (V) = -0.227 to -0.287
Anodic Slope Potential Range (V) = -0.107 to -0.047
Cathodic Slope (A/V) = 5.608E+0
Anodic Slope (A/V) = 4.958E+0
Rct (Ohm) = 5.553E+2
i0 (A) = 4.627E-5

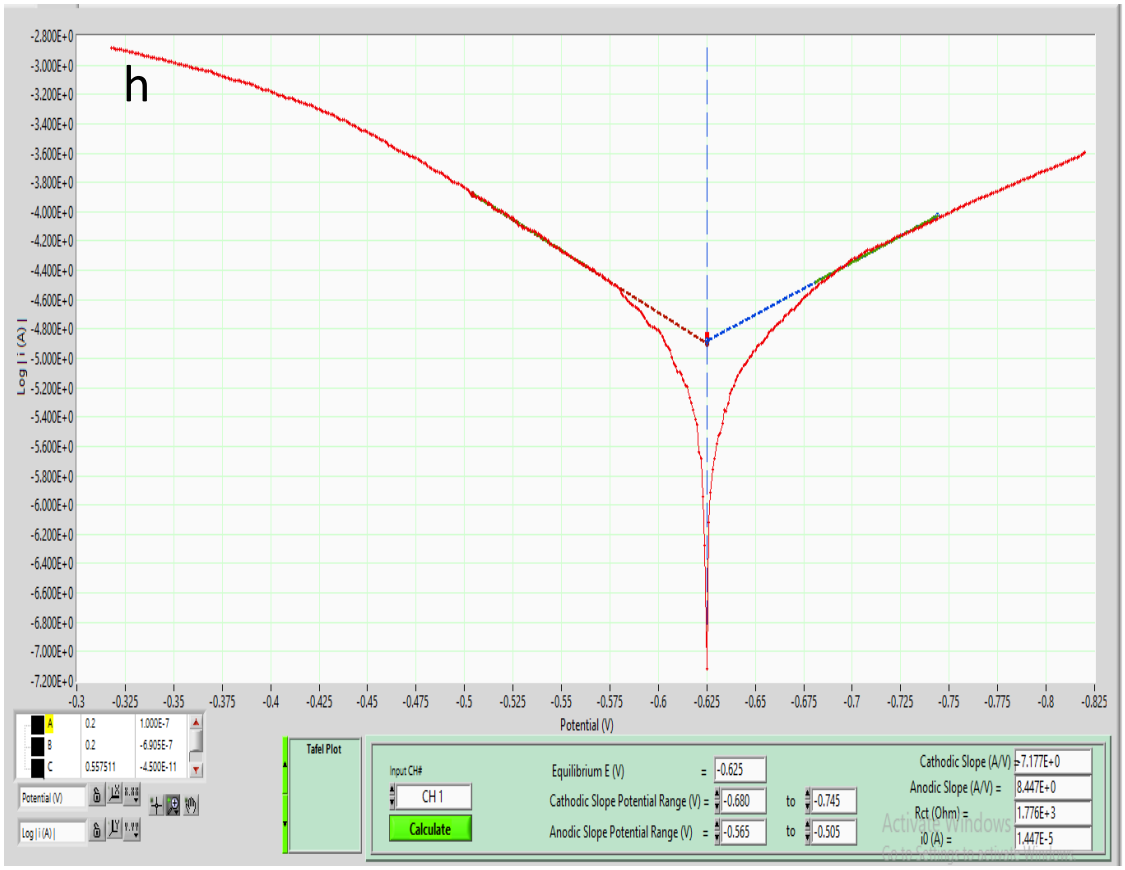
h
Log | i (A) |
Potential (V)
Tafel Plot
Input CH#
CH 1
Calculate
Equilibrium E (V) = -0.625
Cathodic Slope Potential Range (V) = -0.680 to -0.745
Anodic Slope Potential Range (V) = -0.565 to -0.505
Cathodic Slope (A/V) = 7.177E+0
Anodic Slope (A/V) = 8.447E+0
Rct (Ohm) = 1.776E+3
i0 (A) = 1.447E-5

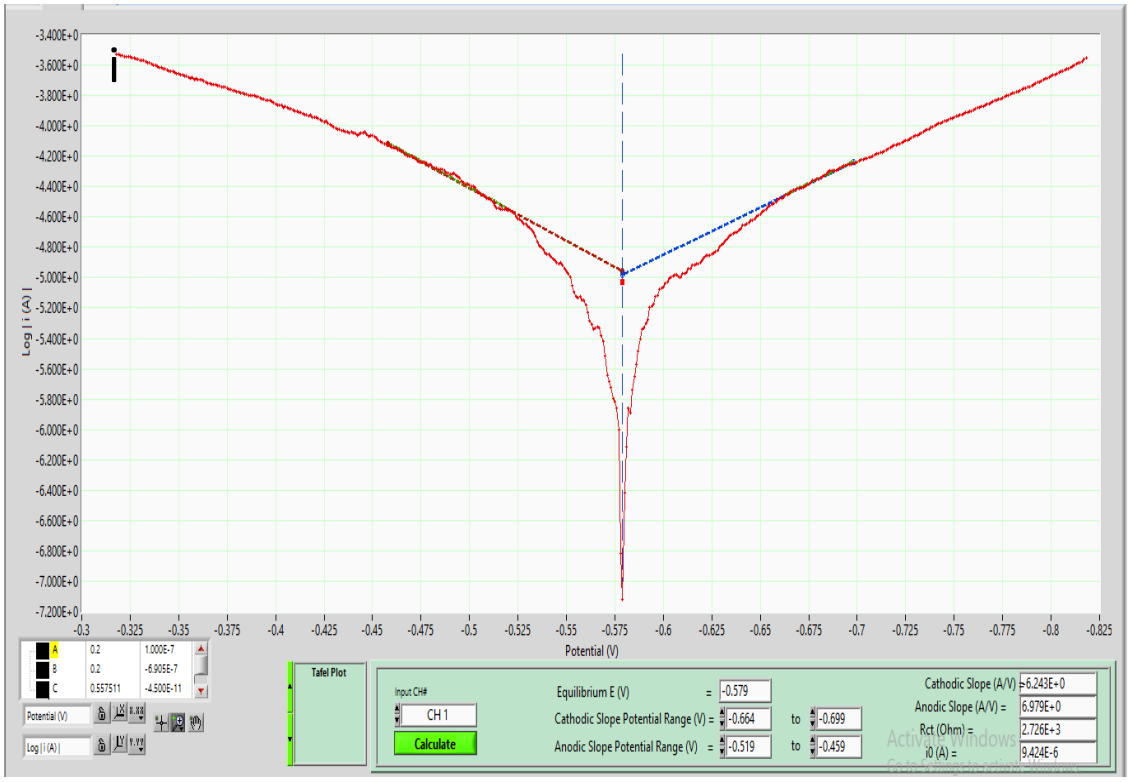

Figure (4.39): polarization of Tafel curves of the (a) substrate, (b) specimen A, (c) specimen B, (d) specimen C, (e) specimen D, (f) specimen E, (g) specimen F, (h) specimen G, and (i) specimen H.

The corrosion resistance increases in the order of MEA and MEA-CNTs. Through comparisons in Figure(4.39c), it can be concluded that specimen B significantly effects with addition of CNTs on the corrosion rate and therefore the P_{eff} as compared with specimen A coatings. In the CNT concentration of 0.2g/100ml, the ($I_{corr.}$) of specimen B composite coating is (81.9µA) and the ($I_{corr.}$) of the specimen A coating is (84.7µA) and the P_{eff} of specimen B improved up to 37.3% for AISI4140; the addition of CNTs makes the coating denser when compared with specimen A; the resistance of the corrosion of composite coating is better which is compatible with the Ref [111].

When the element increase in the alloys as compared with specimen A and became a (5 element), the alloys is called High entropy alloy. This alloys is better than MEAs in corrosion resistance and P_{eff} as shown in the figure (4.38). The best value is achieved when the CNTs' added to HEAs (AlCrFeCoNiCu) specimens, indicating that I_{corr} equal to (9.42 μA) improving the corrosion resistance and P_{eff} . The improved corrosion resistance with addition of CNTs can be attributed to the microstructural evolution of the coating's specimens and the low corrosion resistance of HEA coating without CNTs is due to the compositional segregation which encouraged localized corrosion as agreed with Ref [100].

4.5.1.3 Cycle Polarization Test

The parameters obtained from the current-voltage curve can be associated with the localized corrosion mechanism. Typically, the reading starts at the open circuit potential and scans upwards until breakdown is attained. Then the direction of scan is inverted after specific amount of localized corrosion is established and the passive film is damaged [134]. The potential at which stable pit formed is called breakdown potential (E_b) or pitting potential (E_{pit}). Consequently, the E_{pit} implies the potential over which the pits initiated and developed. If the E_{pit} is high, the material has high resistance to the pitting corrosion. The difference (ΔE) between E_p and E_{prot} will give an indication to the corrosion resistance of the specimen, where the smaller ΔE value mean the highest corrosion resistance.

Figures (4.40-4.41) show the polarization curves for specimens (0 & H) in 3.5% NaCl solution. Significant differences were observed between the curves obtained for each specimen. For substrate specimen, has the lowest E_p and E_{prot} value compared to the susceptibility to pitting corrosion

of the specimen H. The cyclic polarization curves obtained as noted in the Table (4.25), the extent of the hysteresis loop is highly reduced and therefore, the corrosion mechanism operating on the substrate surface is less active when coating.

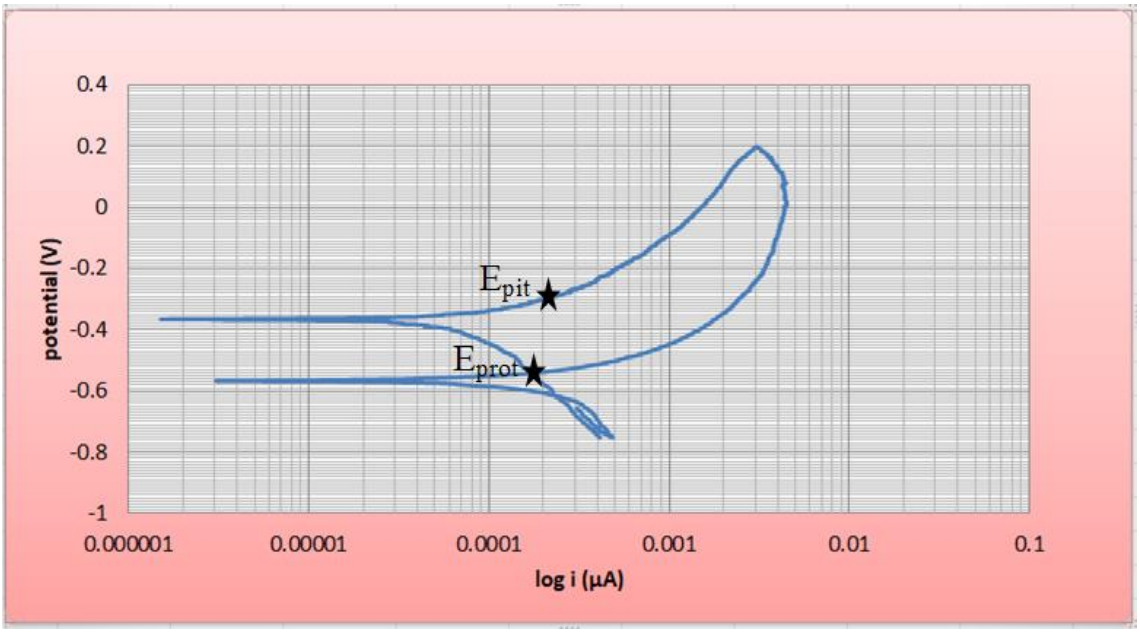

Figure (4.40): Cycle polarization curves of substrate specimen.

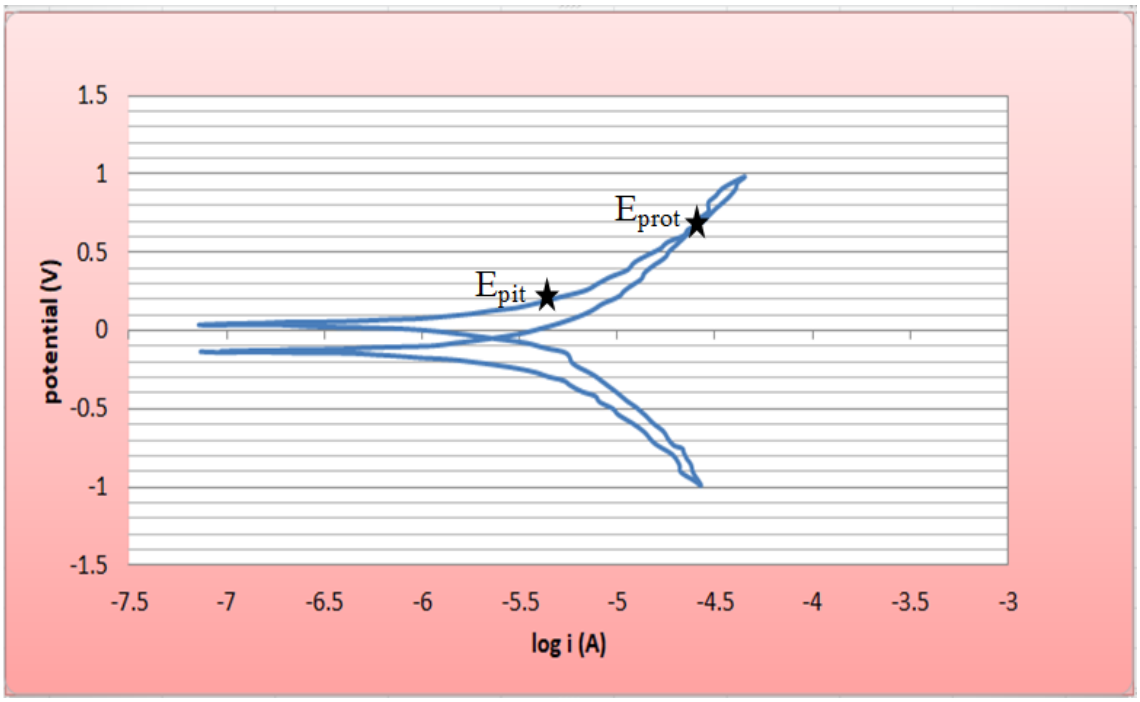

Figure (4.40): Cycle polarization curves of specimen H .

Table (4.25): Values of electrochemical parameters of specimen 0 &H in NaCl solution from cyclic polarization

Specimen code	$E_{pit.}$ (mV)	E_{prot} (mV)	$\Delta E = (E_{pit} - E_{prot})$ (mV)	Improvement percentage (%) $=100^* (\Delta E_0 - \Delta E_H)/ \Delta E_O$
0	-0.3	-0.53	0.23	0
H	0.2	0.7	-0.5	317

Figures (4.40-41) pitting potential (E_{pit}) was determined from the cyclic polarization tests in the specimen H composite coating in NaCl solution. The lowest value of ΔE and current density for the specimen coated with addition CNTs and increased E_{pit} show that improvement percentage is 542% for specimen H. Therefore, based on the results from the cyclic polarization curves, it is suppose that coating layer of specimen H has a strong ability to act as barrier to prevent the localized corrosion attack of aggressive ions of NaCl solution during the corrosion test.

4.6 The Results of All Tests:

The table (4.26) listed the results of all tests which explained that the Specimen H is the best specimen coating.

Table (4.26): The Results of All Specimen Coating Tests.

Specimen Code/ Tests	O	A	B	C	D	E	F	G	H
Thickness(µm)	……	10.83	10.57	10.68	10.19	14.6	13.71	18.36	17.48
Ra (µ)	0.19	0.35	0.32	0.33	0.31	0.29	0.27	0.28	0.24
Microhardness (HV)	189	234	498	319	729	267	683	366	783
Wear Rate $*10^{-4}$ at 5N	1.3	1	0.95	0.87	0.75	0.49	0.4	0.8	0.3
Wear Rate $*10^{-4}$ at 10N	3.6	2.5	2	1.6	1.9	1.2	1.2	1	0.4
Protective efficiency %	**…..**	35.2	37.3	19.4	37	51.5	65	88.9	92.8
Corrosion Rate (mpy)	14.5	12	11.2	13	9.6	9.1	12	1.8	1.15
Adhesion Test (MPa)	34.6	10.8	11.4	11.7	12.2	15.2	16.4	19.8	21.5
Contact angel (θ)	81.5	26	28	35	40	43	46	69.7	77

4.7 Verification of HEAs

In this study, the presence of HEAs forming the coating deposited on the surface of 4140 grade low alloy steel was verified by:

- The presence of individual solid solutions, as well as the absence of inter-metallic compounds, the absence of free elements on the surface of the coating, in addition to what was mentioned, and the presence of all components of the alloy in the EDS test. The formation of HEAs alloy was confirmed by XRD test, as it was proven that there are no free elements or any phases or interfacial compounds in the XRD patterns of the resulting coating when compared with the standard charts for the constituent elements of HEAs alloy.
- It was also confirmed mathematically that the formation of HEAs was calculated by calculating the change in the mixing entropy in equation 4.10, as the equiatomic alloy is of high entropy when ΔS_{mix} is higher than 1.61R, where R is the general constant for gases as shown in Table (4-15) and the mathematical calculations below of non-equiatomic element, which confirms the deposition of the coating is in the form of a high entropy alloy.

Chapter Five :

Conclusions & Recommendations

CHAPTER FIVE: CONCLUSIONS & RECOMMENDATIONS

5.1 Conclusions:

From the obtained results and their discussion several conclusions may be drawn as follows:

1. The increase in the deposition current density leads to the formation of higher internal stresses in the thin films.
2. The coating specimen of -D- is the stronger as compared with the other specimens which thickness equal to (10.19) μm.
3. The surface morphology for the coated specimens is dense, uniform and homogeneous with granular grains that became finer when adding the CNTs.
4. The microstructure of specimen -A- has two distinct phases, one containing Ni, Co and Fe while other with high concentration of Cu.
5. CNTs addition lead to a decrease in the crystallite size.
6. The specimen -G- exhibit better particle growth and distribution compared to specimen -C-.
7. The EDS test of coatings surface emphasize of containing all the constituent components of the alloys coating.
8. A mixture of BCC and FCC phases observed in the XRD pattern of specimens coating.
9. The surface of specimen -A- was the rough surface that leading to lower contact angle as compared to the other specimens.
10. With addition of CNTs, the hardness increased as 2.5 times higher than the HEAs without CNTs.

11. The best value of corrosion rate for specimen –H- composite coating which equals to 1.15 mpy and the protective efficiency was enhanced for this composite coating by 92.8%.
12. Specimen -H- composite coating show the best result of adhesion and wear tests as compared with the other specimens.
13. The specimen -E- is the stable high entropy alloy because of having a higher molar entropies of mixing.

5.2 Recommendations

The following suggestions for future works may be taken into consecration:

1. Studying the other high-entropy alloy systems.
2. Studying other tests rather than those studied for HEAs, such as the fatigue test.
3. Study and preparation of high entropy alloys as bulk.
4. studying the deposition of high entropy alloys on different metals such as carbon steel.
5. Conducting a TEM assay to verify the resulting crystal systems

Chapter Six:

References

References

References

[1] V. E. Gromov, S. V Konovalov, Y. F. Ivanov, and K. A. Osintsev, *Structure and Properties of High-Entropy Alloys*, 1st ed. Switzerland: Springer, 2021.

[2] S. Chikumba and V. V. Rao, "High Entropy Alloys: Development and Applications," doi: 10.15242/iie.e1115005.

[3] S. Praveen and H. S. Kim, "High-Entropy Alloys: Potential Candidates for High-Temperature Applications – An Overview," *Adv. Eng. Mater.*, vol. 20, no. 1, pp. 1–22, 2018, doi: 10.1002/adem.201700645.

[4] D. B. Miracle, J. D. Miller, O. N. Senkov, C. Woodward, M. D. Uchic, and J. Tiley, "Exploration and development of high entropy alloys for structural applications," *Entropy*, vol. 16, no. 1, pp. 494–525, 2014, doi: 10.3390/e16010494.

[5] B. S. J. W. Y. . S. R. Murty, *High-Entropy Alloys*. 2014.

[6] J. William D. Callister and Department, *Fundamentals of Materials Science and Engineering An Interactive*. John Wiley, 2001.

[7] B. Cantor, I. T. H. Chang, P. Knight, and A. J. B. Vincent, "Microstructural development in equiatomic multicomponent alloys," *Mater. Sci. Eng. A*, vol. 375–377, no. 1-2 SPEC. ISS., pp. 213–218, 2004, doi: 10.1016/j.msea.2003.10.257.

[8] J.-W. Yeh, "Nanostructured high-entropy alloys with multiple principal elements: Novel alloy design concepts and outcomes.," *Adv. Eng. Mater.*, vol. 6, no. 5, pp. 299–303, 2004.

[9] Y. Zhang *et al.*, "Microstructures and properties of high-entropy alloys," *Prog. Mater. Sci.*, vol. 61, no. October 2013, pp. 1–93, 2014,

References

doi: 10.1016/j.pmatsci.2013.10.001.

[10] M. C. Gao, P. K. Liaw, J. W. Yeh, and Y. Zhang, *High-entropy alloys: Fundamentals and applications*. 2016.

[11] U. G. and J. B. S. Singha, N. Wanderka*a, B.S. Murtyb, "Decomposition in Multi-component AlCoCrCuFeNi High Entropy Alloy S. Singh," *Acta Mater*, vol. 59, no. 1, pp. 182–190, 2011.

[12] P. K. L. H. Y. Diao, R. Feng, K. A. Dahmen, "Fundamental Deformation Behavior in High-Entropy Alloys: An Overview," *Elsevier user Licens.*, no. 3, pp. 321–329, 2017, doi: 10.7868/80424857017030112.

[13] W. Guo, W. Dmowski, J. Y. Noh, P. Rack, P. K. Liaw, and T. Egami, "Local atomic structure of a high-entropy alloy: An X-Ray and neutron scattering study," *Met. Mater. Trans. A*, vol. 44, no. 5, pp. 1994–1997, 2012, doi: 10.1007/s11661-012-1474-0.

[14] Y. Zhang, *High-Entropy Materials-A Brief Introduction*, vol. 113, no. 9. 2019.

[15] J.-W. Y. W.-R. Wang, W.-L. Wang, S.-C. Wang, Y.-C. Tsai, C.-H. Lai, "Effects of Al addition on the microstructure and mechanical property of AlxCoCrFeNi high-entropy alloys," *Intermetallics*, vol. 26, pp. 44–51, 2012.

[16] J. W. Y. W. R. Wang, W. L. Wang, "Phases, microstructure and mechanical properties of AlxCoCrFeNi high-entropy alloys at elevated temperatures," *J. Alloy. Compd.*, vol. 589, pp. 143– 152, 2014.

[17] Cantor, *Multicomponent and high entropy alloys. Entropy :*, vol. 16. 2014.

References

[18] Y. Z. Zhang, W., P.K. Liaw, "Science and technology in high-entropy alloys.," *Sci. China Mater.*, vol. 61, no. 1, pp. 2–22, 2018.

[19] Z. Li, S. Zhao, R. O. Ritchie, and M. A. Meyers, "Mechanical properties of high-entropy alloys with emphasis on face-centered cubic alloys," *Prog. Mater. Sci.*, vol. 102, pp. 296–345, 2019.

[20] S. Ranganathan, "Alloyed pleasures: Multimetallic cocktails," *Curr. Sci.*, vol. 85, no. 10, pp. 1404–1406, 2003.

[21] F. D. C. Garcia Filho, R. O. Ritchie, M. A. Meyers, and S. N. Monteiro, "Cantor-derived medium-entropy alloys: bridging the gap between traditional metallic and high-entropy alloys," *J. Mater. Res. Technol.*, vol. 17, pp. 1868–1895, 2022.

[22] W. Jiang, Y. Zhu, and Y. Zhao, "Mechanical Properties and Deformation Mechanisms of Heterostructured High-Entropy and Medium-Entropy Alloys: A Review," *Front. Mater.*, vol. 8, no. January, pp. 1–17, 2022.

[23] I. S. Aristeidakis, M.- Ioanna, and T. Tzini, "High Entropy Alloys," University of Thessaly Department of Mechanical Engineering, Laboratory of Materials High, 2016.

[24] Y. Zhang, T. Beijing, and Q. Xing, "High Entropy Alloys-Manufacturing Routes," *Encycl. Mater. Met. Alloy.*, no. May, pp. 0–12, 2020, doi: 10.1016/B978-0-12-819726-4.12123-4.

[25] S. Syed Ghazi and K. R. Ravi, "Phase-evolution in high entropy alloys: Role of synthesis route," *Intermetallics*, vol. 73, pp. 40–42, 2016, doi: 10.1016/j.intermet.2016.03.002.

[26] J. O. N. Senkov, J. M. Scott, S. V. Senkova, D. B. Miracle, and C. F. Woodward, "Microstructure and room temperature properties of a high-entropy TaNbHfZrTi alloy," *Alloy. Compd.*, vol. 509, no. 20, pp.

References

1–17, 2011.

[27] C. Ng *et al.*, “Phase stability and tensile properties of Co-free Al0.5CrCuFeNi2 high-entropy alloys,” *J. Alloys Compd.*, vol. 584, pp. 530–537, Jan. 2014, doi: 10.1016/J.JALLCOM.2013.09.105.

[28] S. M. . D.A. Porter, K.. Easterling, *Phase transformation in metals and alloys*, 3rd ed. CRC Press, 2009.

[29] *ASM Metals Reference Book*, 2nd ed. American Society for Metals, Metals Park, OH, 1984.

[30] T. S. S. and M. Gupta, *High Entropy Alloys Innovations, Advances, and Applications*, 1st ed. Taylor & Francis Group, 2020.

[31] Y. W. • H. D. • Y. Gan, Ed., *Advanced Steels*, 1st ed. Metallurgical Industry Press, 2011.

[32] R. Tuttle, *Alloy Steels*, 1st ed. USA, 2018.

[33] S. Papavinasam, *Corrosion Control in the Oil and Gas Industry: ch 3 Materials*. Ottawa, Ontario, Canada: CorrMagnet Consulting Inc., 2014.

[34] A. I. H. Committee, Ed., *ASM handbook volume 1 : Properties and Selection: Irons, Steels, and High-Performance Alloys*, 10th ed. 1990.

[35] “GRADE GUIDE: AISI 4140 STEEL,” *Metal Supermarkets*, 2018. https://www.metalsupermarkets.com/grade-guide-4140-steel/.

[36] J. W. Yeh, “Alloy design strategies and future trends in high-entropy alloys,” *Jom*, vol. 65, no. 12, pp. 1759–1771, 2013, doi: 10.1007/s11837-013-0761-6.

[37] J. W. Yeh, “Recent progress in high-entropy alloys,” *Ann. Chim. Sci. des Mater.*, vol. 31, no. 6, pp. 633–648, 2006, doi:

References

10.3166/acsm.31.633-648.

[38] W. Liu *et al.*, “High performance DLC/BP and ZnS/YbF3 double-layer protective and antireflective coatings,” *J. Alloys Compd.*, vol. 581, pp. 526–529, 2013, doi: 10.1016/j.jallcom.2013.07.130.

[39] K. Tsai, M. Tsai, and J. Yeh, “Sluggish diffusion in Co – Cr – Fe – Mn – Ni high-entropy alloys,” *Acta Mater.*, vol. 61, no. 13, pp. 4887–4897, 2013, doi: 10.1016/j.actamat.2013.04.058.

[40] A. Sharma, “High Entropy Alloy Coatings and Technology,” *Coatings*, vol. 11, no. 4, p. 372, 2021.

[41] J. Li, Y. Huang, X. Meng, and Y. Xie, “A Review on High Entropy Alloys Coatings : Fabrication Processes and Property Assessment,” vol. 1900343, no. 92, pp. 1–27, 2019, doi: 10.1002/adem.201900343.

[42] *ASM Handbook Volume 18: Friction, Lubrication, and Wear Technology*. 1992.

[43] A. A. Frank Endres, Douglas MacFarlane, *Electrodeposition from Ionic Liquids*. WILEY-VCH Verlag GmbH & Co. KGaA, 2015.

[44] A. S. M. International and H. Committee, Eds., *ASM Metals Handbook Volume 13, Corrosion*. 1987.

[45] P. M. Martin, *Handbook of Deposition Technologies for Films and Coatings*, 3rd Edi. Noyes Publication, 2010.

[46] D. R. Gabe, *Electrodepositlon: the materials science of coatings and substrates*, vol. 28, no. 2. 2013.

[47] M. Schlesinger and M. Paunovic, *Fundamentals of Deposition*. 2006.

[48] A. Brenner and S. Senderoff, “Electrodeposition of Alloys,” *J. Electrochem. Soc.*, vol. 111, no. 2, p. 34C, 1964, doi:

10.1149/1.2426105.

[49] D. Ramimoghadam, S. Bagheri, and S. B. A. Hamid, “Progress in electrochemical synthesis of magnetic iron oxide nanoparticles,” *J. Magn. Magn. Mater.*, vol. 368, pp. 207–229, 2014, doi: 10.1016/j.jmmm.2014.05.015.

[50] M. Schlesinger and M. Paunovic, *Fundamentals of electrochemical deposition*, 2nd ed. 2006.

[51] N. Kanani., *Electroplating. Basic Principles, Processes and Practice*, 1st edditi. Germany: Elsevier, 2004.

[52] V. F. C. Lins, E. S. Cecconello, and T. Matencio, “Effect of the current density on morphology, porosity, and tribological properties of electrodeposited nickel on copper,” *J. Mater. Eng. Perform.*, vol. 17, no. 5, pp. 741–745, 2008, doi: 10.1007/s11665-008-9205-9.

[53] A. J. Avila, “Pulsed Electrodeposition of Alloys.,” *Theory Pr. Pulse Plat.*, vol. I, pp. 189–208, 1986.

[54] Y. D. G. • G. Zangari and Theory, *Theory and Practice of Metal Electrodeposition*. 2011.

[55] H. Jyoti Biswal, P. R. Vundavilli, and A. Gupta, “Investigations on the effect of electrode gap variation over pulse-electrodeposition profile,” *IOP Conf. Ser. Mater. Sci. Eng.*, vol. 653, no. 1, 2019, doi: 10.1088/1757-899X/653/1/012046.

[56] Y. Guo, X. Shang, and Q. Liu, “Microstructure and properties of in-situ TiN reinforced laser cladding CoCr2FeNiTix high-entropy alloy composite coatings,” *Surf. Coatings Technol.*, vol. 344, no. 2017, pp. 353–358, 2018, doi: 10.1016/j.surfcoat.2018.03.035.

[57] X. Li *et al.*, “Influence of NbC particles on microstructure and

mechanical properties of AlCoCrFeNi high-entropy alloy coatings prepared by laser cladding," *J. Alloys Compd.*, vol. 788, pp. 485–494, 2019, doi: 10.1016/j.jallcom.2019.02.223.

[58] J. Cheng, D. Liu, X. Liang, and Y. Chen, "Evolution of microstructure and mechanical properties of in situ synthesized TiC-TiB2/CoCrCuFeNi high entropy alloy coatings," *Surf. Coatings Technol.*, vol. 281, pp. 109–116, 2015, doi: 10.1016/j.surfcoat.2015.09.049.

[59] B. Cantor, I. T. H. Chang, P. Knight, and A. J. B. Vincent, "Microstructural development in equiatomic multicomponent alloys," vol. 377, pp. 213–218, 2004, doi: 10.1016/j.msea.2003.10.257.

[60] O. N. Senkov, G. B. Wilks, J. M. Scott, and D. B. Miracle, "Mechanical properties of Nb25Mo25Ta 25W25 and V20Nb20Mo 20Ta20W20 refractory high entropy alloys," *Intermetallics*, vol. 19, no. 5, pp. 698–706, 2011, doi: 10.1016/j.intermet.2011.01.004.

[61] S. L. Soo Young Lee, Seokyeong Byeon, Hyoung Seop Kim, Hyungyu Jiny, "Deep learning-based phase prediction of high-entropy alloys: Optimization, generation, and explanation," *Mater. Des.*, pp. 1–48, 2020, [Online]. Available: https://doi.org/10.1016/j.surfcoat.2020.126156.

[62] M. J. Chae, A. Sharma, M. C. Oh, and B. Ahn, "Lightweight AlCuFeMnMgTi High Entropy Alloy with High Strength-to-Density Ratio Processed by Powder Metallurgy," *Met. Mater. Int.*, vol. 27, no. 4, pp. 629–638, 2021, doi: 10.1007/s12540-020-00823-5.

[63] G. G. B. A.D Pogrebnjak, V.M. Beresnev, K.V. Smyrnova, Ya.O. Kravchenko, P.V. Zukowski, "The influence of nitrogen pressure on the fabrication of the two-phase superhard nanocomposite

References

(TiZrNbAlYCr)N coatings," *Mater. Lett.*, pp. 2–10, 2017, [Online]. Available: https://doi.org/10.1016/j.matlet.2017.09.121.

[64] C. C. Hongxia Wana, Dongdong Songb, Xiaolei Shia, Yong Caia, Tingting Lia, "Corrosion behavior of Al0.4CoCu0.6NiSi0.2Ti0.25 high-entropy alloy coating via 3D printing laser cladding in a sulphur environment," *J. Mater. Sci. Technol.*, vol. 1, no. 1, pp. 1–6, 2020.

[65] P. J. Barron, A. W. Carruthers, J. W. Fellowes, N. G. Jones, H. Dawson, and E. J. Pickering, "Towards V-based high-entropy alloys for nuclear fusion applications," *Scr. Mater.*, vol. 176, pp. 12–16, 2020, doi: 10.1016/j.scriptamat.2019.09.028.

[66] L. Tian, Z. Feng, and W. Xiong, "Microstructure, microhardness, and wear resistance of AlCoCrFeNiTi/Ni60 coating by plasma spraying," *Coatings*, vol. 8, no. 3, 2018, doi: 10.3390/coatings8030112.

[67] Y. Ma, Y. Ma, Q. Wang, and B. Breitung, "Environmental Science High-entropy energy materials : challenges and," pp. 2883–2905, 2021, doi: 10.1039/d1ee00505g.

[68] J. Talbot, "Corrosion Science and Technology." CRC Press LLC, 1998.

[69] H. H. Uhlig and R. W. Revie, *Corrosion and corrosion control. An introduction to corrosion science and engineering.*, Third Edit. Canada: A JOHN WILEY & SONS, 1985.

[70] G. S. Frankel, "Pitting Corrosion of Metals: A Review of the Critical Factors," *J. Electrochem. Soc.*, vol. 145, no. 6, pp. 2186–2198, Jun. 1998, doi: 10.1149/1.1838615.

[71] W. Yongqiang, S. Hao, L. Na, X. Yanhao, and J. Hemin, "Effect of sigma phase precipitation on the pitting corrosion mechanism of duplex stainless steels," *Int. J. Electrochem. Sci.*, vol. 13, no. 10, pp.

References

9868–9887, 2018, doi: 10.20964/2018.10.38.

[72] A. F. and K. Bobzin, *Friction, Wear and Wear Protection*. Germany, 2011.

[73] DONALD H. BUCKLEY, *Surface effects in adhesion, friction, wear and lubrication*, vol. 85, no. 2. ELSEVIER, 1983.

[74] G. W. Stachowiak, *WEAR – MATERIALS, MECHANISMS AND PRACTICE*. John Wiley & Sons, 2005.

[75] J. R. Davis, *Surface Engineering for Corrosion and Wear Resistance*, vol. 51, no. 1. 2004.

[76] F. Léonard, *The Physics of carbon nanoTube Devices*. William andrew inc., 2009.

[77] C. Hierold, *Carbon Nanotube Devices*, vol. 8. WILEY-VCH Verlag GmbH & Co. KGaA, 2008.

[78] P. J. F. HARRIS, *Carbon Nanotube Science: Synthesis, Properties and Applications Carbon*. University ofReading, UK: CAMBRIDGE UNIVERSITY PRESS, 2009.

[79] E. Dervishi *et al.*, "Carbon nanotubes: Synthesis, properties, and applications," *Part. Sci. Technol.*, vol. 27, no. 2, pp. 107–125, 2009, doi: 10.1080/02726350902775962.

[80] K. T. and V. D. Aravind Kumar Jagadeesan, *Carbon Nanotubes: Synthesis, Properties and Applications*. Century Surface Science - a Handbook, 2020.

[81] W. Contributors, "Gelatin," *Wikipedia, The Free Encyclopedia*, 2021. https://en.wikipedia.org/w/index.php?title=Gelatin&oldid=1046975069 (accessed Sep. 11, 2021).

References

[82] G. H. Jerffery; J. Bassett; J. Mendham; R. C. Denney, *Colorimetry and Spectrophotometry*, 5th Editio. Vogel's Textbook of Quantitative Chemical Analysis Longman, 1989.

[83] Wikipedia contributors, "Chemistry of ascorbic acid," *In Wikipedia, The Free Encyclopedia*, 2021. https://en.wikipedia.org/w/index.php?title=Chemistry_of_ascorbic_acid&oldid=1044948160 (accessed Oct. 02, 2021).

[84] A. R. Allen, A. H.; Tankard, *The Determination of Boric Acid in Cider, Fruits, etc*. Analyst, 1904.

[85] Roman M. Balabin, "Polar (Acyclic) Isomer of Formic Acid Dimer: Gas-Phase Raman Spectroscopy Study and Thermodynamic Parameters," *J. Phys. Chem. A*, vol. 113, no. 17, pp. 4910–8, 2009, doi: 10.1021/jp9002643.

[86] H. Reutemann, Werner; Kieczka, *Formic Acid*. Ullmann's Encyclopedia of Industrial Chemistry, 2000.

[87] ed Haynes, William M., *CRC Handbook of Chemistry and Physics*, 92nd ed. Boca Raton, FL: CRC Press, 2011.

[88] S. S. Zumdahl, *Chemical Principles*, 6th Ed. Houghton Mifflin Company, 2009.

[89] E. C. Donaldson and W. Alam, *Wettability*. 2013.

[90] K.L. Mittal, *Advances in Contact Angle, Wettability and Adhesion Volume 4*. USA: Wiley, 2019.

[91] K. L. Mittal, *Contact Angle, Wettability and Adhesion Volume 6*, vol. 6. 2010.

[92] Y. Hsu, W. Chiang, and J. Wu, "Corrosion behavior of FeCoNiCrCu x high-entropy alloys in 3 . 5 % sodium chloride solution," vol. 92,

pp. 112–117, 2005, doi: 10.1016/j.matchemphys.2005.01.001.

[93] C. Tsai, J. Yeh, and P. Lee, “Effect of the substitution of Co by Mn in Al-Cr-Cu-Fe-Co-Ni high-entropy alloys,” no. December, 2006, doi: 10.3166/acsm.31.685-698.

[94] A. Manzoni and N. W. , H. Daoud , R.V¨olkl , U. Glatzel, “Phase separation in equiatomic AlCoCrFeNi high-entropy alloy,” *Ultramicroscopy*, pp. 10–13, 2013.

[95] L. Y. Maosheng Zheng, Yang Li, Jun Hu , Yuan Zhao, “Preparation of high entropy alloy thin film fenicobimn by electroplating deposition method,” *Mater. Sci.*, vol. 11, no. 10, pp. 344–348, 2014.

[96] V. Soare *et al.*, “Electrochemical deposition and microstructural characterization of AlCrFeMnNi and AlCrCuFeMnNi high entropy alloy thin films,” *Appl. Surf. Sci.*, vol. 358, no. July, pp. 533–539, 2015, doi: 10.1016/j.apsusc.2015.07.142.

[97] J. J. Licavoli, M. C. Gao, J. S. Sears, P. D. Jablonski, and J. A. Hawk, “Microstructure and Mechanical Behavior of High-Entropy Alloys,” vol. 24, no. October, pp. 3685–3698, 2015, doi: 10.1007/s11665-015-1679-7.

[98] M. Löbel, T. Lindner, T. Mehner, and T. Lampke, “Microstructure and Wear Resistance of AlCoCrFeNiTi High-Entropy Alloy Coatings Produced by HVOF,” 2017, doi: 10.3390/coatings7090144.

[99] H. Luo, Z. Li, A. M. Mingers, and D. Raabe, “Corrosion behavior of an equiatomic CoCrFeMnNi high-entropy alloy compared with 304 stainless steel in sulfuric acid solution,” *Corros. Sci.*, no. February, pp. 0–1, 2018, doi: 10.1016/j.corsci.2018.02.031.

[100] A. Aliyu and C. Srivastava, “Microstructure-corrosion property correlation in electrodeposited AlCrFeCoNiCu high entropy alloys-

graphene oxide composite coatings," vol. 686, no. December 2018, 2019.

[101] A. Aliyu and C. Srivastava, "Microstructure and corrosion properties of MnCrFeCoNi high entropy alloy-graphene oxide composite coatings," *Materialia*, vol. 5, no. November 2018, 2019.

[102] A. Aliyu and C. Srivastava, "Microstructure and corrosion performance of AlFeCoNiCu high entropy alloy coatings by addition of graphene oxide," *Materialia*, vol. 8, no. June, 2019.

[103] F. Yoosefan, A. Ashrafi, S. M. Monir vaghefi, and I. Constantin, "Synthesis of CoCrFeMnNi High Entropy Alloy Thin Films by Pulse Electrodeposition: Part 1: Effect of Pulse Electrodeposition Parameters," *Met. Mater. Int.*, vol. 26, no. 8, pp. 1262–1269, 2020, doi: 10.1007/s12540-019-00404-1.

[104] D. Premlata, Singh, U. Pandel, and R. Kumar, "Graphene oxide reinforced high entropy alloy (CuNiFeCrMo-GO) nanocomposite coating deposited by electroless coating method on mild steel," *Mater. Today Proc.*, no. xxxx, 2020, doi: 10.1016/j.matpr.2020.04.717.

[105] S. Singh, S. M. Shaikh, P. K. M. K, B. S. Murty, and C. Srivastava, "Materialia Microstructural homogenization and substantial improvement in corrosion resistance of mechanically alloyed FeCoCrNiCu high entropy alloys by incorporation of carbon nanotubes," vol. 14, no. September, 2020.

[106] C. S. A. Aliyu, M.Y. Rekha, "Microstructure-electrochemical property correlation in electrodeposited CuFeNiCoCr high-entropy alloy-graphene oxide composite coatings.," *Philos. Mag*, vol. 99, pp. 718–735, 2019.

References

[107] A. M. H. Wais, “Wear and Corrosion behavior of Ni-B-CNTs on 4340 Steel Coated by Plasma Nitriding,” College of Materials Engineering / University of Babylon, 2020.

[108] S. M. Vahid Hasannaeimi, Maryam Sadeghilaridjani, *Electrochemical and Corrosion Behavior of Metallic Glasses*. MDPI, 2021.

[109] S. Esmailzadeh, M. Aliofkhazraei, and H. Sarlak, “Interpretation of Cyclic Potentiodynamic Polarization Test Results for Study of Corrosion Behavior of Metals: A Review,” *Prot. Met. Phys. Chem. Surfaces*, vol. 54, no. 5, pp. 976–989, 2018, doi: 10.1134/S207020511805026X.

[110] Y. Shang, J. Brechtl, C. Psitidda, and P. K. Liaw, “Mechanical behavior of high-entropy alloys : A review.”

[111] A. Aliyu and C. Srivastava, “Microstructure and electrochemical properties of FeNiCoCu medium entropy alloy-graphene oxide composite coatings,” *J. Alloys Compd.*, vol. 864, 2021, doi: 10.1016/j.jallcom.2021.158851.

[112] A. Aliyu and C. Srivastava, “Microstructure-corrosion property correlation in electrodeposited AlCrFeCoNiCu high entropy alloys-graphene oxide composite coatings,” *Thin Solid Films*, vol. 686, no. December 2018, p. 137434, 2019, doi: 10.1016/j.tsf.2019.137434.

[113] S. R. S. B.D. Cullity, *Elements of X-Ray Diffraction*, 3rd ed., vol. 108, no. 2. 2014.

[114] Y. H. Zhao and Y. T. Zhu, “Lattice expansion and grain boundary excess volume of nanocrystalline Se prepared by mechanical milling,” *Rev. Adv. Mater. Sci.*, vol. 48, no. 1, pp. 52–61, 2017.

[115] B. Y. Zhang, Y. J. Zhou, J. P. Lin, G. L. Chen, and P. K. Liaw,

References

"Solid-Solution Phase Formation Rules for Multi-component Alloys **," no. 6, pp. 534–538, 2008, doi: 10.1002/adem.200700240.

[116] X. Yang and Y. Zhang, "Prediction of high-entropy stabilized solid-solution in multi-component alloys," *Mater. Chem. Phys.*, vol. 132, pp. 233–238, 2012, doi: 10.1016/j.matchemphys.2011.11.021.

[117] F. Tian, L. K. Varga, N. Chen, J. Shen, and L. Vitos, "Empirical design of single phase high-entropy alloys with high hardness," *Intermetallics*, vol. 58, pp. 1–6, Mar. 2015, doi: 10.1016/J.INTERMET.2014.10.010.

[118] H. Liu, C. Xin, L. Liu, and C. Zhuang, "Effects of different contents of each component on the structural stability and mechanical properties of co-cr-fe-ni high-entropy alloys," *Appl. Sci.*, vol. 11, no. 6, 2021, doi: 10.3390/app11062832.

[119] S. Guo and C. T. Liu, "Phase stability in high entropy alloys: Formation of solid-solution phase or amorphous phase," *Prog. Nat. Sci. Mater. Int.*, vol. 21, no. 6, pp. 433–446, Dec. 2011, doi: 10.1016/S1002-0071(12)60080-X.

[120] M. T. Hernández-Sierra, L. D. Aguilera-Camacho, J. E. Báez-García, J. S. García-Miranda, and K. J. Moreno, "Thermal stability and lubrication properties of biodegradable castor oil on AISI 4140 steel," *Metals (Basel).*, vol. 8, no. 6, pp. 1–15, 2018, doi: 10.3390/met8060428.

[121] Y. Lin, C. L. Li, and C. H. Hsueh, "Effects of cerium addition on microstructures and mechanical properties of CoCrNi medium entropy alloy films," *Surf. Coatings Technol.*, vol. 424, p. 127645, Oct. 2021, doi: 10.1016/J.SURFCOAT.2021.127645.

[122] Q. An *et al.*, "Effects of C and Mo on microstructures and mechanical

properties of dual-phase high entropy alloys," *Intermetallics*, vol. 110, p. 106471, Jul. 2019, doi: 10.1016/J.INTERMET.2019.04.014.

[123] W. X. Chen, J. P. Tu, L. Y. Wang, H. Y. Gan, Z. D. Xu, and X. B. Zhang, "Tribological application of carbon nanotubes in a metal-based composite coating and composites," *Carbon N. Y.*, vol. 41, no. 2, pp. 215–222, 2003, doi: 10.1016/S0008-6223(02)00265-8.

[124] M. Alishahi, S. M. Monirvaghefi, A. Saatchi, and S. M. Hosseini, "The effect of carbon nanotubes on the corrosion and tribological behavior of electroless Ni-P-CNT composite coating," *Appl. Surf. Sci.*, vol. 258, no. 7, pp. 2439–2446, 2012, doi: 10.1016/j.apsusc.2011.10.067.

[125] and Z. Y. W.Lei, K.Mittal, "Adhesion measurement of coatings on biodevices/implants: A critical review"," *Rev. Adhes. Adhes.*, vol. 4, no. 4, pp. 367-396, 2016.

[126] A. H. Korayem, C. Y. Li, Q. H. Zhang, X. L. Zhao, and W. H. Duan, "Effect of carbon nanotube modified epoxy adhesive on CFRP-to-steel interface," *Compos. Part B Eng.*, vol. 79, pp. 95–104, 2015, doi: 10.1016/j.compositesb.2015.03.063.

[127] J. Cho, K. Konopka, K. Rozniatowski, E. García-Lecina, M. S. P. Shaffer, and A. R. Boccaccini, "Characterisation of carbon nanotube films deposited by electrophoretic deposition," *Carbon N. Y.*, vol. 47, no. 1, pp. 58–67, 2009, doi: 10.1016/j.carbon.2008.08.028.

[128] and Y. W. H. Wang, H. Shi, *The Wetting of Leaf Surfaces and Its Ecological Significances", in Wetting and Wettability*. London, United Kingdom: IntechOpen, 2015.

[129] F. Yoosefan, A. Ashrafi, and S. M. Monir vaghefi, "Characterization of Co–Cr–Fe–Mn–Ni High-Entropy Alloy Thin Films Synthesized by

References

Pulse Electrodeposition: Part 2: Effect of Pulse Electrodeposition Parameters on the Wettability and Corrosion Resistance," *Met. Mater. Int.*, vol. 27, no. 1, pp. 106–117, 2021, doi: 10.1007/s12540-019-00584-w.

[130] G. F. Ma, Z. K. Li, H. Ye, C. L. He, H. F. Zhang, and Z. Q. Hu, "Wetting and interface phenomena in the molten Sn/CuFeNiCoCr high-entropy alloy system," *Appl. Surf. Sci.*, vol. 356, pp. 460–466, 2015, doi: 10.1016/j.apsusc.2015.08.090.

[131] S. Arora, N. Kumari, and C. Srivastava, "Microstructure and corrosion behaviour of NiCo-Carbon nanotube composite coatings," *J. Alloys Compd.*, vol. 801, pp. 449–459, 2019, doi: 10.1016/j.jallcom.2019.06.083.

[132] C. S. Ahmed Aliyu, "Phase constitution surface chemistry and corrosion behavior of electrodeposited MnFeCoNiCu high entropy alloy-graphene oxide composite coatings," *Surf. Coatings Technol.*, vol. 429, pp. 2–12, 2022.

[133] K. Krishnaveni, T. S. N. S. Narayanan, and S. K. Seshadri, "Corrosion resistance of electrodeposited Ni-B and Ni-B-Si3N4 composite coatings," *J. Alloys Compd.*, vol. 480, no. 2, pp. 765–770, 2009, doi: 10.1016/j.jallcom.2009.02.053.

[134] S. Sahu, O. J. Swanson, T. Li, A. Y. Gerard, J. R. Scully, and G. S. Frankel, "Localized Corrosion Behavior of Non-Equiatomic NiFeCrMnCo Multi-Principal Element Alloys," *Electrochim. Acta*, vol. 354, p. 136749, Sep. 2020, doi: 10.1016/J.ELECTACTA.2020.136749.

Appendix

Appendix A : The friction coefficient differences versus distance for specimen O to H respectively at 5N

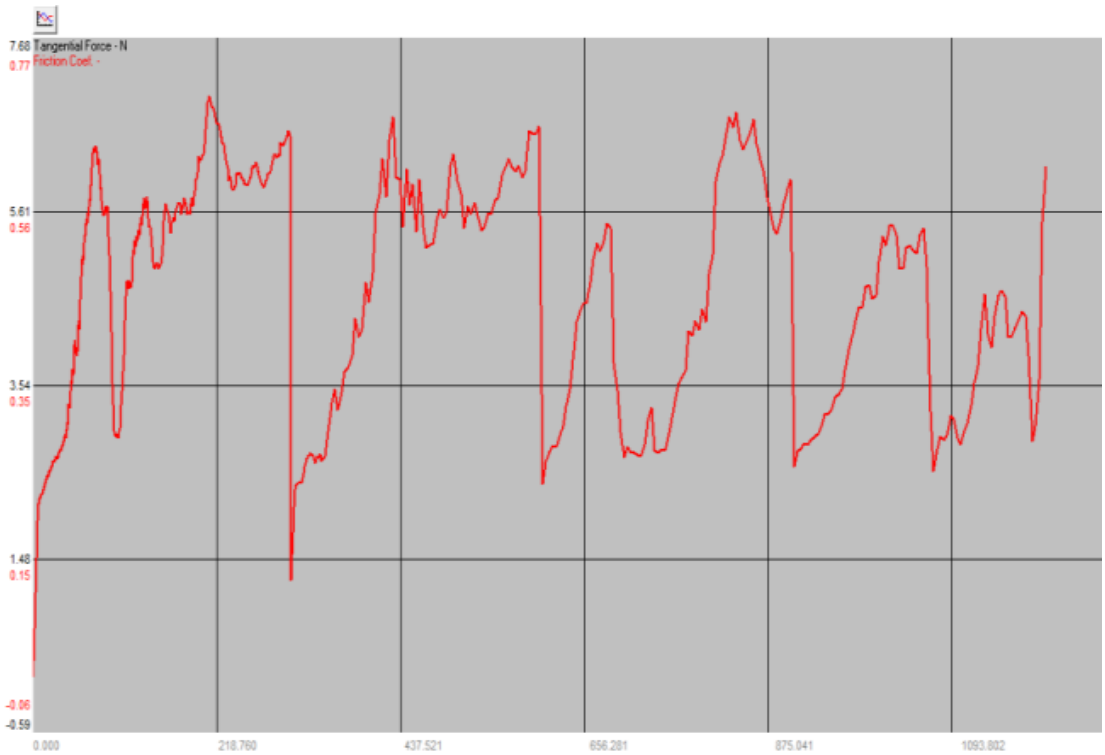

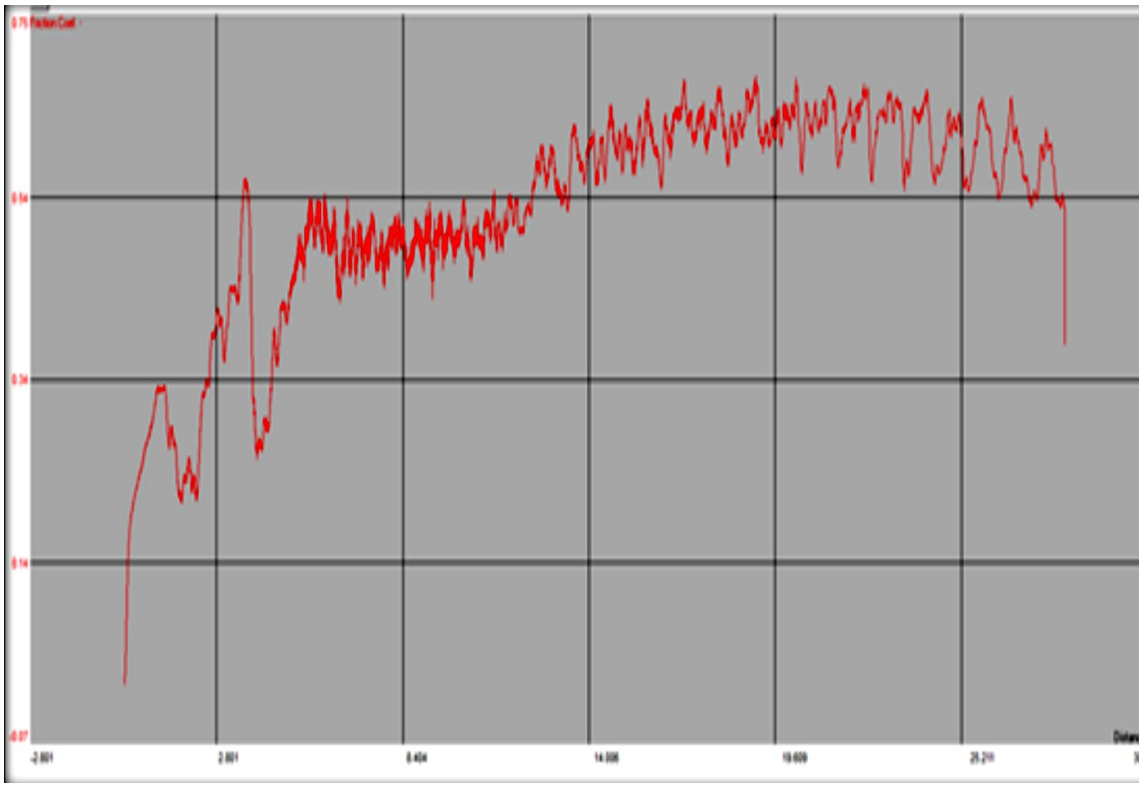

Appendix

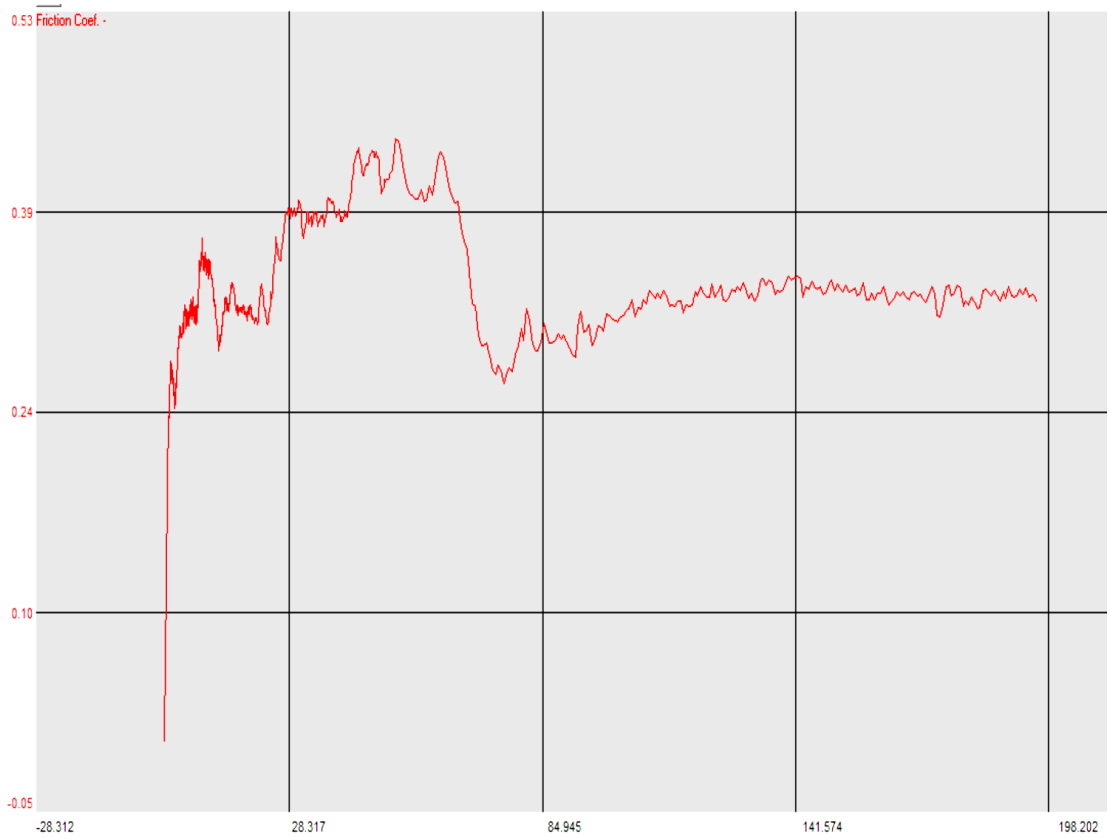
0.53 Friction Coef. -
0.39
0.24
0.10
-0.05
-28.312
28.317
84.945
141.574
198.202

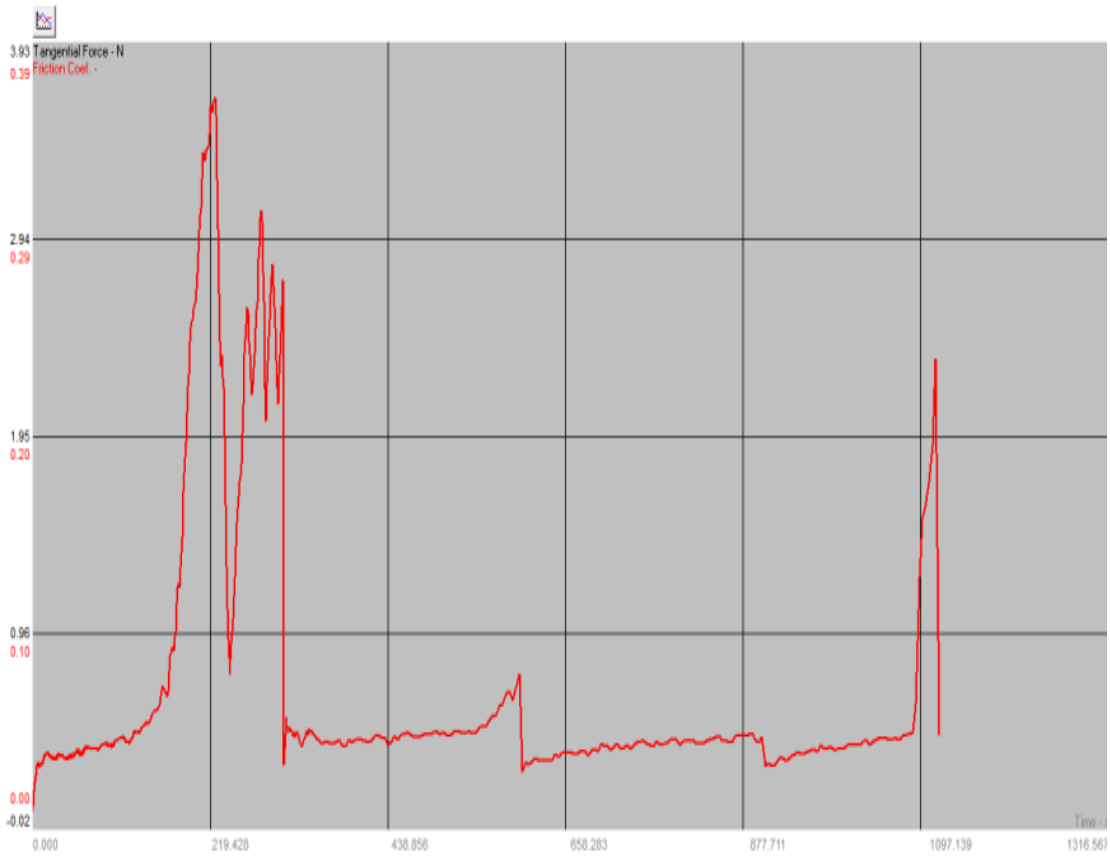
3.93 Tangential Force - N
0.39 Friction Coef. -
2.94
0.29
1.95
0.20
0.96
0.10
0.00
-0.02
0.000
219.428
438.856
658.283
877.711
1097.139
1316.567

Appendix

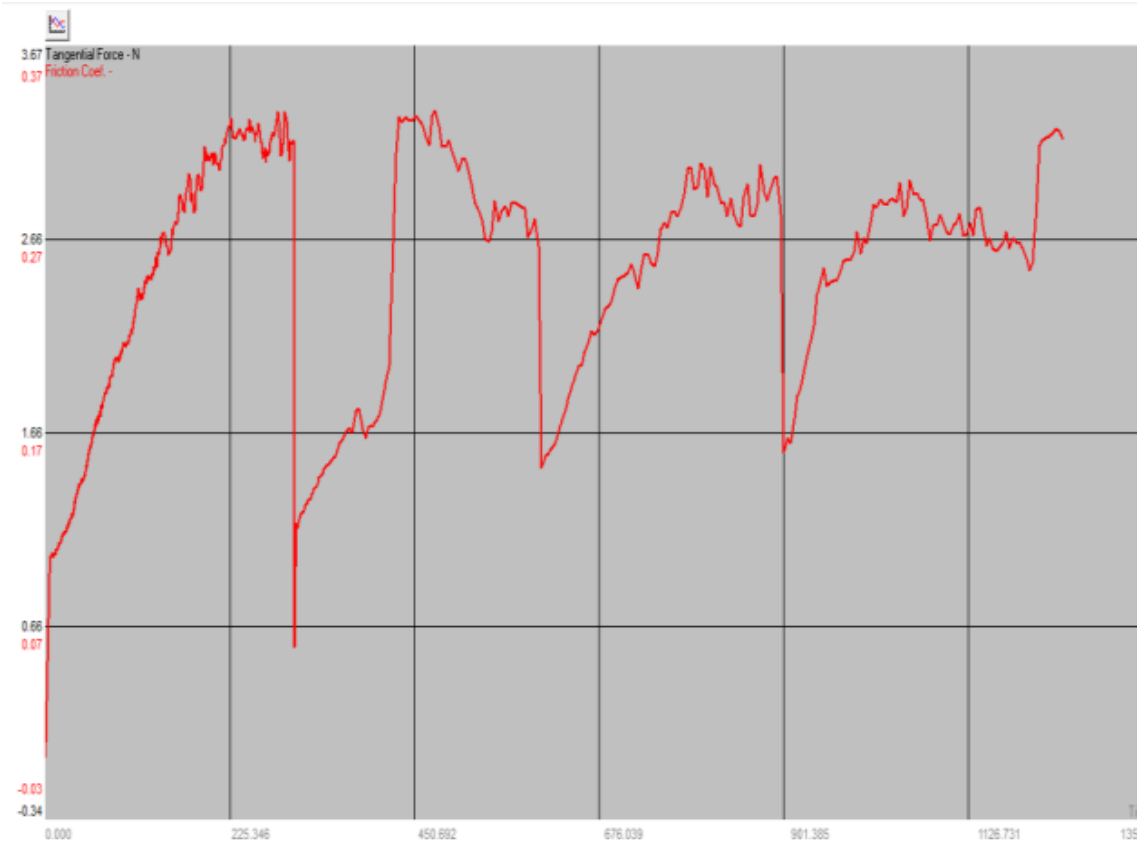
3.67 Tangential Force - N
0.37 Friction Coef. -
2.66
0.27
1.66
0.17
0.66
0.07
-0.03
-0.34
0.000
225.346
450.692
676.039
901.385
1126.731

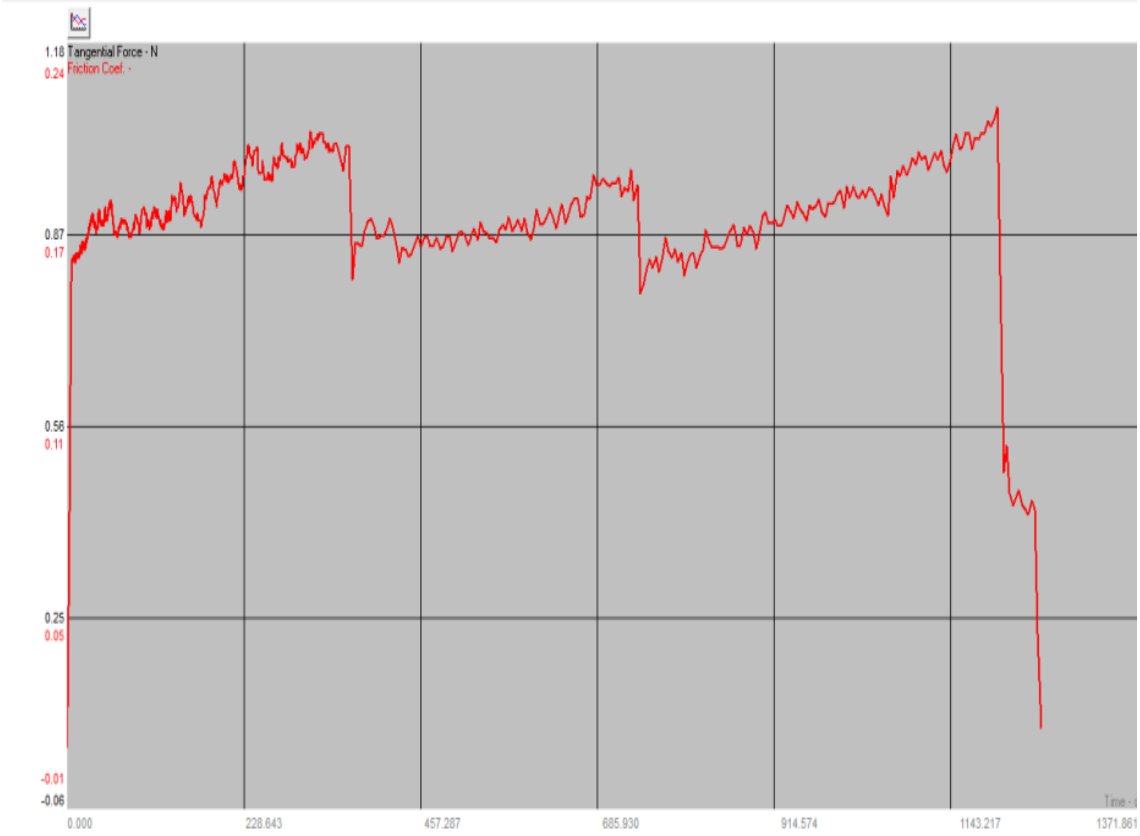
1.18 Tangential Force - N
0.24 Friction Coef. -
0.87
0.17
0.56
0.11
0.25
0.05
-0.01
-0.06
0.000
228.643
457.287
685.930
914.574
1143.217
1371.861

Appendix

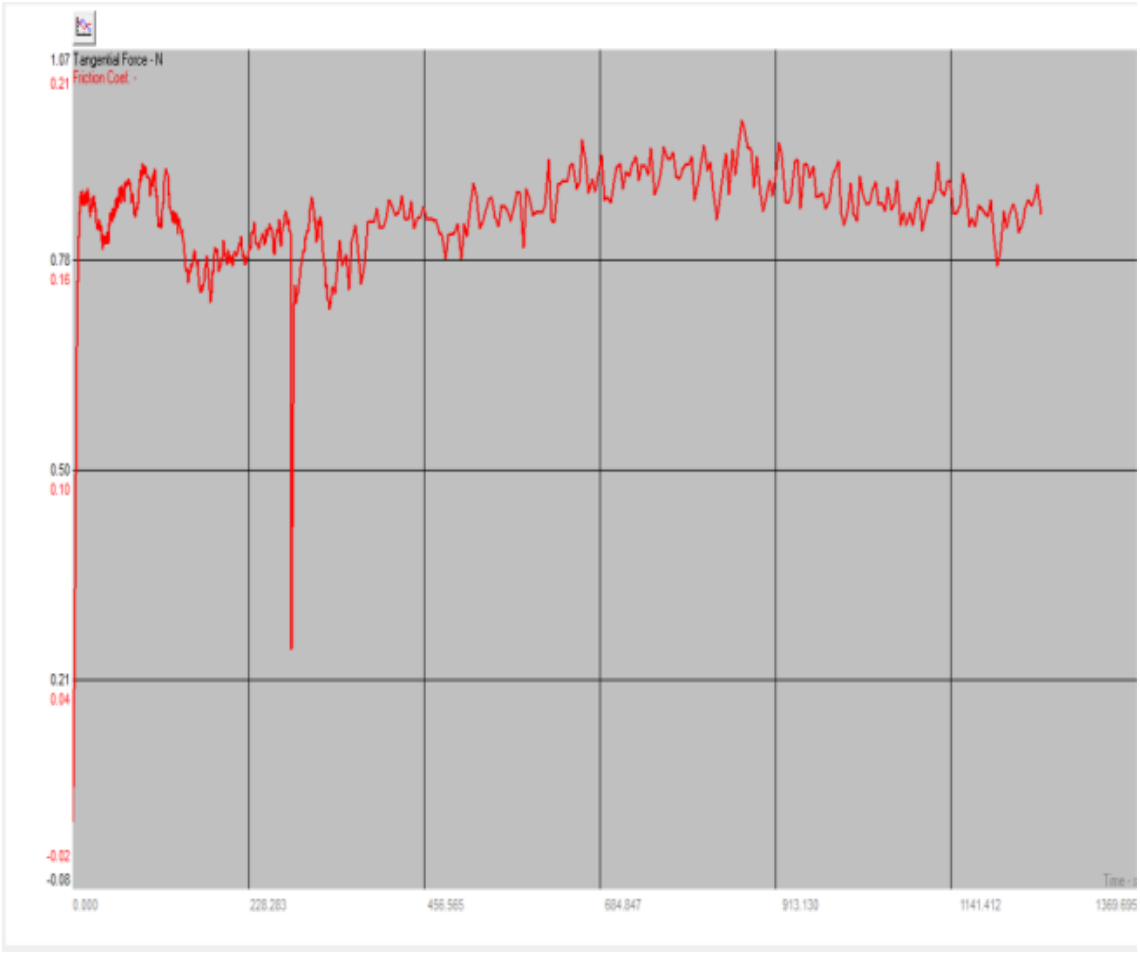
1.07 Tangential Force - N
0.21 Friction Coef. -
0.78
0.16
0.50
0.10
0.21
0.04
-0.02
-0.08
0.000
228.283
456.565
684.847
913.130
1141.412
1369.695

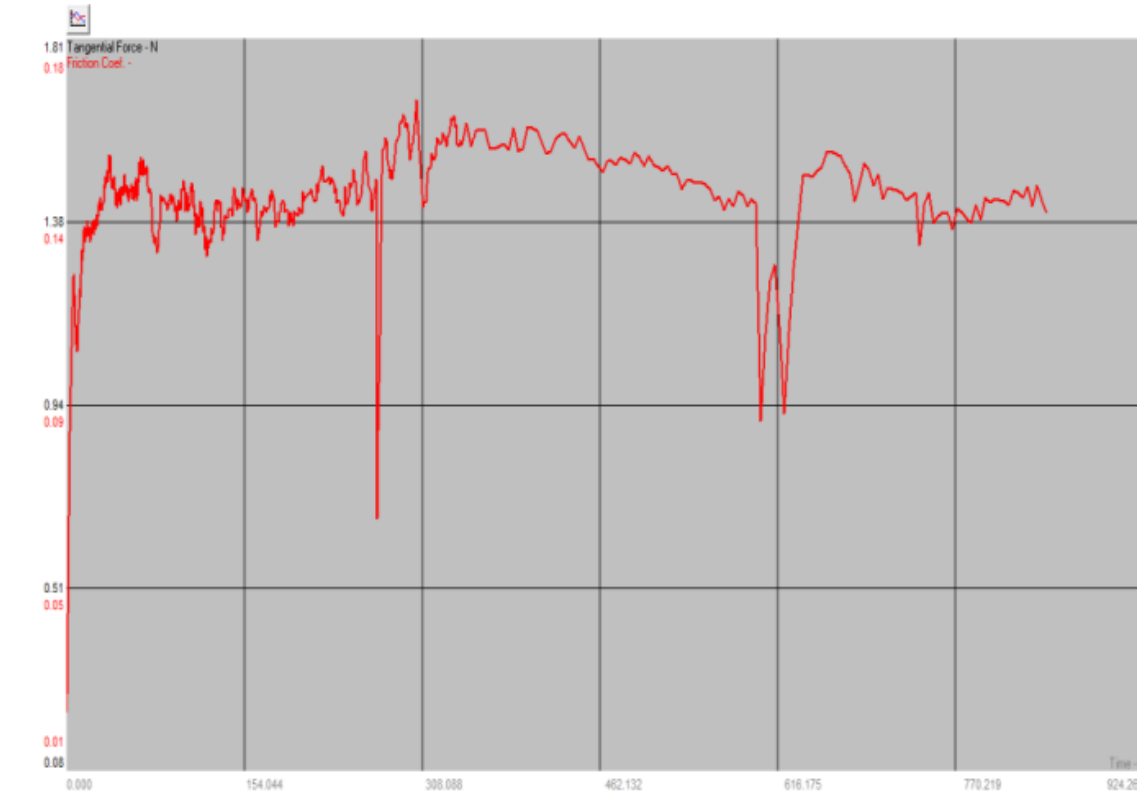
1.81 Tangential Force - N
0.18 Friction Coef. -
1.38
0.14
0.94
0.09
0.51
0.05
0.01
0.08
0.000
154.044
308.088
462.132
616.175
770.219
924.26

Appendix

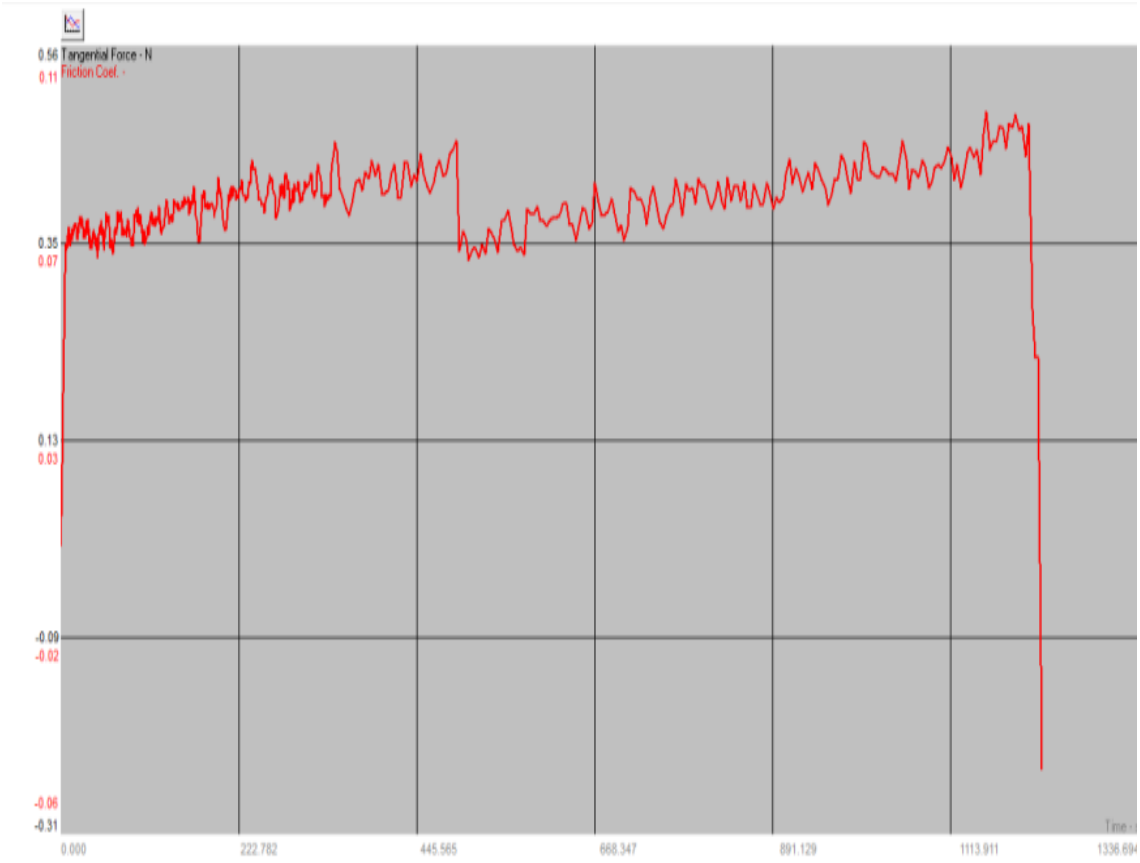

Appendix B : The friction coefficient differences versus distance for specimen O to H respectively at 10N

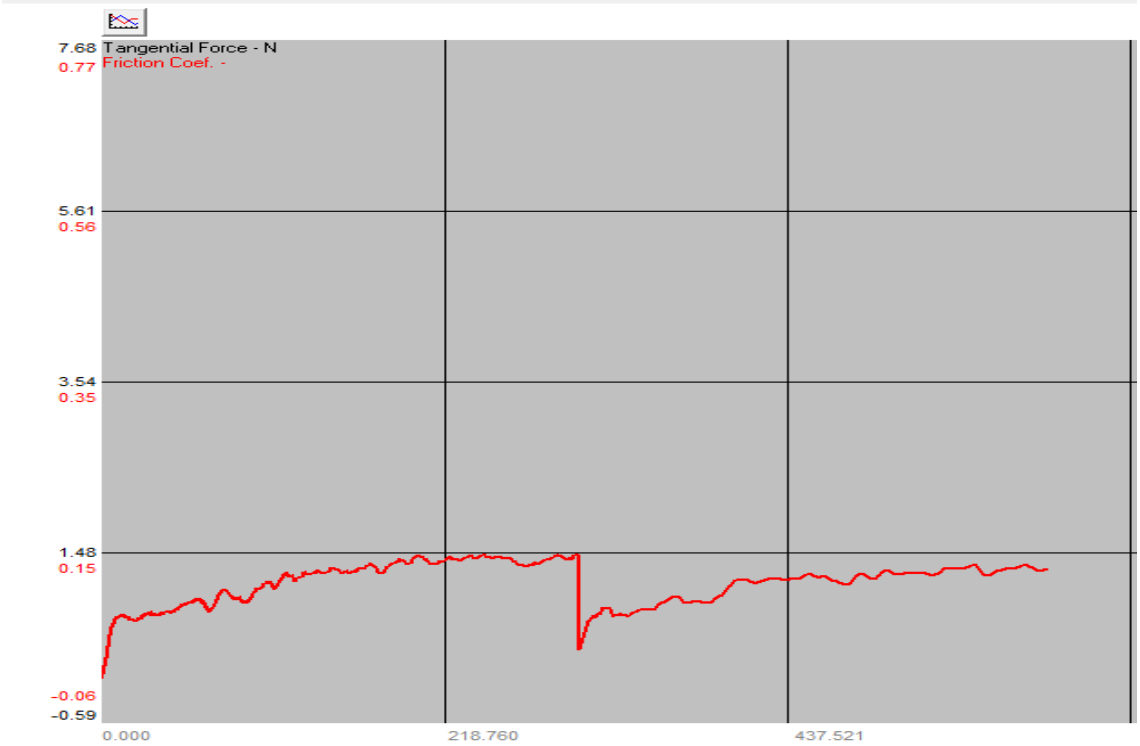

Appendix

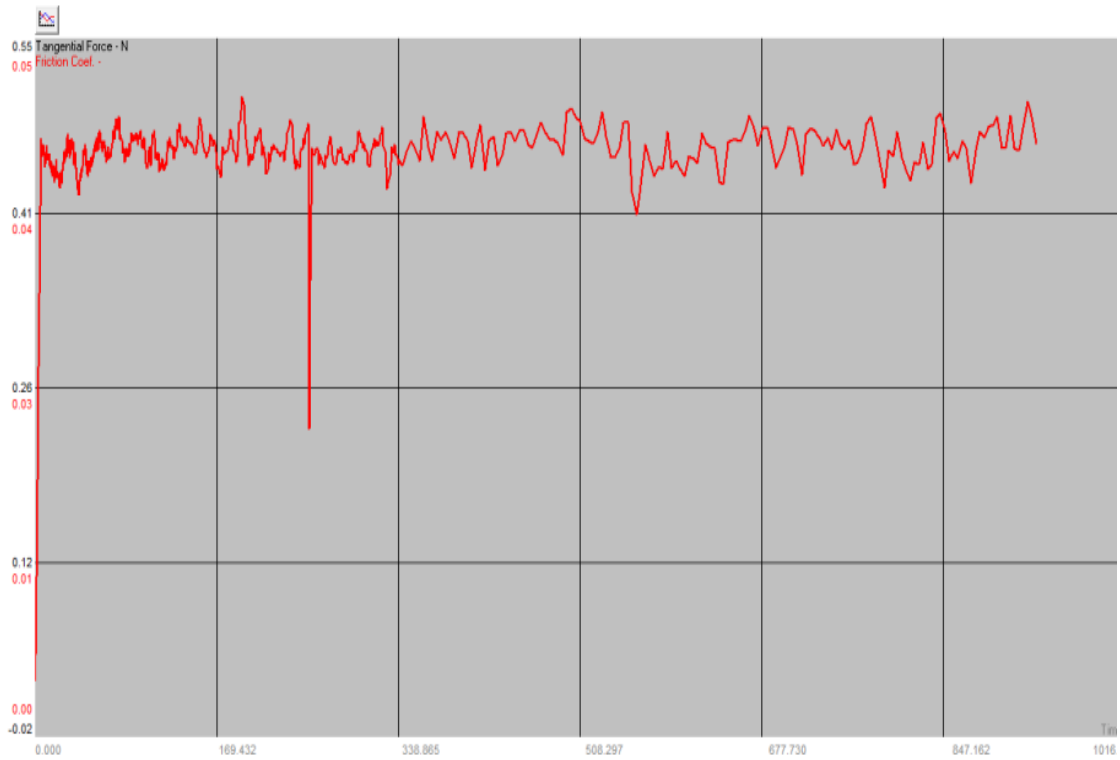
0.55 Tangential Force - N
0.05 Friction Coef. -
0.41
0.04
0.26
0.03
0.12
0.01
0.00
-0.02
0.000
169.432
338.865
508.297
677.730
847.162
1016

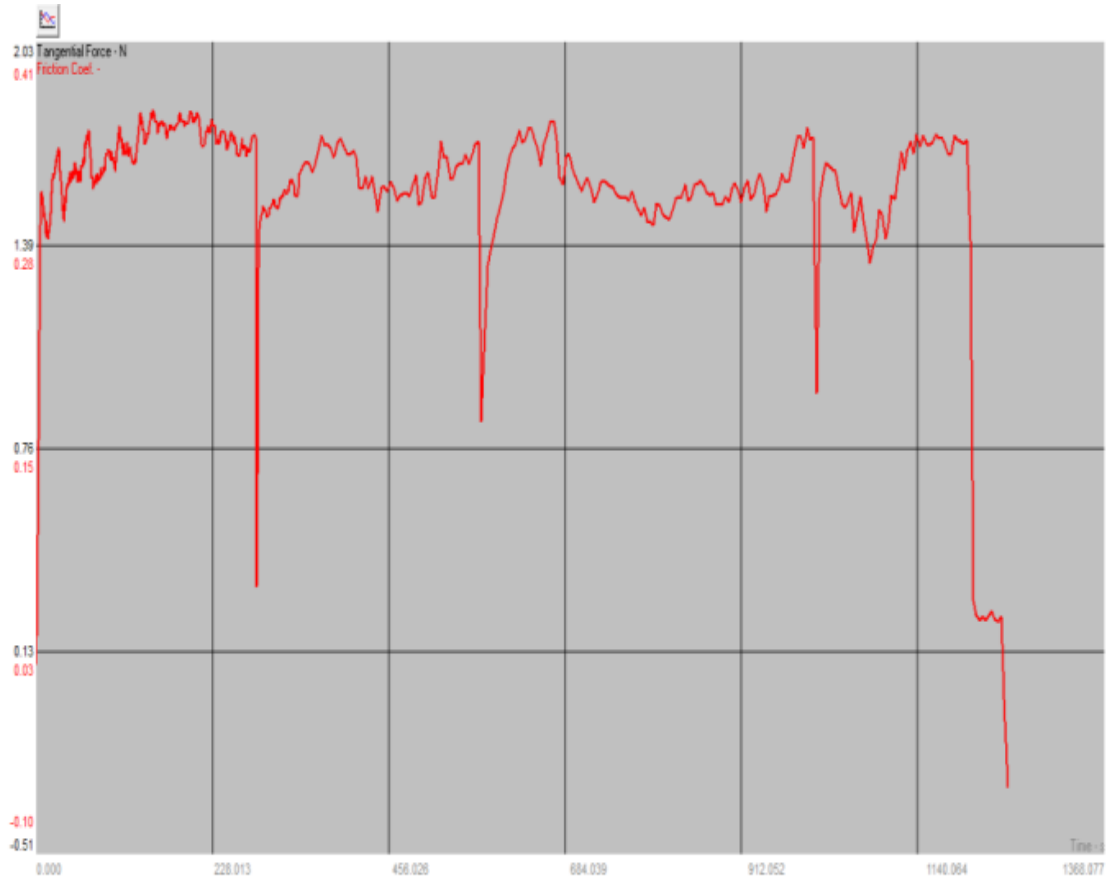
2.03 Tangential Force - N
0.41 Friction Coef. -
1.39
0.28
0.76
0.15
0.13
0.03
-0.10
-0.51
0.000
228.013
456.026
684.039
912.052
1140.064
1368.077

Appendix

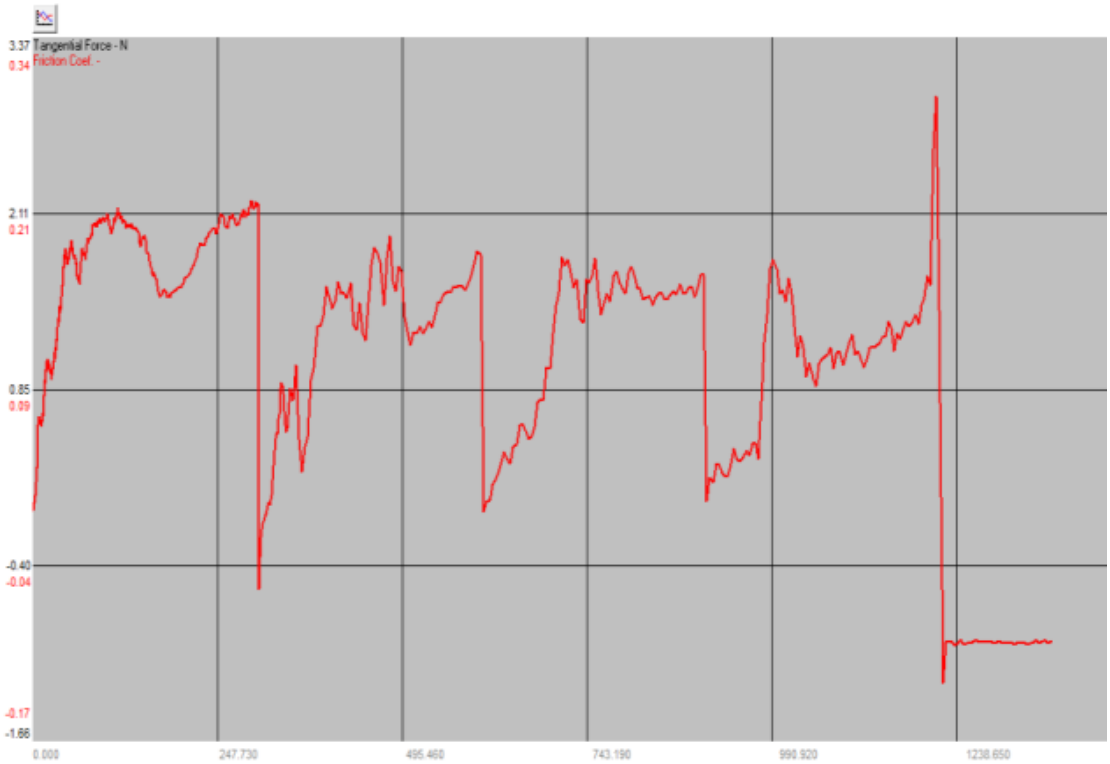
3.37 Tangential Force - N
0.34 Friction Coef. -
2.11
0.21
0.85
0.09
-0.40
-0.04
-0.17
-1.66
0.000
247.730
495.460
743.190
990.920
1238.650

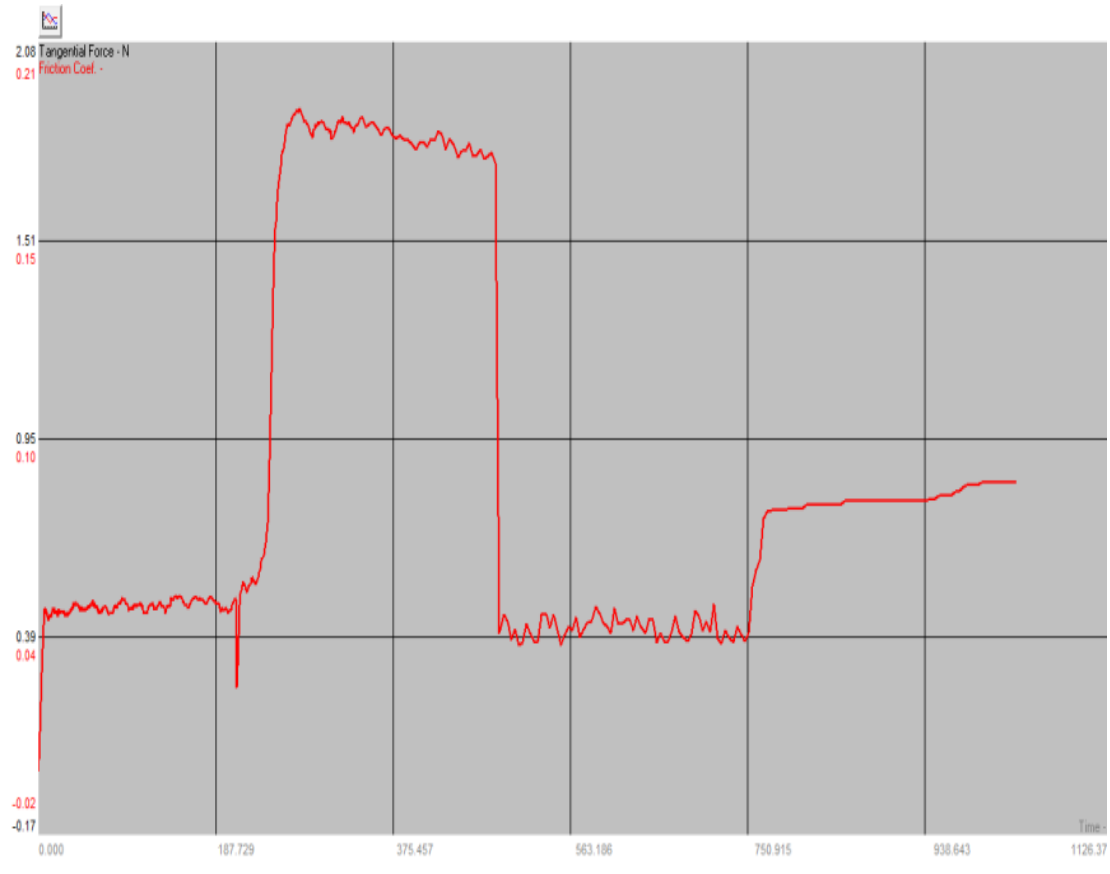
2.08 Tangential Force - N
0.21 Friction Coef. -
1.51
0.15
0.95
0.10
0.39
0.04
-0.02
-0.17
0.000
187.729
375.457
563.186
750.915
938.643
1126.37

Appendix


1.61 Tangential Force - N
0.16 Friction Coef. -
1.20
0.12
0.79
0.08
0.38
0.04
0.00
-0.02
0.000
219.428
438.856
658.283
877.711
1097.139

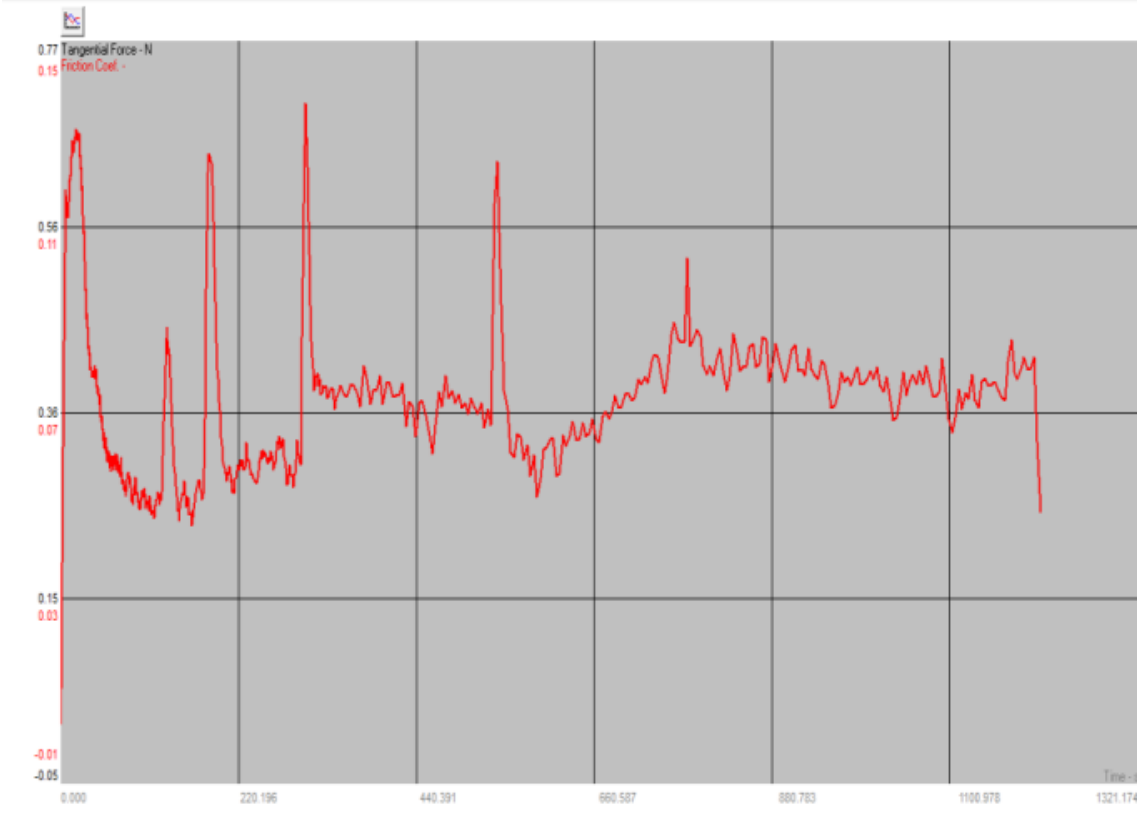
0.77 Tangential Force - N
0.15 Friction Coef. -
0.56
0.11
0.36
0.07
0.15
0.03
-0.01
-0.05
0.000
220.196
440.391
660.587
880.783
1100.978
1321.174

Appendix

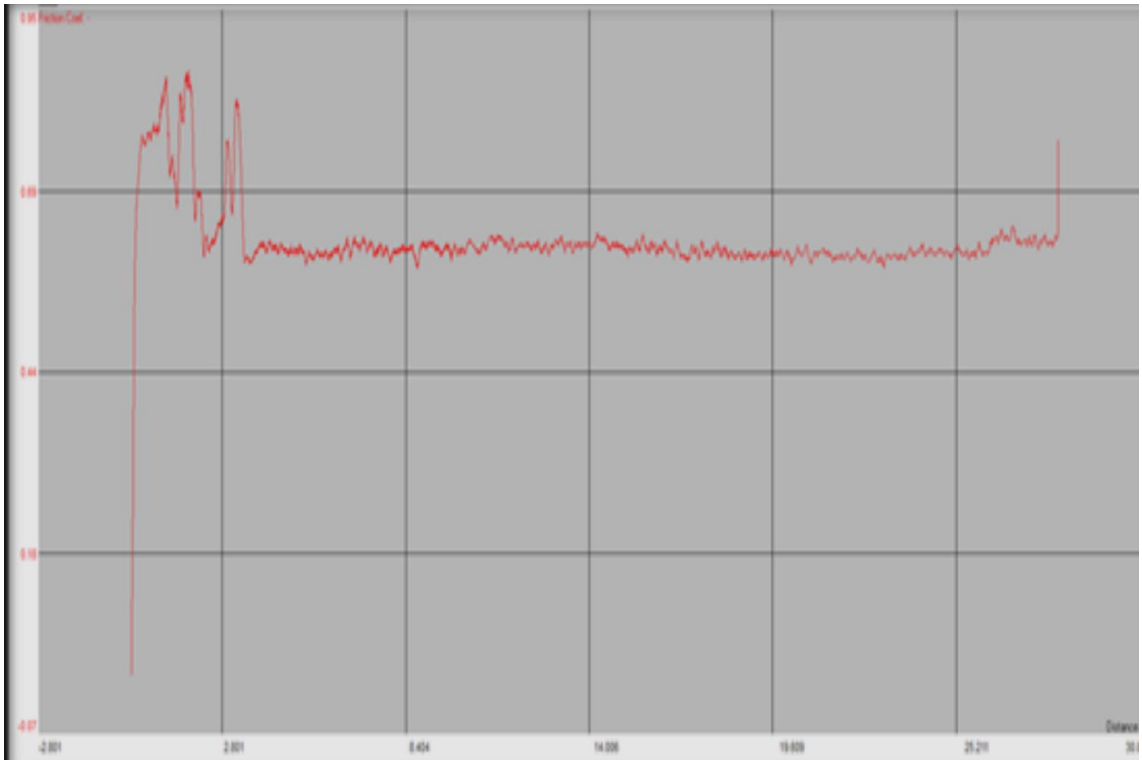

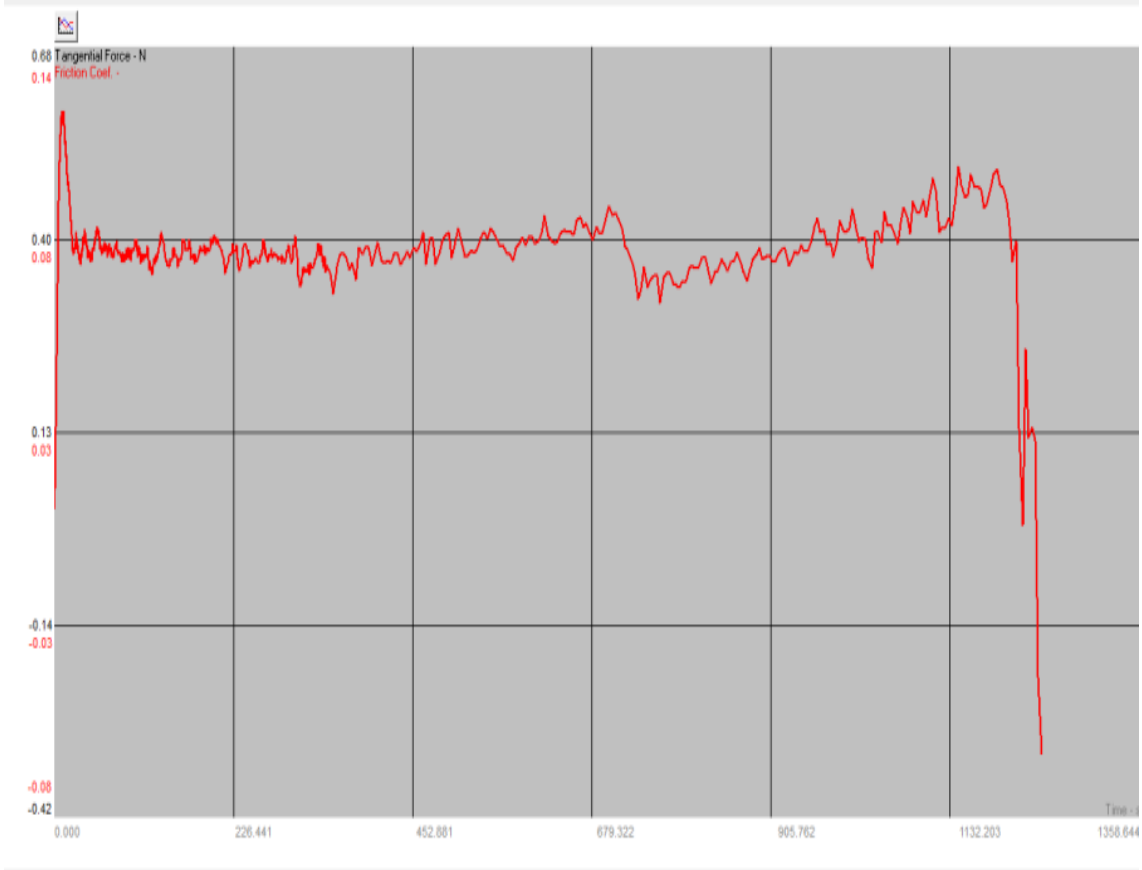
Tangential Force - N
Friction Coef. -
0.68
0.14
0.40
0.08
0.13
0.03
-0.14
-0.03
-0.08
-0.42
0.000
226.441
452.881
679.322
905.762
1132.203
1358.644

Appendix

Appendix C: XRD charts of the consistent elements of coating

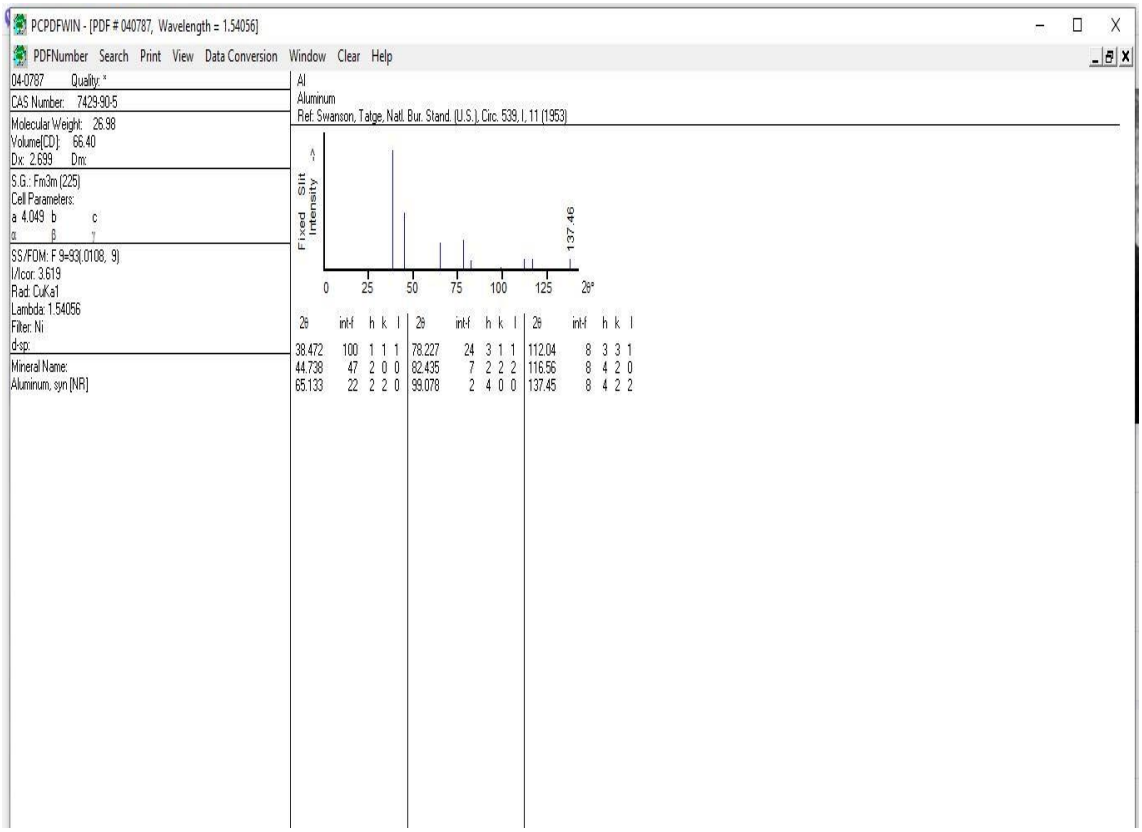

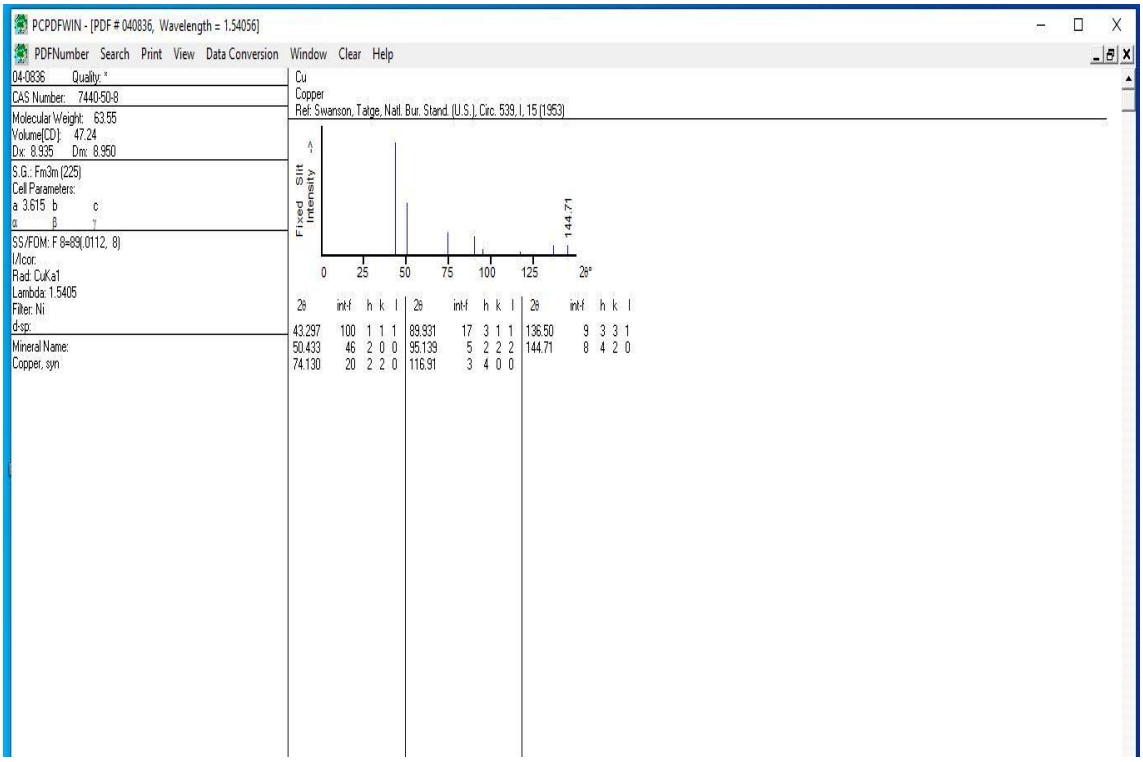

Appendix

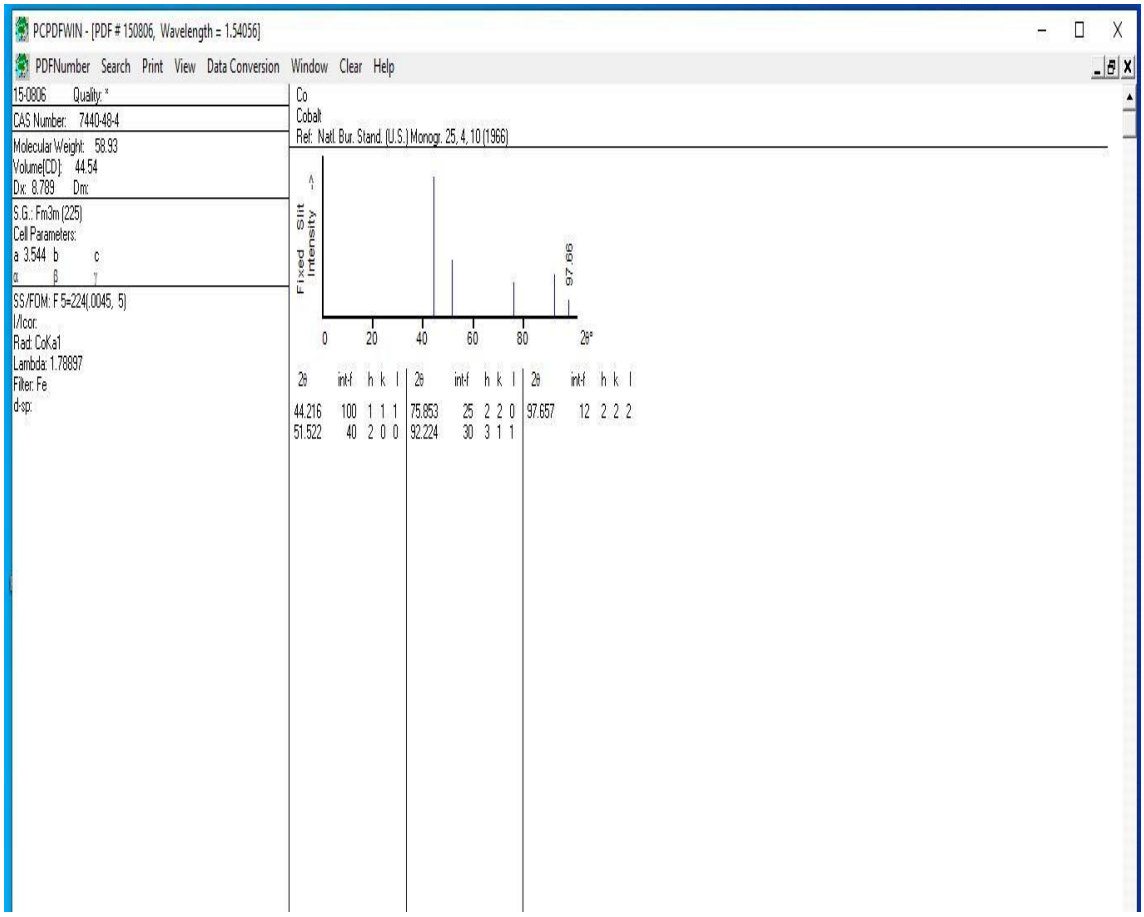
PCPDFWIN - [PDF # 150806, Wavelength = 1.54056]
PDFNumber Search Print View Data Conversion Window Clear Help
15-0806 Quality: *
CAS Number: 7440-48-4
Molecular Weight: 58.93
Volume[CD]: 44.54
Dx: 8.789 Dm:
S.G.: Fm3m (225)
Cell Parameters:
a 3.544 b c
α β γ
SS/FOM: F 5=224(.0045, 5)
I/Icor:
Rad: CoKa1
Lambda: 1.78897
Filter: Fe
d-sp:
Co
Cobalt
Ref: Natl. Bur. Stand. (U.S.) Monogr. 25, 4, 10 (1966)
Fixed Slit Intensity
97.66
0 20 40 60 80 2θ°
2θ int-f h k l 2θ int-f h k l 2θ int-f h k l
44.216 100 1 1 1 75.853 25 2 2 0 97.657 12 2 2 2
51.522 40 2 0 0 92.224 30 3 1 1

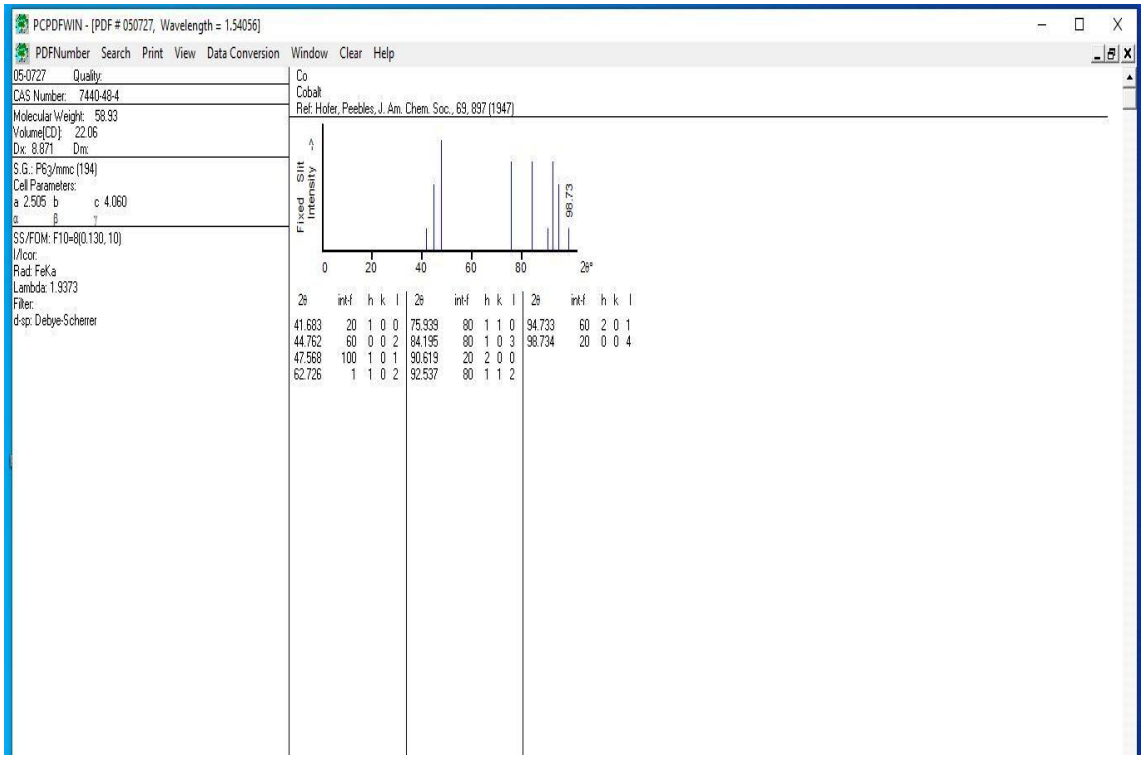
PCPDFWIN - [PDF # 050727, Wavelength = 1.54056]
PDFNumber Search Print View Data Conversion Window Clear Help
05-0727 Quality:
CAS Number: 7440-48-4
Molecular Weight: 58.93
Volume[CD]: 22.06
Dx: 8.871 Dm:
S.G.: P63/mmc (194)
Cell Parameters:
a 2.505 b c 4.060
α β γ
SS/FOM: F10=8(0.130, 10)
I/Icor:
Rad: FeKa
Lambda: 1.9373
Filter:
d-sp: Debye-Scherrer
Co
Cobalt
Ref: Hofer, Peebles, J. Am. Chem. Soc., 69, 897 (1947)
Fixed Slit Intensity
98.73
0 20 40 60 80 2θ°
2θ int-f h k l 2θ int-f h k l 2θ int-f h k l
41.683 20 1 0 0 75.939 80 1 1 0 94.733 60 2 0 1
44.762 60 0 0 2 84.195 80 1 0 3 98.734 20 0 0 4
47.568 100 1 0 1 90.619 20 2 0 0
62.726 1 1 0 2 92.537 80 1 1 2

Appendix

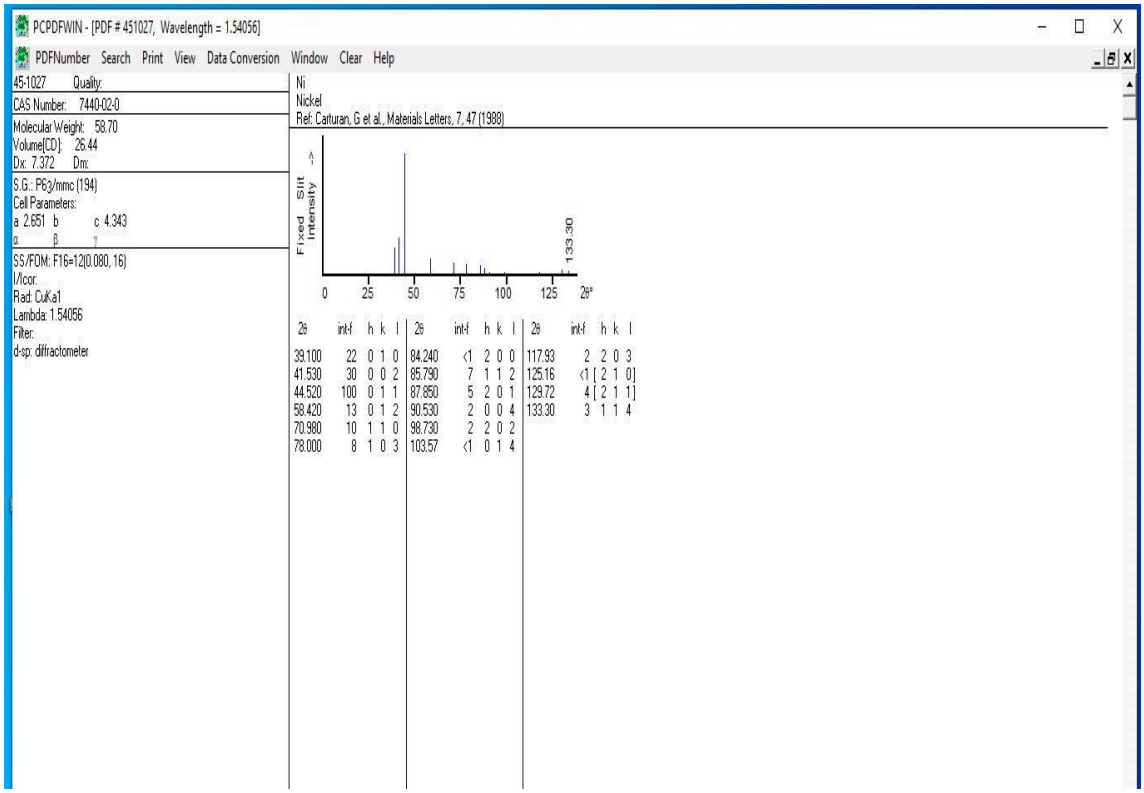
PCPDFWIN - [PDF # 451027, Wavelength = 1.54056]
PDFNumber Search Print View Data Conversion Window Clear Help
45-1027 Quality:
CAS Number: 7440-02-0
Molecular Weight: 58.70
Volume[CD]: 26.44
Dx: 7.372 Dm:
S.G.: P63/mmc (194)
Cell Parameters:
a 2.651 b c 4.343
α β γ
SS/FOM: F16=12(0.080, 16)
I/Icor:
Rad: CuKa1
Lambda: 1.54056
Filter:
d-sp: diffractometer
Ni
Nickel
Ref: Carturan, G et al., Materials Letters, 7, 47 (1988)
Fixed Slit Intensity
133.30
2θ° int-f h k l 2θ° int-f h k l 2θ° int-f h k l
39.100 22 0 1 0 84.240 <1 2 0 0 117.93 2 2 0 3
41.530 30 0 0 2 85.790 7 1 1 2 125.16 <1 [2 1 0]
44.520 100 0 1 1 87.850 5 2 0 1 129.72 4 [2 1 1]
58.420 13 0 1 2 90.530 2 0 0 4 133.30 3 1 1 4
70.980 10 1 1 0 98.730 2 2 0 2
78.000 8 1 0 3 103.57 <1 0 1 4

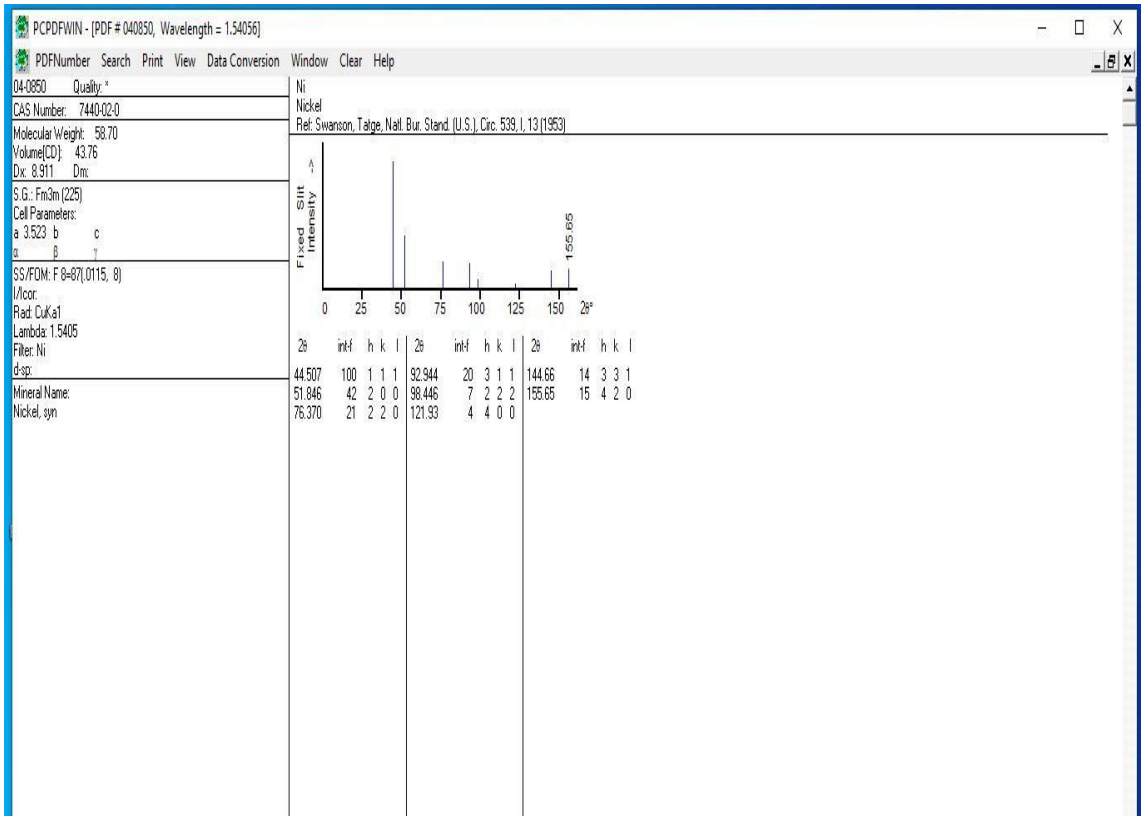
PCPDFWIN - [PDF # 040850, Wavelength = 1.54056]
PDFNumber Search Print View Data Conversion Window Clear Help
04-0850 Quality: *
CAS Number: 7440-02-0
Molecular Weight: 58.70
Volume[CD]: 43.76
Dx: 8.911 Dm:
S.G.: Fm3m (225)
Cell Parameters:
a 3.523 b c
α β γ
SS/FOM: F 8=87(.0115, 8)
I/Icor:
Rad: CuKa1
Lambda: 1.5405
Filter: Ni
d-sp:
Mineral Name:
Nickel, syn
Ni
Nickel
Ref: Swanson, Tatge, Natl. Bur. Stand. (U.S.), Circ. 539, I, 13 (1953)
Fixed Slit Intensity
155.65
2θ° int-f h k l 2θ° int-f h k l 2θ° int-f h k l
44.507 100 1 1 1 92.944 20 3 1 1 144.66 14 3 3 1
51.846 42 2 0 0 98.446 7 2 2 2 155.65 15 4 2 0
76.370 21 2 2 0 121.93 4 4 0 0

Appendix

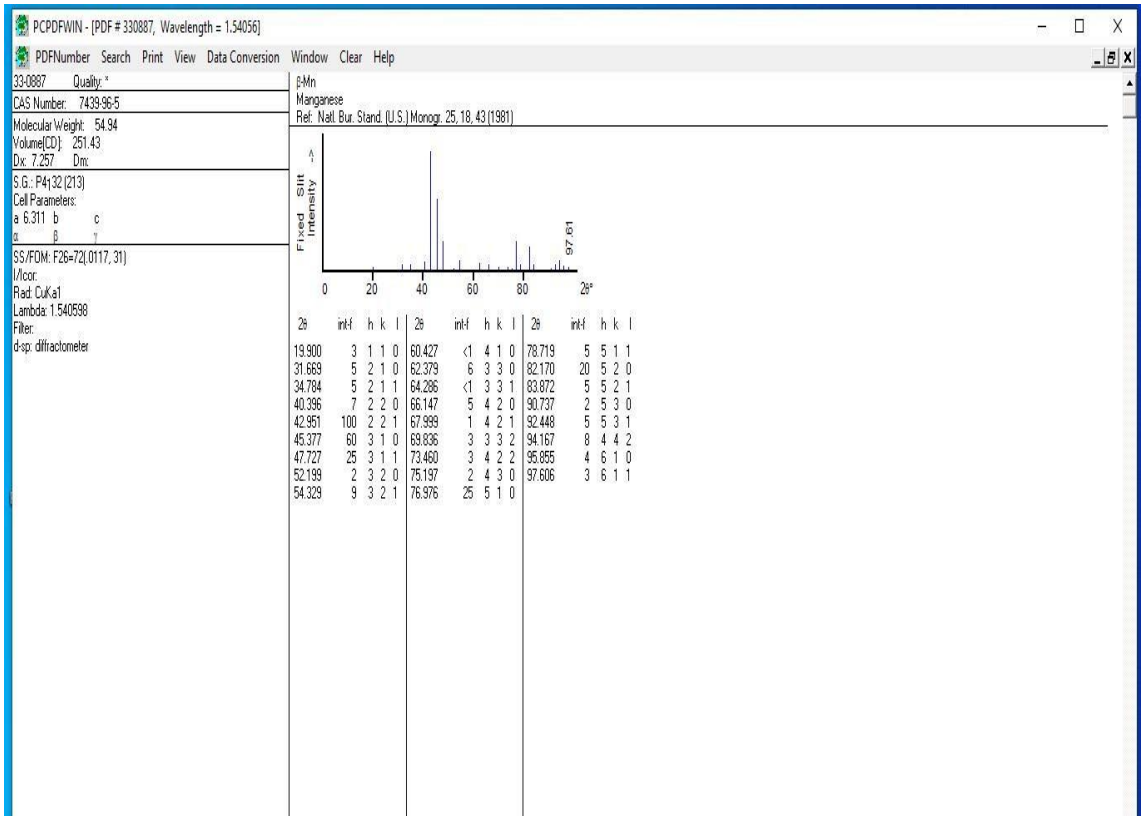
PCPDFWIN - [PDF # 330887, Wavelength = 1.54056]
PDFNumber Search Print View Data Conversion Window Clear Help
33-0887 Quality: *
CAS Number: 7439-96-5
Molecular Weight: 54.94
Volume[CD]: 251.43
Dx: 7.257 Dm:
S.G.: P4132 (213)
Cell Parameters:
a 6.311 b c
α β γ
SS/FOM: F26=72(.0117, 31)
I/Icor:
Rad: CuKa1
Lambda: 1.540598
Filter:
d-sp: diffractometer
β-Mn
Manganese
Ref: Natl. Bur. Stand. (U.S.) Monogr. 25, 18, 43 (1981)
Fixed Slit Intensity
97.61
0 20 40 60 80 2θ°
2θ int-f h k l 2θ int-f h k l 2θ int-f h k l
19.900 3 1 1 0 60.427 <1 4 1 0 78.719 5 5 1 1
31.669 5 2 1 0 62.379 6 3 3 0 82.170 20 5 2 0
34.784 5 2 1 1 64.286 <1 3 3 1 83.872 5 5 2 1
40.396 7 2 2 0 66.147 5 4 2 0 90.737 2 5 3 0
42.951 100 2 2 1 67.999 1 4 2 1 92.448 5 5 3 1
45.377 60 3 1 0 69.836 3 3 3 2 94.167 8 4 4 2
47.727 25 3 1 1 73.460 3 4 2 2 95.855 4 6 1 0
52.199 2 3 2 0 75.197 2 4 3 0 97.606 3 6 1 1
54.329 9 3 2 1 76.976 25 5 1 0

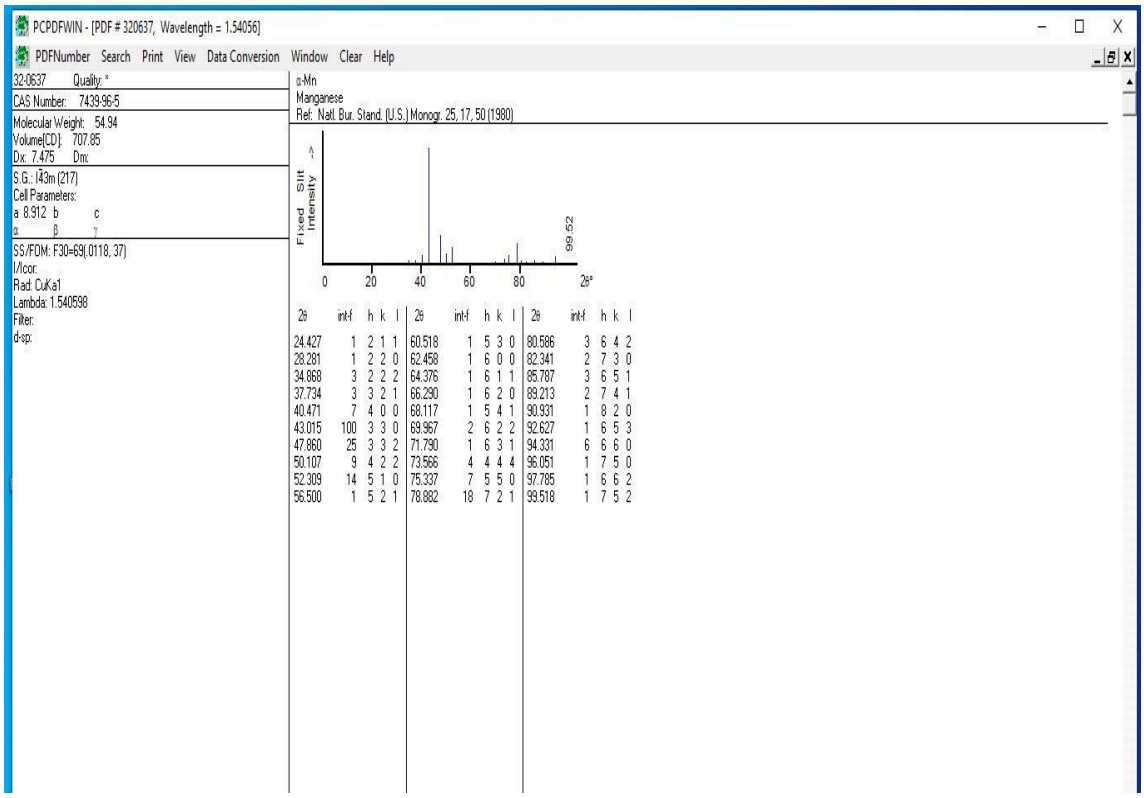
PCPDFWIN - [PDF # 320637, Wavelength = 1.54056]
PDFNumber Search Print View Data Conversion Window Clear Help
32-0637 Quality: *
CAS Number: 7439-96-5
Molecular Weight: 54.94
Volume[CD]: 707.85
Dx: 7.475 Dm:
S.G.: I4̄3m (217)
Cell Parameters:
a 8.912 b c
α β γ
SS/FOM: F30=69(.0118, 37)
I/Icor:
Rad: CuKa1
Lambda: 1.540598
Filter:
d-sp:
α-Mn
Manganese
Ref: Natl. Bur. Stand. (U.S.) Monogr. 25, 17, 50 (1980)
Fixed Slit Intensity
99.52
0 20 40 60 80 2θ°
2θ int-f h k l 2θ int-f h k l 2θ int-f h k l
24.427 1 2 1 1 60.518 1 5 3 0 80.586 3 6 4 2
28.281 1 2 2 0 62.458 1 6 0 0 82.341 2 7 3 0
34.868 3 2 2 2 64.376 1 6 1 1 85.787 3 6 5 1
37.734 3 3 2 1 66.290 1 6 2 0 89.213 2 7 4 1
40.471 7 4 0 0 68.117 1 5 4 1 90.931 1 8 2 0
43.015 100 3 3 0 69.967 2 6 2 2 92.627 1 6 5 3
47.860 25 3 3 2 71.790 1 6 3 1 94.331 6 6 6 0
50.107 9 4 2 2 73.566 4 4 4 4 96.051 1 7 5 0
52.309 14 5 1 0 75.337 7 5 5 0 97.785 1 6 6 2
56.500 1 5 2 1 78.882 18 7 2 1 99.518 1 7 5 2

Appendix

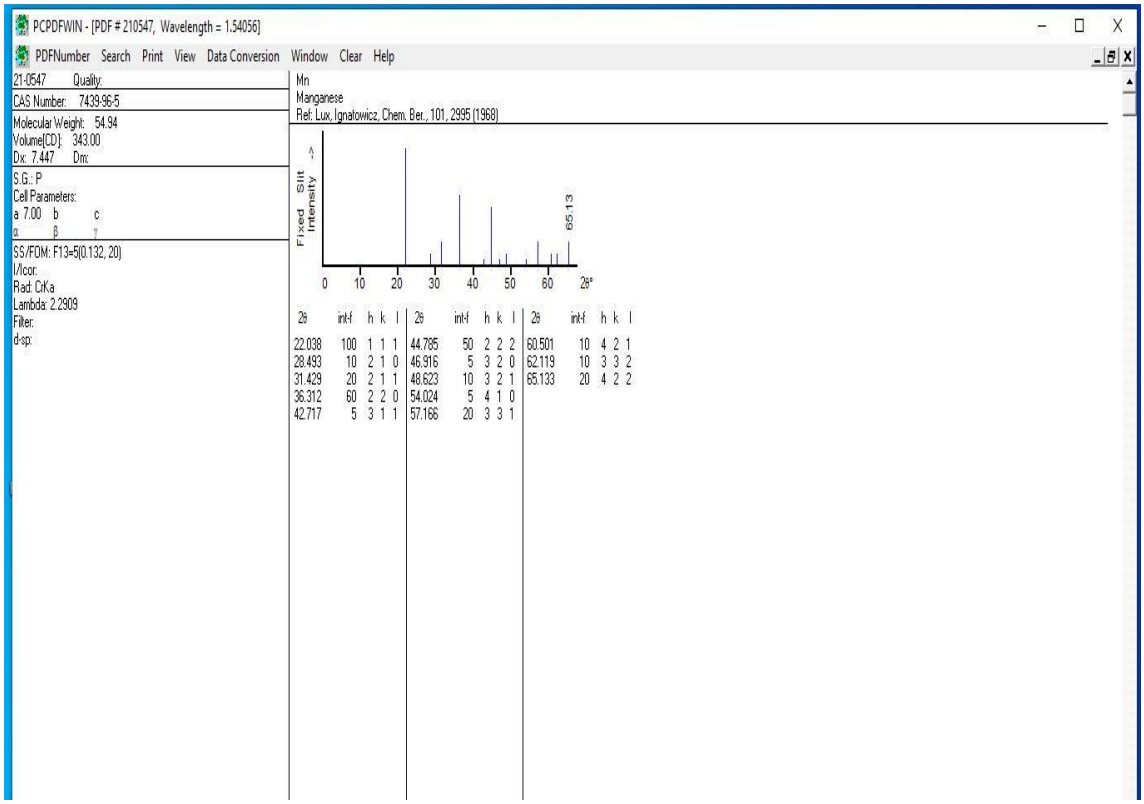
PCPDFWIN - [PDF # 210547, Wavelength = 1.54056]
PDFNumber Search Print View Data Conversion Window Clear Help
21-0547 Quality:
CAS Number: 7439-96-5
Molecular Weight: 54.94
Volume[CD]: 343.00
Dx: 7.447 Dm:
S.G.: P
Cell Parameters:
a 7.00 b c
α β γ
SS/FOM: F13=5(0.132, 20)
I/Icor:
Rad: CrKa
Lambda: 2.2909
Filter:
d-sp:
Mn
Manganese
Ref: Lux, Ignatowicz, Chem. Ber., 101, 2995 (1968)
Fixed Slit Intensity
65.13
0 10 20 30 40 50 60 2θ°
2θ int-f h k l 2θ int-f h k l 2θ int-f h k l
22.038 100 1 1 1 44.785 50 2 2 2 60.501 10 4 2 1
28.493 10 2 1 0 46.916 5 3 2 0 62.119 10 3 3 2
31.429 20 2 1 1 48.623 10 3 2 1 65.133 20 4 2 2
36.312 60 2 2 0 54.024 5 4 1 0
42.717 5 3 1 1 57.166 20 3 3 1

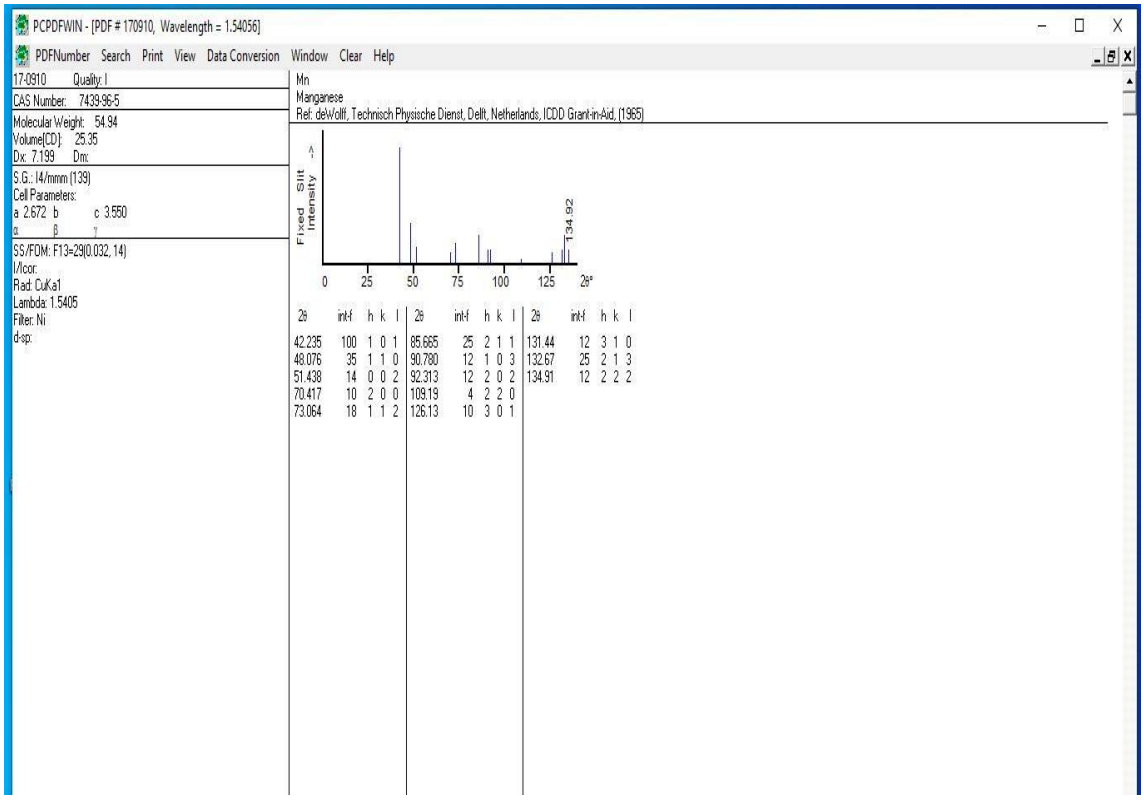
PCPDFWIN - [PDF # 170910, Wavelength = 1.54056]
PDFNumber Search Print View Data Conversion Window Clear Help
17-0910 Quality: I
CAS Number: 7439-96-5
Molecular Weight: 54.94
Volume[CD]: 25.35
Dx: 7.199 Dm:
S.G.: I4/mmm (139)
Cell Parameters:
a 2.672 b c 3.550
α β γ
SS/FOM: F13=29(0.032, 14)
I/Icor:
Rad: CuKa1
Lambda: 1.5405
Filter: Ni
d-sp:
Mn
Manganese
Ref: deWolff, Technisch Physische Dienst, Delft, Netherlands, ICDD Grant-in-Aid, (1965)
Fixed Slit Intensity
134.92
0 25 50 75 100 125 2θ°
2θ int-f h k l 2θ int-f h k l 2θ int-f h k l
42.235 100 1 0 1 85.665 25 2 1 1 131.44 12 3 1 0
48.076 35 1 1 0 90.780 12 1 0 3 132.67 25 2 1 3
51.438 14 0 0 2 92.313 12 2 0 2 134.91 12 2 2 2
70.417 10 2 0 0 109.19 4 2 2 0
73.064 18 1 1 2 126.13 10 3 0 1

Appendix

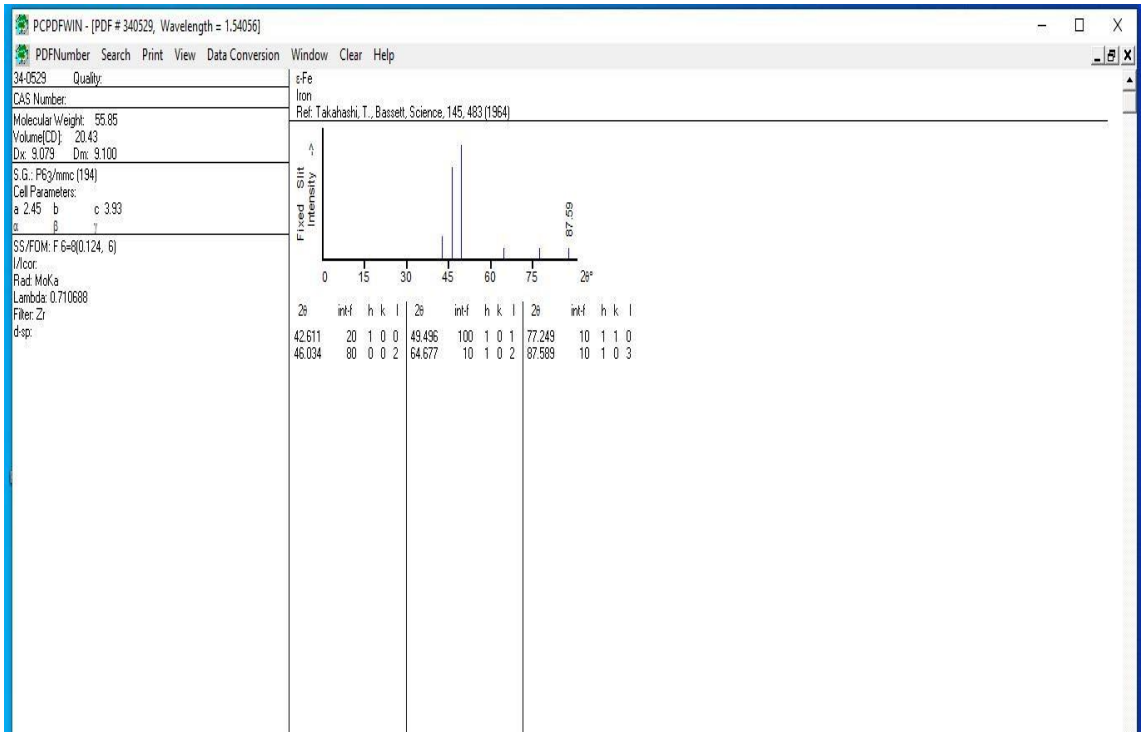
PCPDFWIN - [PDF # 340529, Wavelength = 1.54056]
PDFNumber Search Print View Data Conversion Window Clear Help
34-0529 Quality:
CAS Number:
Molecular Weight: 55.85
Volume[CD]: 20.43
Dx: 9.079 Dm: 9.100
S.G.: P63/mmc (194)
Cell Parameters:
a 2.45 b c 3.93
α β γ
SS/FOM: F 6=8(0.124, 6)
I/Icor:
Rad: MoKa
Lambda: 0.710688
Filter: Zr
d-sp:
ε-Fe
Iron
Ref: Takahashi, T., Bassett, Science, 145, 483 (1964)
Fixed Slit Intensity
87.59
0 15 30 45 60 75 2θ°
2θ int-f h k l 2θ int-f h k l 2θ int-f h k l
42.611 20 1 0 0 49.496 100 1 0 1 77.249 10 1 1 0
46.034 80 0 0 2 64.677 10 1 0 2 87.589 10 1 0 3

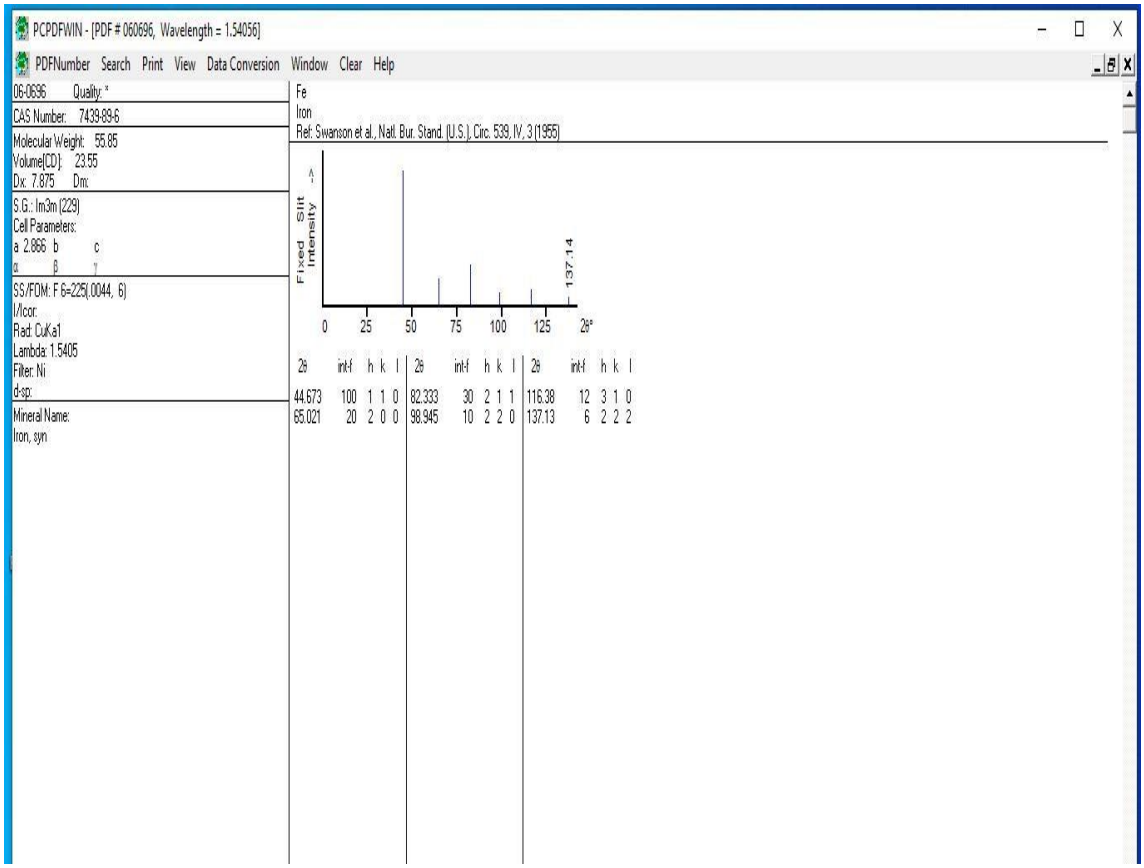
PCPDFWIN - [PDF # 060696, Wavelength = 1.54056]
PDFNumber Search Print View Data Conversion Window Clear Help
06-0696 Quality: *
CAS Number: 7439-89-6
Molecular Weight: 55.85
Volume[CD]: 23.55
Dx: 7.875 Dm:
S.G.: Im3m (229)
Cell Parameters:
a 2.866 b c
α β γ
SS/FOM: F 6=225(.0044, 6)
I/Icor:
Rad: CuKa1
Lambda: 1.5405
Filter: Ni
d-sp:
Mineral Name:
Iron, syn
Fe
Iron
Ref: Swanson et al., Natl. Bur. Stand. (U.S.), Circ. 539, IV, 3 (1955)
Fixed Slit Intensity
137.14
0 25 50 75 100 125 2θ°
2θ int-f h k l 2θ int-f h k l 2θ int-f h k l
44.673 100 1 1 0 82.333 30 2 1 1 116.38 12 3 1 0
65.021 20 2 0 0 98.945 10 2 2 0 137.13 6 2 2 2

Appendix

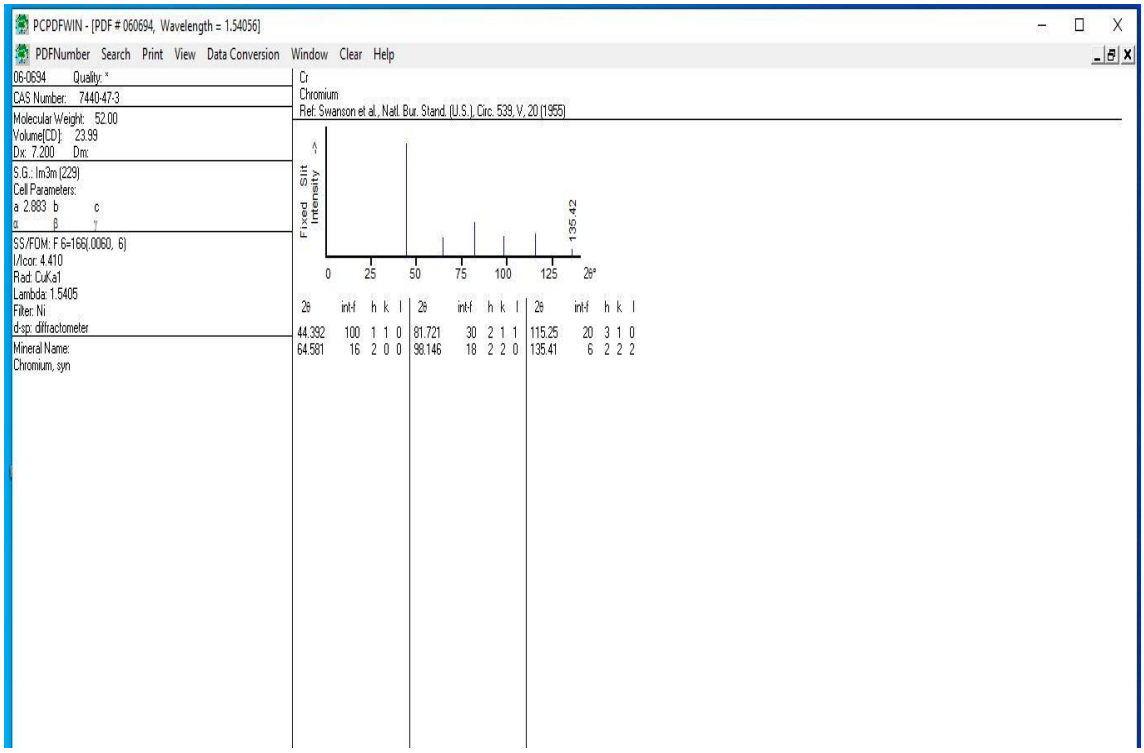
PCPDFWIN - [PDF # 060694, Wavelength = 1.54056]
PDFNumber Search Print View Data Conversion Window Clear Help
06-0694 Quality: *
CAS Number: 7440-47-3
Molecular Weight: 52.00
Volume[CD]: 23.99
Dx: 7.200 Dm:
S.G.: Im3m (229)
Cell Parameters:
a 2.883 b c
α β γ
SS/FOM: F 6=168(.0060, 6)
I/Icor: 4.410
Rad: CuKa1
Lambda: 1.5405
Filter: Ni
d-sp: diffractometer
Mineral Name:
Chromium, syn
Cr
Chromium
Ref: Swanson et al., Natl. Bur. Stand. (U.S.), Circ. 539, V, 20 [1955]
Fixed Slit Intensity
135.42
0 25 50 75 100 125 2θ°
2θ int-f h k l 2θ int-f h k l 2θ int-f h k l
44.392 100 1 1 0 81.721 30 2 1 1 115.25 20 3 1 0
64.581 16 2 0 0 98.146 18 2 2 0 135.41 6 2 2 2

الخلاصة

في هذة الدراسة، تمت دراسة البنية المجهرية وخواص الفولاذ الواطئ السبائكي (AISI 4140) بواسطة ترسيب اغشية رقيقة من سبائك العشوائية العالية والمتوسطة عند درجة حرارة ٣٠ سيليزي وعند دالة حامضية مقدارها ١.٥ وبزمن ١٥ دقيقة.

تم تحضير العينات المراد طلائها بأبعاد (٢٠ * ١٠ ملم). حيث تم ترسيب سبائك العشوائية المتوسطة من املاح العناصر المكونة للسبيكة (حديد نيكل كوبالت نحاس) وبعد ذلك تمت اضافة انابيب الكربون النانوية بنسبة ٠.٢% عند تيار مقدارة ٠.١٦ امبير وبخلط مغناطيسي مستمر. كذلك تم ترسيب سبائك العشوائية العالية المتكونة من (منغنيز كروم حديد كوبلت نيكل) و (المنيوم حديد كوبلت نيكل نحاس) و (المنيوم كروم حديد كوبلت نيكل نحاس) وكذلك تمت اضافة CNTs لتلك الخلطات بنسبة ثابتة مقدارها ٠.٢% حيث تم الترسيب بنفس ظروف عملية الطلاء لكن بتيار مقداره (٠.٤ و ٠.١٦ و ٠.٦٣ امبير) على التوالي.

تم اجراء العديد من الفحوصات المجهرية والاختبارات الميكانيكية والفيزيائية والالكتروكيميائية على العينات قبل وبعد الطلاء كاختبار الصلادة، اختبار البلى، واختبار الخشونة واختبار حيود الاشعة السينية وكذلك اختبار التاكل ، وقياس سمك طبقة الطلاء وقوة الالتصاقية. حيث ان الفحوصات المجهرية تم بواسطة المجهر الالكتروني الماسح للانبعاث الميداني (FESEM) مع استخدام التحليل الطيفي المشتت للطاقة (EDS).

ان نتائج اختبار صلادة فكرز للعينة الاساس مساوية ١٨٩ فكرز والتي ازدادت الى ٢٣٤ صلادة فكرز عند طلاء السبائك العشوائية المتوسطة ولكن عند اضافة انابيب الكربون النانوية للطلاء فان الصلادة ازدادت بمقدار ٢.٥ مرة اعلى من العينة الاساس وكانت افضل قيم الصلادة لسبيكة AlCrFeCoNiCu)-CNTs) حيث وصلت الصلادة الى ٧٨٣ صلادة فكرز وبمقدار تحسن مساوي الى ٧٥.٨%. وكذلك ابدت هذه السبيكة افضل مقاومة تاكل بمحلول كلوريد الصوديوم وكان معدل التاكل مساوي ١.١٥ mpy حيث وصلت كفاءة الطلاء في تلك السبيكة الى ٩٢.٨%.

من جهة اخرى فان سبيكة AlCrFeCoNiCu)-CNT) اظهرت كذلك افضل قوة التصاقية وافضل مقاومة بلى بالمقارنة مع السبائك الاخرى حيث كانت قوة الالتصاق تساوي ٢١.٥ ميكاباسكال ومعدل البلى مساوي الى (١.٢، ١.٤) *١٠$^{-٤}$ عند احمال مساوية الى ٥ و ١٠ نيوتن على التوالي.

من خلال نتائج اختبار خشونة السطح فان سطح سبيكة العشوائية المتوسطة هو السطح الاكثر خشونة ومقدارها ٠.٣٥ مايكرون وهذا يؤدي لجعلها ذو قابلية تبلل عالية مقارنة مع السبائك الاخرى. وكانت سبيكة AlCrFeCoNiCu اعلى سمك لطبقة الطلاء ومقدارها ١٨.٣٦ مايكرمتر.

الفحوصات المجهرية لعينات الطلاء اظهرت ان طبيعة طبقة الطلاء كثيفة ومنتظمة ومتجانسة مع شكل حبيبي والتي تصبح اكثر نعومة باضافة انابيب الكربون النانوية. بالاضافة الى ذلك فان نتائج EDS اثبتت ان سطح الطلاء يحتوي على جميع العناصر المكونة لسبائك الطلاء. ومن جهة اخرى فان تحليل نتائج حيود الاشعة السينية اظهرت ان الطلاء يتكون من مزيج طوري FCC , BCC